

# Recent Advances in Design and Signal Processing for Antenna Arrays 2020

Lead Guest Editor: Wei Liu

Guest Editors: Arjuna Madanayake, Lei Yu, Qing Shen, and Jingjing Cai





---

**Recent Advances in Design and Signal  
Processing for Antenna Arrays 2020**

International Journal of Antennas and Propagation

---

**Recent Advances in Design and Signal  
Processing for Antenna Arrays 2020**

Lead Guest Editor: Wei Liu

Guest Editors: Arjuna Madanayake, Lei Yu, Qing  
Shen, and Jingjing Cai



---

Copyright © 2023 Hindawi Limited. All rights reserved.

This is a special issue published in “International Journal of Antennas and Propagation.” All articles are open access articles distributed under the Creative Commons Attribution License, which permits unrestricted use, distribution, and reproduction in any medium, provided the original work is properly cited.

# Chief Editor

Slawomir Koziel, Iceland

## Editorial Board

Kush Agarwal, Singapore  
Ana Alejos, Spain  
Mohammad Ali, USA  
Rodolfo Araneo, Italy  
Hervé Aubert, France  
Paolo Baccarelli, Italy  
Xiulong Bao, Ireland  
Pietro Bolli, Italy  
Stefania Bonafoni, Italy  
Paolo Burghignoli, Italy  
Shah Nawaz Burokur, France  
Giuseppe Castaldi, Italy  
Giovanni Andrea Casula, Italy  
Luca Catarinucci, Italy  
Felipe Catedra, Spain  
Marta Cavagnaro, Italy  
Maggie Y. Chen, USA  
Shih Yuan Chen, Taiwan  
Renato Cicchetti, Italy  
Riccardo Colella, Italy  
Laura Corchia, Italy  
Lorenzo Crocco, Italy  
Claudio Curcio, Italy  
Francesco D'Agostino, Italy  
María Elena de Cos Gómez, Spain  
Alessandro Di Carlofelice, Italy  
Giuseppe Di Massa, Italy  
Michele D'Urso, Italy  
Francisco Falcone, Spain  
Miguel Ferrando Bataller, Spain  
Flaminio Ferrara, Italy  
Ravi Gangwar, India  
Claudio Gennarelli, Italy  
Farid Ghanem, Algeria  
Sotirios K. Goudos, Greece  
Rocco Guerriero, Italy  
Kerim Guney, Turkey  
Ashish Gupta, India  
Tamer S. Ibrahim, USA  
Muhammad Ramlee Kamarudin, Malaysia  
Dmitry V. Kholodnyak, Russia  
Rajkishor Kumar, India  
Ping Li, China  
Ding-Bing Lin, Taiwan

Angelo Liseno, Italy  
Pierfrancesco Lombardo, Italy  
Lorenzo Luini, Italy  
Praveen Kumar Malik, India  
Atsushi Mase, Japan  
Diego Masotti, Italy  
Christoph F. Mecklenbräuer, Austria  
Ahmed Toaha Mobashsher, Australia  
Ananda S. Mohan, Australia  
Jose-Maria Molina-Garcia-Pardo, Spain  
Giuseppina Monti, Italy  
Giorgio Montisci, Italy  
Andrea Francesco Morabito, Italy  
N. Nasimuddin, Singapore  
Mohammad H. Neshati, Iran  
Symeon Nikolaou, Cyprus  
Giacomo Oliveri, Italy  
Amrindra Pal, India  
Dr. Sandeep Kumar Palaniswamy, India  
Mauro Parise, Italy  
Ikmo Park, Republic of Korea  
Josep Parrón, Spain  
Shobhitkumar Patel, India  
Anna Pietrenko-Dabrowska, Poland  
Khaled ROUABAH, Algeria  
Ahmad Safaai-Jazi, USA  
Safieddin Safavi-Naeini, Canada  
Stefano Selleri, Italy  
Raffaele Solimene, Italy  
Gina Sorbello, Italy  
Seong-Youp Suh, USA  
Larbi Talbi, Canada  
Luciano Tarricone, Italy  
Sreenath Reddy Thummaluru, India  
Giuseppe Torrisi, Italy  
Trushit Upadhyaya, India  
Chien-Jen Wang, Taiwan  
Mustapha C E Yagoub, Canada  
Shiwen Yang, China  
Yuan Yao, China  
Tao Zhou, China  
Muhammad Zubair, Pakistan



# Contents

## **Recent Advances in Design and Signal Processing for Antenna Arrays 2020**

Wei Liu , Arjuna Madanayake, Lei Yu , Qing Shen , and Jingjing Cai 




Editorial (2 pages), Article ID 9843456, Volume 2023 (2023)

## **Thinned Virtual Array for Cramer Rao Bound Optimization in MIMO Radar**

Xia Li  and Buhong Wang 

Research Article (13 pages), Article ID 1408498, Volume 2021 (2021)

## **Development of a Pin Diode-Based Beam-Switching Single-Layer Reflectarray Antenna**

Muhammad Inam Abbasi , Muhammad Yusof Ismail , and Muhammad Ramlee Kamarudin 

Research Article (9 pages), Article ID 8891759, Volume 2020 (2020)

## **Maximum Likelihood Angle-Range Estimation for Monostatic FDA-MIMO Radar with Extended Range Ambiguity Using Subarrays**

Kaikai Yang, Sheng Hong , Qi Zhu, and Yanheng Ye




Research Article (10 pages), Article ID 4601208, Volume 2020 (2020)

## **Nonuniformly Spaced Array with the Direct Data Domain Method for 2D Angle-of-Arrival Measurement in Electronic Support Measures Application from 6 to 18 GHz**

Chen Wu  and Janaka Elangage


Research Article (23 pages), Article ID 9651650, Volume 2020 (2020)

## **Spread Sea Clutter Suppression in HF Hybrid Sky-Surface Wave Radars Based on General Parameterized Time-Frequency Analysis**

Zhuo-qun Wang , Ya-jun Li , Jun-nan Shi, Peng-fei Wang, Ai-hua Liu , Xin-fan Xia, and De-hong Chen

Research Article (12 pages), Article ID 7627521, Volume 2020 (2020)

## **Two-Dimensional Beampattern Synthesis for Polarized Smart Antenna Array and Its Sparse Array Optimization**

Zhikun Chen , Tao Li, Dongliang Peng, and Kang Du

Research Article (13 pages), Article ID 2196049, Volume 2020 (2020)

## Editorial

# Recent Advances in Design and Signal Processing for Antenna Arrays 2020

Wei Liu <sup>1</sup>, Arjuna Madanayake,<sup>2</sup> Lei Yu <sup>3</sup>, Qing Shen <sup>4</sup>, and Jingjing Cai <sup>5</sup>

<sup>1</sup>University of Sheffield, Sheffield, UK

<sup>2</sup>Florida International University, Miami, FL, USA

<sup>3</sup>Harbin Institute of Technology, Harbin, China

<sup>4</sup>Beijing Institute of Technology, Beijing, China

<sup>5</sup>Xidian University, Xi'an, China

Correspondence should be addressed to Wei Liu; [w.liu@sheffield.ac.uk](mailto:w.liu@sheffield.ac.uk)

Received 14 May 2022; Accepted 14 May 2022; Published 3 February 2023

Copyright © 2023 Wei Liu et al. This is an open access article distributed under the Creative Commons Attribution License, which permits unrestricted use, distribution, and reproduction in any medium, provided the original work is properly cited.

Compared with a single physical antenna, an antenna array has the capability for effective interference suppression/beamforming, direction of arrival (DOA) estimation, target tracking, and localization with its additional spatial degrees of freedom (DOFs) exploited by advanced signal processing algorithms [1–4]. It has received considerable attention given its wide range of applications in radar, sonar, sensor networks, navigation, biomedical engineering, wireless communications, etc., and one good example is the 2020 IEEE 5-Minute Video Clip Contest (5-MICC) about beamforming with more than 5000 researchers casting their votes in the process [5]. In particular, the antenna array design and signal processing is one of the fundamental techniques in wireless communication systems of the 5G and beyond since the two underpinning 5G technologies, massive multiple-input multiple-output (MIMO) and millimetre wave communications, are all based on antenna array systems [6, 7]. It will continue playing a significant role in many other aspects in the future, such as Internet of Things (IoT) and integrated sensing and communication (ISAC) [8–10], both of which are potential technologies for 6G wireless communication systems and intelligent transportation systems with extensive research activities already attracted in the community.

Given the continued importance of design and signal processing for antenna arrays and also following the success of the first special issue published in 2016 focusing on the same topic [11], we were approached by the journal office to organize a second special issue with the same topic. The aim of

this current special issue is to present the most recent advances in the area of design and signal processing for various antenna arrays and their applications, by inviting both review articles and original contributions from researchers working in this very important area, and in total, we received 15 submissions and 6 were accepted for publication.

The accepted papers cover a wide range of topics within the specified area of the special issue. Roughly speaking, they fall into the following four main topics. The first topic is antenna design for array applications, including one paper titled “Development of a Pin Diode-Based Beam-Switching Single-Layer Reflectarray Antenna” [12]; the second topic is antenna array pattern synthesis, including one paper titled “Two-Dimensional Beampattern Synthesis for Polarized Smart Antenna Array and Its Sparse Array Optimization” [13]; the third topic is direction/angle of arrival estimation, including two papers, titled “Thinned Virtual Array for Cramer Rao Bound Optimization in MIMO Radar” and “Nonuniformly Spaced Array with the Direct Data Domain Method for 2D Angle-of-Arrival Measurement in Electronic Support Measures Application from 6 to 18 GHz” [14, 15], respectively; the last topic is target detection and localization (range/velocity/angle estimation) based on antenna arrays, including two papers, titled “Spread Sea Clutter Suppression in HF Hybrid Sky-Surface Wave Radars Based on General Parameterized Time-Frequency Analysis” and “Maximum Likelihood Angle-Range Estimation for Monostatic FDA-MIMO Radar with Extended Range Ambiguity Using Subarrays” [16, 17], respectively.

## Conflicts of Interest

We declare no conflicts of interest regarding the publication of this special issue.

## Acknowledgments

Finally, we would like to thank the authors for their valuable contributions to this special issue and the anonymous reviewers for their kind help and constructive comments, without which we would not have been able to complete this special issue with the set of high-quality papers in such a short period of time.

Wei Liu  
Arjuna Madanayake  
Lei Yu  
Qing Shen  
Jingjing Cai

## References

- [1] R. T. Compton, *Adaptive Antennas: Concepts and Performance*, Prentice-Hall, Englewood Cliffs, NJ, 1988.
- [2] H. L. Van, *Trees, Optimum Array Processing, Part IV of Detection, Estimation, and Modulation Theory*, Wiley, New York, 2002.
- [3] W. Liu and S. Weiss, *Wideband Beamforming: Concepts and Techniques*, John Wiley & Sons, Chichester, UK, 2010.
- [4] Q. Luo, S. Gao, W. Liu, and C. Gu, *Low-cost Smart Antennas*, John Wiley & Sons, 2019.
- [5] W. Liu, M. R. Anbiyai, X. Jiang, L. Zhang, and L. Marcenaro, "Let there Be a beam: highlights from the 2020 IEEE five-minute Video Clip contest," *IEEE Signal Processing Magazine*, vol. 37, no. 5, pp. 157–162, 2020.
- [6] F. Boccardi, R. W. Heath, A. Lozano, T. L. Marzetta, and P. Popovski, "Five disruptive technology directions for 5G," *IEEE Communications Magazine*, vol. 52, no. 2, pp. 74–80, 2014.
- [7] W. Roh, J. Seol, J. Park et al., "Millimeter-wave beamforming as an enabling technology for 5G cellular communications: theoretical feasibility and prototype results," *IEEE Communications Magazine*, vol. 52, no. 2, pp. 106–113, 2014.
- [8] T. L. Marzetta, E. G. Larsson, H. Yang, and H. Q. Ngo, *Fundamentals of Massive MIMO*, Cambridge Univ. Press, Cambridge, U.K, 2016.
- [9] K. V. Mishra, M. R. Bhavani Shankar, V. Koivunen, B. Ottersten, and S. A. Vorobyov, "Toward millimeter-wave joint radar communications: a signal processing perspective," *IEEE Signal Processing Magazine*, vol. 36, no. 5, pp. 100–114, September 2019.
- [10] Y. Cui, F. Liu, X. Jing, and J. Mu, "Integrating sensing and communications for ubiquitous IoT: applications, trends, and challenges," *IEEE Network*, vol. 35, no. 5, pp. 158–167, 2021.
- [11] W. Liu, D. C. McLernon, A. W. H. Khong, and L. Yu, "Recent advances in design and signal processing for antenna arrays," *International Journal of Antennas and Propagation*, vol. 2, 2016.
- [12] M. I. Abbasi, M. Y. Ismail, and M. R. Kamarudin, "Development of a pin diode-based beam-switching single-layer reflectarray antenna," *International Journal of Antennas and Propagation*, vol. 2020, Article ID 8891759, 9 pages, 2020.
- [13] Z. K. Chen, T. Li, D. L. Peng, and K. Du, "Two-dimensional beam pattern synthesis for polarized smart antenna array and its sparse array optimization," *International Journal of Antennas and Propagation*, vol. 2020, Article ID 2196049, 13 pages, 2020.
- [14] X. Li and B. H. Wang, "Thinned virtual array for Cramer Rao bound optimization in MIMO radar," *International Journal of Antennas and Propagation*, vol. 2021, Article ID 1408498, 13 pages, 2021.
- [15] C. Wu and J. Elangage, "Nonuniformly spaced array with the direct data domain method for 2D angle-of-arrival measurement in electronic support measures application from 6 to 18 GHz," *International Journal of Antennas and Propagation*, vol. 2020, Article ID 9651650, 23 pages, 2020.
- [16] Z. Q. Wang, Y. J. Li, J. N. Shi et al., "Spread sea clutter suppression in HF hybrid sky-surface wave radars based on general parameterized time-frequency analysis," *International Journal of Antennas and Propagation*, vol. 2020, Article ID 7627521, 12 pages, 2020.
- [17] K. K. Yang, S. Hong, Q. Zhu, and Y. H. Ye, "Maximum likelihood angle-range estimation for monostatic FDA-MIMO radar with extended range ambiguity using sub-arrays," *International Journal of Antennas and Propagation*, vol. 2020, Article ID 4601208, 10 pages, 2020.



## Research Article

# Thinned Virtual Array for Cramer Rao Bound Optimization in MIMO Radar

Xia Li  and Buhong Wang 

Information and Navigation College, Air Force Engineering University, Xi'an 710077, China

Correspondence should be addressed to Buhong Wang; [wbhgroup@aliyun.com](mailto:wbhgroup@aliyun.com)

Received 31 July 2020; Revised 5 December 2020; Accepted 28 December 2020; Published 15 January 2021

Academic Editor: Qing Shen

Copyright © 2021 Xia Li and Buhong Wang. This is an open access article distributed under the Creative Commons Attribution License, which permits unrestricted use, distribution, and reproduction in any medium, provided the original work is properly cited.

By transmitting multiple independent waveforms at the transmit side and processing echoes of spatial targets at the receive side, Multiple Input Multiple Output (MIMO) radar enjoys virtual array aperture expansion and more degree of freedom (DOF), both of which favors the application of direction finding or estimation of direction of arrival (DOA). The expanded virtual aperture provides higher angular resolution which also promotes the precision of DOA estimation, and the extra DOF brought by waveform diversity can be leveraged to focus energy in certain spatial region for better direction-finding capacity. However, beamspace methods which match certain beampatterns suffer from deteriorated performance and complexity in implementation, and the advantage of virtual array aperture is limited by its virtual element redundancy. As an important performance indicator of DOA estimation, Cramer-Rao Bound (CRB) is closely connected to the array configuration of the system. To reduce the complexity of the system and improve CRB performance at the same time, in this paper, the virtual array of MIMO radar is designed directly by selecting outputs from matched filters at the receive side. For the sake of fair comparison, both scenarios with and without priori directions are considered to obtain optimized virtual array configuration, respectively. The original combinatorial problems are approximated by sequential convex approximations methods which produce solutions with efficiency. Numerical results demonstrate that the proposed method can provide thinned virtual arrays with excellent CRB performance.

## 1. Introduction

In various applications of radar system, such as beamforming and interference suppression, the Direction of Arrival (DOA) is often needed as a priori information [1]. Inversely, the performance of DOA estimation can be improved by proper beamforming and interference suppression [2]. Therefore, DOA estimation is a prerequisite for various applications as well as the purpose after other processing procedures, which is of great importance to the array of the radar system [3].

The performance of DOA estimation is related to the properties of array, which includes the aperture and structure of the array. In MIMO radar, each element of transmit array sends one of multiple independent waveforms, the echoes of which are received by the receive array and processed through matched filters. The data after matched filtering operation is

equivalent to the one received by an array with larger array aperture, which is often referred to as virtual array. The aperture of virtual array is usually larger than that of both transmit and receive array, which is helpful for DOA estimation since larger aperture is productive for angle resolution [4]. However, such expansion of virtual array aperture is limited by the redundancy of virtual array elements rendered by the adoption of uniform array configuration at both transmit and receive side. Even though both transmit array and receive array are uniformly distributed without spatial tapering in most cases of MIMO radar, the virtual array configuration obtained by the spatial convolution of transmit array and receive array is characterized by the fact that one element in the virtual array may correspond to several pairs consisting of elements from both transmit array and receive array, producing redundancies of virtual array elements [5]. Such redundancy not only leads to the waste of element

resources and increase of hardware complexity but also produces array shading effect which often adds unwanted weights on the virtual array elements, contributing to the reduction of array performance. To tackle the redundancy of virtual array and reduce the hardware cost and complexity of the system, references [6–8] propose to model the virtual array as polynomial and decompose the polynomial to obtain thinned polynomials which represent both transmit array and receive array. In these problems, the virtual array is given as a uniform one to eliminate negative effects brought by unwanted weights in the virtual array and obtain thinned transmit and receive arrays to reduce hardware complexity. However, the number of possible solutions, i.e., the possible combinations of thinned transmit and receive arrays, are limited due to the intrinsic nature of spatial convolution. To enlarge the scope of solution space and obtain larger virtual aperture while preserving the thinned transmit array and receive array, mathematical tools such as difference sets [9], cyclic difference sets [10], and almost difference sets [11], as well as numerical optimization methods such as genetic algorithm [12] and simulated annealing [13] are proposed to obtain more available solutions for thinned transmit and receive array given the same number of elements, whereas the optimality of solutions depends on the initial points for the numerical problems and the computational complexity of the problem is much larger than polynomial decomposition. To obtain an even larger virtual aperture with thinned transmit array and receive array, coprime array [14–16] and nested array [17–19] are proposed together with the difference co-array processing method, which utilizes  $O(N)$  elements to achieve  $O(N^2)$  or even  $O(N^4)$  DOF. In this way, larger DOF promotes parameter identifiability and angular resolution of the array, but such difference co-array-based array configuration is prone to error and distortion from the multipath effect in practical applications. These array configurations for the MIMO radar are focused on improving DOA estimation performance by expanding virtual array aperture using thinned transmit array and receive array [20]. However, larger virtual aperture does not necessarily translate to higher estimation precision of the MIMO radar [21].

The performance of DOA estimation depends on the effective array aperture on the direction to be estimated, which means that the array configuration with the best DOA estimation performance is determined by the DOA to be estimated [22]. In fact, as a metric representing the limit performance of array and DOA estimation, the Cramer–Rao Bound (CRB) is closely related to the array configuration of the system and the estimated direction [23]. Meanwhile, in practical applications of direction finding, priori information on the estimated direction is often available. Therefore, in order to fully utilize DOF from the configuration of the virtual array to achieve lower total CRB, a thinned virtual array is proposed. The work of this paper is summarized as follows:

- (1) The signal model of the MIMO radar is proposed, in which the virtual array expansion and the connection between virtual array configurations are discussed. Since the performance of DOA estimation or

CRB of the MIMO radar depends on the structure of virtual array, the connection between virtual array structure, fisher information matrix (FIM), and CRB is discussed to reveal the impact of array configuration on the direction-finding performance of certain spatial targets, and analytical expressions are derived.

- (2) Due to the uniformity in the distribution of elements in both transmit array and receive array, elements in the virtual array are redundant. Reducing such redundancy not only decreases the hardware complexity and waste of system resources but also provides potential for utilizing the DOF provided from the configuration of the array by incorporating priori DOA information in the structure of thinned array to achieve lower total CRB of the system. In this way, the redundancy of the virtual array structure is analysed and relation between the total CRB and virtual array configuration is generalized to derive the CRB expression of thinned virtual array configuration.
- (3) Based on these analyses, the optimization problem for obtaining thinned virtual array is proposed. Both the scenario with and without directional information are considered. Because of the fractional structure and nonconvex constraints, the solution to the original form of the proposed problem requires enumeration with high-computational complexity. To solve the problem efficiently, the Dinkelbach method is used to approximate the original problem into a series of subproblems, all of which can be solved iteratively. The final solution to the problem is obtained by solving another optimal integer constraint problem. Numerical results show CRB and DOA estimation performance to validate the advantage of the proposed thinned virtual array.

It should be noted that the goal of this paper is thinning the virtual array configuration directly through turning off some of matched filters on the receive side rather than designing thinned transmit and receive arrays to obtain thinned virtual array. Compared to thinning transmit array and receive array, respectively, the proposed scheme has the following advantages:

- (1) Even though thinning transmit and receive arrays separately achieve more reduction of hardware resources than thinning virtual array directly, such separated scheme has fewer DOF for increased performance due to limited number of virtual array structures formed by spatial convolution of transmit and receive array structures, whose combinations are also limited. Meanwhile, the joint scheme can produce arbitrary virtual array configuration by turning off matched filters and thus enjoys more possibilities for increased system performance.
- (2) The direct thinning of virtual array entails a precondition that the virtual array must be fully filled or at least one virtual element exists at the sensor

positions of the obtained array. In other words, the joint scheme requires both transmit array and receive array to be fully filled, which appears to waste hardware resources than that of the separated scheme. However, the precondition of fully filled also implies that the proposed joint scheme can be achieved without changing configuration of physical elements in transmit array and receive array. This enables fast deployment of the proposed scheme on obsolete systems with filled arrays, and fast reconfiguration of virtual array on the MIMO radar at work. The proposed scheme is neither better than any other existing ways of thinning virtual arrays nor the one with lowest cost or fastest speed. Rather, this scheme is proposed to provide a possibility to improve the direction-finding performance with more DOF on existing MIMO radar systems.

The rest of the paper is organized as follows. Section 2 introduces the signal model, which deals with virtual array aperture expansion in the MIMO radar, redundancy in virtual array structure, and the connection between virtual array and CRB. The design of thinned virtual array for optimization of CRB is discussed in Section 3, considering both scenarios with and without priori directional information. Numerical results are provided in Section 4, followed by conclusion in Section 5.

## 2. Signal Model

Consider a MIMO radar system with transmit array of  $M_t$  elements and receive array of  $M_r$  elements. The position of the  $m$ th transmit array element is  $(x_m, y_m)$  ( $m = 1, \dots, M_t$ ) and the position of the  $n$ th receive array element is  $(x_n, y_n)$  ( $n = 1, \dots, M_r$ ). Assume that the distance between transmit and receive arrays is much fewer than wavelength  $\lambda$  so that the target direction with respect to transmit array is the same as the target direction with respect to receive array, and all elements in both transmit and receive arrays share the same carrier frequency  $F_c$ . It is also assumed that there are  $L$  targets with elevation angles  $\theta_l$  ( $l = 1, \dots, L$ ) and azimuth angles  $\phi_l$  ( $l = 1, \dots, L$ ). In the transmit array, each element transmits an orthogonal waveform towards the target, and the complex envelope of the waveform at the  $m$ th element can be denoted as

$$s_m(t) = \rho \phi_m(t), \quad m = 1, \dots, M_t, \quad (1)$$

where  $t$  denotes fast-time index, i.e., the time index within a radar pulse,  $\rho$  is the energy coefficient of waveform to normalize the sum of energy of all transmitted waveforms as constant, And  $\phi_m(t)$  is the  $m$ th orthogonal baseband waveform. After up conversion, the signal sent from the  $m$ th element can be correspondingly denoted as  $s_m(t)\exp(j2\pi F_c t)$ , where the term  $\exp(j2\pi F_c t)$  represents the carrier.

The radar echo signal at the  $l$ th target is represented as

$$r_1(t, \tau) = \rho \beta_l(\tau) \mathbf{a}^T(\theta_l) \boldsymbol{\phi}(t) \exp(j2\pi F_c t), \quad (2)$$

where  $\beta_l(\tau)$  denotes the reflection coefficient of the  $l$ th target,  $\mathbf{a}(\theta_l)$  is the transmit steering vector corresponding to the  $l$ th target, and  $\boldsymbol{\phi}(t) = [\phi_1(t), \phi_2(t), \dots, \phi_{M_t}(t)]^T$  is the vector consists of  $M_t$  orthogonal waveforms. It should be noted that the reflection coefficient within a single radar pulse remains the same yet different between different pulses.

All orthogonal waveforms from the transmit array is reflected from the target and captured by the receive array. The received signal is then down-converted to baseband by multiplying with  $\exp(-j2\pi F_c t)$ . In this way, the  $M_r \times 1$  baseband equivalent of received echo signal can be expressed as

$$\mathbf{x}(t, \tau) = \sum_{l=1}^L r_l(t, \tau) \exp(-j2\pi F_c t) \mathbf{b}(\theta_l) + \mathbf{z}(t, \tau), \quad (3)$$

where  $\tau$  represents slow time index, which is the index of radar pulse,  $\mathbf{b}(\theta_l)$  denotes the steering vector corresponding to the  $l$ th target with direction  $\theta_l$ , and  $\mathbf{z}(t, \tau)$  is an  $M_r \times 1$  Gaussian white noise.

*2.1. Virtual Array Aperture Expansion.* The transmit steering vector and receive steering vector can be expressed as

$$\begin{aligned} \mathbf{a}(\theta) &= \exp[jk_0(x_1 u_x + y_1 u_y), \dots, jk_0(x_{M_t} u_x + y_{M_t} u_y)]^T, \\ \mathbf{b}(\theta) &= \exp[jk_0(x_1 u_x + y_1 u_y), \dots, jk_0(x_{M_r} u_x + y_{M_r} u_y)]^T, \end{aligned} \quad (4)$$

where  $k_0 = (2\pi/\lambda)$ ,  $u_x = \cos \theta \cos \phi$ , and  $u_y = \cos \theta \sin \phi$ .

Since the transmitted equivalent waveforms are orthogonal or linearly independent from each other, the component corresponding to a single waveform can be extracted using matched filters on the receive array. After going through the down conversion at the receiver side, the  $M_r \times 1$  baseband equivalent data vector corresponding to the  $m$ th orthogonal waveform can be expressed as

$$\mathbf{x}_m(\tau) = \int_T \mathbf{x}(t, \tau) \phi_m^*(t) dt, \quad m = 1, \dots, M_t. \quad (5)$$

Stacking all data component vectors corresponding to different waveforms in a columnwise manner, an  $M_t M_r \times 1$  virtual data vector can be obtained as

$$\begin{aligned} \mathbf{v}(\tau) &= \rho \sum_{l=1}^L \beta_l(\tau) (\mathbf{a}(\theta_l) \otimes \mathbf{b}(\theta_l)) + \tilde{\mathbf{z}}(\tau) \\ &= \rho \sum_{l=1}^L \beta_l(\tau) \mathbf{u}(\theta_l) + \tilde{\mathbf{z}}(\tau), \end{aligned} \quad (6)$$

where

$$\mathbf{u}(\theta) = \mathbf{a}(\theta) \otimes \mathbf{b}(\theta) \quad (7)$$

denotes  $M_t M_r \times 1$  virtual array steering vector and  $\tilde{\mathbf{z}}(\tau)$  is  $M_t M_r \times 1$  noise term with covariance matrix as  $\sigma_z^2 \mathbf{I}_{M_t M_r}$

It can be inferred from (7) that the virtual data vector can be seen as a signal received by an  $M_t M_r \times 1$  array. This is equivalent to the case that spatial signal is received by a virtual array with larger aperture, which is depicted in Figure 1. Usually, an array with larger aperture implies better

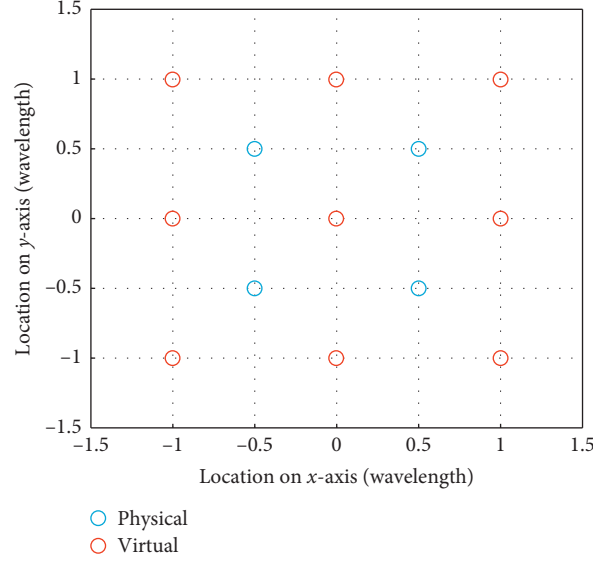


FIGURE 1: Virtual array expansion.

DOA estimation performance, yet this is not the case with MIMO radar virtual array. To demonstrate the effect of virtual array design on the performance of direction finding, the connection between virtual array structure and CRB is to be discussed in Section 2.2.

**2.2. Connection between Virtual Array and CRB.** To simplify subsequent analysis, the following vectors are defined based on the location of array elements:

$$\begin{aligned}
 \mathbf{x} &= [x_1 + x_1, x_1 + x_2, \dots, x_1 + x_{M_r}, x_2 + x_1, \dots, x_2 + x_{M_r}, \dots, x_{M_t} + x_{M_r}]^T, \\
 \mathbf{y} &= [y_1 + y_1, y_1 + y_2, \dots, y_1 + y_{M_r}, y_2 + y_1, \dots, y_2 + y_{M_r}, \dots, y_{M_t} + y_{M_r}]^T, \\
 \mathbf{x}_x &= [(x_1 + x_1)^2, \dots, (x_1 + x_{M_r})^2, (x_2 + x_1)^2, \dots, (x_2 + x_{M_r})^2, \dots, (x_{M_t} + x_{M_r})^2]^T, \\
 \mathbf{y}_y &= [(y_1 + y_1)^2, \dots, (y_1 + y_{M_r})^2, (y_2 + y_1)^2, \dots, (y_2 + y_{M_r})^2, \dots, (y_{M_t} + y_{M_r})^2]^T, \\
 \mathbf{x}_y &= [(x_1 + x_1)(y_1 + y_1), \dots, (x_{M_t} + x_{M_r})(y_{M_t} + y_{M_r})]^T.
 \end{aligned} \tag{8}$$

Assume that a target locates at  $(\theta, \phi)$ , where  $\theta$  is the elevation and  $\phi$  is the azimuth. During one specific pulse, the  $k$ th sample signal received by the system is  $\mathbf{y}(k)$ ,  $k = 0, 1, \dots, N - 1$ . Stack all data by columns to form new column vector:

$$\mathbf{z} = [\mathbf{v}(0)^T, \dots, \mathbf{v}(N-1)^T]^T. \tag{9}$$

Let the array response of system in the noise-free condition be

$$\mathbf{u}(k) = \sum_{l=1}^L \rho \beta_l \mathbf{b}(\theta_l, \phi_l) \mathbf{a}^T(\theta_l, \phi_l) \phi(k). \tag{10}$$

Then,

$$\mathbb{E}\{\mathbf{z}\} = \mathbf{u} = [\mathbf{u}(0)^T, \dots, \mathbf{u}(N-1)^T]^T. \tag{11}$$

This means that the received data  $\mathbf{z}$  conforms to the complex Gaussian distribution with  $\mathbf{u}$  as mean and  $\sigma_z^2 \mathbf{I}_{M_r K}$  as covariance matrix, which also implies that the estimator  $\mathbf{z}$  is the minimum variance unbiased estimator of  $\mathbf{u}$ . The probability density function (PDF) is

$$p(\mathbf{z}, \Omega) = \frac{1}{\pi^{M_r N} \sigma_z^{2M_r N}} \exp \left\{ -\frac{1}{\sigma_z^2} (\mathbf{z} - \mathbf{u})^H (\mathbf{z} - \mathbf{u}) \right\}. \tag{12}$$

For the existence of minimum variance, it is assumed that the PDF satisfies the regularity condition:

$$\mathbb{E} \left[ \frac{\partial \ln p(\mathbf{z}, \Omega)}{\partial \Omega} \right] = 0, \quad \text{for all } \Omega, \tag{13}$$

where the expectation operator is taken with respect to the PDF  $p(\mathbf{z}, \Omega)$ . For each element in the parameter vector  $\Omega = [\theta, \phi]^T$ , the lower bound of the estimation variance of each element exists. Such lower bound is the so-called CRB.

CRB can be derived by conducting inverse operation on the Fisher information matrix:

$$\text{var}(\hat{\Omega}_i) \geq [\mathbf{J}^{-1}]_{ii}, \quad 1 \leq i \leq 2, \quad (14)$$

where  $\text{var}(\bullet)$  denotes the variance,  $\hat{\Omega}_i$  is the estimate of the  $i$ th element in the parameter vector, and  $[\mathbf{J}^{-1}]_{ii}$  denotes the  $(i, i)$  element in the inverse of the Fisher information matrix  $\mathbf{J}$ , which is the  $i$ th element on the diagonal.

The element of the Fisher information matrix can be given by the following expression:

$$\mathbf{J}_{i,j} = f(\Omega_i, \Omega_j) = \mathbb{E} \left[ \frac{\partial \ln p(\mathbf{z}, \boldsymbol{\Omega})}{\partial \Omega_i} \frac{\partial \ln p(\mathbf{z}, \boldsymbol{\Omega})}{\partial \Omega_j} \right]. \quad (15)$$

The Fisher information matrix, therefore, can be expressed as

$$\mathbf{J} = \begin{bmatrix} f(\theta, \theta) & f(\theta, \phi) \\ f(\phi, \theta) & f(\phi, \phi) \end{bmatrix}. \quad (16)$$

Among all elements in the matrix, the Fisher information corresponding to the parameter  $\theta$  is

$$f(\theta, \theta) = G \sin^2 \theta (Q_{xx} \cos^2 \phi + Q_{yy} \sin^2 \phi + Q_{xy} \sin(2\phi)), \quad (17)$$

where  $G$  represents the constant term irrelevant to the directions and  $Q_{xx}$ ,  $Q_{yy}$ , and  $Q_{xy}$  are called inertia momentum, which are defined as follows:

$$\begin{aligned} Q_{xx} &= \sum_{m=1}^{M_t} \sum_{n=1}^{M_r} (x_m + x_n)^2 = \mathbf{1}^T \mathbf{X}_x, \\ Q_{yy} &= \sum_{m=1}^{M_t} \sum_{n=1}^{M_r} (y_m + y_n)^2 = \mathbf{1}^T \mathbf{y}_y, \\ Q_{xy} &= \sum_{m=1}^{M_t} \sum_{n=1}^{M_r} (x_m + x_n)(y_m + y_n) = \mathbf{1}^T \mathbf{x}_y. \end{aligned} \quad (18)$$

The Fisher information corresponding to the parameter  $\phi$  is

$$f(\phi, \phi) = G \cos^2 \theta (Q_{xx} \sin^2 \phi + Q_{yy} \cos^2 \phi - Q_{xy} \sin(2\phi)). \quad (19)$$

Note that the matrix  $\mathbf{J}$  is symmetric, and the cross-term is therefore

$$\begin{aligned} f(\theta, \phi) &= f(\phi, \theta) \\ &= \frac{G}{4} \sin(2\theta) [(Q_{xx} - Q_{yy}) \sin(2\phi) - 2Q_{xy} \cos(2\phi)]. \end{aligned} \quad (20)$$

The derivation of (17), (19), and (20) is provided in Appendix A.

As discussed above, the CRB matrix is defined to be the inverse of the matrix  $\mathbf{J}$  so that the CRB of parameter  $\theta$  can be expressed as

$$C(\theta, \theta) = f(\phi, \phi) [f(\theta, \theta) f(\phi, \phi) - f^2(\theta, \phi)]^{-1}. \quad (21)$$

Similarly, the CRB of parameter  $\phi$  can be expressed as

$$C(\phi, \phi) = f(\theta, \theta) [f(\theta, \theta) f(\phi, \phi) - f^2(\theta, \phi)]^{-1}. \quad (22)$$

It can be revealed from above that the array configuration has an important impact on CRB through inertia momentum. In the same way, the virtual array configuration has an effect on the CRB of the MIMO radar through inertia momentum of virtual array elements. The redundancy of elements in virtual array from uniform virtual array configuration and the comparison between thinning transmit array and receive array and thinning virtual array are discussed in Section 2.3.

**2.3. Redundancy in Virtual Array Structure.** It has been mentioned in Section 2.2 that the virtual data vector obtained from the matched filtering on the  $M_r \times 1$  receive array, which receives echoes of orthogonal waveforms from  $M_t \times 1$  transmit array, can be considered as the signal received by an  $M_t M_r \times 1$  array. In this way, a virtual array with virtual expanded aperture is achieved, which is helpful for DOA estimation. However, multiple elements occupy the same locations in the virtual array, causing the redundancy in the virtual array. These redundant elements not only renders inadequate use of virtual elements from the transmit array and receive array but also affects the output of virtual elements brought by intrinsic weighting from the redundancy. The redundancy of elements in the virtual array is sketched in Figure 2, where the height on each location denotes the number of repetitive elements in the virtual array aperture, which implies the level of redundancy. Such redundancy cannot be eliminated through the thinning in transmit array or receive array since the virtual array steering vector is constructed by the spatial convolution of transmit and receive steering vectors. Furthermore, the DOF in thinning transmit array and receive array separately is limited due to the fact that once an element in transmit array or receive array is not in their thinned counterparts, all virtual elements corresponding to the discarded element are not in the thinned virtual array. To reduce the redundancy in the virtual array and increase the DOF in the design of thinned virtual array, more flexible ways of thinning are needed.

To serve the purpose of increasing DOF for designing thinned virtual array, the structure of MIMO is considered. In the receive array of the MIMO radar, each element is followed by several matched filters, each of which corresponds to one independent waveforms from transmit array so that each waveform component in the echoes can be separated after match filtering operation. In this way, each element in the receive array is followed by  $M_r$  matched filters, paired with  $M_t$  orthogonal waveforms in the transmit array; the total number of matched filters is  $M_t M_r$ , which is the same as the dimensions of virtual steering vector and virtual data vector. In fact, thanks to the orthogonality of waveforms, each output data component from each matched filters is equivalent to the output from element in the virtual array which takes virtual location determined by its

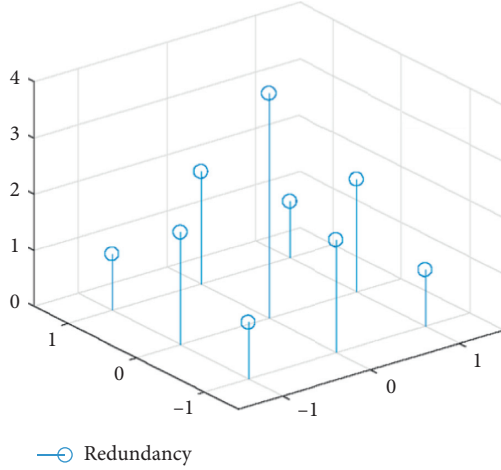


FIGURE 2: Redundancy in virtual array.

corresponding transmit and receive elements. When some matched filters are failed or unable to produce normal results, such failure of matched filters can also be seen as that of virtual elements. Therefore, by adjusting the output of each matched filter, different elements in the virtual array can be selected to implement specific virtual array configuration so that the redundancy of virtual array elements is reduced and the DOF in the virtual array is utilized in a more flexible manner, e.g., exploiting the connection between the virtual array structure and system performance.

To realize the direct thinning of virtual array, a virtual array thinning vector is defined as  $\mathbf{w} \in \{0, 1\}^{M_t M_r}$ , which means  $\mathbf{w}$  only contains ones and zeros. For each element in  $\mathbf{w}$ , 1 indicates that this element is in the thinned virtual array and 0 indicates that this element is not. Assuming that  $K$  elements are to be selected from  $M_t M_r$  elements to compose thinned virtual array, the gravity center of the thinned virtual array can be expressed as

$$\begin{aligned} x_c &= \frac{1}{K} \sum_i^{M_t M_r} w_i x_i = \frac{1}{K} \mathbf{w}^T \mathbf{x}, \\ y_c &= \frac{1}{K} \sum_i^{M_t M_r} w_i y_i = \frac{1}{K} \mathbf{w}^T \mathbf{y}, \end{aligned} \quad (23)$$

where  $w_i$  denotes the  $i$ th elements in the vector  $\mathbf{w}$ . For the sake of simplicity and without the loss of generality, assume the gravity center of virtual thinned array locates at the origin of the plane, i.e.,

$$\begin{aligned} x_c &= \frac{1}{K} \mathbf{w}^T \mathbf{x} = 0, \\ y_c &= \frac{1}{K} \mathbf{w}^T \mathbf{y} = 0. \end{aligned} \quad (24)$$

The moment of inertia in the thinned virtual array can be expressed as

$$Q_{wxx} = \mathbf{w}^T \mathbf{x}_x, \quad (25)$$

$$Q_{wyy} = \mathbf{w}^T \mathbf{y}_y, \quad (26)$$

$$Q_{wxy} = \mathbf{w}^T \mathbf{x}_y. \quad (27)$$

In this way, the element in the Fisher information matrix of thinned virtual array can be rewritten as

$$\begin{aligned} f_w(\theta, \theta) &= G \sin^2 \theta \cdot (Q_{wxx} \cos^2 \phi + Q_{wyy} \sin^2 \phi + Q_{wxy} \sin(2\phi)), \\ f_w(\phi, \phi) &= G \cos^2 \theta \cdot (Q_{wxx} \sin^2 \phi + Q_{wyy} \cos^2 \phi + Q_{wxy} \sin(2\phi)), \\ f_w(\theta, \phi) &= \frac{G}{4} \sin(2\theta) \cdot [(Q_{wxx} - Q_{wyy}) \sin(2\phi) - 2Q_{wxy} \cos(2\phi)]. \end{aligned} \quad (28)$$

### 3. Design of Thinned Virtual Array for Optimization of CRB

In Section 2.2, the connection between virtual array configuration and CRB is revealed, indicating the reduction redundancy and inflexibility in virtual array design can be avoided by directly thinning virtual array through selection of matched filters on the receiver array. The specific configuration of thinned virtual array, however, should be considered carefully in the specific condition. If priori direction of the target is not available or not considered, the thinned virtual array with the best CRB performance is the one that meets the isotropic condition; if priori direction of target is available, the virtual array with optimized CRB performance depends on the given information of the target. Note that the optimization of CRB usually takes the trace minimization of the CRB matrix, namely, to solve the following problem:

$$\min_{\mathbf{c}} \text{tr}(\mathbf{C}). \quad (29)$$

The thinned virtual array without or with priori direction is to be considered in the following.

**3.1. Thinned Virtual Array without Priori Direction.** In the case where no priori information on target direction is available, the best thinned virtual array is isotropic, namely, the CRB performance should be decoupled from elevation and azimuth angles of the target. Therefore, the following conditions is to be satisfied:

$$\begin{aligned} Q_{wxx} &= Q_{wyy} = Q, \\ Q_{wxy} &= 0, \end{aligned} \quad (30)$$

so that the CRB matrix can be rewritten as

$$\mathbf{C} = \mathbf{J}^{-1} = \frac{1}{G} \begin{bmatrix} \frac{1}{(\cos^2\theta)Q} & 0 \\ 0 & \frac{1}{(\sin^2\theta)Q} \end{bmatrix}, \quad (31)$$

which also implies

$$\min_Q \frac{1}{(\sin^2\theta\cos^2\theta)Q}. \quad (32)$$

Note that (32) holds for any angle  $\theta$ . The problem can thus be rewritten as

$$\max_Q Q. \quad (33)$$

It can be implied from (25), (26), and (33) that the optimized isotropic thinned virtual array is composed of elements on the aperture boundaries. This is because boundary elements ensures the largest possible array aperture to obtain the largest  $Q$ , which is in accordance with the observation in [4]. However, as also pointed out by [4], the optimized isotropic thinned virtual array without aperture limit does not exist since the  $Q$  value can be arbitrarily large by expanding aperture on every direction so that CRB can be reduced arbitrarily. This also implies that CRB, which is small enough, can be obtained by a virtual array aperture which is large enough, which is impractical in real-world applications. Besides, the design focused on expanding virtual array aperture renders ambiguity, which is not suitable for the applications which needs enhanced DOA estimation performance.

Meanwhile, the isotropic condition in (30) adds the constraint that the virtual array is symmetric around the gravity center of the aperture, which is difficult to satisfy too. Furthermore, even with constraints on the array aperture, since the array only contains boundary elements, the best possible isotropic array still suffers from high sidelobes, which affects the performance of DOA estimation.

To mitigate the effect of high sidelobes from boundary aperture, the following problem is to be considered:

$$\begin{aligned} \max_{\mathbf{w}} \quad & \mathbf{w}^T \mathbf{x}_x \\ \text{s.t.} \quad & \mathbf{w} \in \{0, 1\}^{M_t M_r} \\ & \mathbf{w}^T \mathbf{x} = 0 \\ & \mathbf{w}^T \mathbf{y} = 0 \\ & \mathbf{1}^T \mathbf{w} = K \\ & \mathbf{w}^T \mathbf{x}_y = 0 \\ & \mathbf{w}^T (\mathbf{x}_x - \mathbf{y}_y) = 0 \\ & \mathbf{w}^T \mathbf{C}_{t,j} \mathbf{w} \leq \delta_{t,j}, \end{aligned} \quad (34)$$

where  $\mathbf{1}$  denotes all-one vector,  $\mathbf{C}_{t,j} = \text{real}(\mathbf{v}_{t,j} \mathbf{v}_{t,j}^H)$  and is the cross-correlation vector between the target steering vector and the steering vector of the  $j$ th interference, and  $\delta_{t,j}$  represents desired peak sidelobe.

Note that (34) is not convex due to the binary constraint, and this combinatorial problem is to be solved through exhaustive search. To reduce computational complexity from exhaustive search, it is necessary to seek a balance or a trade-off between computational complexity and efficiency through convex approximation to the original problem. In this paper, a sequential convex approximation of (34) is proposed. Specifically, the binary constraint  $\mathbf{w} \in \{0, 1\}$  is equivalent to the difference between two convex constraints, i.e.,

$$\begin{aligned} A: \quad & \mathbf{w} \in [0, 1], \\ B: \quad & \mathbf{w}^T \mathbf{w} - \mathbf{w}^T \mathbf{1} < 0, \end{aligned} \quad (35)$$

where  $\mathbf{1}$  denotes a vector of all ones.

This means that the binary constraint  $\mathbf{w} \in \{0, 1\}$  in (34) can be expressed as a maximization problem, namely,

$$\begin{aligned} \max_{\mathbf{w}} \quad & \mathbf{w}^T \mathbf{w} - \mathbf{w}^T \mathbf{1} \\ \text{s.t.} \quad & \mathbf{w} \in [0, 1]. \end{aligned} \quad (36)$$

It is evident that the objective function does not meet the requirement for the maximization problem. However, the term can be approximated in an affine form by its first-order Taylor decomposition. Note that the derivative of  $\mathbf{w}^T \mathbf{w}$  is  $2\mathbf{w}$ , and thus the objective function in the  $k$ th iteration can be approximated by

$$2\mathbf{w}^T \mathbf{w}^{(k)} - \mathbf{w}^{(k)T} \mathbf{w}^{(k)} - \mathbf{w}^T \mathbf{1}. \quad (37)$$

Therefore, (34) can be approximated by iterative convex problems as follows:

$$\begin{aligned} \max_{\mathbf{w}} \quad & \mathbf{w}^T (\mathbf{x}_x + 2\mu \mathbf{w}^{(k)} - \mu \mathbf{1}) - \mathbf{w}^{(k)T} \mathbf{w}^{(k)} \\ \text{s.t.} \quad & \mathbf{w} \in \{0, 1\}^{M_t M_r} \\ & \mathbf{w}^T \mathbf{x} = 0 \\ & \mathbf{w}^T \mathbf{y} = 0 \\ & \mathbf{1}^T \mathbf{w} = K \\ & \mathbf{w}^T \mathbf{x}_y = 0 \\ & \mathbf{w}^T (\mathbf{x}_x - \mathbf{y}_y) = 0 \\ & \mathbf{w}^T \mathbf{C}_{t,j} \mathbf{w} \leq \delta_{t,j}, \end{aligned} \quad (38)$$

where  $\mu$  is the parameter controlling CRB and the degree of thinning in the array. By adjusting  $\mu$  properly, the trade-off between the CRB and the degree of thinning can be achieved.

The direct thinning of virtual array without priori direction is summarized in Table 1.

**3.2. Thinned Virtual Array with Priori Direction.** It can be inferred from (17), (19), and (20) that each element in the Fisher information matrix is connected to both the DOA of target and array configuration. Such connection also implies that the array configuration with optimized CRB performance is angle specific, namely, an array that is optimal for one target direction is not for another target direction.

TABLE 1: Thinning virtual array without priori direction.

Steps	Procedure
Step 1	Initialize parameters $\mu$ , $\mathbf{w}^{(0)}$ , and $I$ ; set $k = 0$
Step 2	If sidelobe level is to be considered, determine $j$ and $\delta_{t,j}$
Step 3	Solve problem (32) or (34) to obtain $\mathbf{w}^{(k)}$
Step 4	$k = k + 1$ ; if $k < I$ , go to step 3; if $k \geq I$ , go to step 5
Step 5	$\mathbf{w}^{(I)}$ consists of indices of selected active elements

Considering the condition with priori direction, the isotropic virtual array proposed in Section 3.1 is not the most desirable. Instead, the array only needs to detect certain regions of interest with high precision while it still preserves the capacity to detect targets outside those regions. If priori information of target direction is available, e.g., from the results from detection of the isotropic array over the whole angle region, the optimal thinned virtual array can be obtained through optimizing the CRB matrix over the sector of interest, which exploits the DOF from direct thinning of virtual array and the connection between CRB and virtual array configuration.

The elevation  $\theta$  and azimuth  $\phi$  of a single target is assumed priori known in the following discussions. Since the CRB matrix is the inverse of the Fisher information matrix, the elements on the main diagonal of CRB matrix can be expressed as

$$C_{\theta\theta} = \frac{1}{G} \cdot \frac{1}{\sin^2\theta} \cdot \frac{Q_{wxx}\sin^2\phi + Q_{wyy}\cos^2\phi - Q_{wxy}\sin(2\phi)}{Q_{wxx}Q_{wyy} - Q_{wxy}^2}, \quad (39)$$

$$C_{\phi\phi} = \frac{1}{G} \cdot \frac{1}{\cos^2\theta} \cdot \frac{Q_{wxx}\cos^2\phi + Q_{wyy}\sin^2\phi - Q_{wxy}\sin(2\phi)}{Q_{wxx}Q_{wyy} - Q_{wxy}^2}. \quad (40)$$

The derivation for (39) and (40) are provided in the supplementary material.

To optimize the CRB of virtual array, the trace of the CRB matrix is the target, which is

$$\text{tr}(\mathbf{C}) = \frac{1}{G} \cdot \frac{\alpha Q_{wxx} + \beta Q_{wyy} + \zeta Q_{wxy}}{Q_{wxx}Q_{wyy} - Q_{wxy}^2}, \quad (41)$$

where

$$\alpha = \frac{\sin^2\phi}{\sin^2\theta} + \frac{\cos^2\phi}{\cos^2\theta}, \quad (42)$$

$$\beta = \frac{\cos^2\phi}{\sin^2\theta} + \frac{\sin^2\phi}{\cos^2\theta}, \quad (43)$$

$$\zeta = \frac{\sin(2\phi)}{\cos^2\theta} - \frac{\sin(2\phi)}{\sin^2\theta}. \quad (44)$$

The elements in the thinned virtual array is selected by choosing the  $M_t M_r \times 1$  binary vector  $\mathbf{w}$ , where elements with index of zero values is not included in the thinned virtual array and elements with index of ones is included in

the thinned virtual array. The design of thinned virtual array with minimized trace of the CRB matrix can therefore be represented as

$$\begin{aligned} \min_{\mathbf{w}} \quad & \frac{\mathbf{w}^T (\tilde{\alpha} \mathbf{x}_x \mathbf{1}^T + \tilde{\beta} \mathbf{y}_y \mathbf{1}^T + \tilde{\zeta} \mathbf{x}_y \mathbf{1}^T) \mathbf{w}}{\mathbf{w}^T (\mathbf{x}_x \mathbf{y}_y^T - \mathbf{x}_y \mathbf{x}_y^T) \mathbf{w}} \\ \text{s.t.} \quad & \mathbf{w}^T \mathbf{x} = 0 \\ & \mathbf{w}^T \mathbf{y} = 0 \\ & \mathbf{1}^T \mathbf{w} = K, \end{aligned} \quad (45)$$

where  $\tilde{\alpha} = (\alpha/K)$ ,  $\tilde{\beta} = (\beta/K)$ , and  $\tilde{\zeta} = (\zeta/K)$ .

Note that problem (45) is a fraction of quadratic terms which is nonconvex, thus cannot be solved using convex methods. To avoid large computational complexity from exhaustive search, problem (45) can be approximated by introducing matrix variable  $\mathbf{W}$ . According to the property of the trace of matrix, (45) can be rewritten as

$$\begin{aligned} \min_{\mathbf{w}, \mathbf{W}} \quad & \frac{\text{tr}(\mathbf{WN})}{\text{tr}(\mathbf{WD})} \\ \text{s.t.} \quad & \mathbf{w}^T \mathbf{x} = 0 \\ & \mathbf{w}^T \mathbf{y} = 0 \\ & \mathbf{1}^T \mathbf{w} = K, \\ & \mathbf{W} \geq \mathbf{w} \mathbf{w}^T, \end{aligned} \quad (46)$$

where  $\mathbf{N} = \tilde{\alpha} \mathbf{x}_x \mathbf{1}^T + \tilde{\beta} \mathbf{y}_y \mathbf{1}^T + \tilde{\zeta} \mathbf{x}_y \mathbf{1}^T$ , and  $\mathbf{D} = \mathbf{x}_x \mathbf{y}_y^T - \mathbf{x}_y \mathbf{x}_y^T$ .

Note that the fraction structure ( $\text{tr}(\mathbf{WN})/\text{tr}(\mathbf{WD})$ ) is still nonconvex. To facilitate the solution of (46), it should be noted that the fractional problem is usually transformed as the following problem:

$$F(\eta) = \text{tr}(\mathbf{WN}) - \eta \text{tr}(\mathbf{WD}). \quad (47)$$

(47) can be solved using the Dinkelbach method, which is briefly given as follows:

Step 1: initialize the parameter  $\eta^{(1)}$  and  $\varepsilon$ , where  $\eta^{(1)}$  is the initial value of  $\eta$  and  $\varepsilon$  is the threshold value where the function  $F(\eta)$  converges.

Step 2: given  $\eta^{(k)}$ , the following problem is to be solved to obtain the optimal value  $\mathbf{w}^{(k)}$ ,  $\mathbf{W}^{(k)}$  and corresponding function value  $F(\eta^{(k)})$ :

$$\begin{aligned} \min_{\mathbf{w}, \mathbf{W}} \quad & F(\eta^{(k)}) \\ \text{s.t.} \quad & \mathbf{w}^T \mathbf{x} = 0 \\ & \mathbf{w}^T \mathbf{y} = 0 \\ & \mathbf{1}^T \mathbf{w} = K, \\ & \mathbf{W} \geq \mathbf{w} \mathbf{w}^T, \end{aligned} \quad (48)$$

Step 3: if  $F(\eta^{(k)}) \leq \varepsilon$ , the iteration terminates;  $\mathbf{w}^{(k)}$  and  $\mathbf{W}^{(k)}$  are the output. Otherwise, let



$$\eta^{(k+1)} = \frac{\text{tr}(\mathbf{W}^{(k)}\mathbf{N})}{\text{tr}(\mathbf{W}^{(k)}\mathbf{D})}, \quad (49)$$

and go back to Step 2.

It should be noted that the optimal parameter  $\mathbf{w}^{(k)}$  does not meet the constraint of the original problem (45), and optimal thinned binary vector is to be deduced by solving the optimal integer constrained problem. Specifically, in order to obtain vector  $\mathbf{w}$  with zeros and ones as each element, the following problem is to be solved.

$$\begin{aligned} \min_{\mathbf{w}} \quad & \|\mathbf{w} - \mathbf{w}^{(k)}\| \\ \text{s.t.} \quad & \mathbf{w} \in \{0, 1\}^{M_t M_r} \\ & \sum_{i=1}^{M_t M_r} \mathbf{w}_i = K. \end{aligned} \quad (50)$$

The design of thinned virtual array with priori direction is summarized in Table 2.

#### 4. Simulation Results

In this section, the advantage of the proposed thinned virtual array is validated by simulation results. To give a fair comparison between difference array configurations, numerical simulations in several scenarios are to be considered. First, in the case without priori direction, the virtual array formed by linear transmit array and receive array is thinned, which can be divided into two types, namely, the isotropic (type 1) which only cares about CRB performance and another type (type 2) that takes into consideration both the CRB and sidelobe performance. The performance of type 1 and type 2 are compared to demonstrate the difference between these two methods. Next, in the case with priori direction, the virtual array formed by square transmit array and receive array is thinned, which involves three types, namely, the isotropic (type 3) which does not consider the priori direction, the directional (type 4) which is thinned based on the priori direction, and the one with wrong priori direction (type 5). The performance of type 3, type 4, and type 5 are compared to demonstrate that type 4 has the lowest total CRB which achieves better DOA estimation performance. Lastly, to prove the universal efficacy of the proposed thinned virtual array, the total CRB of multiple different directional thinned virtual arrays (type 4), obtained with corresponding elevation and azimuth, is compared with the total CRB of the isotropic (type 3) thinned virtual array and that of the one with priori direction other than the actual target direction (type 5).

*4.1. Example 1.* To provide comparison between different linear thinned virtual arrays, a linear MIMO radar array is considered, which is composed of  $M_t = 5$  transmit elements and  $M_r = 5$  receive elements. The interelement distance  $d_t$  is half of wavelength in transmit array, and the distance between elements in the receive array is set as  $d_r = M_t d_t$  to expand array aperture as much as possible. In different

TABLE 2: Thinning virtual array with priori direction.

Steps	Procedure
Step 1	Initialize parameters $\mathbf{W}^{(0)}$ , $\mathbf{w}^{(0)}$ , $\eta^{(0)}$ , $\varepsilon$ , $K$ , and $(\theta, \phi)$ Set $k = 0$
Step 2	Obtain parameter $\alpha$ , $\beta$ , and $\zeta$ from $(\theta, \phi)$
Step 3	Given $\eta^{(k)}$ , solve problem (43) Obtain $\mathbf{w}^{(k)}$ and $\mathbf{W}^{(k)}$
Step 4	$k = k + 1$ , and obtain $\mathbf{w}^{(k+1)}$ by (44)
Step 5	Solve problem (45) to obtain the binary $\mathbf{w}$

thinned virtual arrays, the number of virtual elements is chosen to be  $K = 10$ . Assume a single target locates at  $\theta = 10^\circ$ , and the target direction is estimated using the maximum likelihood method. For type 2 array, the maximum allowed sidelobe is set to be  $\zeta = -10$  dB. Problems (33) and (34) are solved separately to obtain the optimal type 1 array and type 2 array, which is shown in Figures 3 and 4.

As shown in Figures 3 and 4, since it only considers the CRB performance, the elements in the optimal type 1 array is concentrated on two sides of the array to achieve the largest aperture which in turn produces the largest moment of inertia. In contrast, the distribution of elements in the optimal type 2 array is more even since it considers counteracting sidelobes.

The overall beam pattern of two types of virtual array in conventional beamforming is exhibited in Figure 5.

As revealed in Figure 5, the optimal type 1 array has narrower mainlobe, which agrees with the fact that type 1 array concentrates its elements on the edge of its aperture. However, higher sidelobe also appears in the isotropic type 1 array since virtual elements concentrate on two sides of the virtual aperture. In contrast, the optimal type 2 array has lower sidelobe than type 1 array does, but the mainlobe width of the optimal type 2 array is wider than that of optimal type 1 array due to the changed distribution of elements in the virtual array. The observation above reveals proper balance or trade-off between mainlobe width and sidelobe level, depending on actual applications.

To give a fair comparison between different virtual arrays and minimize the effect of DOA estimation methods, the maximum likelihood method is adopted in this section. Note that the DOA estimates by the maximum likelihood method is also the maximum likelihood estimate of true target directions, which converges to CRB asymptotically. The Mean Square Error (MSE) and CRB of different thinned virtual array under different SNR conditions are depicted in Figure 6.

As indicated in Figure 6, the CRB of type 1 array is lower than the CRB of type 2 array. Nevertheless, in the low SNR condition ranging from 0 dB to 5 dB, the threshold SNR of type 2 array is lower than that of type 1 array. This implies that type 2 array performs better in low SNR region than type 1 array. The comparison between two types of thinned virtual array indicates that incorporating the beam pattern performance into the design process, lower SNR threshold or better noise reduction capacity can be achieved which helps to improve DOA estimation performance in low SNR region.

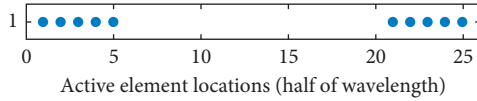


FIGURE 3: Type 1 array configuration.

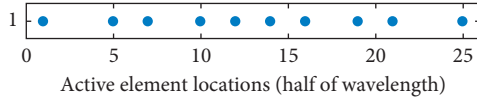


FIGURE 4: Type 2 array configuration.

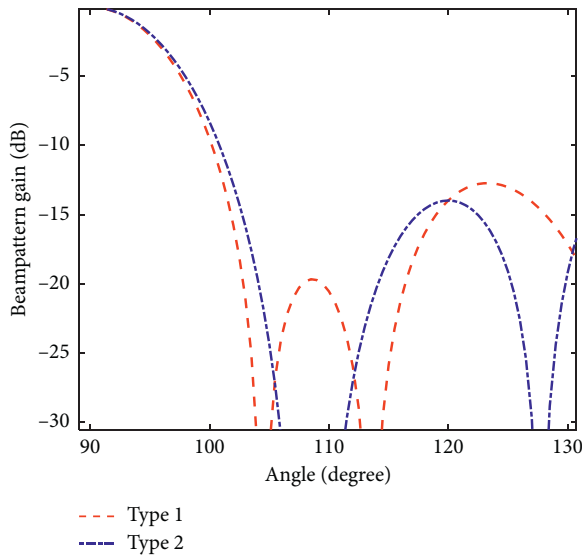


FIGURE 5: Beampattern of type 1 and type 2 arrays.

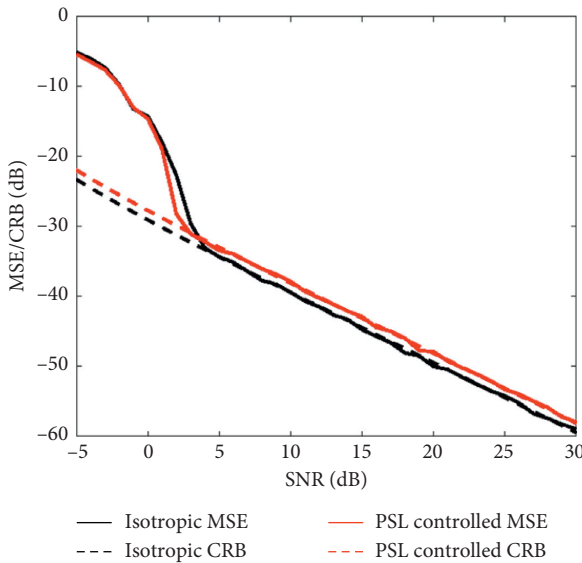


FIGURE 6: Mean Square Error and Cramer-Rao Bound of type 1 and type 2 array.

**4.2. Example 2.** In this example, the performance of different thinned virtual arrays is compared in the scenario with priori direction.

Consider a planar MIMO radar array, where  $M_t = 9$  and  $M_r = 9$ . Both transmit and receive arrays take on uniform square structure with interelement distance being half of wavelength, as depicted in Figures 7 and 8. This indicates that the virtual array exhibits a  $5 \times 5$  square layout with 25 effective virtual elements, as depicted in Figure 9. Assume that a single target locates with elevation  $\theta = 18^\circ$  and azimuth  $\phi = 156^\circ$ . Problem (33) and problem (46) are solved to obtain the isotropic thinned virtual array which does not take into account the priori direction (type 3) and the directional thinned virtual array which incorporates the priori direction in the design of thinned virtual array (type 4). Both the two types of thinned virtual array structures are shown in Figures 10 and 11.

As depicted in Figures 10 and 11, the elements in the optimal type 3 array are located on the boundary of array and are symmetric around the gravity center of virtual array aperture. In contrast, the elements in the optimal type 4 array which takes into account priori direction do not locate on the boundary of array but conforms to distribution that changes according to the priori direction. Even though elements are not on the boundary of the aperture of type 4 array, they are still symmetric around the gravity center due to the symmetry of moment of inertia and the even number of elements.

Similarly to the case in Example 1, the correlation method is exploited to estimation DOA of the target by two types of thinned virtual arrays. In different SNR conditions, the total MSE of both elevation and azimuth and the total CRB is shown in Figure 12.

As exhibited in Figure 12, the total CRB of the optimal type 4 array is lower than that of the optimal type 3 array. The comparison between the total MSE of two types of array indicates that the total MSE of the optimal type 4 array is close to CRB even in low SNR condition (less than  $-2$  dB); the total MSE of the optimal type 3 array, however, does not converge to the total CRB until the SNR is larger than 3 dB. In other words, the SNR threshold of type 4 array is 5 dB lower than that of type 3 array. These observations imply that the priori direction information contributes to total MSE performance in the low SNR condition. The optimal type 4 array introduces priori information and enjoys low total MSE even in low SNR condition, while the optimal type 3 array has higher SNR threshold since the priori direction information is not present in the isotropic thinned virtual array.

**4.3. Example 3.** In this example, the generality of the performance of directional thinned virtual array in cases with different priori directions is demonstrated. Assume that the SNR is 10 dB, the azimuth angles changes from  $0^\circ$  to  $180^\circ$  with  $1^\circ$  as step; other conditions remain the same as in Example 2. In each case with different azimuth angles, the total CRB of isotropic thinned virtual array (type 3), directional thinned virtual array (type 4), and the thinned virtual array with priori azimuth at  $150^\circ$  (type 5) are depicted in Figure 13.

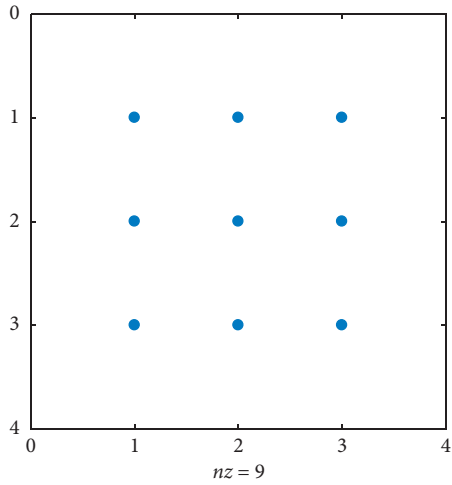


FIGURE 7: Transmit array configuration.

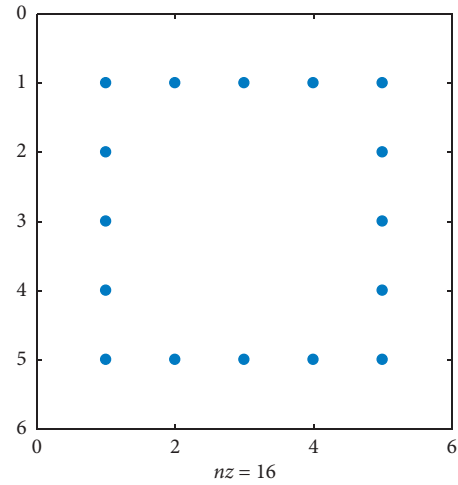


FIGURE 10: Type 3 thinned virtual array configuration.

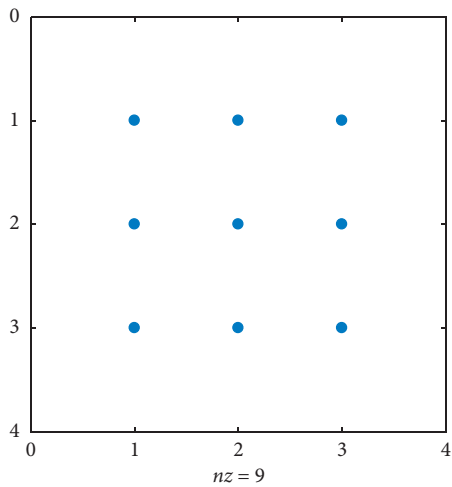


FIGURE 8: Receive array configuration.

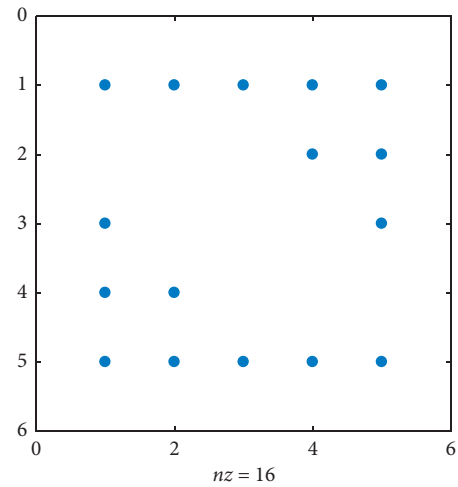


FIGURE 11: Type 4 thinned virtual array configuration.

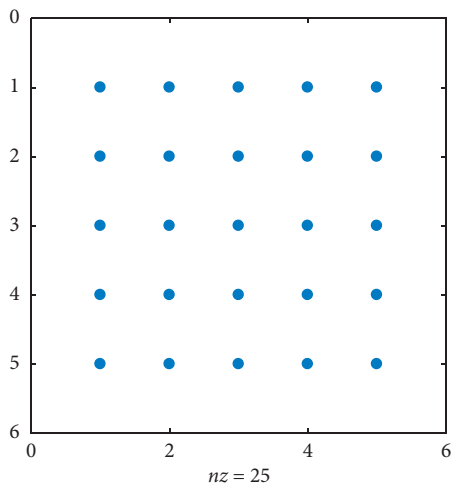


FIGURE 9: Full virtual array configuration.

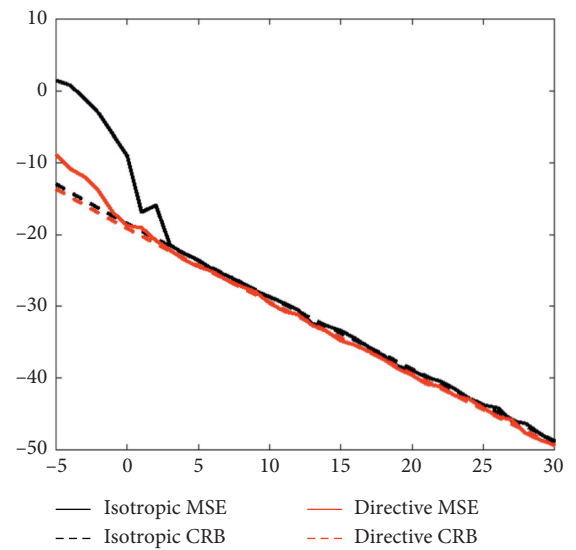


FIGURE 12: Total MSE and total CRB of type 3 and type 4 array.

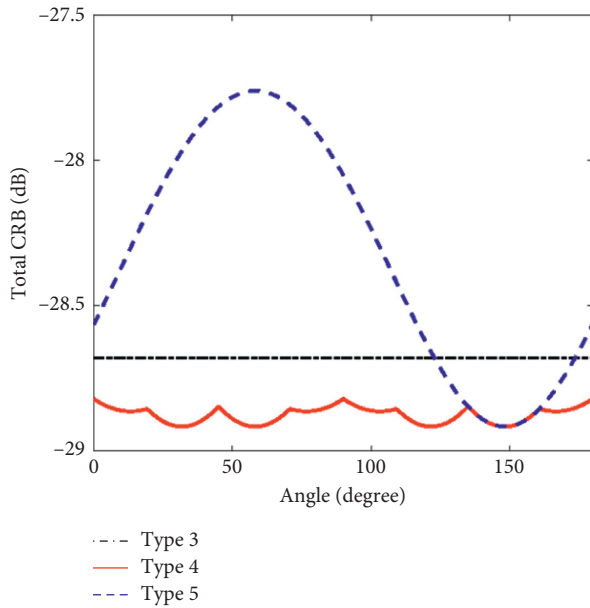


FIGURE 13: Total CRB of different virtual arrays against different azimuth with fixed elevation.

As displayed in Figure 13, the total CRB of the optimal type 3 array is constant over different azimuth angles since the virtual array is isotropic. In comparison, the total CRB of the optimal type 4 array experiences fluctuation over different azimuth angles, but remains close and is lower than that of isotropic type 3 array. For the directional type 5 array, its total CRB is low when the direction of actual target coincides with the priori one; however, when the direction of the actual target is different from the priori direction, the total CRB increases, indicating the direction-finding performance of virtual thinned array is reduced since its DOA estimation is misled by the wrong priori information. These observations indicate that when elevation is fixed yet azimuth sweeps over different angles, by taking the optimal thinned virtual array on each direction, the total CRB remains lower than that of isotropic thinned virtual array while remaining constant compared to the optimal directional thinned virtual array with fixed priori direction. These observations also indicate that reconfiguration of thinned virtual array according to priori information of spatial targets is a feasible way of obtaining total CRB which is lower than that of isotropic thinned virtual array over different spatial angles.

## 5. Conclusions

In this paper, the method for designing thinned virtual arrays in the MIMO radar is proposed. The connection between total CRB and virtual array is analysed, based on which the thinning of virtual array is proposed both in case with and without priori directions. In order to solve the quadratic fractional problems efficiently, the original non-convex problem is approximated by a series of convex problems which can be solved iteratively, the solution of which is used as the reference point in the optimal integer

constraint problem to obtain the binary solution which satisfies the requirement of the original problem. Simulation results show that the thinned virtual array can achieve proper balance between DOA estimation and sidelobe performance when no priori direction is present. When priori direction is available, the directional thinned virtual array achieves lower total CRB and total MSE than the isotropic thinned virtual array without priori direction does. Future work may include implementation of rapid changing of virtual array structure through matched filters and adaptive virtual array reconfiguration in real-time applications.

## Data Availability

The data used in the simulation of the manuscript is available in open-source Octave software.

## Conflicts of Interest

The authors declare that there are no conflicts of interest regarding the publication of this paper.

## Acknowledgments

This work was supported in part by the National Natural Science Foundation of China under Grant 61671465.

## Supplementary Materials

Appendix: derivation of elements in the Fisher information matrix and CRB matrix. (*Supplementary Materials*)

## References

- [1] J. Li, X. Zhang, W. Chen, and T. Hu, "Reduced-dimensional ESPRIT for direction finding in monostatic MIMO radar with double parallel uniform linear arrays," *Wireless Personal Communications*, vol. 77, no. 1, pp. 1–19, 2014.
- [2] N. H. Lehmann, E. Fishler, A. M. Haimovich et al., "Evaluation of transmit diversity in MIMO-radar direction finding," *IEEE Transactions on Signal Processing*, vol. 55, no. 5, pp. 2215–2225, 2007.
- [3] H. Chen, Y. Peng, W. Li, and J. Yang, "Manifold studies on fundamental limits of direction-finding multiple-input multiple-output radar systems," *IET Radar, Sonar & Navigation*, vol. 6, no. 8, pp. 708–718, 2012.
- [4] H. Chen, Z. Zhuang, X. Li, and H. Wang, "Performance bounds of direction finding and its applications for multiple-input multiple-output radar," *IET Radar, Sonar & Navigation*, vol. 8, no. 3, pp. 251–263, 2014.
- [5] R. D. Fry, D. A. Gray, and L. A. Balzan, "MIMO arrays and array shading," in *Proceedings of the 2009 IET International Radar Conference*, Guilin, China, 2009.
- [6] W. Wang, H. Shao, and J. Cai, "MIMO antenna array design with polynomial factorization," *International Journal of Antennas and Propagation*, vol. 2013, Article ID 358413, 9 pages, 2013.
- [7] S. Gu, K. Li, and X. Ren, "Antenna array design in MIMO radar using NSK polynomial factorization algorithm," *International Journal of Antennas and Propagation*, vol. 2016, Article ID 4580479, 10 pages, 2016.

- [8] H. Liu, Q. Xu, and G. Jin, "MIMO antenna polynomial weighted average design method of downward-looking array SAR," *International Journal of Antennas and Propagation*, vol. 2017, Article ID 3029847, 18 pages, 2017.
- [9] J. Dong, Q. Li, and W. Guo, "A combinatorial method for antenna array design in minimum redundancy MIMO radars," *IEEE Antennas and Wireless Propagation Letters*, vol. 8, pp. 1150–1153, 2009.
- [10] J. Dong, R. Shi, W. Lei, and Y. Guo, "Minimum redundancy MIMO array synthesis by means of cyclic difference sets," *International Journal of Antennas and Propagation*, vol. 2013, Article ID 323521, 9 pages, 2013.
- [11] J. Dong, F. Liu, Y. Guo et al., "MIMO radar array thinning optimization exploiting almost difference sets," *Optik*, vol. 127, no. 10, pp. 4455–4460, 2016.
- [12] G. Oliveri and A. Massa, "Genetic algorithm (GA)-enhanced almost difference set (ADS)-based approach for array thinning," *IET Microwaves, Antennas & Propagation*, vol. 5, no. 3, pp. 305–315, 2011.
- [13] J. Dong, J. Yang, W. Lei et al., "Antenna array design in MIMO radar using cyclic difference sets and simulated annealing," in *Proceedings of the 2012 International Conference on Microwave and Millimeter Wave Technology (ICMMT)*, pp. 1–4, Shenzhen, China, 2012.
- [14] Q. Wu, F. Sun, P. Lan, G. Ding, and X. Zhang, "Two-dimensional direction-of-arrival estimation for co-prime planar arrays: a partial spectral search approach," *IEEE Sensors Journal*, vol. 16, no. 14, pp. 5660–5670, 2016.
- [15] S. Qin, Y. D. Zhang, and M. G. Amin, "DOA estimation of mixed coherent and uncorrelated targets exploiting coprime MIMO radar," *Digital Signal Processing*, vol. 61, pp. 26–34, 2017.
- [16] J. Li and D. Jiang, "Low-complexity propagator based two dimensional angle estimation for coprime MIMO radar," *IEEE Access*, vol. 6, pp. 13931–13938, 2018.
- [17] M. Yang, L. Sun, X. Yuan, and B. Chen, "Improved nested array with hole-free DCA and more degrees of freedom," *Electronics Letters*, vol. 52, no. 25, pp. 2068–2070, 2016.
- [18] M. Yang, L. Sun, X. Yuan, and B. Chen, "A new nested MIMO array with increased degrees of freedom and hole-free difference coarray," *IEEE Signal Processing Letters*, vol. 25, no. 1, pp. 40–44, 2018.
- [19] W. Zheng, X. Zhang, and J. Shi, "Sparse extension array geometry for DOA estimation with nested MIMO radar," *IEEE Access*, vol. 5, pp. 9580–9586, 2017.
- [20] J. Shi, G. Hu, X. Zhang, F. Sun, and H. Zhou, "Sparsity-based two-dimensional DOA estimation for coprime array: from sum-difference coarray viewpoint," *IEEE Transactions on Signal Processing*, vol. 65, no. 21, pp. 5591–5604, 2017.
- [21] J. Shi, G. Hu, X. Zhang, and F. Sun, "Sparsity-based DOA estimation of coherent and uncorrelated targets with flexible MIMO radar," *IEEE Transactions on Vehicular Technology*, vol. 68, no. 6, pp. 5835–5848, 2019.
- [22] D. M. Kitavi, K. T. Wong, and C.-C. Hung, "An L-shaped array with nonorthogonal axes-its Cramér-Rao bound for direction finding," *IEEE Transactions on Aerospace and Electronic Systems*, vol. 54, no. 1, pp. 486–492, 2018.
- [23] Y.-h. Tang, X.-f. Ma, W.-x. Sheng, and Y. Han, "Transmit beamforming for DOA estimation based on Cramer-Rao bound optimization in subarray MIMO radar," *Signal Processing*, vol. 101, pp. 42–51, 2014.

## Research Article

# Development of a Pin Diode-Based Beam-Switching Single-Layer Reflectarray Antenna

Muhammad Inam Abbasi <sup>1</sup>, Muhammad Yusof Ismail <sup>2</sup>,  
and Muhammad Ramlee Kamarudin <sup>2</sup>

<sup>1</sup>Centre for Telecommunication Research & Innovation (CETRI),  
Faculty of Electrical and Electronic Engineering Technology (FTKEE), Universiti Teknikal Malaysia Melaka (UTeM),  
Melaka 76100, Malaysia

<sup>2</sup>Universiti Tun Hussein Onn Malaysia (UTHM), 86400 Batu Pahat, Johor, Malaysia

Correspondence should be addressed to Muhammad Inam Abbasi; [muhammad\\_inamabbasi@yahoo.com](mailto:muhammad_inamabbasi@yahoo.com)

Received 7 September 2020; Revised 13 October 2020; Accepted 13 December 2020; Published 29 December 2020

Academic Editor: Lei Yu

Copyright © 2020 Muhammad Inam Abbasi et al. This is an open access article distributed under the Creative Commons Attribution License, which permits unrestricted use, distribution, and reproduction in any medium, provided the original work is properly cited.

This paper presents a practical demonstration for the design and development of a switchable planar reflectarray using PIN diodes in the X-band frequency range. Waveguide scattering parameter measurements for the unit cells and far-field measurements of the periodic reflectarrays have been carried out to verify the predicted results. Reflectarray unit cell measurements demonstrated a frequency tunability of 0.36 GHz with a dynamic phase range of 226°. On the other hand, the designed 6 × 6 periodic reflectarray has been shown to achieve beam switching from +6° to -6° with different switching states of PIN diodes. This type of beam switching can be used in satellite communication for specific region coverage.

## 1. Introduction

Reflectarray is principally a planar reflector which consists of an array of resonant microstrip patch elements printed on a dielectric substrate and is illuminated by a feed horn. Reflectarrays offer the simplicity and high gain associated with their reflector counterparts, while providing fast, adaptive beam-forming capabilities of phased arrays at the same time. On the other hand, limited bandwidth and higher loss are some of the major drawbacks of reflectarrays that limit their use in many applications, as discussed in [1–5].

The design of beam-forming or beam-switching reflectarray depends on the reflectarray configuration where the reflected phase from each of the resonant elements can be controlled either mechanically or electronically. The reflected beam can be directed in the desired direction, which makes a reflectarray capable of achieving a wide-angle electronic beam scanning. Such a beam-forming approach can have many advantages over traditional tunable antenna array architectures, including a significant reduction in

hardware required per element and increased efficiency [6]. Researchers have investigated different techniques for beam steering antennas such as the use of nonlinear dielectric materials [7–9], the integration of Radio Frequency Microelectro Mechanical Systems (RF MEMS) as switches [10, 11], loading varactor diodes with the patch elements and varying the varactor capacitance by using various biasing [12, 13], using aperture coupled elements where the tuning circuit can be located on the nonresonating surface of the element in order to control the contributed phase from each element [14], and using mechanical movement of the antenna [15]. Some other researchers have also proposed the use of PIN diodes for beam switching where the diodes can be switched ON and OFF using an external biasing circuit, and hence, the reflectarray beam can be controlled [16–19]. However, most of these works propose complex multilayer design topology using various dielectric substrates.

This work presents the design and analysis of switchable reflectarrays for beam shaping realization with optimum reflection loss and enhanced bandwidth performance. PIN

diodes have been used for beam switching in reflectarrays demonstrated through simulations and measurements of unit cells, as well as periodic arrays. The reflectarray unit cells comprise of an optimum performance single layer structure having printed patch elements with incorporated slot and gap configurations. The proposed design demonstrates a simple structure with reduced chances of mutual coupling between the adjacent elements of reflectarray.

## 2. Frequency Switchable Reflectarray Unit Cells

Reflectarray unit cells were designed in the X-band frequency range using Rogers Rt/D 5880 ( $\epsilon_r = 2.2$ ,  $\tan \delta = 0.0009$ ), and PIN diodes were integrated into the gap introduced on the slot embedded patch element, as shown in Figure 1(a). The detailed design configuration and analysis of the rectangular slot embedded patch elements have already been presented by in [20]. Waveguide scattering parameter measurements [21] were carried out for a unit cell that comprised of two patch elements with dimensions of  $L_p \times W_p = 9.4 \text{ mm} \times 10 \text{ mm}$  each, which were printed on a substrate of  $L_s \times W_s = 15 \text{ mm} \times 30 \text{ mm}$ . The slot length was kept at 0.6 mm, while the width was  $0.5W_p$ . The vertical gap was introduced with a 0.6 mm width in order to fit the PIN diode.

For the electronic switching of a PIN diode-based design, a GaAs MA4GP907 PIN diode manufactured by MACOM was used. This PIN diode has a series capacitance of 0.025 pF and low series resistance of  $4.2 \Omega$ . The PIN diodes were soldered on the surface of the patch element and were powered by a power supply using a biasing circuit. 1.33 V were supplied, and a  $100 \Omega$  resistor was used. RF choke was implemented using quarter-wavelength segments and radial stub on the biasing circuit in order to block RF from reaching to the power supply. DC block capacitors were not required in this case because there is no physical connection between the RF source (network analyzer) and DC source (power supply). Figure 1(b) shows the fabricated unit cells and complete setup for frequency switchable reflectarray unit cell scattering parameter measurements.

Reflection loss and the reflection phase were measured within an X-band frequency range, and a close agreement between measured and simulated results was observed. Figure 2(a) shows a comparison between measured and simulated reflection loss curves for fabricated samples. It can be observed from Figure 2(a) that, in the OFF state of PIN diode, the measured resonant frequency is close to the simulated resonant frequency. The fabricated unit cell resonated at 9.40 GHz with a reflection loss of 2.60 dB, while the simulations for OFF state of PIN diode provided a resonant frequency of 9.38 GHz with 1.61 dB reflection loss. When the PIN diodes were switched ON, a clear change in frequency was observed for the fabricated samples. In the ON state, the measured resonant frequency was observed to be 9.04 GHz with reflection losses of 3.91 dB. At the same time, the simulation results for the ON state of the PIN diode exhibited a reflection loss of 2.88 dB at a resonant frequency of 8.99 GHz. The maximum discrepancy between measured and simulated reflection loss was observed to be 0.99 dB and 1.03 dB in OFF and ON states of PIN diodes, respectively.

Moreover, extra noise or ripples with a maximum level of 0.25 dB were observed. The reason for this discrepancy can be fabrication quality, which may be affected by the soldering of diodes and photoetching process, as well as the difference between actual material properties and the properties given in the datasheet. Figure 2(b) shows the comparison between the measured and simulated reflection phase. A close agreement between the measured and simulated phase can be observed in Figure 2(b) except the ripples found towards the edges of the measured curves. These ripples can be linked to the same sources, which caused a discrepancy in the reflection loss curves. As shown in Figure 2(a), the dynamic phase range ( $\Delta\phi_d$ ) was calculated at the central frequency of two resonant curves in OFF and ON states of PIN diodes. It can be observed from that a maximum frequency tunability of 0.36 GHz and a dynamic phase range of  $226^\circ$  were demonstrated by the PIN diode-based unit cell measurements. The results are in close agreement with the results obtained by 3D EM simulators of CST MWS and Ansoft HFSS, which practically validates the proposed design.

## 3. Switchable Periodic Reflectarray Design

After the characterization of the reflectarray unit cells and the achievement of the required progressive phase distribution, switchable periodic reflectarrays were designed. In order to design the periodic arrays, a mathematical model has been developed which guides to the exact placement of the unit cells in the array environment. The developed mathematical model has then been applied to design the periodic arrays and perform the far-field measurements. The following sections will explain the procedure and result in details.

*3.1. Mathematical Modelling for the Periodic Reflectarray Design.* In order to design a reflectarray antenna, the most imperative scrutiny is the analysis of the total electric field on the patch elements printed on the dielectric substrate with a conductive ground plane on the other side. The total electric field on a reflectarray consists of the incident field and the reflected and scattered elements of the field. Therefore, the total electric field can be given by

$$\bar{E}_t = \left[ 1 + \bar{R}(\theta_i, \varphi_i) + \bar{S}(\theta_i, \varphi_i, L_i, W_i) \right] \cdot \bar{E}_0 e^{jk_0(xu_i + yv_i - z\cos\theta_i)}. \quad (1)$$

In the case of a waveguide simulator technique, the general relation for the total electric field excited in the Y-direction can be written as

$$\bar{E}_{tw} = \bar{\bar{G}}_{YY} \cdot \bar{J}_Y + \bar{E}_{Yinc} \left( l + \bar{\bar{G}}_{YY} \right), \quad (2)$$

where  $\bar{\bar{G}}$  is Green's function,  $\bar{J}$  is the current density, and  $l$  is the length of the unit cell patch element, and  $\bar{J}_Y$  can be given by

$$\bar{J}_Y = \sum_n A_n \varphi_n(x, y), \quad (3)$$

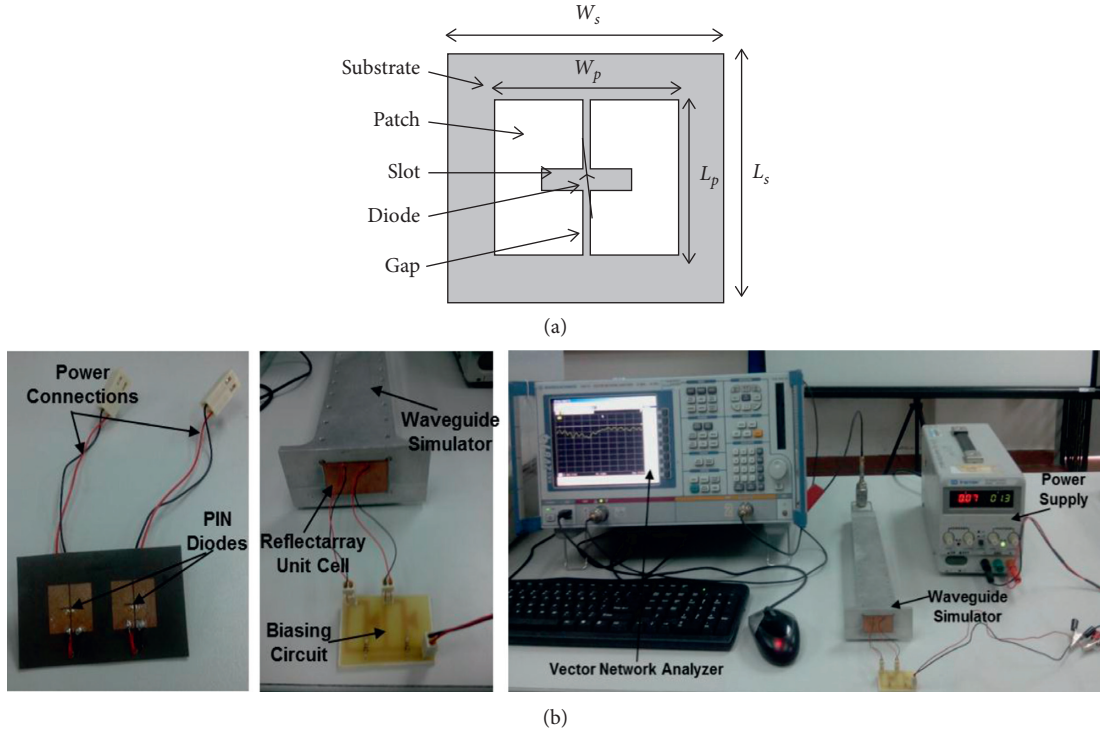


FIGURE 1: Reflectarray unit cell. (a) Proposed design configuration. (b) Fabricated unit cell, biasing circuit, and complete measurements setup.

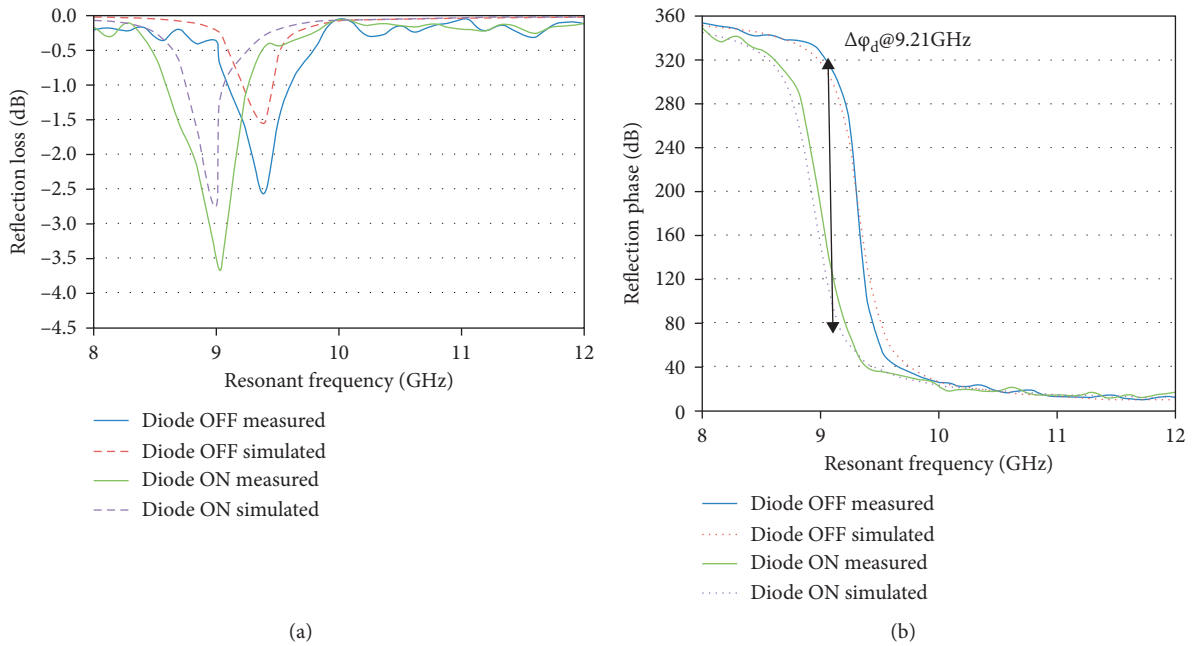


FIGURE 2: PIN diode-based active unit cells of reflectarrays. (a) Measured and simulated reflection loss curves. (b) Measured and simulated reflection phase curves.

where  $A_n$  is the unknown vector coefficient and  $\varphi_n$  is the required phase from an individual patch element of a reflectarray in order to form a progressive phase distribution.

In order to calculate the phase shift for the elements on the X-axis, trigonometric identities can be used as follows:

$$\varphi = -\frac{2\pi}{3} \cot^{-1} \frac{f}{x_i \pm \Delta X}, \quad (4)$$

where  $f$  is the vertical distance of feed from the surface of the array and  $x_i$  is the distance between the center of the  $i$ th



element and the point perpendicular to the feed and  $\varphi$  is in degrees. Once  $\varphi$  is calculated for different values of  $x = x_i$ ,  $y = 0$ , the phase shift for all the array elements can be obtained. This method simplifies the calculation of the required phase shift from each of the array elements and reduces the complexity and time required for the periodic reflectarray design. The abovementioned technique can also be used for the progressive phase distribution with offset feed reflectarrays as shown in Figure 3. In the case of offset feed reflectarrays,  $\Delta X$  has to be introduced as the distance between the feed and the line perpendicular to the array centre. Figure 3 shows the geometry of the centre feed and offset feed reflectarrays for different planar reflector designs. The feeds  $F_1$  and  $F_2$  are placed at the offset distance of  $\Delta X = X_0 - X_2$  and  $\Delta X = X_0 - X_2$ , respectively.

The abovementioned analysis provides a general formula for the design of a planar reflector with progressive phase distribution for any dielectric material and either centre or offset feed configuration. In order to obtain the progressive phase distribution of a planar reflector designed with different dielectric substrates, the material properties should be incorporated in equation (4). The material properties affect the reflection coefficient ( $\Gamma$ ), which affects the reflection phase of the planar reflector. In the case of reflectarray antennas,  $\Gamma$  depends on the attenuation due to dielectric and conductor loss, which are given by

$$\alpha_d = \frac{\omega}{2} \sqrt{(\mu_0 \epsilon_0 \epsilon_r)} \tan \delta, \quad (5)$$

$$\alpha_c = \frac{8.68}{WZ_m} \sqrt{\left(\frac{\omega \mu_0}{2\sigma_c}\right)},$$

where  $\alpha_d$  and  $\alpha_c$  are attenuation due to dielectric and copper loss, respectively.

After incorporation of the effects of dielectric and copper attenuation on  $\Gamma$  and reflection phase of the planar reflector, equation (4) can be written as

$$\varphi = -\frac{2\pi}{3} \cot^{-1} \frac{f}{K(x_i \pm \Delta X_f)}. \quad (6)$$

In equation (6),  $K$  is a variable that relates  $\phi$  with  $\Gamma$  and depends on resonant frequency and material properties, which affect the radiated and scattered fields. The value of  $K$  will be higher for the materials with higher values of dielectric permittivity and loss tangent. Therefore,  $K$  is directly proportional to attenuation due to the dielectric and conductor, and  $K$  can be given by

$$K = C \cdot (\alpha_d + \alpha_c), \quad (7)$$

where  $C$  is a compensation variable and varies with different design requirements and materials used. Finally, equation (6) can be written as

$$\varphi = -\frac{2\pi}{3} \cot^{-1} \frac{f}{C \cdot (\alpha_d + \alpha_c)(x_i \pm \Delta X_f)}. \quad (8)$$

In order to implement the mathematical model for periodic arrays designed using different dielectric materials,

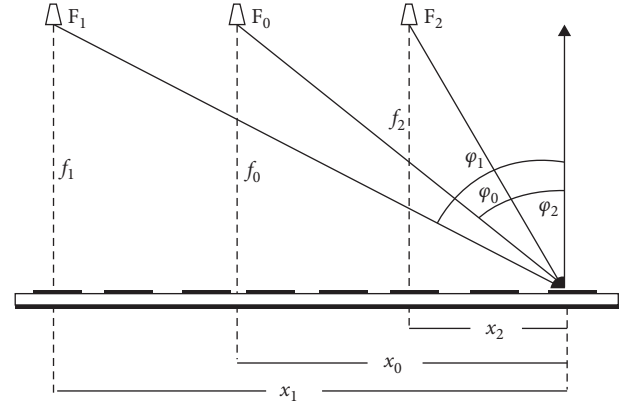


FIGURE 3: Reflection phase from different feed points in a planar reflector.

the compensation factor  $C$  can be expanded by relating  $C$ , with different material properties, and finally, the reflection phase of the individual elements can be given by

$$\varphi = -\frac{2\pi}{3} \cot^{-1} \frac{f}{x(\epsilon_r / \tan \delta)(\alpha_d + \alpha_c)(x_i \pm X_f)}, \quad (9)$$

where  $x$  is a constant that has to be derived for different materials. Values of  $C$  have been estimated as a function of material properties and the desired frequency range.

In order to demonstrate the functionality of the developed mathematical modelling, phase distribution for different offset fed reflectarrays was obtained. An offset of  $0.5\lambda$  (15 mm for 10 GHz) has been used for five different feed positions placed at  $f=f_0$  (centre feed),  $f=f_0-\lambda$ ,  $f=f_0+\lambda$ ,  $f=f_0-1/2\lambda$ , and  $f=f_0+1/2\lambda$ . The required reflection phases for progressive phase distribution of planar reflectors with different offset feed positions are shown in Figure 4. It can be observed from Figure 4 that a phase shift is required because of an offset in the feed position. However, for a particular design (constant number of elements and material properties), the phase values obtained by mathematical modelling for a radius of the circle are independent of the feed positions.

**3.2. Array Design and Far-Field Measurements.** Active arrays with a  $6 \times 6$  slot and gap embedded patch elements were designed and fabricated, and the PIN diodes were incorporated on half of the resonant elements (18 diodes) for the demonstration of radiation pattern measurements of beam-switching reflectarrays. In order to achieve the progressive phase distribution using the individual unit cells of reflectarray, the phase shift was obtained by varying the width of the rectangular slots. There were no changes made in the dimensions of the gap and properties of the PIN diodes.

The PIN diodes were forward biased with a 1.33 V forward voltage and a biasing resistance of 100  $\Omega$ . Therefore, the total current demanded by the antenna was 239.4 mA. Figure 5 shows the fabricated  $6 \times 6$  element reflectarray with connectors attached to it. As shown in Figure 5, the biasing circuit was used to bias the 18 PIN

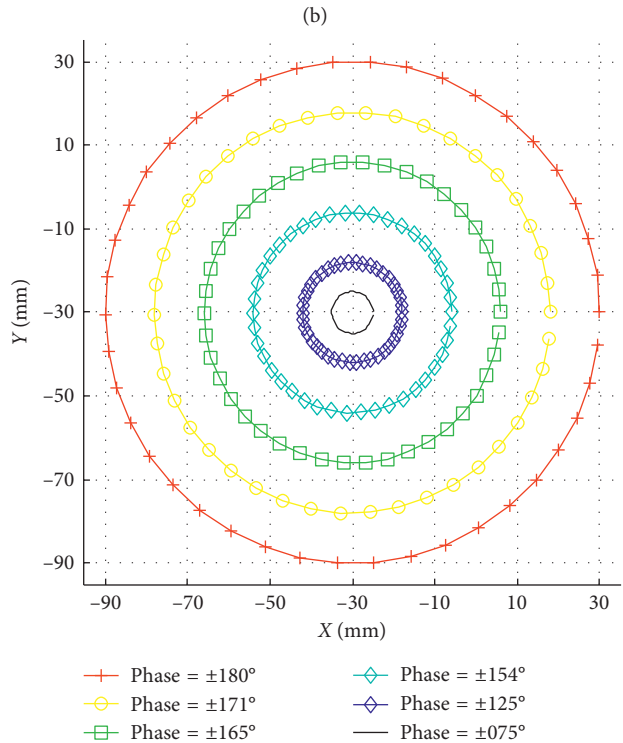
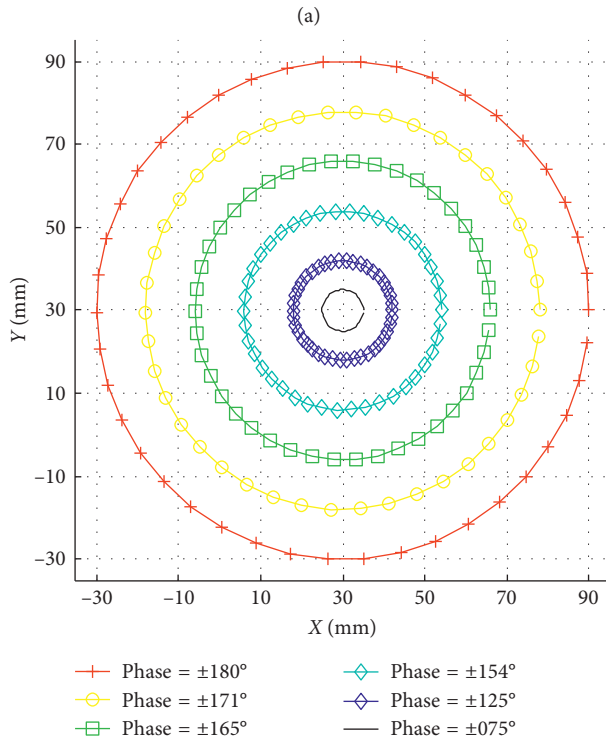
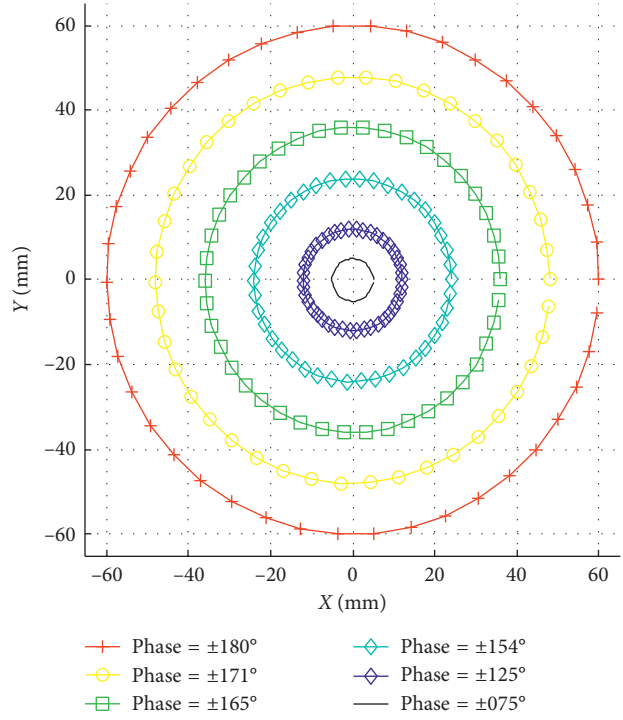
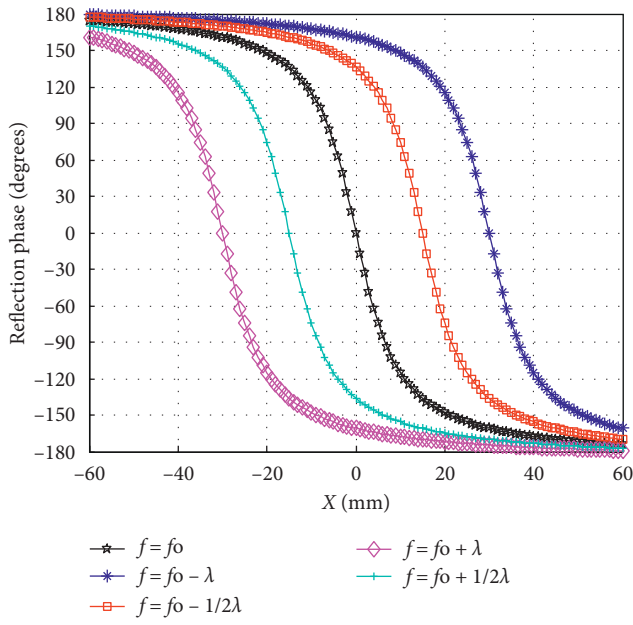


FIGURE 4: Continued.

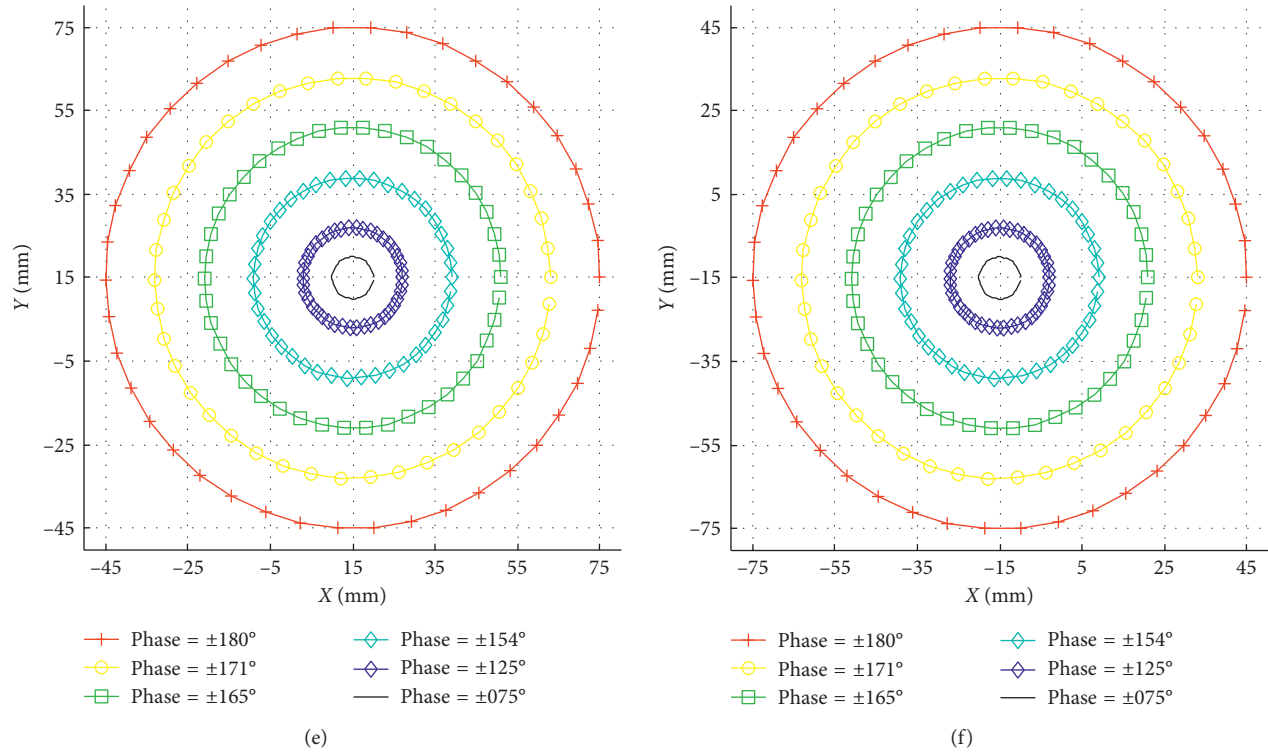


FIGURE 4: Required reflection phase curves for a planar reflector ( $8 \times 8$  elements) (a) with different feed positions, (b)  $f=f_0$  (centre feed), (c)  $f=f_0-\lambda$ , (d)  $f=f_0+\lambda$ , (e)  $f=f_0-1/2\lambda$ , and (f)  $f=f_0+1/2\lambda$ .

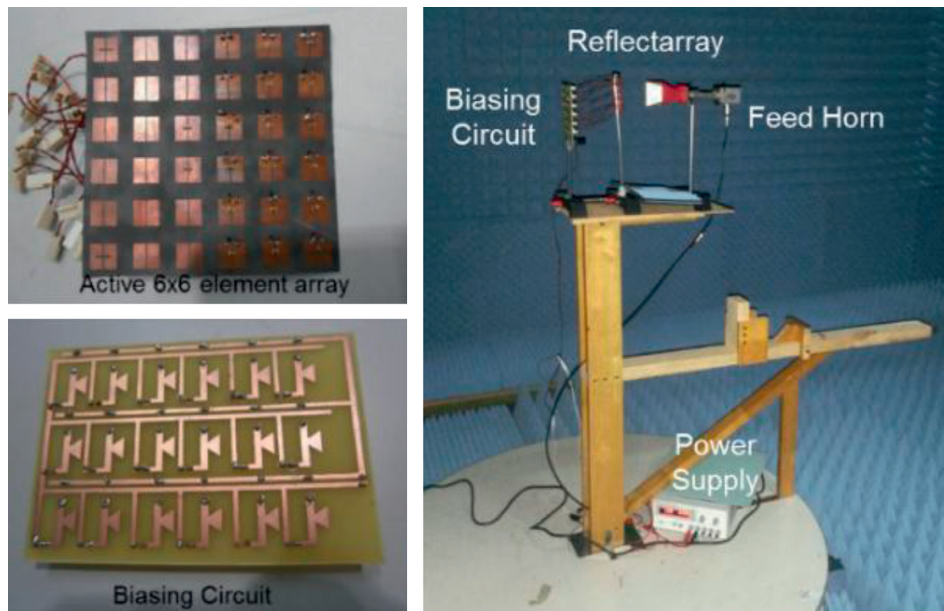


FIGURE 5: Fabricated  $6 \times 6$  element active array, biasing circuit, and complete far-field measurement setup for an active reflectarray antenna.

diodes where the power was supplied using a power supply placed inside the anechoic chamber. The reflectarray antenna was placed at a far-field distance from a standard X-band transmitting horn antenna. The feed horn has a gain of around 7.5 dB at 10 GHz. The transmitter and

receiver were connected with a control station and a network analyzer placed outside the chamber. A turntable was used to rotate the reflectarray antenna, and far-field measurement results were stored in the control station. A very close agreement between measured and simulated far-

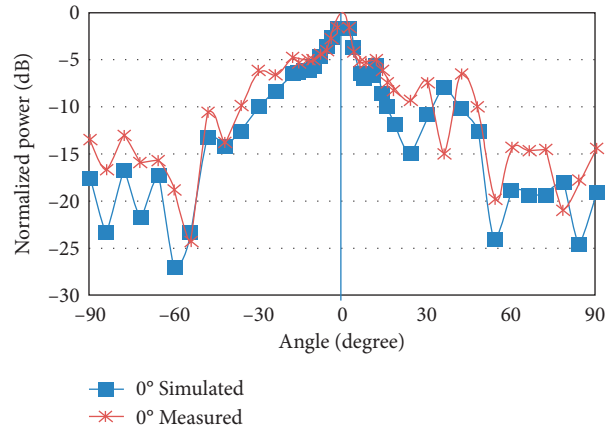


FIGURE 6: Measured and simulated radiation patterns for  $0^\circ$  primary beam at 10 GHz.

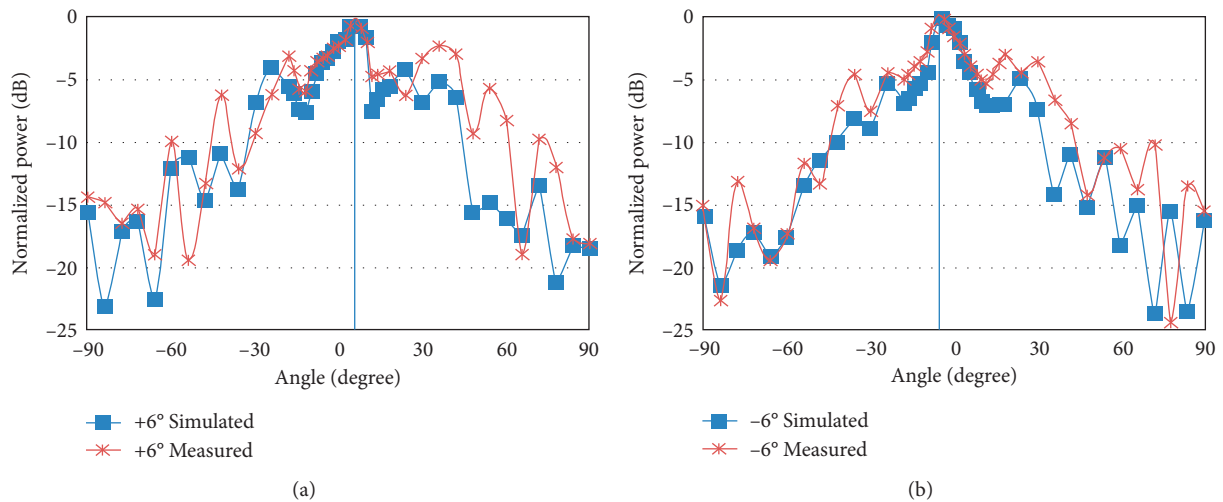


FIGURE 7: Measured and simulated radiation patterns of reflectarrays. (a)  $+6^\circ$  switched beam. (b)  $-6^\circ$  switched beam at 10 GHz.

field radiation pattern results was demonstrated where measured 3 dB beamwidth of  $13.3^\circ$  for  $0^\circ$  beam was observed as compared to 3 dB beamwidth of  $12.9^\circ$  generated during simulations as shown in Figure 6.

A switched beam of  $+6^\circ$  was achieved by forward biasing (ON state) of the diodes keeping the diodes on the right side of the array. Therefore, half of the array resonant elements on the left side, without diodes, were considered to be in the OFF state of PIN diodes. In the OFF state, a PIN diode acts as an open circuit with a very low series capacitance. Keeping this in view, the assumption of elements without diodes as in the OFF state can be acceptable for demonstration purposes. A switched beam of  $-6^\circ$  was demonstrated by changing the configuration of reflectarray in such a way that the PIN diode loaded elements were placed on the left side of the array. This was achievable because of the symmetricity of the reflectarray design and positioning of the PIN diodes. The switched beam configurations also provided a good agreement between simulated and measured results. Figure 7(a) shows a comparison between measured and simulated

results for  $+6^\circ$  switched beam configuration, where measured and simulated 3 dB beamwidth were observed to be  $13.2^\circ$  and  $13.8^\circ$ , respectively. While for  $-6^\circ$ , switched beam measured 3 dB beamwidth was observed to be  $13.3^\circ$  as compared to the simulated 3 dB beamwidth of  $14.0^\circ$  as shown in Figure 7(b). The maximum discrepancy in the case of active reflectarray antenna design was observed to be  $0.7^\circ$ ; however, the trend of beam switching for measured radiation patterns is similar to the simulated radiation patterns. Moreover, the cross polarization levels were observed to be below  $-20$  dB which are considered satisfactory for this type of antenna.

The comparison between the measured and simulated antenna gains was also carried out as shown in Table 1. A maximum gain of 13 dB was observed in the case of  $0^\circ$  beam. The gain was observed to be slightly lower in the case of switched beams which can be due to the effects caused by the introduction of PIN diodes. The  $-1$  dB gain bandwidth was also obtained for the  $0^\circ$  beam by measuring the gain at different frequencies and observing the bandwidth at 1 dB

TABLE 1: Comparison between simulated and measured gain values at 10 GHz.

Beam	Simulated gain (dB)	Measured gain (dB)
0°	13.0	12.72
+6°	12.8	12.62
-6°	12.8	12.58

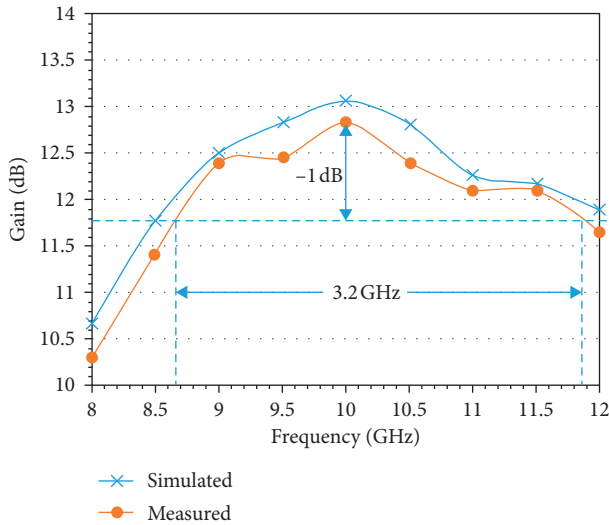


FIGURE 8: Measured and simulated gain of reflectarrays of 0° beam in the X-band frequency range.

below the maximum gain at 10 GHz. Figure 8 shows the comparison between the simulated and measured results of gain at different frequencies in the X-band frequency range. The 1 dB was observed to be 32% or 3.2 GHz as demonstrated in Figure 8.

Generally, there are some discrepancies observed by the comparison of simulated and measured results of different performance parameters. The discrepancy in the measured and simulated results can mainly be attributed to the losses added because of the additional circuitry used for biasing of active reflectarrays. The PIN diodes were soldered on the resonant patch elements using conducting materials, which can add up to the conductor losses. Moreover, during the fabrication and soldering process, the arrays were exposed to very high temperatures. This high temperature can vary the material properties of the dielectric substrate, and the soldering can affect the conductivity of the copper used for resonant patches. Overall, it can be concluded that the results successfully demonstrated the feasibility of applying the developed technique for the design of switchable reflectarrays for beam-shaping realization.

#### 4. Conclusions

Switchable reflectarrays for beam-shaping realization can be designed using PIN diodes on the slot and gap embedded resonant patch elements of reflectarrays. The performance of the unit cells and the PIN diodes has to be optimized for the effective design of active reflectarrays. Furthermore, the sidelobe levels and 3 dB beamwidth demonstrated in this

work can be improved by increasing the number of elements in the periodic array. Such beam switching can be used in a number of applications, including Earth observatory systems, where a geostationary orbit can cover the whole Earth within  $\pm 9^\circ$ .

#### Data Availability

The corresponding author can be contacted for any supporting data.

#### Conflicts of Interest

The authors declare that they have no conflicts of interest.

#### Acknowledgments

Research funding for this work was fully provided by the Ministry of Higher Education, Malaysia, under the Prototype Research Grant Scheme (PRGS, VOT 0904) and Research Acculturation Collaborative Effort (RACE, VOT 1119).

#### References

- [1] J. Huang and J. Encinar, *Reflectarray Antennas: Broadband Techniques*, Wiley, Hoboken, NJ, USA, 2007.
- [2] M. Y. Ismail and M. Inam Abbasi, "Performance improvement of reflectarrays based on embedded slots configurations," *Progress in Electromagnetics Research C*, vol. 14, pp. 67–78, 2010.
- [3] M. Fazelifar, S. Jam, and R. Basiri, "Design and fabrication of a wideband reflectarray antenna in Ku and K bands," *AEU - International Journal of Electronics and Communications*, vol. 95, pp. 304–312, 2018.
- [4] G.-T. Chen, Y.-C. Jiao, and G. Zhao, "A reflectarray for generating wideband circularly polarized orbital angular momentum vortex wave," *IEEE Antennas and Wireless Propagation Letters*, vol. 18, no. 1, pp. 182–186, 2019.
- [5] M. Karimipour and I. Aryanian, "Demonstration of broadband reflectarray using unit cells with spline-shaped geometry," *IEEE Transactions on Antennas and Propagation*, vol. 67, no. 6, pp. 3831–3838, 2019.
- [6] S. V. Hum, M. Okoniewski, and R. J. Davies, "Realizing an electronically tunable reflectarray using varactor diode-tuned elements," *IEEE Microwave and Wireless Components Letters*, vol. 15, no. 6, pp. 422–424, 2005.
- [7] M. Y. Ismail, W. Hu, R. Cahill et al., "Phase Agile reflectarray cells based on liquid crystals," *IEEE Proceedings - Microwaves, Antennas and Propagation*, vol. 1, no. 4, pp. 809–814, 2007.
- [8] W. Hu, M. Y. Ismail, R. Cahill et al., "Tunable liquid crystal patch element," *IET Electronic Letters*, vol. 42, no. 9, pp. 509–511, 2006.
- [9] A. Mossinger, R. Marin, S. Mueller, J. Freese, and R. Jakoby, "Electronically reconfigurable reflectarrays with nematic liquid crystals," *IET Electronics Letters*, vol. 42, no. 16, pp. 899–900, 2006.
- [10] H. Rajagopalan, Y. Rahmat, and W. A. Imbriale, "RF MEMES actuated reconfigurable reflectarray patch-slot element," *IEEE Transactions on Antennas and Propagation*, vol. 56, no. 12, pp. 3689–3699, 2008.
- [11] F. A. Tahir, H. Aubert, and E. Girard, "Equivalent electrical circuit for designing MEMS-controlled reflectarray phase

- shifters," *Progress in Electromagnetics Research*, vol. 100, pp. 1–12, 2010.
- [12] L. Boccia, F. Venneri, G. Amendola, and G. D. Massa, "Application of varactor diodes for reflectarray phase control," *IEEE International Symposium of Antennas and Propagation Society*, vol. 3, pp. 132–135, 2002.
- [13] S. V. Hum, M. Okoniewski, and R. Davies, "Modeling and design of electronically tunable reflectarrays," *IEEE Transactions on Antennas and Propagation*, vol. 55, no. 8, pp. 2200–2210, 2007.
- [14] M. Riel and J. J. Laurin, "Design of an electronically beam scanning reflectarray using aperture-coupled elements," *IEEE Transactions on Antennas and Propagation*, vol. 55, no. 5, pp. 1260–1266, 2007.
- [15] M. I. Abbasi, M. H. Dahri, M. H. Jamaluddin, N. Seman, M. R. Kamarudin, and N. H. Sulaiman, "Millimeter wave beam steering reflectarray antenna based on mechanical rotation of array," *IEEE Access*, vol. 7, pp. 145685–145691, 2019.
- [16] E. Carrasco, M. Barba, and J. A. Encinar, "X-band reflectarray antenna with switching-beam using PIN diodes and gathered elements," *IEEE Transactions on Antennas and Propagation*, vol. 60, no. 12, pp. 5700–5708, 2012.
- [17] H. Yang, F. Yang, S. Xu et al., "A 1-bit  $10 \times 10$  reconfigurable reflectarray antenna: design, optimization, and experiment," *IEEE Transactions on Antennas and Propagation*, vol. 64, no. 6, pp. 2246–2254, 2016.
- [18] J. Han, L. Li, G. Liu, Z. Wu, and Y. Shi, "A wideband 1 bit  $12 \times 12$  reconfigurable beam-scanning reflectarray: design, fabrication, and measurement," *IEEE Antennas and Wireless Propagation Letters*, vol. 18, no. 6, pp. 1268–1272, 2019.
- [19] H. Zhang, X. Chen, Z. Wang, Y. Ge, and J. Pu, "A 1-bit electronically reconfigurable reflectarray antenna in X band," *IEEE Access*, vol. 7, pp. 66567–66575, 2019.
- [20] M. Y. Ismail and M. Inam, "Resonant Elements for Tunable Reflectarray Antenna Design," *International Journal of Antennas and Propagation*, vol. 2012, Article ID 9148686, 6 pages, 2012.
- [21] M. Inam and M. Y. Ismail, "Reflection loss and bandwidth performance of X-band infinite reflectarrays: simulations and measurements," *Microwave and Optical Technology Letters*, vol. 53, no. 1, pp. 77–80, 2011.

## Research Article

# Maximum Likelihood Angle-Range Estimation for Monostatic FDA-MIMO Radar with Extended Range Ambiguity Using Subarrays

Kaikai Yang, Sheng Hong , Qi Zhu, and Yanheng Ye

School of Information Engineering, Nanchang University, Nanchang 330031, China

Correspondence should be addressed to Sheng Hong; shenghong@ncu.edu.cn

Received 29 May 2020; Revised 31 July 2020; Accepted 17 August 2020; Published 8 September 2020

Guest Editor: Qing Shen

Copyright © 2020 Kaikai Yang et al. This is an open access article distributed under the Creative Commons Attribution License, which permits unrestricted use, distribution, and reproduction in any medium, provided the original work is properly cited.

In this paper, we consider the joint angle-range estimation in monostatic FDA-MIMO radar. The transmit subarrays are first utilized to expand the range ambiguity, and the maximum likelihood estimation (MLE) algorithm is first proposed to improve the estimation performance. The range ambiguity is a serious problem in monostatic FDA-MIMO radar, which can reduce the detection range of targets. To extend the unambiguous range, we propose to divide the transmitting array into subarrays. Then, within the unambiguous range, the maximum likelihood (ML) algorithm is proposed to estimate the angle and range with high accuracy and high resolution. In the ML algorithm, the joint angle-range estimation problem becomes a high-dimensional search problem; thus, it is computationally expensive. To reduce the computation load, the alternating projection ML (AP-ML) algorithm is proposed by transforming the high-dimensional search into a series of one-dimensional search iteratively. With the proposed AP-ML algorithm, the angle and range are automatically paired. Simulation results show that transmitting subarray can extend the range ambiguity of monostatic FDA-MIMO radar and obtain a lower cramer-rao low bound (CRLB) for range estimation. Moreover, the proposed AP-ML algorithm is superior over the traditional estimation algorithms in terms of the estimation accuracy and resolution.

## 1. Introduction

The frequency diverse array (FDA) concept was first proposed at the 2006 IEEE Radar Conference and has received widespread attention because of its range-dependent beam pattern [1–3]. The FDA range-dependent beam pattern is generated by the different carrier frequencies of the array elements; that is, there is a frequency increment between the FDA array element carrier frequency, and the frequency increment is much smaller than the reference array element carrier frequency. Compared with traditional phased array, the FDA has obvious advantages in applications such as beamforming [4], target detection and positioning [5], deceptive jamming suppression [6], and secure communication [7].

The multiple input multiple output (MIMO) radar has excellent spatial resolution and target detection performance

[8, 9]. Combining FDA and MIMO radar can increase FDA degrees-of-freedom (DOFs). There are two types of FDA-MIMO radar, which are the bistatic FDA-MIMO radar and the monostatic FDA-MIMO radar. The bistatic FDA-MIMO radar has the serious problem of angle-range coupling, which increases the difficulty of joint angle-range estimation [10]. However, the angle and range parameters are decoupled in the monostatic FDA-MIMO radar, which facilitates the joint angle-range estimation [11].

Although the angle and range parameters are decoupled in the monostatic FDA-MIMO radar, there exists another serious problem of range ambiguity. The problem of unambiguous range in the monostatic FDA-MIMO radar was pointed in [12], where the maximum unambiguous range was derived. In monostatic FDA-MIMO radar, only within a limited range, the range of target can be estimated without ambiguity, and the unambiguous range is inversely

proportional to the frequency increment. To our best knowledge, there is only one work discussing how to extend the unambiguous range of monostatic FDA-MIMO radar at present. Inspired by [5], reference [13] proposed double-pulses method to extend the unambiguous range, which is to transmit double-pulses with different frequency increments at different times. However, transmitting double-pulses at different times will reduce the real-time performance of the radar system. Inspired by the method of angle and range decoupled using subarrays in traditional FDA (uniform linear array and uniform frequency increment) radar [14] and bistatic FDA-MIMO radar [10], we propose to extend the range ambiguity for the monostatic FDA-MIMO radar using subarrays. In this method, the FDA transmitting array is uniformly divided into subarrays with different frequency increments. Compared with the double-pulse method, the proposed method can reduce the time cost of the monostatic FDA-MIMO radar system. Meanwhile, in traditional monostatic FDA-MIMO radar, reducing the frequency increment can extend the unambiguous range. However, reducing the frequency increment, the cramer-rao low bound (CRLB) of the range estimation will increase accordingly. The proposed transmitting subarrays can solve this contradictory problem, and a lower-range estimation CRLB while extending the unambiguous range can be obtained.

In addition, the joint angle and range estimation with unambiguous range in monostatic FDA-MIMO radars has received a lot of attention. In [15], the angle and range estimation CRLB, MSE, and resolution of monostatic FDA-MIMO radar were analysed and compared with traditional MIMO radar, which illustrated the advantages of monostatic FDA-MIMO radar. The multiple signal classification (MUSIC) algorithm was utilized in monostatic FDA-MIMO radar [16], where the resolution threshold for angle and range estimation was analysed. In [17], the estimation of signal parameters via rotational invariance techniques (ESPRIT) algorithm was used to estimate the target angle and range without search. Compared with the searching algorithm (e.g., MUSIC), the calculation cost of ESPRIT algorithm is reduced, but the estimation accuracy is lower than the searching algorithm. In [18], by using the sparseness of the target in the space, the sparse model of the received signal in monostatic FDA-MIMO radar was established. The sparse model was solved using convex optimization, and finally the angle and range were estimated in a single snapshot. In [12], the design of the coprime array was applied to the monostatic FDA-MIMO radar, which further improves the DOFs. At the same time, an angle and range estimation based on Bayesian learning algorithm was proposed. Reconstruction algorithm based on compressed sensing always subject to the grid-mismatch effect and deteriorating the estimation performance [19]. The off-grid angle and range estimation approach for monostatic FDA-MIMO radar with single snapshot based on decoupled atomic norm minimization (DANM) is proposed in [20]. And the estimation performance is better than orthogonal matching pursuit (OMP).

In above related works, the classic MUSIC and ESPRIT algorithms are widely used in angle and range estimation for

monostatic FDA-MIMO. However, as a classic parameter estimation algorithm, maximum likelihood estimation (MLE) [21] has not been discussed for angle and range estimation in monostatic FDA-MIMO radar. According to the estimation theory, the estimation performance of MLE is better than MUSIC and ESPRIT algorithms, and the estimation result is closer to the parameter estimation CRLB. Considering this paucity, in this paper, we first utilize the MLE algorithm to estimate angle and range jointly in the monostatic FDA-MIMO radar. The log-likelihood function of angle-range estimation is derived, and the maximum likelihood (ML) cost function of the angle and range is obtained. Since the cost function of MLE requires high-dimensional search, the computation load is heavy. To improve the computational efficiency, we propose the alternating projection (AP) ML algorithm, which transforms the high-dimensional search into a series of one-dimensional iterative search [22]. In addition, the angle and range are automatically paired during the iteration.

In this paper, the transmitting steering vector of traditional FDA and FDA with subarrays are derived, based on which the signal model of monostatic FDA-MIMO radar with transmitting subarrays is given. Then, the reason and principle of extending unambiguous range by transmitting subarrays are illustrated. The expression for the unambiguous range of the proposed method is derived and compared with the existing method. After extending the range ambiguity, we utilize the MLE algorithm within the unambiguous range to estimate the angle and range jointly in monostatic FDA-MIMO radar. To further reduce the computational load, the AP-MLE is proposed. In the simulation results, the effectiveness of the proposed method to expand the range ambiguity is verified. The CRLB of angle and range is derived. The estimation performance of the proposed AP-ML estimation algorithm is evaluated, which confirms the superiority of the proposed method in the monostatic FDA-MIMO radar with subarrays.

The main contributions of this paper are summarized as follows:

- (i) The method to extend the range ambiguity by transmitting subarrays is proposed in the monostatic FDA-MIMO radar. Compared with the existing method of decreasing the frequency increment in monostatic FDA-MIMO radar, the proposed method can obtain a lower range estimate CRLB. Compared with the existing double-pulse method, the proposed method can reduce the time cost of the radar system.
- (ii) The AP-ML algorithm for joint angle and range estimation in the monostatic FDA-MIMO radar with transmitting subarrays is proposed. The specific algorithm flow is given, and the estimation performance is evaluated. Simulation results show that the estimation accuracy and resolution ability of the proposed AP-MLE algorithm are significantly superior over the classic MUSIC and ESPRIT algorithms.



Notations: Superscripts  $[\cdot]^T$ ,  $[\cdot]^H$ , and  $(\cdot)^{-1}$  denote complex transpose, conjugate transpose, and inverse operation, respectively.  $\otimes$  denotes Kronecker product.  $\text{lcm}(\cdot)$  denotes least common multiple operation.  $\propto$  means proportional relationship.  $\text{trace}(\cdot)$  denotes trace operation.  $\odot$  denotes Hadamard product.  $\text{Re}(\cdot)$  means taking the real part.  $\mathbf{1}_{2 \times 2}$  represents  $2 \times 2$  matrix filled with ones.

## 2. Signal Model

The frequency diverse array is different from the traditional array in that there is a nonzero frequency increment  $\Delta f$  in the carrier frequency between its array elements, and this frequency increment  $\Delta f$  is much smaller than the carrier frequency of the reference array element. The carrier frequency of the  $m$ -th array element is

$$f_m = f_1 + (m-1)\Delta f, \quad m = 1, 2, \dots, M, \quad (1)$$

where  $f_1$  represents the reference array element carrier frequency, and  $M$  represents the number of array elements.

In this paper, we consider a monostatic FDA-MIMO radar system with transmitting subarrays. The transmitting subarray monostatic FDA-MIMO radar system is shown in Figure 1. The transmitting array is uniformly divided into  $K$  subarrays, where each subarray is a ULA with  $M$  array elements, the spacing between subarrays element and subarrays is  $d_t$ . Assuming the frequency increment of the  $k$ -th subarray is  $\Delta f_k$ . Receiving array is a ULA with  $N$  array elements, and the spacing between receiving array elements is  $d_r$ .

Suppose there is a target at the far field of the monostatic FDA-MIMO radar. The angle of the target relative to the array is  $\theta$ , and the two-way propagation range of the target is  $r$ . In this case, the transmitting steering vector of transmitting array is [10]

$$\mathbf{a}_t(\theta, r) = [\mathbf{a}_{t1}(\theta, r)^T, \dots, \mathbf{a}_{tk}(\theta, r)^T, \dots, \mathbf{a}_{tK}(\theta, r)^T]^T, \quad (2)$$

where  $\mathbf{a}_{k1}(\theta, r)$  is the transmitting steering vector of the  $k$ -th subarray and  $\mathbf{a}_{k1}(\theta, r)$  can be expressed as [1-3]

$$\mathbf{a}_{k1}(\theta, r) = e^{-j(2\pi/c)((k-1)Md_t f_1 \sin(\theta) - (f_{k1} - f_{11})r)} [1, \dots, e^{-j(M-1)\Delta\varphi_k(\theta, r)}]^T, \quad (3)$$

where  $\Delta\varphi_k(\theta, r) = (2\pi/c)(d_t f_1 \sin(\theta) - \Delta f_k r)$  and  $c$  is speed of light.  $f_{k,1}$  represents the carrier frequency of the first element of the  $k$ -th subarray, and definition  $f_{k,m}$  represents the carrier frequency of the  $m$ -th element of the  $k$ -th subarray, which can be written as

$$f_{k,m} = f_{k,1} + (m-1)\Delta f_k, \quad m = 1, 2, \dots, M. \quad (4)$$

If  $K=1$  or  $\Delta f_1 = \dots = \Delta f_k = \dots = \Delta f_K$  and  $f_{k,1} = f_{k-1,1} + M\Delta f_{k-1}$ , the transmitting subarrays degenerates into nontransmitting subarrays (transmitting frequency diverse array with ULA and uniform frequency increment).

Assuming the transmitting subarrays transmit KM orthogonal signals, the narrow-band complex signal

transmitted by the  $m$ -th element in the  $k$ -th subarray can be expressed as

$$s_{k,m}(t) = \phi_{k,m}(t)e^{j2\pi f_{k,m}t}, \quad (5)$$

where  $\phi_{k,m}(t)$  represents the  $km$ -th orthogonal signal.

Suppose there are  $P$  static and irrelevant targets in the far field. The transmitting subarrays transmit  $KM$  signals, after the target is reflected, the signal is received and sampled by the receiving array, after matched filtering, the received signal can be written as [10, 20]

$$\mathbf{x}(l) = \sum_{p=1}^P \mathbf{a}_r(\theta_p) \otimes \mathbf{a}_t(\theta_p, r_p) \beta_p(l) + \mathbf{n}(l), \quad l = 1, \dots, L, \quad (6)$$

where  $L$  is snapshots of the received signal,  $\theta_p$  indicates the angle (direction of arrival (DOA) and direction of departure (DOD)) of the  $p$ -th target, and  $r_p$  indicates the two-way range for the  $p$ -th target.  $\beta_p(l)$  represents the complex amplitude of the received  $p$ -th target, and  $\mathbf{a}_r(\theta_p) = [1, \dots, e^{j(2\pi/c)(N-1)d_r f_1 \sin(\theta_p)}]^T$  is the receiving array steering vector.  $\mathbf{n}(l)$  is the  $MN$ -dimensional complex Gaussian noise vector with zero mean and variance of  $\sigma^2$ .

Equation (6) can be written as

$$\mathbf{x}(l) = \mathbf{A}\boldsymbol{\beta}(l) + \mathbf{n}(l), \quad l = 1, \dots, L, \quad (7)$$

where  $\mathbf{A} = [\mathbf{a}_r(\theta_1) \otimes \mathbf{a}_t(\theta_1, r_1), \dots, \mathbf{a}_r(\theta_P) \otimes \mathbf{a}_t(\theta_P, r_P)] \in \mathbb{C}^{KNM \times P}$  is the array manifold matrix,  $\boldsymbol{\beta}(l) = [\beta_1(l), \dots, \beta_P(l)]^T \in \mathbb{C}^{P \times 1}$  is the complex amplitude vector of  $P$  targets.

## 3. Extend the Range Ambiguity Using Subarrays

In traditional radar system, ambiguity range is caused by range-folded echo due to pulse repetition frequency (PRF). However, in FDA-MIMO radar, the angle-range of the target can be estimated jointly. Similarly, the range ambiguity problem also exists in FDA-MIMO radar. The range ambiguity in FDA-MIMO radar is caused by the multiple peak values in range dimension of the angle-range beamforming [13]. In this section, we explain the range ambiguity problem from the angle-range estimation principle. In this case, the problem of the multiple peak values in range dimension of the angle-range beamforming turns into the multiple peak values in range dimension of the angle-range spectrum. In addition, we use method of subarrays to extend the range between the multiple peaks and it is equivalent to extending unambiguous range in FDA-MIMO radar.

It can be seen from equation (7) that the angle and range in monostatic FDA-MIMO are decoupled. The angle of the target can be estimated separately from the receiving steering vector. Subsequently, the range of the target can be estimated from the transmitting steering vector. When estimating the angle and range of  $p$ -th target for transmitting frequency diverse array with ULA and uniform frequency increment, it is equivalent to estimating the phase difference  $\Delta\varphi(\theta_p, r_p) = (2\pi/c)(d_t f_1 \sin \theta_p - \Delta f r_p)$  in the

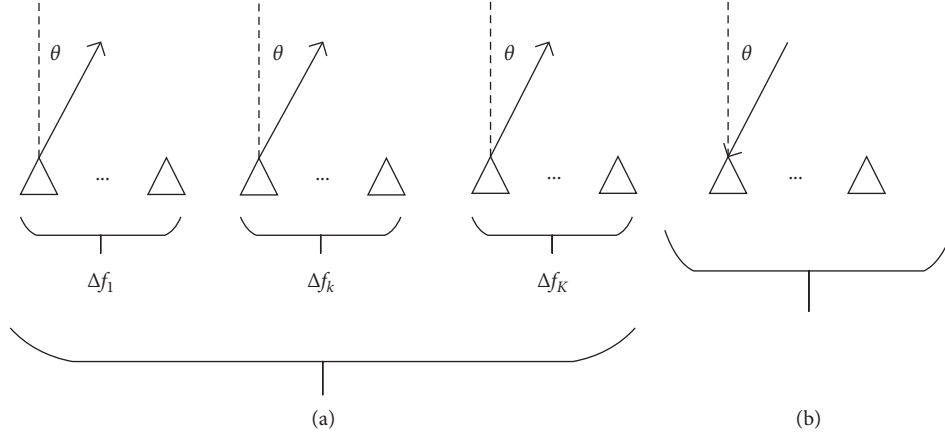


FIGURE 1: Transmitting subarrays monostatic FDA-MIMO radar system. (a) Transmitting array. (b) Receiving array.

transmitting steering vector and the phase difference  $\Delta\varphi(\theta_p) = (2\pi/c)(d_r f_1 \sin \theta_p)$  in the receiving steering vector. Obviously, the angle  $\theta_p$  of  $p$ -th target can be estimated from the receiving steering vector without unambiguous. The range  $r_p$  of  $p$ -th target can be estimated from the transmitting steering vector. However, the phase difference  $\Delta\varphi(\theta_p, r_p)$  is ambiguous with range.

We suppose the estimated value  $\phi$  for the phase difference  $\Delta\varphi(\theta_p, r_p)$  by the estimation algorithms is in the range of  $[-\pi, \pi)$ , i.e.,  $\phi \in [-\pi, \pi)$ . The range of the  $p$ -th target can be retrieved from the equation  $\Delta\varphi(\theta_p, r_p) = \phi$ ,  $\phi \in [-\pi, \pi)$ . We assume that the truth value of the  $p$ -th target range is  $r_t$  and the truth value of the  $p$ -th target angle is  $\theta_t$ . Then, we have

$$\left(\frac{2\pi}{c}\right)(d_t f_1 \sin \theta_t - \Delta f(r_t + q r_{\text{amb}})) = \phi, \quad q = 0, \pm 1, \pm 2, \dots, \quad (8)$$

where  $r_{\text{amb}}$  is the ambiguity range. From (8), we can see that  $r_{\text{amb}} = c/\Delta f$ , which means that the range ambiguity is determined by the frequency increment  $\Delta f$ . We can also

conclude that there is a periodic ambiguity in the estimated range and the periodic range is  $c/\Delta f$ . That means the maximum unambiguous detection range of monostatic FDA-MIMO radar is  $c/\Delta f$  and the maximum unambiguous range is inversely proportional to the frequency increment. Hence, we propose the subarrays method to handle the ambiguity range and extend the maximum unambiguous range.

In this paper, we utilize the method of transmitting subarrays to extend the maximum unambiguous range for monostatic FDA-MIMO radar. In the transmitting subarrays, the frequency increment of the  $k$ -th subarray is  $\Delta f_k$ . When range of the target estimated from the transmitter with transmitting subarrays, it is equivalent to estimating the phase difference  $\Delta\varphi_k(\theta_p, r_p) = (2\pi/c)(d_t f_1 \sin \theta_p - \Delta f_k r_p)$  in the transmitting steering vector and angle of the  $p$ -th target estimated from receiving steering vector before. We suppose the estimated value  $\phi_k$  for the phase difference  $\Delta\varphi_k(\theta_p, r_p)$  of  $k$ -th subarray by the estimation algorithms is in the range of  $[-\pi, \pi)$ , i.e.,  $\phi_k \in [-\pi, \pi)$ . In this case, the ambiguous rule of transmitting subarrays is determined by

$$\left\{ \begin{array}{l} \left(\frac{2\pi}{c}\right)(d_t f_1 \sin \theta_t - \Delta f_1(r_t + q_1 r_{\text{amb}}^1)) = \phi_1, q_1 = 0, \pm 1, \pm 2, \dots, \\ \vdots \\ \left(\frac{2\pi}{c}\right)(d_t f_1 \sin \theta_t - \Delta f_k(r_t + q_k r_{\text{amb}}^k)) = \phi_k, q_k = 0, \pm 1, \pm 2, \dots, \\ \vdots \\ \left(\frac{2\pi}{c}\right)(d_t f_1 \sin \theta_t - \Delta f_K(r_t + q_K r_{\text{amb}}^K)) = \phi_K, q_K = 0, \pm 1, \pm 2, \dots, \end{array} \right. \quad (9)$$

where  $r_{\text{amb}}^k$  is the maximum unambiguous range of the  $k$ -th subarray. Similarly, we can conclude that there is a periodic ambiguity in the range estimated by  $k$ -the subarray and the

periodic range is  $c/\Delta f_k$ . From equation (9), we can conclude that the maximum unambiguous range of transmitting subarrays satisfies

$$q_{\text{amb}}^{\text{max}} = q_1 r_{\text{amb}}^1 = \dots = q_k r_{\text{amb}}^k = \dots = q_K r_{\text{amb}}^K, \quad q = 0, \pm 1, \pm 2, \dots, \quad (10)$$

where  $r_{\text{amb}}^{\text{max}}$  is the maximum unambiguous range of transmitting subarrays. Hence, from the equations (9) and (10), the maximum unambiguous range of monostatic FDA-MIMO radar with transmitting subarrays is

$$r_{\text{amb}}^{\text{max}} = \text{lcm}\left(\frac{c}{\Delta f_1}, \dots, \frac{c}{\Delta f_k}, \dots, \frac{c}{\Delta f_K}\right). \quad (11)$$

From equation (11), if  $((c/\Delta f_1), \dots, (c/\Delta f_k), \dots, (c/\Delta f_K))$  satisfies the coprime relationship, the maximum unambiguous range is  $(c/\Delta f_1) \times \dots \times (c/\Delta f_k) \times \dots \times (c/\Delta f_K)$ . Therefore, a reasonable configuration of the transmitting subarrays can greatly extend the unambiguous range of the monostatic FDA-MIMO radar. On the contrary, if  $K=1$  or  $\Delta f_1 = \dots = \Delta f_k = \dots = \Delta f_K$  and  $f_{k,1} = f_{k-1,1} + M\Delta f_{k-1}$ , transmitting subarrays degenerate into nontransmitting subarrays, the unambiguous range will be greatly reduced.

Maximum unambiguous range of traditional, double-pulses, and transmitting subarrays monostatic FDA-MIMO radar is shown in Table 1. The maximum unambiguous range of traditional monostatic FDA-MIMO radar is  $c/\Delta f$ . The maximum unambiguous range of transmitting double-pulses monostatic FDA-MIMO radar is  $\text{lcm}((c/\Delta f_1), (c/\Delta f_2))$  and the maximum unambiguous range of transmitting subarrays monostatic FDA-MIMO radar is  $\text{lcm}((c/\Delta f_1), \dots, (c/\Delta f_k), \dots, (c/\Delta f_K))$ . Therefore, both the method of double-pulse and transmitting subarrays can extend the maximum unambiguous range. If the method of double-pulse is to obtain the same size of the maximum unambiguous range as the transmitting subarrays, it is necessary to transmit  $K$ -pulses with different frequency increments at different times, which will greatly increase the time cost of the radar system. Compared with the method of double-pulses, the method of transmitting subarrays can reduce the time cost of the radar system.

#### 4. The AP-ML Algorithm for Angle-Range Estimation

**4.1. ML Algorithm for Angle-Range Estimation.** In this part, the MLE algorithm is used to estimate angle and range for monostatic FDA-MIMO. First, the log-likelihood function of angle and range estimation is derived. Second, through simplification, the ML cost function about angle and range estimation is obtained. Finally, an AP algorithm is used for dimensionality reduction iterative search. In iterative search, angle and range are automatically matched, and no additional angle and range matching algorithm is required.

According to equation (7) array receiving signal model, the parameter to be estimated is  $\eta = \{\theta^T, \mathbf{r}^T, \mathbf{Z}, \sigma^2\}$ , where

$$\boldsymbol{\theta} = [\theta_1, \theta_2, \dots, \theta_P]^T, \quad (12a)$$

$$\mathbf{r} = [r_1, r_2, \dots, r_P]^T, \quad (12b)$$

$$\mathbf{Z} = [\boldsymbol{\beta}(1)^T, \dots, \boldsymbol{\beta}(L)^T, \dots, \boldsymbol{\beta}(L)^T]. \quad (12c)$$

Under the complex Gaussian noise with zero mean variance of  $\sigma^2$ , suppose the noises are independent of each other, the noise and signal also satisfy the independent relationship. At this time, the array received signal obeys  $\mathbf{X} \sim N_c(\mathbf{A}\mathbf{S}, \sigma^2 \mathbf{I}_{KMNL})$  [23], and the joint probability density function (PDF) of  $\mathbf{X}$  can be represented as

$$f_X(\mathbf{X}; \boldsymbol{\eta}) = \prod_{l=1}^L \frac{1}{(2\pi\sigma^2)^{KMNL/2}} \exp\left[-\frac{(\mathbf{x}(l) - \mathbf{A}\boldsymbol{\beta}(l))^H (\mathbf{x}(l) - \mathbf{A}\boldsymbol{\beta}(l))}{2\sigma^2}\right], \quad (13)$$

where  $\mathbf{X} = [\mathbf{x}(1), \dots, \mathbf{x}(L), \dots, \mathbf{x}(L)]$ .

By performing the logarithm operation on the joint PDF, the log-likelihood function is obtained as

$$L(\boldsymbol{\eta}) = \ln\{f_X(\mathbf{X}; \boldsymbol{\eta})\} = -\frac{KMNL}{2} \ln(2\pi\sigma^2) \quad (14)$$

$$- \frac{1}{2\sigma^2} \sum_{l=1}^L (\mathbf{x}(l) - \mathbf{A}\boldsymbol{\beta}(l))^H (\mathbf{x}(l) - \mathbf{A}\boldsymbol{\beta}(l)).$$

By taking the derivative of  $\sigma^2$  setting the derivative function to zero, we can obtain the maximum likelihood estimation of  $\sigma^2$  as

$$\hat{\sigma}^2 = \frac{1}{KMNL} \sum_{l=1}^L (\mathbf{x}(l) - \mathbf{A}\boldsymbol{\beta}(l))^H (\mathbf{x}(l) - \mathbf{A}\boldsymbol{\beta}(l)). \quad (15)$$

Substituting  $\hat{\sigma}^2$  into equation (13), the new log-likelihood function as

$$L(\boldsymbol{\theta}, \mathbf{r}, \mathbf{Z}) = \frac{KMNL}{2} - \frac{KMNL}{2} \cdot \ln\left(\frac{2\pi}{KMNL} \sum_{l=1}^L (\mathbf{x}(l) - \mathbf{A}\boldsymbol{\beta}(l))^H (\mathbf{x}(l) - \mathbf{A}\boldsymbol{\beta}(l))\right). \quad (16)$$

From equation (16), the new log-likelihood function satisfies the following relationship:

$$L(\boldsymbol{\theta}, \mathbf{r}, \mathbf{Z}) \propto - \sum_{l=1}^L (\mathbf{x}(l) - \mathbf{A}\boldsymbol{\beta}(l))^H (\mathbf{x}(l) - \mathbf{A}\boldsymbol{\beta}(l)). \quad (17)$$

Then, the maximum likelihood estimation of angle and range becomes

$$(\hat{\boldsymbol{\theta}}, \hat{\mathbf{r}}, \hat{\mathbf{Z}})_{\text{ML}} = \arg \max_{\boldsymbol{\theta}, \mathbf{r}, \mathbf{Z}} (L(\boldsymbol{\theta}, \mathbf{r}, \mathbf{Z})). \quad (18)$$

Because  $\mathbf{x}(l) = \mathbf{A}\boldsymbol{\beta}(l) + \mathbf{n}(l)$  is a linear model about  $\boldsymbol{\beta}(l)$ , we can know from the best likelihood estimation theorem of the linear model

$$\hat{\boldsymbol{\beta}}(l)_{\text{ML}} = (\mathbf{A}^H \mathbf{A})^{-1} \mathbf{A}^H \mathbf{x}(l). \quad (19)$$

Taking equations (19) into (18) and simplifying, the maximum likelihood cost function for angle and range estimation can be described as

TABLE 1: Maximum unambiguous range of traditional, double-pulses, and transmitting subarrays monostatic FDA-MIMO radar.

FDA	Traditional	Double-pulses	Transmitting subarrays
Maximum unambiguous range (m)	$c/\Delta f$	$\text{lcm}((c/\Delta f_1), (c/\Delta f_2))$	$\text{lcm}((c/\Delta f_1), \dots, (c/\Delta f_k), \dots, (c/\Delta f_K))$

$$(\hat{\boldsymbol{\theta}}, \hat{\mathbf{r}})_{\text{ML}} = \arg \max_{\boldsymbol{\theta}, \mathbf{r}} \text{trace}(\mathbf{P}_A \mathbf{R}), \quad (20)$$

where  $\mathbf{P}_A = \mathbf{A}(\mathbf{A}^H \mathbf{A})^{-1} \mathbf{A}^H$  is the projection matrix and  $\mathbf{R} = (1/L) \sum_{l=1}^L \mathbf{x}(l) \mathbf{x}^H(l)$  is the signal covariance matrix.

ML cost function is a high-dimensional search problem. When the number of targets is  $P$ , a global search will be conducted in the  $2P$ -dimensional space. In order to improve the calculation efficiency, we further simplify the  $2P$ -dimensional search into a series of one-dimensional iterative search by AP algorithm.

**4.2. AP Iterative Search for ML Cost Function.** AP algorithm is a simple and effective method to solve the multidimensional searching problem. It simplifies the multidimensional searching into a series of one-dimensional searching and thus can greatly reduce the computational load. However, if the objective function is not convex, the initial value of the parameter will greatly influence the result of searching. In order to prevent the algorithm from falling into the local optimal value, a good initialization parameter value is very important. The method in [24] is used to initialize angle and range.

Firstly, the first group of angle and range initial values is obtained as follows:

$$(\hat{\theta}_1^{(0)}, \hat{r}_1^{(0)}) = \arg \max_{\theta, r} \text{trace}\{\mathbf{P}_{\mathbf{a}_r(\theta) \otimes \mathbf{a}_t(\theta, r)} \mathbf{R}\}. \quad (21)$$

After that, the second group of angle and range is solved by

$$(\hat{\theta}_2^{(0)}, \hat{r}_2^{(0)}) = \arg \max_{\theta, r} \text{trace}\left\{\mathbf{P}\left[\mathbf{a}_r(\hat{\theta}_1^{(0)}) \otimes \mathbf{a}_t(\hat{\theta}_1^{(0)}, \hat{r}_1^{(0)})\right]_{\mathbf{a}_r(\theta) \otimes \mathbf{a}_t(\theta, r)} \mathbf{R}\right\}. \quad (22)$$

According to the method of equations (21) and (22), initialize the  $P$  groups of angle and range in sequence.

Next, iteratively update the  $P$  groups of angle and range until the algorithm iteration stop condition is satisfied. In the iterative process, perform a one-dimensional search for angle and range, respectively:

$$\hat{\theta}_p^{(j+1)} = \arg \max_{\theta} \text{trace}\left\{\mathbf{P}\left[\hat{\mathbf{A}}(\Theta^{(j)})_{\mathbf{a}_r(\theta) \otimes \mathbf{a}_t(\hat{\theta}_p^{(j)}, \hat{r}_p^{(j)})}\right] \mathbf{R}\right\}, \quad (23)$$

$$\hat{r}_p^{(j+1)} = \arg \max_r \text{trace}\left\{\mathbf{P}\left[\hat{\mathbf{A}}(\Theta^{(j)})_{\mathbf{a}_r(\hat{\theta}_p^{(j)}) \otimes \mathbf{a}_t(\hat{\theta}_p^{(j)}, r)}\right] \mathbf{R}\right\}, \quad (24)$$

where  $\Theta^{(j)}$  represents the  $P$ -1 pair angle and range from the  $j$ -th iteration, which can be described as

$$\Theta^{(j)} = [(\theta_1^{(j)}, r_1^{(j)}), \dots, (\theta_{p-1}^{(j)}, r_{p-1}^{(j)}), (\theta_{p+1}^{(j)}, r_{p+1}^{(j)}), \dots, (\theta_p^{(j)}, r_p^{(j)})]. \quad (25)$$

Finally, the iteration stop condition is

$$|\hat{\theta}_p^{(j+1)} - \hat{\theta}_p^{(j)}| \leq \delta, \quad (26)$$

$$|\hat{r}_p^{(j+1)} - \hat{r}_p^{(j)}| \leq \varepsilon, \quad (27)$$

where  $p = 1, \dots, P$ ,  $\delta$ , and  $\varepsilon$  are error thresholds. When (26) and (27) are satisfied at the same time or the iteration reaches the maximum number, the iteration stops.

The steps for the angle and range estimation in monostatic FDA-MIMO radar using AP-MLE are described as follows:

Step 1:  $j=0$ , initialize the angle-range parameters according to equations (21) and (22).

Step 2:  $j=j+1$ , iteratively and update the angle and range parameters according to equations (23) and (24).

Step 3: if (26) and (27) are satisfied, or the maximum number of iterations is reached, the algorithm stops, otherwise repeat Step 2.

## 5. Simulation Results

In this part, we design some experiments to prove the efficiency of the proposed method of transmitting subarrays to extend the unambiguous range for monostatic FDA-MIMO radar and the superiority of the proposed AP-ML angle and range estimation for monostatic FDA-MIMO radar.

**5.1. Simulation 1.** In order to verify the effectiveness of the proposed transmitting subarrays to extend the unambiguous range for monostatic FDA-MIMO radar, simulation 1 gives the unambiguous range of transmitting subarrays monostatic FDA-MIMO radar and nontransmitting subarrays monostatic FDA-MIMO radar by MUSIC spectrum.

Consider the number of transmitting subarrays is  $K=2$ , the number of subarrays elements is  $M=6$ , and the frequency increment  $\Delta f_1$  of the first subarray is 2 kHz. The frequency increment  $\Delta f_2$  of the second subarray is 5 kHz. The carrier frequency of the first subarray reference array element is 10 GHz, and the carrier frequency of the second subarray reference array element is 10.000012 GHz. The number of array elements of the receiving array is  $N=8$ , and  $d_t = d_r = (c/2f_{\text{KM}})$ . Suppose a target is located at  $(20^\circ, 50 \text{ km})$ , under the conditions of signal-to-noise ratio (SNR)=20 dB, and the number of snapshots  $L$  is 100, the following gives the monostatic FDA-MIMO MUSIC spectrum with frequency increment  $\Delta f_1 = \Delta f_2 = 2 \text{ kHz}$ ,  $\Delta f_1 = \Delta f_2 = 5 \text{ kHz}$ , and  $\Delta f_1 = 2 \text{ kHz}$ ,  $\Delta f_2 = 5 \text{ kHz}$ .

Figure 2 shows the MUSIC spectrum with  $\Delta f_1 = \Delta f_2 = 2$  kHz; in this case, the unambiguous range of nontransmitting subarrays (traditional FDA) is 150 km. Figure 3 shows the MUSIC spectrum with  $\Delta f_1 = \Delta f_2 = 5$  kHz; in this case, the unambiguous range of nontransmitting subarrays is 60 km. Figure 4 shows the MUSIC spectrum with  $\Delta f_1 = 2$  kHz and  $\Delta f_2 = 5$  kHz; in this case, the unambiguous range of transmitting subarrays is 300 km. Comparing Figures 2 and 3, under the traditional FDA, the unambiguous range is inversely proportional to the frequency increment. Comparing Figures 2–4, it can be concluded that the proposed transmitting subarrays can extend the unambiguous range for monostatic FDA-MIMO radar.

**5.2. Simulation 2.** In order to verify the correctness of the proposed AP-ML angle and range estimation for transmitting subarrays monostatic FDA-MIMO radar, simulation 2 gives the estimation result of AP-MLE.

Suppose three targets located at  $(-10^\circ, 151$  km),  $(5^\circ, 152$  km), and  $(30^\circ, 154$  km), and transmitting subarrays  $K=2$ , the number of each subarray elements  $M=6$ ,  $\Delta f_1 = 2$  kHz, and  $\Delta f_2 = 5$  kHz. Obviously three targets are within the unambiguous range. In the case of SNR = 10 dB and snapshot number  $L = 100$ , 100 Monte Carlo simulation results are given in Figure 5. The angle search step is  $0.05^\circ$ , and the range search step is 5 m.

Figure 5 shows the angle and range estimation results of AP-MLE within the unambiguous range. From Figure 5, we can know the AP-MLE algorithm can complete the angle and range estimation for transmitting subarrays monostatic FDA-MIMO radar. At SNR = 10 dB, 100 estimations are closer to the real angle and range. In addition, in the AP iteration, the 3 groups of angle and range are automatically paired without additional pairing algorithm.

**5.3. Simulation 3.** Simulation 3 uses the average number of iterations curves versus SNR to represent the efficiency of the AP-ML angle and range estimation for transmitting subarrays monostatic FDA-MIMO radar. The simulation conditions are the same as for simulation 2.

Figure 6 gives the average number of iterations curves versus SNR of AP-ML angle and range estimation for transmitting subarrays monostatic FDA-MIMO radar. As the SNR increases, the number of iterations required decreases. When SNR is greater than or equal to 20 dB, AP-MLE only needs about two iterations and the efficiency of the AP-MLE is significant.

**5.4. Simulation 4.** In order to evaluate the estimation performance of the AP-MLE algorithm, the AP-MLE root mean square error (RMSE) of the angle and range against the SNR is compared with the MUSIC algorithm, ESPRIT algorithm (angle and range pairing algorithm in [25]), paper [13], and angle-range estimation CRLB. The CRLB expression is given by equation (28), the angle and range RMSE expressions are given by equations (35) and (36).

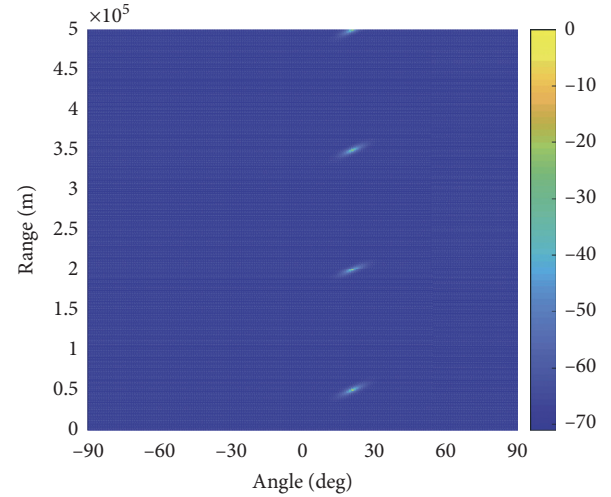


FIGURE 2: MUSIC spectrum with  $\Delta f_1 = \Delta f_2 = 2$  kHz.

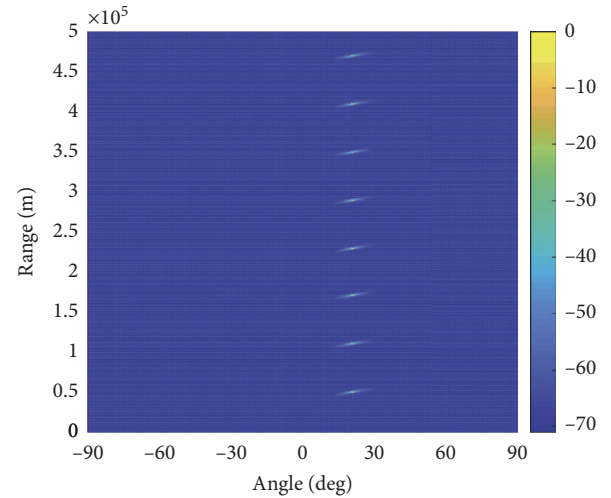


FIGURE 3: MUSIC spectrum with  $\Delta f_1 = \Delta f_2 = 5$  kHz.

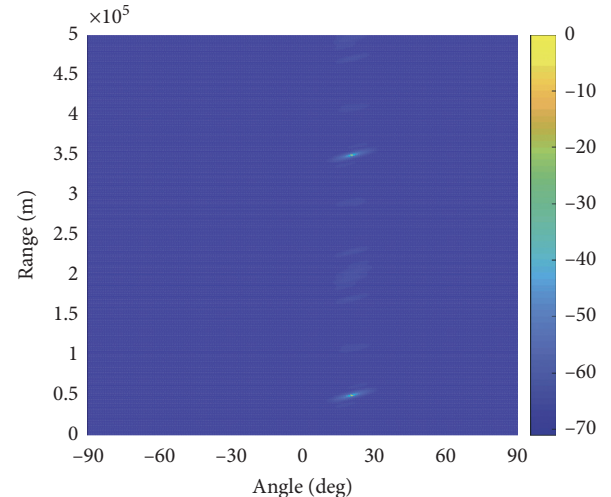


FIGURE 4: MUSIC spectrum with  $\Delta f_1 = 2$  kHz and  $\Delta f_2 = 5$  kHz.

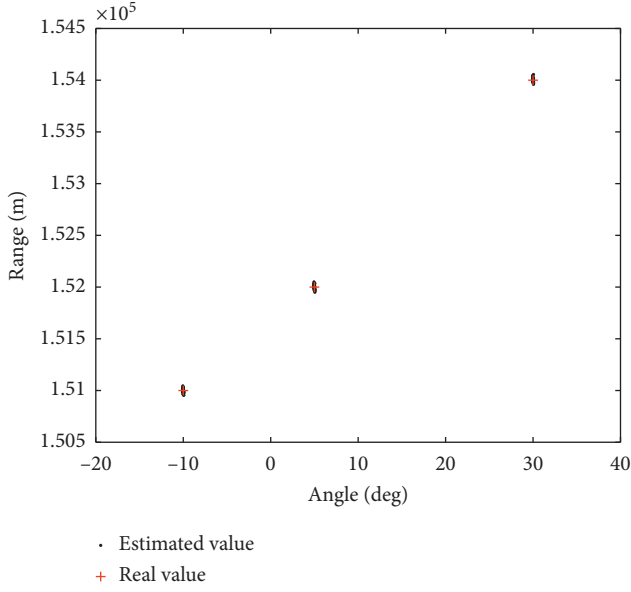


FIGURE 5: Angle and range estimation results of AP-MLE.

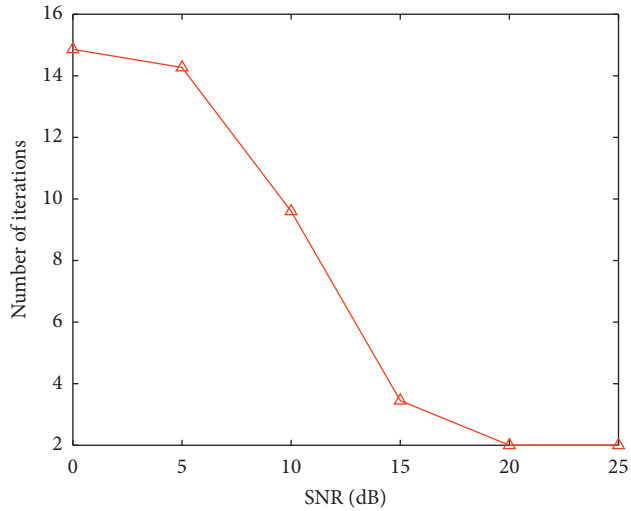


FIGURE 6: Average number of iterations curves versus SNR.

$$\text{CRLB}(\Theta) = \frac{\sigma^2}{2L} \left\{ \text{Re} \left[ \left( \mathbf{C}^H \mathbf{P}_A^\perp \mathbf{C} \right) \odot \left( \mathbf{R}_\beta \otimes \mathbf{1}_{2 \times 2} \right) \right] \right\}^{-1}, \quad (28)$$

where

$$\Theta = [\theta_1, r_1, \dots, \theta_p, r_p, \dots, \theta_p, r_p]^T, \quad (29)$$

$$\mathbf{C} = [\mathbf{d}(\theta_1), \mathbf{d}(r_1), \dots, \mathbf{d}(\theta_p), \mathbf{d}(r_p), \dots, \mathbf{d}(\theta_p), \mathbf{d}(r_p)], \quad (30)$$

$$\mathbf{d}(\theta_p) = \frac{\partial \mathbf{a}_r(\theta_p) \otimes \mathbf{a}_t(\theta_p, r_p)}{\partial \theta_p}, \quad (31)$$

$$\mathbf{d}(r_p) = \frac{\partial \mathbf{a}_r(\theta_p) \otimes \mathbf{a}_t(\theta_p, r_p)}{\partial r_p}, \quad (32)$$

$$\mathbf{R}_\beta = \frac{1}{L} \sum_{l=1}^L \beta(l) \beta^H(l), \quad (33)$$

$$\mathbf{P}_A^\perp = \mathbf{I} - \mathbf{P}_A. \quad (34)$$

From equations (31) and (32), the frequency increments have a significant effect on the CRLB of range estimation and have no significant effect on the CRLB of angle estimation. Therefore, we mainly consider the effect of the frequency increment setting on the CRLB of range estimate in this simulation.

$$\text{RMSE}_\theta = \frac{1}{P} \sum_{p=1}^P \sqrt{\frac{1}{D} \sum_{d=1}^D (\hat{\theta}_p^d - \theta_p)^2}, \quad (35)$$

$$\text{RMSE}_r = \frac{1}{P} \sum_{p=1}^P \sqrt{\frac{1}{D} \sum_{d=1}^D (\hat{r}_p^d - r_p)^2}, \quad (36)$$

where  $\hat{\theta}_p^d$  is the angle value of the  $p$ -th target estimated at the  $d$ -th time,  $\hat{r}_p^d$  is the range value of the  $p$ -th target estimated at the  $d$ -th time, and  $D$  is the number of Monte Carlo simulations.

Suppose three targets are located at  $(-5^\circ, 11 \text{ km})$ ,  $(10^\circ, 13 \text{ km})$ , and  $(35^\circ, 14 \text{ km})$ , where the angle search step is  $0.01^\circ$  and the range search step is  $1 \text{ m}$ . The number of simulations  $D = 200$  and other simulation conditions are the same as simulation 2.

Figure 7 shows angle CRLB and RMSE curves versus SNR and Figure 8 shows range CRLB and RMSE curves versus SNR. From Figures 7 and 8, as the SNR increases, the angle and range RMSE of paper [13], MUSIC, ESPRIT, AP-MLE, and CRLBs decrease continuously. However, the angle and range RMSE of AP-MLE is closest to angle and range CRLB. So, the performance of angle and range estimation of AP-MLE is better than paper [13], MUSIC, and ESPRIT, and the ESPRIT is the worst.

Next, according to the range estimation CRLB with  $\Delta f_1 = \Delta f_2 = 2 \text{ kHz}$ ,  $\Delta f_1 = \Delta f_2 = 3 \text{ kHz}$ ,  $\Delta f_1 = \Delta f_2 = 5 \text{ kHz}$ , and  $\Delta f_1 = 2 \text{ kHz}$ ,  $\Delta f_2 = 5 \text{ kHz}$  in Figure 8, the nontransmitting subarrays monostatic FDA-MIMO radar range estimation CRLB decreases with increasing frequency. However, from equation (8), the max unambiguous range decreases with increasing frequency. Hence, it is impossible to obtain a low-range CRLB and a large unambiguous range at the same time in nontransmitting subarrays monostatic FDA-MIMO radar. However, lower-range estimation CRLB and large unambiguous range can be obtained at the same time in transmitting subarrays monostatic FDA-MIMO radar. That means the proposed transmitting subarrays can solve the relationship between the low-range estimation CRLB and large unambiguous range contradiction.

**5.5. Simulation 5.** We measure resolution by the resolution probability of the targets. The expression for the threshold is  $\chi = \min[(\sqrt{(\theta_{p1} - \theta_{p2})^2 + (r_{p1} - r_{p2})^2})/2]$ ,  $p_1, p_2 = 1, \dots$ ,

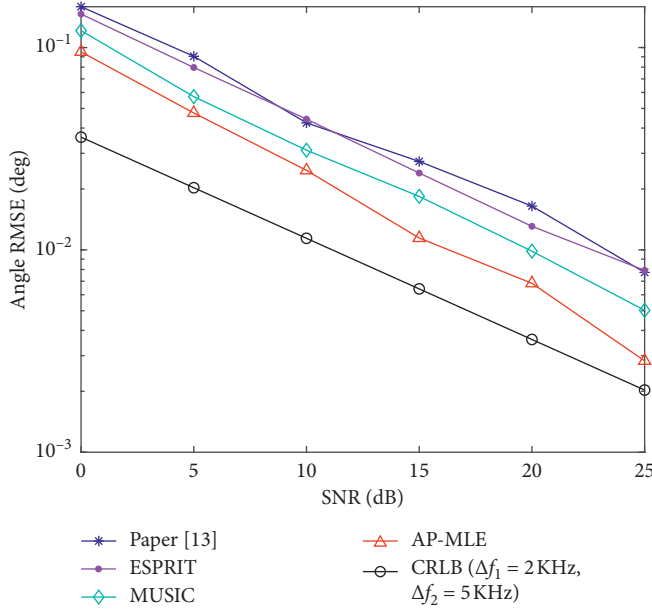


FIGURE 7: Angle CRLB and RMSE curves versus SNR.

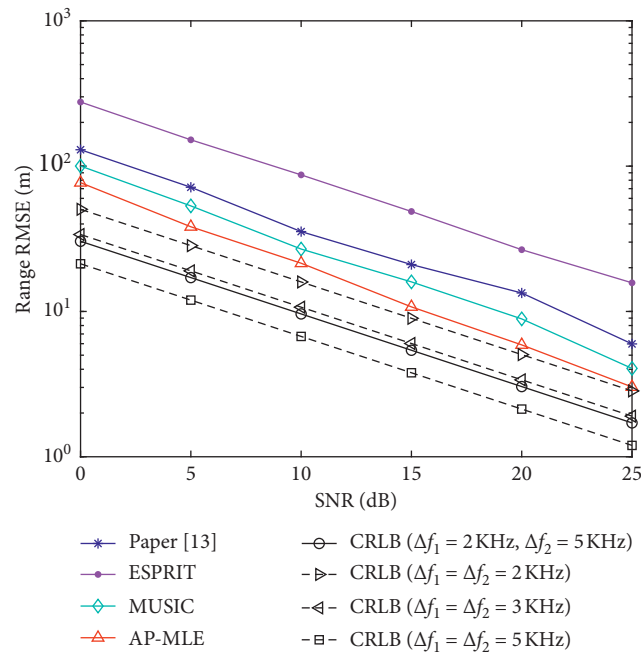


FIGURE 8: Range CRLB and RMSE curves versus SNR.

$P$ ,  $p_1 \neq p_2$ . If the absolute error of the estimation than  $\chi$ , the estimation is considered a failure resolution. The estimation angle and range are mapped to the wrong target, which leads to a large error, so that the different targets cannot be distinguished correctly.

Assume that two targets are located at  $(10^\circ, 11 \text{ km})$  and  $(15^\circ, 11.5 \text{ km})$ . Other simulation conditions are the same as simulation 2.

Figure 9 gives the resolution probability curves versus SNR. From Figure 9, as the SNR increases, the resolution

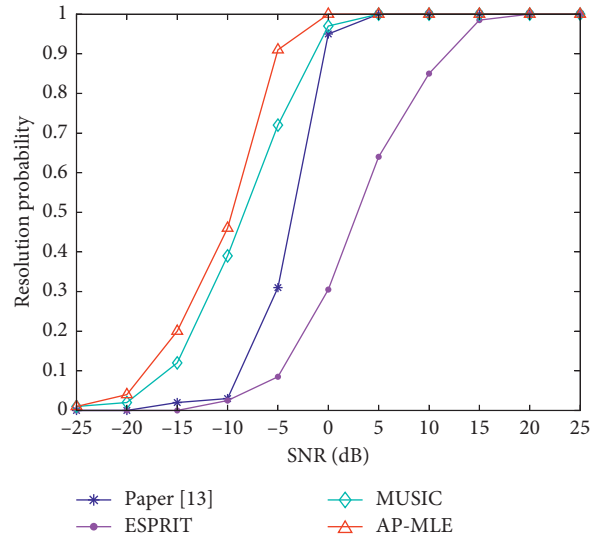


FIGURE 9: Resolution probability curves versus SNR.

probability of AP-MLE reaches 1 at the fastest. From the trend of the curve change, we can conclude the resolution probability of AP-MLE is the best, MUSIC is second, paper [13] is third, and the ESPRIT is the slowest. In addition, the resolution capability of AP-MLE is obviously greater than paper [13], MUSIC, and ESPRIT, and the ESPRIT algorithm.

## 6. Conclusions

This paper proposes to extend the unambiguous range of the monostatic FDA-MIMO radar using the transmitting sub-arrays. Meanwhile, the proposed transmitting subarrays can solve the relationship between the low range estimation CRLB and large unambiguous range contradiction. In addition, the AP-ML angle and range estimation for monostatic FDA-MIMO radar are proposed. The simulation results prove the superiority of AP-ML angle and range estimation for monostatic FDA-MIMO radar in estimation accuracy and resolution.

## Data Availability

The simulation data used to support the findings of this study are included within the article.

## Conflicts of Interest

The authors declare that there are no conflicts of interest regarding the publication of this paper.

## Acknowledgments

This work was supported by the National Natural Science Foundation of China (61661032), the Young Natural Science Foundation of Jiangxi Province (20181BAB202002), the China Postdoctoral Science Foundation (2017M622102), and the Foundation from China Scholarship Council (201906825071).

## References

- [1] P. Antonik, M. C. Wicks, H. D. Griffiths et al., "Frequency diverse array radars," in *Proceedings of the IEEE Conference on Radar*, pp. 215–217, IEEE, Verona, NY, USA, April 2006.
- [2] A. Basit, W. Khan, S. Khan et al., "Development of frequency diverse array radar technology: a review," *IET Radar Sonar & Navigation*, vol. 12, no. 2, pp. 165–175, 2017.
- [3] W.-Q. Wang, "Frequency diverse array antenna: new opportunities," *IEEE Antennas and Propagation Magazine*, vol. 57, no. 2, pp. 145–152, 2015.
- [4] W.-Q. Wang, "Range-angle dependent transmit beam pattern synthesis for linear frequency diverse arrays," *IEEE Transactions on Antennas and Propagation*, vol. 61, no. 8, pp. 4073–4081, 2013.
- [5] W. Wang and H. Shao, "Range-angle localization of targets by a double-pulse frequency diverse array radar," *IEEE Journal of Selected Topics in Signal Processing*, vol. 8, no. 1, pp. 106–114, 2014.
- [6] J. Xu, G. Liao, S. Zhu, and H. C. So, "Deceptive jamming suppression with frequency diverse MIMO radar," *Signal Processing*, vol. 113, pp. 9–17, 2015.
- [7] J. Lin, Q. Li, J. Yang, H. Shao, and W.-Q. Wang, "Physical-layer security for proximal legitimate user and eavesdropper: a frequency diverse array beamforming approach," *IEEE Transactions on Information Forensics and Security*, vol. 13, no. 3, pp. 671–684, 2018.
- [8] D. W. Bliss and K. W. Forsythe, "Multiple-input multiple-output (MIMO) radar and imaging: degrees of freedom and resolution," in *Proceedings of the Thirty-Seventh Asilomar Conference on Signals, Systems & Computers*, pp. 54–59, Pacific Grove, CA, USA, November 2003.
- [9] K. W. Forsythe, D. W. Bliss, and G. S. Fawcett, "Multiple-input multiple-output (MIMO) radar: performance issues," in *Proceedings of the Thirty-Eighth Asilomar Conference on Signals, Systems and Computers*, pp. 310–315, Pacific Grove, CA, USA, November 2004.
- [10] C. Cui, J. Xu, R. Gui, W.-Q. Wang, and W. Wu, "Search-free DOD, DOA and range estimation for bistatic FDA-MIMO radar," *IEEE Access*, vol. 6, pp. 15431–15445, 2018.
- [11] J. Xu, G. Liao, S. Zhu, L. Huang, and H. C. So, "Joint range and angle estimation using MIMO radar with frequency diverse array," *IEEE Transactions on Signal Processing*, vol. 63, no. 13, pp. 3396–3410, 2015.
- [12] S. Qin, Y. D. Zhang, M. G. Amin, and F. Gini, "Frequency diverse coprime arrays with coprime frequency offsets for multitarget localization," *IEEE Journal of Selected Topics in Signal Processing*, vol. 11, no. 2, pp. 321–335, 2017.
- [13] Y. Song, G. Zheng, and G. Hu, "A combined ESPRIT-MUSIC method for FDA-MIMO radar with extended range ambiguity using staggered frequency increment," *International Journal of Antennas and Propagation*, vol. 2019, Article ID 3056074, 7 pages, 2019.
- [14] L. Huang, X. Li, P.-C. Gong, and Z. He, "Frequency diverse array radar for target range-angle estimation," *COMPEL - The International Journal for Computation and Mathematics in Electrical and Electronic Engineering*, vol. 35, no. 3, pp. 1257–1270, 2016.
- [15] J. Xiong, W.-Q. Wang, and K. Gao, "FDA-MIMO radar range-angle estimation: CRLB, MSE, and resolution analysis," *IEEE Transactions on Aerospace and Electronic Systems*, vol. 54, no. 1, pp. 284–294, 2018.
- [16] C. Cui, Y. Yan, W. Wang et al., "Resolution threshold of music algorithm for FDA-MIMO radar," in *Proceedings of the 2018 IEEE Radar Conference (RadarConf18)*, IEEE, Oklahoma City, CA, USA, pp. 0230–0234, April 2018.
- [17] Y. Yan, J. Cai, and W. Wang, "Two-stage ESPRIT for unambiguous angle and range estimation in FDA-MIMO radar," *Digital Signal Processing*, vol. 92, pp. 151–165, 2019.
- [18] H. Chen and H. Shao, "Sparse reconstruction based target localization with frequency diverse array MIMO radar," in *Proceedings of the 2015 IEEE China Summit and International Conference on Signal and Information Processing (ChinaSIP)*, pp. 94–98, Chengdu, China, July 2015.
- [19] T. Liu, F. Wen, L. Zhang, and K. Wang, "Off-grid DOA estimation for colocated MIMO radar via reduced-complexity sparse Bayesian learning," *IEEE Access*, vol. 7, pp. 99907–99916, 2019.
- [20] W. Tang, H. Jiang, and S. Pang, "Gridless angle and range estimation for FDA-MIMO radar based on decoupled atomic norm minimization," in *Proceedings of the 2019 IEEE International Conference on Acoustics, Speech and Signal Processing (ICASSP)*, pp. 4305–4309, IEEE, Brighton, UK, May 2019.
- [21] P. Stoica and A. Nehorai, "MUSIC, maximum likelihood, and Cramer-Rao bound: further results and comparisons," *IEEE Transactions on Acoustics, Speech, and Signal Processing*, vol. 38, no. 12, pp. 2140–2150, 1990.
- [22] J. A. Tropp, I. S. Dhillon, R. W. Heath, and T. Strohmer, "Designing structured tight frames via an alternating projection method," *IEEE Transactions on Information Theory*, vol. 51, no. 1, pp. 188–209, 2005.
- [23] I. Bekkerman and J. Tabrikian, "Target detection and localization using MIMO radars and sonars," *IEEE Transactions on Signal Processing*, vol. 54, no. 10, pp. 3873–3883, 2006.
- [24] I. Ziskind and M. Wax, "Maximum likelihood localization of multiple sources by alternating projection," *IEEE Transactions on Acoustics, Speech, and Signal Processing*, vol. 36, no. 10, pp. 1553–1560, 1988.
- [25] C. Duofang, C. Baixiao, and Q. Guodong, "Angle estimation using ESPRIT in MIMO radar," *Electronics Letters*, vol. 44, no. 12, pp. 770–771, 2008.



## Research Article

# Nonuniformly Spaced Array with the Direct Data Domain Method for 2D Angle-of-Arrival Measurement in Electronic Support Measures Application from 6 to 18 GHz

Chen Wu  and Janaka Elangage

*Defence Research and Development Canada, Ottawa Research Centre, Ottawa K1A 0Z4, Canada*

Correspondence should be addressed to Chen Wu; [chen.wu@drdc-rddc.gc.ca](mailto:chen.wu@drdc-rddc.gc.ca)

Received 27 May 2020; Revised 24 July 2020; Accepted 3 August 2020; Published 2 September 2020

Guest Editor: Jingjing Cai

Copyright © 2020 Chen Wu and Janaka Elangage. This is an open access article distributed under the Creative Commons Attribution License, which permits unrestricted use, distribution, and reproduction in any medium, provided the original work is properly cited.

This paper introduces a 2D angle-of-arrival (AoA) estimator, which has a 6–18 GHz 7-element nonuniformly spaced array (NSA) and a Direct Data Domain- (D3-) based AoA algorithm for a 2D isotropic-element planar array (IEPA). A 2D calibration and data-transformation method is developed to convert the NSA data to the output of the IEPA, so that the NSA-measured data can be used in the D3 algorithm. Using the steering vector (SV) of the IEPA and the results derived from the D3 method, a new 2D AoA searching method is also developed, which offers frequency-independent performance defined by the probability of AoA estimation, when the required estimation accuracy and signal-to-noise ratio (SNR) are given. For the applications of electronic support measures, this paper also presents the use of precalculated SV and data-transformation matrix databases built on preselected frequency points and a 2D-angle grid that is close to uniformly distributed directions. The simulation results show that with good SNR ( $\geq 15$  dB), the estimator can have 50% probability of AoA estimation with root mean square error (RMSE) less than or equal to  $1^\circ$  using just a few samples from the NSA. Moreover, the study focuses on the applications with low SNR by using more samples from the NSA. Results show that the estimator has 52% and 80% probabilities of AoA estimation with  $\text{RMSE} \leq 1^\circ$  and  $5^\circ$ , respectively, for phase- or frequency-modulated radar pulses, when the SNR is within  $[-10, 0]$  dB. The study also shows that the estimator prefers a circular-shaped planar array with a triangular interelement pattern, since it presents more symmetrical characteristics from different azimuth angles.

## 1. Introduction

The angle-of-arrival (AoA) of the signal of interest (SOI) is the most important measurement parameter in an electronic support measures (ESM) system to de-interleave intercepted radar signals, especially in detecting and classifying low probability of intercept signals [1]. Traditionally, spinning direction-finding (DF) antenna, amplitude-comparison, phase-comparison, and interferometry methods are popular AoA measurement methods in ESM systems [2–10]. In addition, there are many microwave DF systems developed for wireless communication applications [11]. From a signal-processing perspective, there are a number of algorithms used for signal DF applications. Among them, multiple signal classification (MUSIC) [12] and estimation of signal

parameters via rotation invariance techniques (ESPIRT) [13] have been used for many years with different array configurations for different applications. As examples, currently, these methods are used for 2D AoA estimations for mixed circular and noncircular incident signals for massive multiple-input multiple-output systems [14] and for uniform rectangular array [15]. However, to apply these methods, a stable signal environment is generally required, since the signal covariance matrix needs to be formed. A new approach for AoA estimation was introduced using information geometry (IG) [16]. Based on IG, Dong et al. [17] introduced a simple scaling transform-based information geometry (STRIG) method, which has more consistent performance than the original IG method while having a high AoA estimation resolution. Lonkeng and Zhuang [18]

presented a research on 2D DF estimation using arbitrary arrays in MIMO systems and introduced the 2D Fourier domain line search MUSIC algorithm. Krishnaveni et al. [19], Devendra and Manjunathachari [20], and Barua et al. [21] have surveyed some directions of arrival methods. Many other AoA estimators have also been developed, which focus on different array structures and faster processing speeds. Some examples are given in [22–28].

There are also some AoA estimation methods that are based on compressive sensing (CS) theory [29–31]. Gurbuz et al. [32, 33] applied CS to estimate acoustic wave AoA by focusing on one receiving channel sampling at Nyquist rate and the other channels sampling at CS rate. Using the target bearing as a sparse vector, Cevher et al. [34] demonstrated multielement circular acoustic sensor arrays to obtain the bearings of multiple sources by applying an  $l_1$ -norm minimization solution called the Dantzig selector [35]. Wu and Elangage [36] introduced a CS-based ultra-wideband 2D AoA estimation scheme that can estimate AoA of the SOI from 2 to 18 GHz without any a priori knowledge of the intercepted signals. Other examples of treating AoA estimation as a sparse recovery problem can be found in [37–40]. Bayesian CS- (BCS-) based AoA estimation was also developed in [41–43]. The key advantage of the BCS AoA estimator is its ability to estimate signal AoA with few measured data from each element in the array.

To estimate the AoA of SOI in a nonstationary environment and to avoid having to form a signal covariance matrix, the Direct Data Domain (D3) method was introduced [44–47]. Using the D3 method and the concept of signal cyclostationarity, Sarker et al. [48] introduced a method that can handle a number of signals along with their various coherent and noncoherent multipaths and interferences, even when the number of signals exceeds the number of antenna elements. This was demonstrated using a 12-element uniform linear array. Some examples of using the D3 method for AoA estimations can be found in [49–54].

Most aforementioned methods and their usages on antenna arrays are suitable for narrow-band applications, as the array elements and their configurations closely relate to the signal wavelengths. Hence, they can be used mainly for AoA estimations in communication applications. Interferometry-based AoA measurement systems have been widely used in ESM systems for 2D AoA measurements in ultra-wide frequency ranges [2–4]. It is desirable to use the longest possible baseline in the array, to achieve low variance measurement results. However, longer baselines require higher signal-to-noise ratios (SNRs) in order to resolve the ambiguity using the associated trigonometric functions. In addition, even if the wideband antenna elements, such as cavity-backed spiral antennas (CBSA), are used in the five-element array in [2], the spacing of the short baseline in the array is chosen to be less than half of the wavelength of the highest frequency of interest. As a result, several different five-element interferometers are required to cover a wide operational frequency range. This results in a large antenna array footprint. Pasala et al. [5] introduced a three-element interferometer array that used multimodes in the elements

to avoid the short baseline required in the conventional five-element array configuration. The long baseline (larger array footprint) is still required to resolve the ambiguity. However, these large-footprint arrays are problematic for small airborne platforms, such as CubeSats (U-class spacecraft) [55], small unmanned aerial vehicles [56, 57], and drones.

In this paper, we propose a novel 2D angle-of-arrival (AoA) estimator for ESM applications from 6 to 18 GHz in low SNR environments with frequency-independent performance, when the SNR and the required estimation accuracy are given. This includes the following contributions:

- (i) A 2D 7-element compact nonuniformly spaced array (NSA) is designed with CBSA elements operating from 6 to 18 GHz, which has an array footprint that is smaller than a circle having a 41.4 mm radius.
- (ii) A 2D AoA measurement system applies the D3 method on the measured time-domain data (snapshots) from the 7-element NSA. This includes the following:
  - (a) A 2D data transformation from the 7-element NSA-measured data to a 2D isotropic-element planar array (IEPA) data is introduced in order to use the NSA data in the D3 method for AoA estimation, and six different 2D IEPAs are considered.
  - (b) Using 2D IEPA steering vector (SV) and the results derived from the D3 method, a new objective function is introduced for searching the AoA of the SOI solution in both azimuth (Az) and elevation (El) angles. This (1) avoids having to solve the ambiguity problem encountered in interferometric arrays and (2) gives the estimator a frequency-independent performance.
  - (c) Using a 3D icosphere, a 2D-angle grid is introduced to give a near-uniform angular distribution in the field of view (FOV) of the 7-element NSA. On this grid, the data-transformation matrix database and SVs of IEPAs are precalculated at a list of preselected frequency points and stored in a computer prior to AoA estimations. Hence, the estimator can be used for ESM applications without a priori knowledge of the SOI.
- (iii) Since the focus of this development is ESM application in low SNR environments, different SNR levels are studied with four different commonly used radar waveforms. They are the following: (1) a 13-chip Barker-coded waveform, (2) a 20-chip two-valued frequency-coded waveform [58], (3) a 16-chip poly-phase-coded waveform, and (4) a ultra-wideband (100 MHz chirp) frequency-modulated continuous waveform (FMCW).

In addition to the above contributions, the findings of this study are highlighted as follows:

- (i) The preferred IEPA for this application has a circular-shape, which also has the least number of elements.
- (ii) The new AoA estimation scheme shows frequency-independent performance defined by the probability of AoA estimation, when the required AoA estimation accuracy is specified for a fixed SNR. This performance results from using the nonuniformly (nonregularly) spaced CBSA array, applying the 2D data transformation to convert measured data from the NSA to a planar array and then using the new 2D AoA searching method introduced in this paper.
- (iii) In general, the more snapshots used in AoA estimation, the better the accuracy that can be achieved or the higher the probability of AoA estimation for a given SNR and desired accuracy.
- (iv) The estimator can estimate 2D AoA using few snapshots in a high SNR environment.

The paper is organized as follows: The 7-element NSA design is presented in Section 2. The AoA estimation algorithm for a planar array with isotropic radiators in free space is then discussed in Section 3. Section 4 presents a 2D data transformation that maps the time-domain sampled data (or snapshots) from the 7-element NSA to the data of an IEPA, so that the D3 method introduced in Section 3 can be applied. Section 5 discusses how to apply the AoA estimation method to an ESM system with ultrawide frequency range without a priori knowledge of the frequency of the SOI. The simulation results and discussion are presented in Section 6. The last section gives the conclusions and future work. There are four appendixes in this paper. Appendix A defines the six IEPAs. A description of the 2D-angle grid on the vertices of a unit icosphere is given in Appendix B. Four commonly used radar waveforms with their parameters are given in Appendix C. Appendix D explains the reasons why the estimator has frequency-independent performance with respect to the probability of AoA estimation mentioned above.

## 2. Design of a 7-Element 6–18 GHz NSA

Figure 1 illustrates the 7-element CBSA array, and Figure 2 shows nonuniform interelement spacings. The element locations in  $XY$ -plane are given in Table 1. The reasons for choosing the element locations are to ensure that (1) element spacings in  $X$  and  $Y$  directions are as close to half the wavelength of the highest operational frequency as possible, (2) the distances between adjacent element centers are bigger than the diameter of the CBSA element, and (3) the overall array footprint is as small as possible. As a result, the average element spacing in both  $X$  and  $Y$  directions is about 8.44 mm, which is a little bigger than half of the free-space wavelength at 18 GHz, i.e., 8.33 mm. The element used in the NSA is a commercial-off-the-shelf 6 to 18 GHz CBSA with 24.4 mm diameter. In addition to ultra-wideband operational frequency band of the array, another advantage of using the CBSA element is the possibility of neglecting the performance changes caused by the mutual coupling

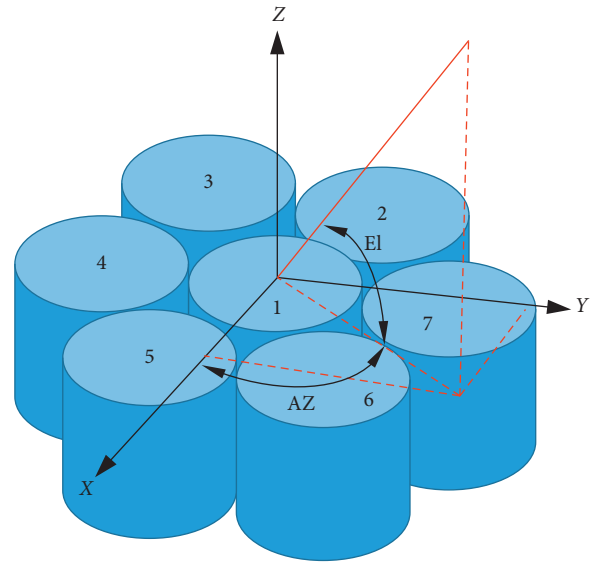


FIGURE 1: A 3D illustration of the 7-element CBSA NSA. The phase-reference center is at the first element center.

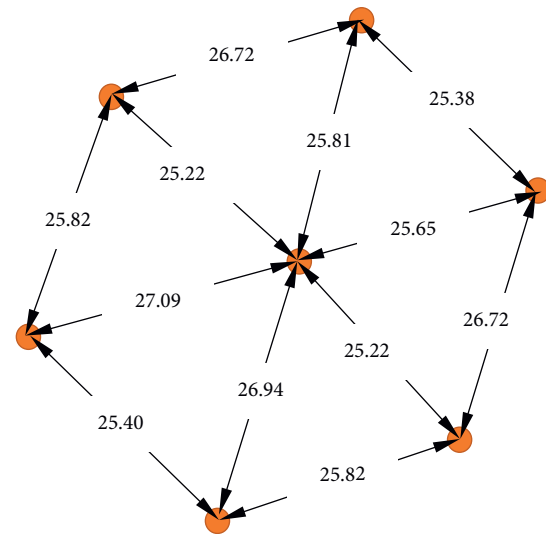


FIGURE 2: The top view of element centers with interelement spacings (unit is in mm).

TABLE 1: Antenna element locations.

Element	$px_n$ (mm)	$py_n$ (mm)	$pz_n$ (mm)
1	0.0	0.0	0.0
2	24.74	6.79	0.0
3	6.79	24.74	0.0
4	-18.75	16.87	0.0
5	-25.90	-7.94	0.0
6	-7.94	-25.90	0.0
7	16.87	-18.75	0.0

between adjacent elements in the array [59]. It is mainly because the element has about  $80^\circ$  to  $100^\circ$  3 dB beamwidth in its broadside and very low radiation, when El-angle approaches  $0^\circ$ . Examples of measured antenna radiation can be found in [60].

### 3. AoA Estimation from a Planar Array with Isotropic Elements

Before discussing the AoA estimation algorithm for the NSA, this section briefly presents the AoA estimation algorithm for a planar array with isotropic elements, which is the 2D version of the development given in [48]. Although, in this study, the D3 method was applied to 2D planar arrays given in Appendix A, the AoA estimation method proposed in this section can also be applicable to other sparse array structures, such as 2D nested array [22].

**3.1. SOI Representation.** The intercepted signal output at the  $n^{\text{th}}$  antenna element in an IEPA can be expressed as a complex envelop signal:

$$x_n(t) = A_n(t)e^{(j2\pi f_c t + \phi)} + \aleph(t) + \Omega, \quad (1)$$

where  $A$ ,  $f_c$  and  $\phi$  are the amplitude, frequency and initial phase of the waveform of the SOI, respectively.  $\aleph$  is the white Gaussian noise added by the receiver. In the following simulations, it is added to the signal in each receiving channel based on the signal-to-noise ratio (SNR) defined in each simulation and the power of the SOI.  $n = (1, 2, \dots, NN)$  and  $NN$  is the total number of elements in the IEPA.  $\Omega$  represents other unwanted signals, such as jamming signals. Since signal collision or pulse collision is not considered in this study,  $\Omega$  is excluded in the latter equations. If the received signal in (1) is sampled at a set of time instants  $m = (1, 2, \dots, M, M + 1)$ , the collected data can be expressed as

$$x_n(m) = A_n(m)e^{(j2\pi f_c m \cdot dt + \phi)} + \aleph(m), \quad (2)$$

where  $dt$  is the temporal sampling interval.

If the phase reference is at the center element of the array, and it is located at the origin of the coordinate system, the received signal of the  $m^{\text{th}}$  snapshot at the  $n^{\text{th}}$  element is

$$x_n(m) = A_n(m)e^{\{j2\pi/\lambda\} [px_n \cos(\text{El})\cos(\text{Az}) + py_n \cos(\text{El})\sin(\text{Az}) + pz_n \sin(\text{El})]} + \aleph(m), \quad (3)$$

where  $\lambda$  is the SOI free-space wavelength,  $(\text{Az}, \text{El})$  is the SOI incident direction, and  $(px_n, py_n, pz_n)$  are given in Table 1.

**3.2. Cyclostationarity of the SOI.** The cyclostationarity is a nonlinear transformation operating on a signal, and it generates finite-strength additive sine-wave components that result in spectral lines [61]. A signal  $x(t)$  is assumed to

be having a cyclostationary feature with cycle-frequency  $\eta$ , if and only if the product  $x(t) \cdot x(t - \tau)$ , for some delay  $\tau$ , shows a spectral line at frequency  $\eta$ .

The signals to be detected in our problem are cosine-wave based signals, for example,

$$A(t)\cos(2\pi f_c t). \quad (4)$$

Let us assume the second-order nonlinear transformation, which is equivalent to multiplying the signal with its shifted version or simply to square the SOI; the new signal has a cycle-frequency  $\eta$  that can be

$$A^2(t) \cdot \cos^2(2\pi f_c t) = \left(\frac{A^2(t)}{2}\right)\cos(2\pi\eta t) + \text{constant}, \quad (5)$$

$$\eta = 2f_c, \quad (6)$$

where it assumes that the delay or shift is zero. The complex envelope form of (5) is

$$A^2(t)e^{j2\pi\eta t}. \quad (7)$$

In many applications, the SOI cyclostationary information is a priori known information, for example, the cycle-frequency of the carrier frequency between two communication sites. However, in ESM, the intercepted signal frequency ( $f_c$ ) has to be estimated.

**3.3. D3-Based AoA Method for an IEPA.** First, let us apply a second-order nonlinear transform to the signal in (2) as we did in (5) and then regroup the transformed signals into the signal with cycle-frequency and other frequency components. We have

$$x_n^2(m) = A^2(m)e^{j2\pi\eta m \cdot dt} + \text{Others}, \quad (8)$$

where Others includes other frequency components not around  $\eta = 2f_c$  and noise. Note that, in this study, the signal collision is not considered; i.e., the signal to be processed only has one carrier in the current RF receiver band, even though the receiver can be tuned from 6 to 18 GHz. Using  $M + 1$  temporal snapshots from each element of an  $NN$ -element IEPA, the following matrix equation can be constructed. The detailed derivation and discussion are given in Chapter 7 of [48] for a linear array case. Here, we extend it to the 2D planar array application:

$$\mathbf{Z}_{(NN+1) \times M} \mathbf{W}_{M \times 1} = \mathbf{E}_{(NN+1) \times 1}, \quad (9)$$

where

$$\mathbf{Z} = \begin{bmatrix} 1 & \dots & e^{j2\pi(M-1)\eta \cdot dt} \\ x_1^2(1) - x_1^2(2)e^{-j2\pi\eta \cdot dt} & \dots & x_1^2(M) - x_1^2(M+1)e^{-j2\pi\eta \cdot dt} \\ \vdots & \dots & \vdots \\ x_{NN}^2(1) - x_{NN}^2(2)e^{-j2\pi\eta \cdot dt} & \dots & x_{NN}^2(M) - x_{NN}^2(M+1)e^{-j2\pi\eta \cdot dt} \end{bmatrix}, \quad (10)$$

$\mathbf{W}$  is the unknown weight vector that can be detailed as

$$\mathbf{W} = \begin{bmatrix} w_1 \\ w_2 \\ \vdots \\ w_M \end{bmatrix}, \quad (11)$$

and  $\mathbf{E}$  is the excitation vector, given as

$$\mathbf{E} = \begin{bmatrix} C \\ 0 \\ \vdots \\ 0 \end{bmatrix}. \quad (12)$$

The length of column vector  $\mathbf{E}$  is  $NN + 1$ , and the constant  $C$  can be arbitrarily selected and it also satisfies the following relation with weight vector:

$$C = \sum_{m=1}^M w_m e^{j2\pi(m-1)\eta \cdot dt}. \quad (13)$$

However, (13) is not a necessary condition since the constant  $C$  gets factored out in the final AoA computation. Equation (13) expresses that the sum of the weights produces a gain factor  $C$ , when they are applied to the SOI at the cycle-frequency. The Moore–Penrose pseudo-inverse was used to solve (9) in order to obtain  $\mathbf{W}$ , which has  $\|\mathbf{W}\|_2 = C/\sqrt{M}$ .

The elements from the second row and after in (10) can be written as  $x_n^2(m) - x_n^2(m+1)e^{-j2\pi\eta \cdot dt}$ , which tells that the SOI component at the cycle-frequency  $\eta = 2f_c$  is removed from the matrix elements. Thus, the weight vector  $\mathbf{W}$  obtained from (9) minimizes the noise and other frequency components and simultaneously satisfies (13). This is one of the reasons why the algorithm has the ability to measure weak signals from noise and can give a good estimation of the AoA of the SOI.

The advantages of (9) are as follows: (1) the temporal data are directly used without being converted to frequency domain, and no covariance matrix is required and (2) the number of time-domain snapshots can be very small, e.g.,  $M + 1 = 2$ , in high SNR cases. Hence, it can be used in dynamic signal environments with good SNR.

**3.4. Detecting SOI by Estimating Its AoA Using IEPA.** For a given element  $n$  in an IEPA, when the  $(n + 1)^{\text{th}}$  row of matrix  $\mathbf{Z}$  in (10) is multiplied with the weight-vector  $\mathbf{W}$ , one has

$$\sum_{m=1}^M \{x_n^2(m) - x_n^2(m+1) \cdot e^{-j2\pi\eta \cdot dt}\} w_m = 0. \quad (14)$$

From (14), considering  $w_m \neq 0$ ,  $e^{j2\pi\eta \cdot dt} \neq 0$ , and (13), the following equation can be derived:

$$\frac{1}{C} \sum_{m=1}^M x_n^2(m) w_m = e^{\{j4\pi/\lambda_{\text{est}}\} [px_n \cos(\text{El}) \cos(\text{Az}) + py_n \cos(\text{El}) \sin(\text{Az})]}, \quad (15)$$

where it is assumed that  $pz_n = 0$ ,  $\lambda_{\text{est}} = (c/f_{c_{\text{est}}})$ , and  $c$  is the speed of light in free space. Equation (15) unveils some important results including the following:

- (i) The operation  $\sum_{m=1}^M x_n^2(m) w_m$  means that the weight vector applies a filter to the squared values of snapshots.
- (ii) The sum of the filtered data in the Item-1 above only relates to the AoA of SOI.
- (iii) The weights only can be used to filter the current set of squared values of snapshots used in (9) to minimize the undesired signal at the output. If snapshots are changed, the weights obtained from (9) will be changed accordingly, but the sum will not be changed.

The Item-3 in the above discussion reflects the dynamic nature of this method, where the processing only deals with the current set of snapshots fed to (9).

Since (15) uses the  $n^{\text{th}}$  element's measured snapshots and has two unknowns ( $\text{Az}, \text{El}$ ), the solution can be calculated using any two elements in the array to form two equations from (15). However, we are going to introduce a new approach to find AoA in the following sections, which uses the IEPA SV and a 2D searching method. The advantage of the new approach is the ability to avoid having to pick answers from an unlimited number of solutions of inverse trigonometric functions and the possibility of finding AoA solution with no dependency on frequency at a fixed SNR. The reason for the frequency-independent behavior is discussed in Appendix D.

This new AoA searching method is the second important reason that explains why our scheme can robustly measure the weak signals and how it can offer a good estimation of AOA of the SOI. The novelty of this approach is using all the  $NN$  elements together for the AoA solution, rather than using a few elements in the array to find the AoA solution from inverse trigonometric functions.

**3.5. IEPA Steering Vector and Objective Function.** If an IEPA is located at the origin of the Cartesian coordinate system, its SV for an incoming plane wave is

$$\mathbf{sv} = \begin{bmatrix} e^{j\hat{\mathbf{k}} \cdot \vec{\mathbf{r}}_1} \\ e^{j\hat{\mathbf{k}} \cdot \vec{\mathbf{r}}_2} \\ \vdots \\ e^{j\hat{\mathbf{k}} \cdot \vec{\mathbf{r}}_n} \\ \vdots \\ e^{j\hat{\mathbf{k}} \cdot \vec{\mathbf{r}}_{NN}} \end{bmatrix}, \quad (16)$$

where  $\hat{\mathbf{k}}$  is the wave vector and  $\vec{\mathbf{r}}_n$  is the displacement vector from the signal source to the  $n^{\text{th}}$  element in the array.

If the center element of the array is located at the origin and its phase is used as the phase reference, then the array SV becomes

$$\mathbf{sv}(az, el) = \begin{bmatrix} e^{j(2\pi/\lambda)[px_1 \cos(el)\cos(az) + py_1 \cos(el)\sin(az)]} \\ e^{j(2\pi/\lambda)[px_2 \cos(el)\cos(az) + py_2 \cos(el)\sin(az)]} \\ \vdots \\ 1 \\ \vdots \\ e^{j(2\pi/\lambda)[px_n \cos(el)\cos(az) + py_n \cos(el)\sin(az)]} \\ \vdots \\ e^{j(2\pi/\lambda)[px_{NN} \cos(el)\cos(az) + py_{NN} \cos(el)\sin(az)]} \end{bmatrix}. \quad (17)$$

The SV at the center element is equal to one. It is also assumed that all the elements have the same locations in  $z$  direction.

Comparing (17) with (15), one can find that in order to estimate the AoA ( $Az, El$ ), a 2D searching method can be used to find  $(az_e, el_e)$  by

$$\min_{\substack{az=az_e \\ el=el_e}} \sum_{n=1}^{NN} \left| sv_n^2(az, el) - \frac{1}{C} \sum_{m=1}^M x_n^2(m)w_m \right|^2, \quad (18)$$

where  $sv_n^2$  is the square of  $sv_n$  at the  $n^{\text{th}}$  isotropic element in (17) with  $\lambda = \lambda_{\text{est}}$ , which is the same as the right side of (15). The details of the searching method will be given in Section 5.

#### 4. AoA Estimation Using the 7-Element NSA-Measured Snapshots

This section discusses how to use snapshots from the 7-element NSA to estimate the AOA of the SOI by taking advantage of the 2D D3-based AoA method discussed in the last section.

*4.1. 2D Transformation Matrix to Convert 7-Element NSA-Measured Data to IEPA Data in Free Space.* Consider a setup for the 7-element NSA calibration. A far-field source at frequency  $f_c$  is placed along the direction  $(az(p), el(p))$ , and the measured phasor voltages at 7 output ports can be expressed as  $y_n(p, f_c)$  ( $n = 1, 2, \dots, 7$ ). Here,  $p$  indicates the source at the  $p^{\text{th}}$  direction. If this source is moved in total  $P$  directions and at each direction, one collects the phasor voltage at each element, a measured data matrix  $\mathbf{Y}_{7 \times P}(f_c)$  can be obtained. Then, replacing the NSA by an  $NN$ -element IEPA and performing the same measurement, the output phasor voltage matrix from the planar array  $\mathbf{U}_{NN \times P}(f_c)$  can be created. In reality, instead of making measurement, it can be calculated, since the isotropic element in free space does not exist.

The goal is to find the best-fit data-transformation matrix that satisfies

$$\mathbf{T}_{NN \times 7}(f_c) \cdot \mathbf{Y}_{7 \times P}(f_c) = \mathbf{U}_{NN \times P}(f_c). \quad (19)$$

This equation can be solved using the least square method. It is achieved by minimizing the following function:

$$\min_{\mathfrak{S}} \left\| \mathbf{U}_{NN \times P}(f_c) - \mathbf{T}_{NN \times 7}(f_c) \cdot \mathbf{Y}_{7 \times P}(f_c) \right\|, \quad (20)$$

where  $\mathfrak{S}$  is the best-fit transformation matrix. In order to have a unique solution of (20), the number of  $P$  directions must be greater than or equal to the number of antenna elements in the planar array.

For frequency  $f_c$ , the transformation matrix ( $\mathfrak{S}$ ) has to be stored in computer memory. Then, during the operation, snapshots  $\mathbf{Y}_{7 \times 1}(m, Az, El, f_c)$  from the NSA can be converted to snapshots of the  $NN$ -element IEPA by

$$\mathbf{U}_{NN \times 1}(m, Az, El, f_c) = \mathfrak{S}_{NN \times 7}(f_c) \mathbf{Y}_{7 \times 1}(m, Az, El, f_c), \quad (21)$$

where the incident direction  $(Az, El)$  of SOI should be within the limits of those directions during the calibration, but not necessary to be one of the  $P$  directions. This is called the off-grid case. After that, the AoA of SOI can be estimated using the algorithm discussed in the previous section.

Note that different frequencies  $f_c$  have different transformation matrices. Obtaining the transformation matrices for the 6–18 GHz radar ESM applications without a priori knowledge of the frequency of SOI is discussed in Section 5.

*4.2. Discussion.* The calibration method and the data-transformation given in (19) to (21) can be applied to planar arrays of any size and any shape. Six different IEPAs are used in this study to demonstrate the approach. These arrays are presented in Appendix A.

In real applications, the data-transformation introduced in this section

- (i) eliminates the nonuniformity in the real array, which means it transfers a NSA into a regular-spaced IEPA
- (ii) converts a 3D real antenna problem into an isotropic-element regular-spaced array problem in free space
- (iii) takes into account the mutual coupling between elements in a real array, when the  $\mathbf{Y}$  matrix is measured
- (iv) removes the inconsistency among receiver channels, when the NSA elements are connected to RF receivers
- (v) can remove the electromagnetic interferences by the presence of near-field scatterers, for example, the body of the platform, if the calibration measurement is performed with a platform in a big microwave anechoic chamber

#### 5. Application of the Method to ESM

In the discussion of Sections 3 and 4, although the snapshots measured in time domain are used in (10) and (15) to calculate the weight vector in (11), the method still requires

the carrier frequency of the intercepted radar signal for the following purposes:

- (i) To obtain the cycle-frequency
- (ii) To determine the IEPA SV
- (iii) To determine the data-transformation matrix, which has to be obtained and stored in computer memory prior to AoA measurements

Unfortunately, in radar ESM applications, the SOI carrier frequency has to be estimated ( $f_{c_{est}}$ ). This section introduces an approach to deal with this problem.

First, let us discuss how to obtain the precalculated SV database and the transformation matrix  $\mathfrak{F}$  database for a given IEPA based on the 2D-angle grid introduced in Appendix B. Then, we give the detailed steps of using these databases for AoA estimations.

**5.1. Precalculated SV Database and  $\mathfrak{F}$  Database.** From 6 to 18 GHz, total 2401 equal-spaced frequency points ( $f_{c_i}$ ) are preselected to develop the databases, so that the frequency step is 5 MHz. For an IEPA, the SV database can be written as

$$\text{squared\_SV}(f_{c_i}, z) = \text{sv}_n^2(\text{az}_z(p), \text{el}_z(p), f_{c_i}), \quad (22)$$

where  $n = 1, 2, \dots, NN$  and  $i = 1, 2, \dots, 2401$ .  $z = 1, 2, \dots, 36$ , and  $p$  is the  $p^{\text{th}}$  direction in the  $z^{\text{th}}$  angle zone shown in Figure 17(a) in Appendix B.  $P_{\text{total}} = \sum_{z=1}^{36} P(z) = 29495$ , where  $P(z)$  is the total directions in the  $z^{\text{th}}$  angle zone.

The  $\mathfrak{F}$  matrix used in (21) is developed in each angle zone at every frequency ( $f_{c_i}$ ) and can be written as

$$\mathfrak{F}_{NN \times 7}(f_{c_i}, z). \quad (23)$$

Basically, the number of directions  $P$  in (19) is replaced by  $P(z)$  in each angle zone. Hence, for each planar array, at every frequency point and within each angle zone, a pair of precalculated squared-SV and  $\mathfrak{F}$  matrix is saved in the computer memory.

**5.2. AoA Measurement without a Priori Knowledge of the Carrier of the SOI.** During the AoA measurement, once the  $f_{c_{est}}$  is obtained from the ESM system, the closest frequency point ( $f_{c_i}$ ) in ( $f_{c_i}, i = 1, 2, \dots, 2401$ ) can be found and the corresponding squared-SV( $f_{c_i}, z$ ) and  $\mathfrak{F}_{NN \times 7}(f_{c_i}, z)$  are used in the AoA estimation. To search AoA solution, the second term in (18) obtained by the D3 method is compared with the first term at each direction defined by the 2D-angle grid in Figure 17(a) in Appendix B through 36 angle zones. Then, the direction that gives the minimum sum value in (18) is used as the solution.

## 6. Simulation Results and Discussion

In this section, the simulation results are first presented based on the probability of AoA measurement versus SNR under the conditions of (1) different RMSE requirements

and (2) using different ( $M + 1$ ) snapshots during estimations. The RMSE of each AoA estimation is defined as

$$\sqrt{\frac{(\Delta \text{Az})^2 + (\Delta \text{El})^2}{2}}, \quad (24)$$

where  $\Delta \text{Az}$  and  $\Delta \text{El}$  are the measurement errors in Az- and El-angle, respectively. Then, the estimation errors in Az- and El-angles are discussed. Finally, the results of the use of a small number of snapshots for AoA estimation under high SNR conditions are also shown.

Simulation cases consist of the data which are processed by the six planar arrays on four different waveforms using different number of snapshots ( $M + 1$ ) that varies from 2 to 1025. In each case,

- (i) A section of  $M + 1$  consecutive snapshots is sent to AoA calculation. The starting point of a section of  $M + 1$  data is randomly selected within a pulse of different waveforms discussed in Appendix C.
- (ii) There is a total of 100000 AoA estimations.
- (iii) The incident wave in each AoA estimation is generated as follows:
  - (a) The carrier frequency is uniform-randomly picked in [6, 18] GHz.
  - (b) The SNR of each processed signal is uniform-randomly chosen in [-20, 20] dB. It is assumed that the seven receivers add the same noise power to the received signals. The noise power is calculated based on the received signal power, and the noise has white Gaussian distribution.
  - (c) The incident direction in off-grid case is also uniform-randomly selected in the FOV.

### 6.1. Probability of AoA Estimation

**6.1.1. Comparison with Different IEPAs.** Tables 2–5 provide the SNRs that yield 50% or better probability of AoA estimation using 129, 257, 513, and 1025 snapshots, respectively, from the six different arrays (described in Appendix A) under different estimation accuracy requirements. In these tables, the values in bold, but not italicized, show the lowest SNR in a group of 6 SNRs produced by the 6 planar arrays, and the bold italic and normal italic values indicate the largest and the second largest SNRs in a data group, respectively. An IEPA with a lower SNR in a group means that it has a better capability of measuring AoA than the arrays with higher SNRs. This is because the array can estimate AoA of weaker signals than the rest of arrays which need stronger signals for the same accuracy.

From these tables, one can observe that Array-3 has 41 out of 64 values given in bold and Array-5 scores 21. This indicates that Array-3 is the best array among the 6 planar arrays to give a good AoA estimation, and Array-5 is the next to Array-3. Note that both of these two arrays are circular-shaped planar arrays with different interelement patterns.

On the other hand, one can see that Array-6 and Array-1 share the most bold-italicized and italic values. Array-6 has 50

TABLE 2: SNR (dB) values when arrays can produce 50% correct results using 129 snapshots under different estimation accuracies.

	RMSE $\leq 1^\circ$ (Array-1, 2, 3, 4, 5, 6)	RMSE $\leq 2^\circ$ (Array-1, 2, 3, 4, 5, 6)	RMSE $\leq 5^\circ$ (Array-1, 2, 3, 4, 5, 6)	RMSE $\leq 10^\circ$ (Array-1, 2, 3, 4, 5, 6)
WF-1	0.58/-0.94/- <b>1.00</b> /-0.42/-0.79/ <b>0.87</b>	-2.30/-3.85/- <b>4.04</b> /-2.34/-3.50/- <b>2.02</b>	-5.12/-6.56/- <b>6.74</b> /-5.27/-6.50/- <b>5.04</b>	- <b>6.90</b> /-7.92/-7.79/-7.03/- <b>8.03</b> /-6.94
WF-2	0.71/-0.89/- <b>0.95</b> /0.28/-0.84/ <b>0.95</b>	-2.16/-3.83/- <b>3.91</b> /-2.21/-3.65/- <b>1.81</b>	-5.04/-6.43/- <b>6.62</b> /-5.01/-6.58/- <b>4.98</b>	-6.89/-8.02/-7.87/-6.87/- <b>8.10</b> /-6.71
WF-3	0.63/-0.90/- <b>1.00</b> /0.57/-0.70/ <b>0.92</b>	-2.19/-3.74/- <b>3.82</b> /-2.24/-3.63/- <b>1.96</b>	-5.05/- <b>6.75</b> /-6.67/-5.18/-6.40/- <b>4.88</b>	-6.97/-7.81/-7.85/-6.86/- <b>7.99</b> /-6.80
WF-4	0.81/-0.75/- <b>0.81</b> /0.48/-0.65/ <b>0.87</b>	-2.11/-3.78/- <b>3.85</b> /-2.34/-3.61/- <b>1.88</b>	-5.06/-6.69/-6.66/-5.07/- <b>6.70</b> /- <b>4.92</b>	-6.91/-7.87/-7.68/-6.96/- <b>7.98</b> /-6.71

TABLE 3: SNR (dB) values when arrays can produce 50% correct results using 257 snapshots under different estimation accuracies.

	RMSE $\leq 1^\circ$ (Array-1, 2, 3, 4, 5, 6)	RMSE $\leq 2^\circ$ (Array-1, 2, 3, 4, 5, 6)	RMSE $\leq 5^\circ$ (Array-1, 2, 3, 4, 5, 6)	RMSE $\leq 10^\circ$ (Array-1, 2, 3, 4, 5, 6)
WF-1	-1.33/-2.95/- <b>3.13</b> /-1.58/-3.03/- <b>1.18</b>	-4.03/-5.72/-5.71/-4.01/- <b>5.76</b> /- <b>3.88</b>	- <b>6.80</b> /-8.13/- <b>8.38</b> /-6.86/-8.34/-6.83	-8.75/-9.56/-9.50/- <b>8.06</b> /- <b>9.58</b> /-8.48
WF-2	-1.26/-2.90/- <b>3.19</b> /-1.39/-2.67/- <b>1.16</b>	-3.94/-5.55/- <b>5.76</b> /-4.12/-5.61/- <b>3.93</b>	-6.85/-8.14/-8.27/-6.92/- <b>8.55</b> /- <b>6.59</b>	- <b>8.43</b> /-9.50/-9.60/-8.62/- <b>9.69</b> /-8.67
WF-3	-1.28/-2.99/- <b>3.23</b> /-1.62/-2.88/- <b>1.20</b>	-4.15/-5.74/- <b>5.86</b> /-4.36/-5.55/- <b>3.85</b>	-6.86/-8.39/-8.22/-6.94/- <b>8.53</b> /- <b>6.70</b>	- <b>8.54</b> /-9.56/-9.57/-8.58/- <b>9.81</b> /-8.60
WF-4	-1.12/-2.53/- <b>2.85</b> /-1.31/-2.62/- <b>0.95</b>	- <b>3.38</b> /-5.25/- <b>5.59</b> /-3.94/-5.07/-3.63	-6.41/-7.98/-7.87/- <b>6.38</b> /- <b>8.28</b> /-6.43	-8.32/-9.36/- <b>9.51</b> /-8.26/-9.35/- <b>8.20</b>

TABLE 4: SNR (dB) values when arrays can produce 50% correct results using 513 snapshots under different estimation accuracies.

	RMSE $\leq 1^\circ$ (Array-1, 2, 3, 4, 5, 6)	RMSE $\leq 2^\circ$ (Array-1, 2, 3, 4, 5, 6)	RMSE $\leq 5^\circ$ (Array-1, 2, 3, 4, 5, 6)	RMSE $\leq 10^\circ$ (Array-1, 2, 3, 4, 5, 6)
WF-1	-3.29/-5.00/- <b>4.99</b> /-3.36/-4.77/- <b>3.07</b>	-5.68/-7.59/- <b>7.66</b> /-5.82/-7.47/-5.69	-8.47/-9.91/-9.87/-8.40/- <b>9.94</b> /- <b>8.38</b>	-10.20/-11.33/-11.06/- <b>10.11</b> /- <b>11.37</b> /-10.29
WF-2	-3.30/-4.88/- <b>5.15</b> /-3.41/-4.84/- <b>2.97</b>	-5.60/-7.39/- <b>7.68</b> /-5.66/-7.33/- <b>5.56</b>	-8.37/-9.99/- <b>10.10</b> /-8.45/-9.04/- <b>8.18</b>	-10.24/-11.17/-11.06/-10.28/- <b>11.20</b> /- <b>10.17</b>
WF-3	-3.24/-5.01/- <b>5.04</b> /-3.32/-4.95/- <b>2.83</b>	-5.76/-7.60/- <b>7.82</b> /-5.93/-7.38/- <b>5.64</b>	- <b>8.41</b> /-9.88/- <b>9.99</b> /-8.55/-9.90/-8.53	-10.13/-11.12/-11.24/-10.06/- <b>11.28</b> /- <b>9.94</b>
WF-4	-2.06/-3.71/- <b>3.72</b> /-2.23/-3.63/- <b>1.87</b>	-4.54/-6.36/- <b>6.52</b> /-4.81/-6.19/- <b>4.24</b>	-7.16/-8.91/- <b>8.92</b> /-7.37/-8.70/- <b>7.11</b>	-8.92/-10.06/-10.03/-8.93/- <b>10.18</b> /- <b>8.87</b>

TABLE 5: SNR (dB) values when arrays can produce 50% correct results using 1025 snapshots under different estimation accuracies.

	RMSE $\leq 1^\circ$ (Array-1, 2, 3, 4, 5, 6)	RMSE $\leq 2^\circ$ (Array-1, 2, 3, 4, 5, 6)	RMSE $\leq 5^\circ$ (Array-1, 2, 3, 4, 5, 6)	RMSE $\leq 10^\circ$ (Array-1, 2, 3, 4, 5, 6)
WF-1	-4.98/-6.72/- <b>6.99</b> /-5.18/-6.73/- <b>4.78</b>	-7.46/-9.18/- <b>9.59</b> /-7.45/-8.97/- <b>7.27</b>	-10.06/-11.73/- <b>11.79</b> /-10.25/-11.54/- <b>9.98</b>	-11.87/-12.86/-12.56/-11.75/- <b>12.96</b> /- <b>11.66</b>
WF-2	-4.83/-6.72/- <b>6.85</b> /-5.05/-6.49/- <b>4.71</b>	-7.20/-9.01/- <b>9.11</b> /-7.39/-8.91/- <b>7.07</b>	- <b>9.88</b> /-11.40/- <b>11.50</b> /-9.99/-11.48/-9.98	- <b>11.35</b> /-12.57/-12.60/-11.46/- <b>12.75</b> /-11.36
WF-3	- <b>4.88</b> /-6.66/- <b>6.91</b> /-5.21/-6.48/-4.92	-7.50/-9.11/- <b>9.43</b> /-7.43/-9.17/- <b>7.22</b>	- <b>10.02</b> /-11.51/- <b>11.81</b> /-10.10/-11.58/-10.08	-11.84/-12.72/-12.73/-11.73/- <b>13.03</b> /- <b>11.69</b>
WF-4	-0.63/-0.63/- <b>0.97</b> /0.71/-0.54/ <b>1.25</b>	-3.57/-3.57/- <b>3.58</b> /-2.01/-3.27/- <b>1.77</b>	-5.92/-5.92/-6.06/-4.66/- <b>6.34</b> /- <b>4.48</b>	-7.50/-7.50/-7.48/-6.50/- <b>7.51</b> /- <b>6.31</b>

bold-italicized and 7 italic values, and Array-1 has 11 bold-italicized and 38 italic values. This makes Array-6 to be the least favorite array among the 6 IEPAs, and Array-1 is the next. It is interesting to note that both Array-6 and Array-1 are rectangular-shaped planar arrays with different interelement patterns.

The above observation shows that our AoA estimation method prefers the planar array with symmetrical element distribution that can be seen from different Az-angles. In addition, Array-3 has the least number of elements. Hence it needs shorter computation time than the other arrays. Since Array-3 is the most favorable planar array out of the 6 arrays, the discussion in the rest of this paper uses the data produced by Array-3.

6.1.2. *Probability of AoA Estimation versus SNR.* Figures 3 and 4 show the results of probabilities of AoA estimation from Array-3 with estimation accuracies of  $1^\circ$  and  $5^\circ$ , respectively. Each subplot of these figures has 4 curves that present the results of 4 waveforms. From them, the following observations can be made:

- (i) When shorter snapshots are used in AoA calculations, i.e., subplots of in Figures 3(a) and (b) and Figures 4(a) and (b), the 4 curves of the 4 waveforms are very close to each other.
- (ii) When the number of snapshots is increased, the method still gives very close results for the first three waveforms, but the result of WF-4 starts deviating

from other results as shown in Figures 3(c) and (d) and Figures 4(c) and (d). Eventually, when  $M + 1 = 1025$  in Figures 3(d) and 4(d), the results are worse than those in Figures 3(a-c) and Figures 4(a-c). This is because a longer sequence of FMCW snapshots covers a wider frequency range than those with a shorter sequence of snapshots. Hence it gives a bigger carrier frequency estimation error during calculations that degrades the probability of AoA estimation. Note that, in this study, a 100 MHz chirp signal has been used.

- (iii) In general, when more snapshots are used in the calculations, better estimation results can be achieved. This can also be clearly observed in Figure 5.

6.2. *AoA Estimation versus Frequency and SNR.* The probabilities of AoA estimation versus frequency and SNR are shown in Figures 6–9 for four different waveforms. From these figures, the following observations can be made:

- (i) For a given estimation accuracy, i.e., RMSE, at different frequencies, the method has about the same AoA estimation performance against the SNR. The explanation of this performance can be found in Appendix D.
- (ii) Again, the corresponding subplots in first three figures are basically similar, i.e., the method gives similar estimation performances for WF-1 to WF-3.



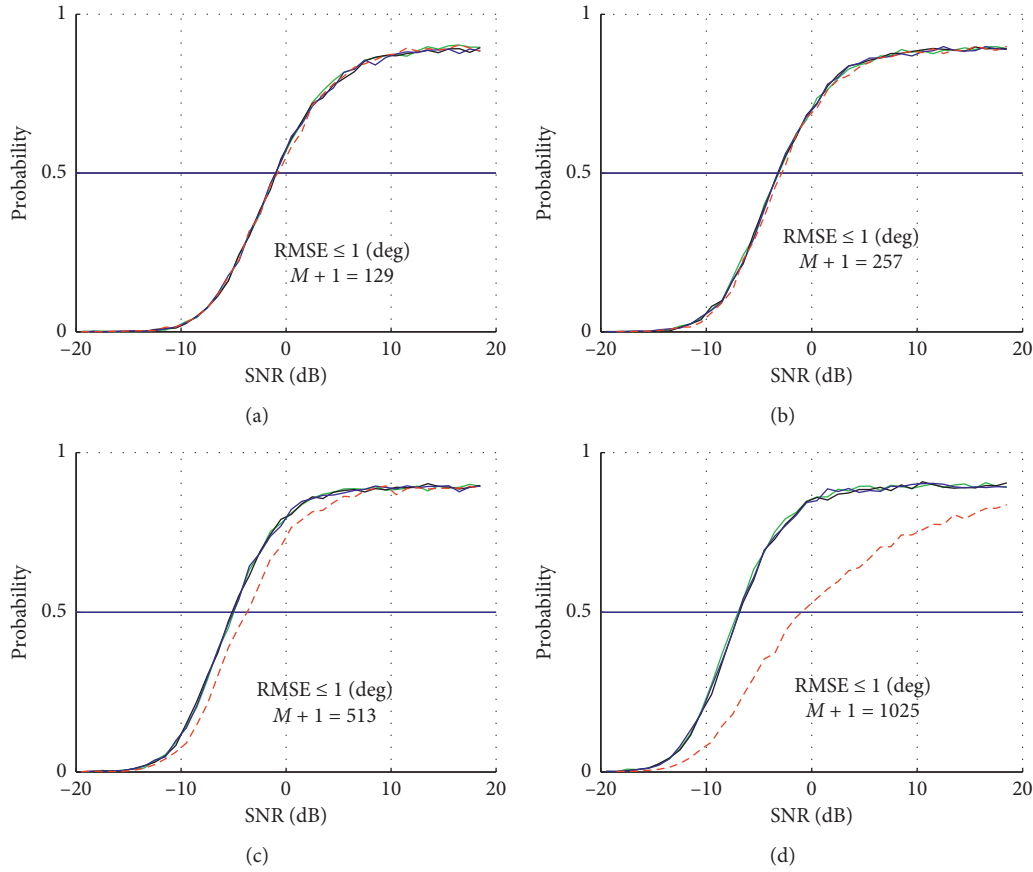


FIGURE 3: Probability of AoA measurement of Array-3, when  $\text{RMSE} \leq 1^\circ$ . Dashed line is WF-4 result.

- (iii) The subplots in Figure 9 are different from the corresponding subplots in the other figures, and the performances are not as good as in the other figures due to the reason discussed above.

### 6.3. Estimation Error Distributions in Az and El.

Figures 10–13 show the histograms of estimation errors of Az and El, when SNR is in different ranges with  $M + 1 = 1025$ . By comparing the left column and the right column in each figure, one can find the following:

- (i) The Az-error spreads wider than El-error, which indicates that the AoA estimation method produces better estimation results in El than in Az
- (ii) The lower the SNR, the wider the spread as expected
- (iii) Array-3 has almost the same estimation error distributions when it processes the first three waveforms

Tables 6–9 list the percentages of the absolute value of estimation errors that are less than or equal to  $1^\circ$  and  $5^\circ$ , when the SNR is in different ranges and  $M + 1 = 1025$ . The results shown in these tables confirm that the method has better estimation in El-angle than in Az-angle, which results from the definitions of Az- and El-angles.

Data in these tables also show the following:

- (i) When the SNR increases from  $[0 \ 10]$  dB to  $[10 \ 20]$  dB, the method does not improve much of its estimation accuracy.
- (ii) From Tables 6 and 7, when the SNR is greater than 0 dB, the estimation performance is mainly determined by the Az-angle estimation. The results in columns of “Both Az and El” and “Az” are very close to each other, and the results in columns of “El” are better than those in columns of “Az” for both  $|\text{Er}| \leq 1^\circ$  and  $|\text{Er}| \leq 5^\circ$  cases.
- (iii) From Table 8 ( $-10 \text{ dB} \leq \text{SNR} \leq 0 \text{ dB}$ ), although the SNR is less than 0 dB, the overall estimation performance is slightly less than that of Az-angle estimation accuracy in both  $|\text{Er}| \leq 1^\circ$  and  $|\text{Er}| \leq 5^\circ$  cases. This means that the method starts producing bigger estimation errors in El. Nevertheless, the method still can produce better than 52% and 80% probabilities of AoA estimation with errors less than or equal to  $1^\circ$  and  $5^\circ$ , respectively, for the first three waveforms and better than 33% and 67% probabilities of AoA estimation with errors less than and equal to  $1^\circ$  and  $5^\circ$  for WF-4 with 513 snapshots.
- (iv) When the SNR is in  $[-20 \ -10]$  dB, the method still has the capability of making some estimations and produce better than 20% probability of AoA estimation with errors within  $5^\circ$  for the first three waveforms.

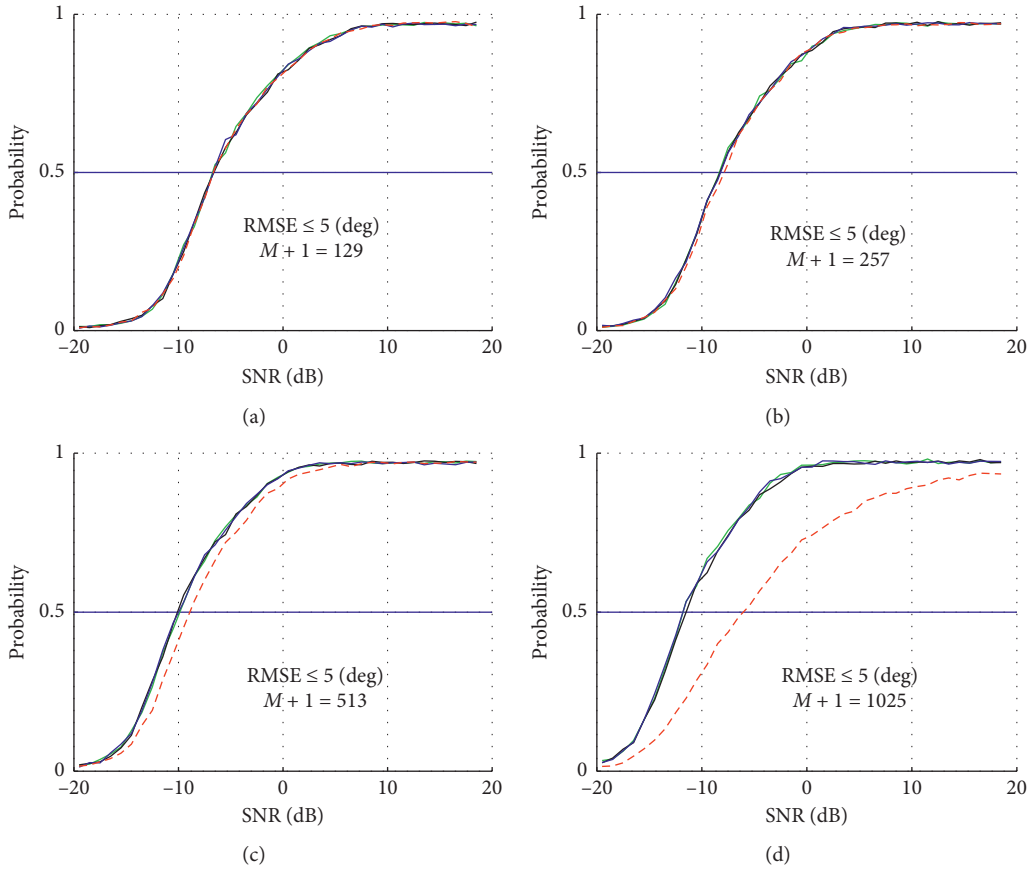


FIGURE 4: Probability of AoA measurement of Array-3, when  $RMSE \leq 5^\circ$ . Dashed line is WF-4 result.

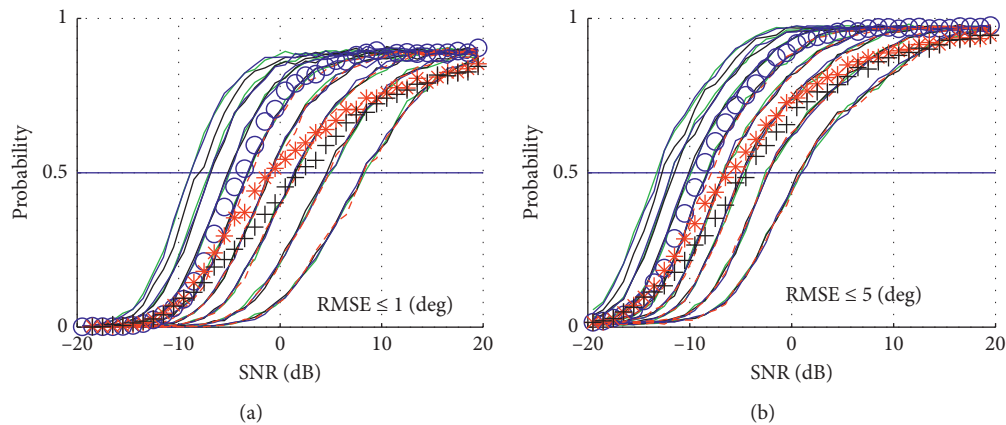


FIGURE 5: Probability of AoA measurement of Array-3 on 4 different waveforms with  $M + 1 = 17, 33, 65, 129, 257, 513,$  and  $1025$  from right to left in each subplot. Each group of data has 4 curves related to 4 waveforms. ooooo, \*\*\*\*\*, and +++++ lines are the results of calculations on WF-4 using 513, 1025, and 2049 snapshots, respectively.

6.4. Probability of AoA Estimation Using Few Snapshots. To study the AoA estimation performance of the method in a good SNR environment, a total of 100000 SNR samples are randomly picked in  $[-20 50]$  dB, and the results are shown in Figure 14. There are four groups of curves in each subplot of

the figure. They represent the use of 2, 3, 5, and 9 snapshots in the estimations. In each group of curves, there are four curves for four waveforms. Figure 14 shows that the method can have good probability of AoA estimation using just a few snapshots from the 7-element NSA. For example, with about

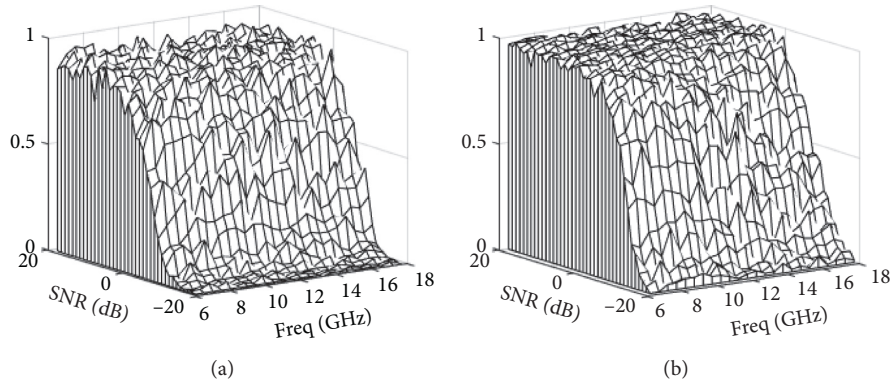


FIGURE 6: Array-3 probability of AoA estimation versus frequency and SNR: (a)  $RMSE \leq 1^\circ$  and (b)  $RMSE \leq 5^\circ$ , when  $M + 1 = 1025$  for WF-1.

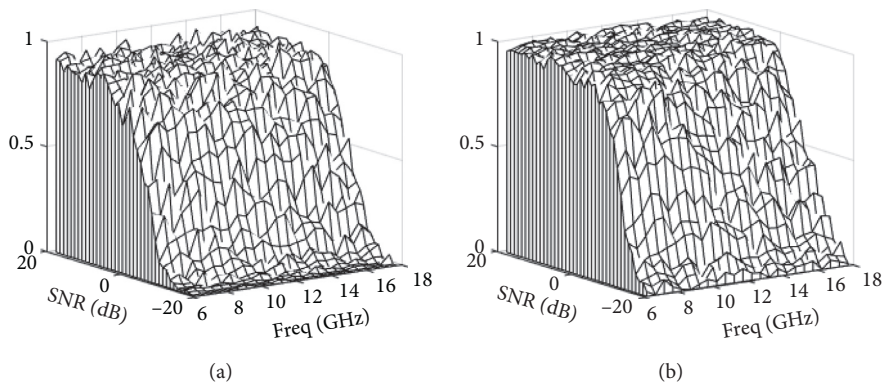


FIGURE 7: Array-3 probability of AoA estimation versus frequency and SNR: (a)  $RMSE \leq 1^\circ$  and (b)  $RMSE \leq 5^\circ$ , when  $M + 1 = 1025$  for WF-2.

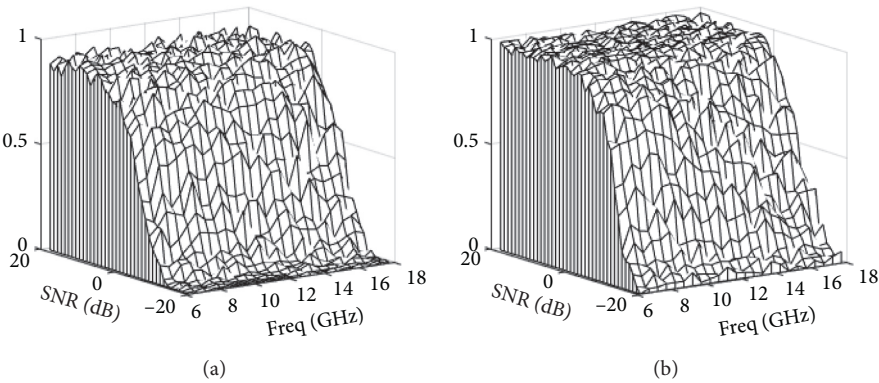


FIGURE 8: Array-3 probability of AoA estimation versus frequency and SNR: (a)  $RMSE \leq 1^\circ$  and (b)  $RMSE \leq 5^\circ$ , when  $M + 1 = 1025$  for WF-3.

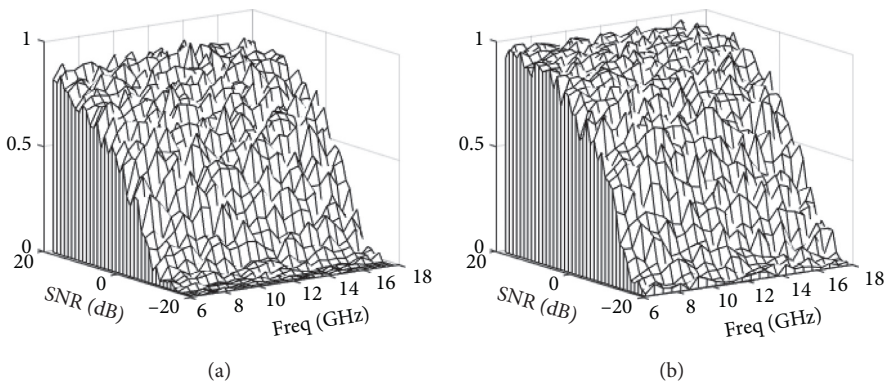


FIGURE 9: Array-3 probability of AoA estimation versus frequency and SNR: (a)  $RMSE \leq 1^\circ$  and (b)  $RMSE \leq 5^\circ$ , when  $M + 1 = 1025$  for WF-4.

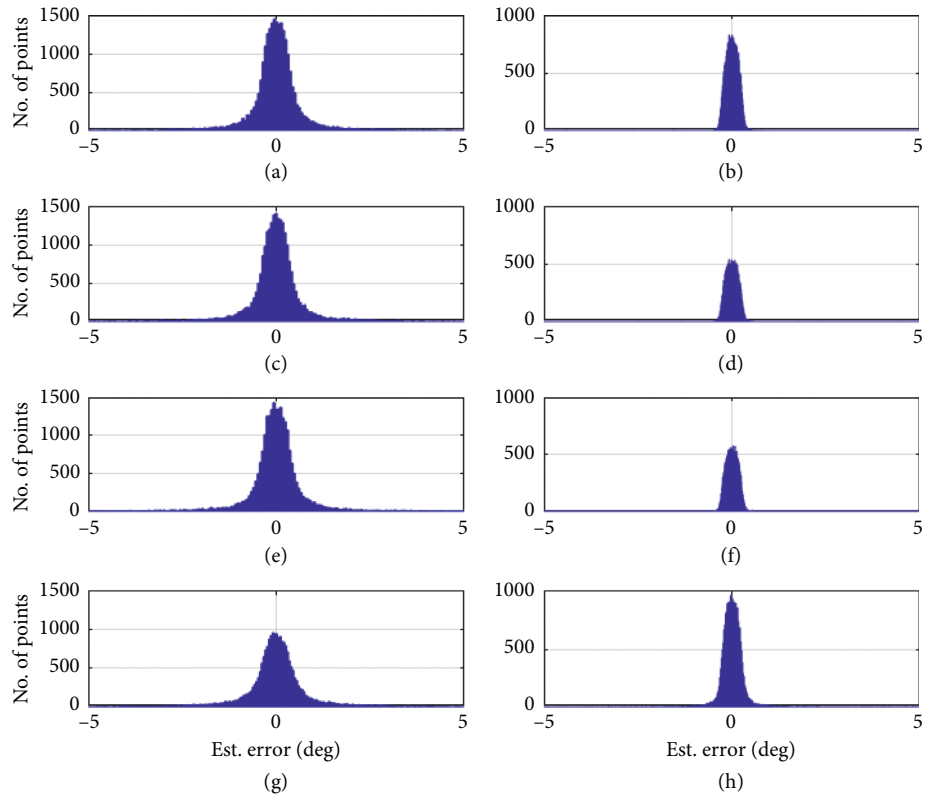


FIGURE 10: The histograms of Az (left column) and El (right column) estimation errors, when  $10 \text{ dB} \leq \text{SNR} \leq 20 \text{ dB}$  with 1025 snapshots. (a, b) WF-1; (c, d) WF-2; (e, f) WF-3; (g, h) WF-4.

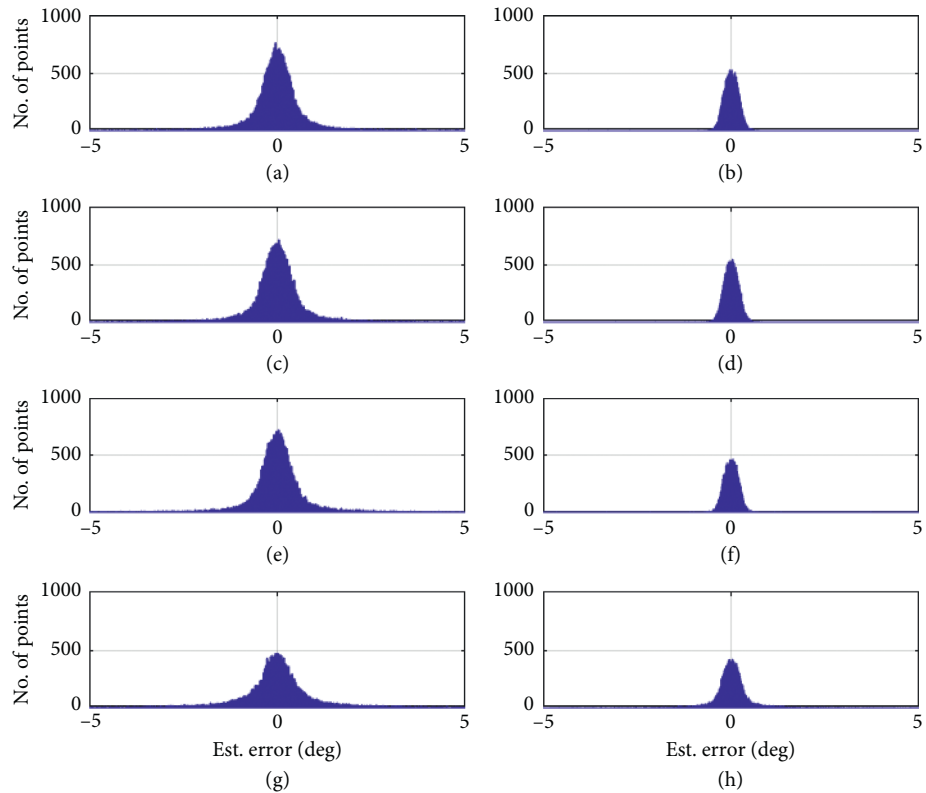


FIGURE 11: The histograms of Az (left column) and El (right column) estimation errors, when  $0 \text{ dB} \leq \text{SNR} \leq 10 \text{ dB}$  with 1025 snapshots. (a, b) WF-1; (c, d) WF-2; (e, f) WF-3; (g, h) WF-4.

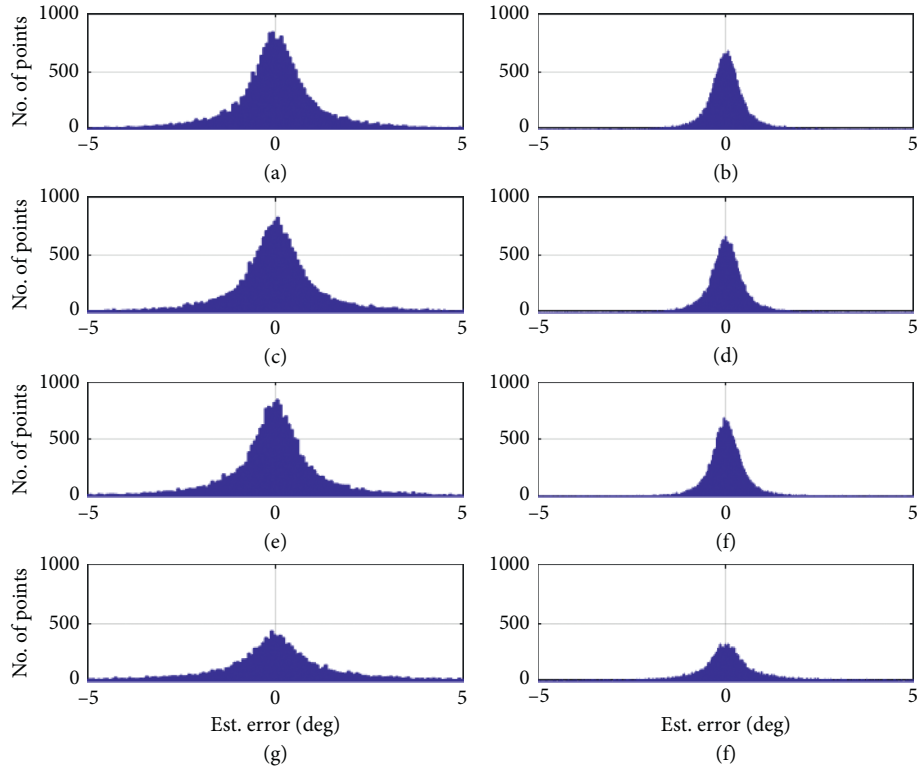


FIGURE 12: The histograms of Az (left column) and El (right column) estimation errors, when  $-10 \text{ dB} \leq \text{SNR} \leq 0 \text{ dB}$  with 1025 snapshots. (a, b) WF-1; (c, d) WF-2; (e, f) WF-3; (g, h) WF-4.

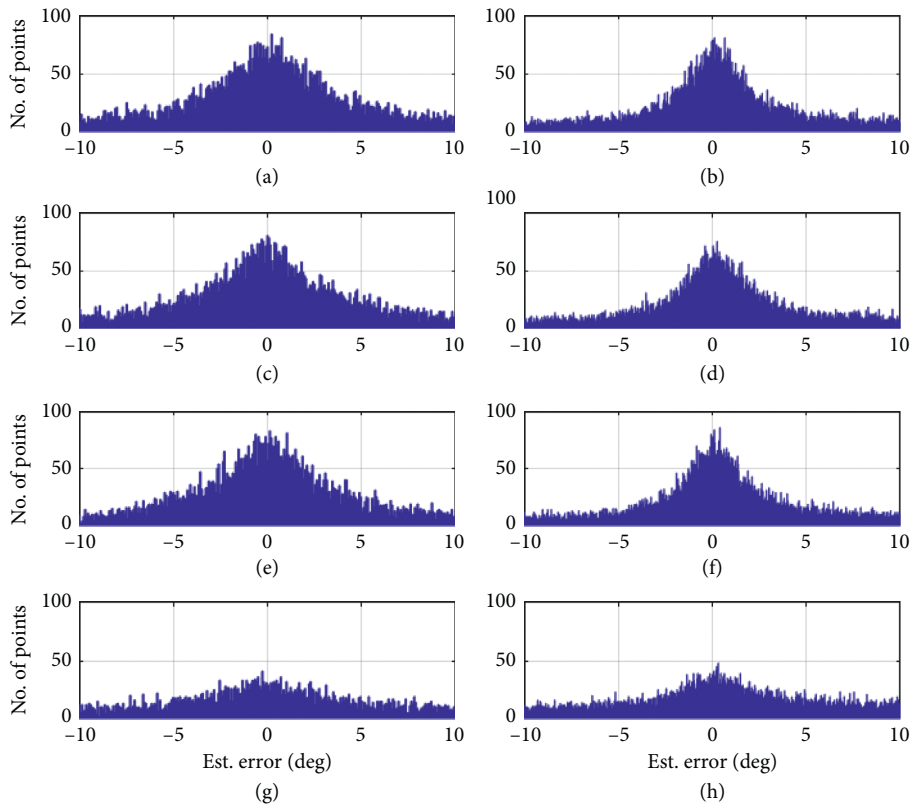


FIGURE 13: The histograms of Az (left column) and El (right column) estimation errors, when  $-20 \text{ dB} \leq \text{SNR} \leq -10 \text{ dB}$  with 1025 snapshots. (a, b) WF-1; (c, d) WF-2; (e, f) WF-3; (g, h) WF-4.

TABLE 6: Array-3 probability of AoA estimation using 1025 snapshots ( $10 \text{ dB} \leq \text{SNR} \leq 20 \text{ dB}$ ).

	Both Az and El, $ \text{Er}  \leq 1^\circ$ $ \text{Er}  \leq 5^\circ$	Az, $ \text{Er}  \leq 1^\circ$ $ \text{Er}  \leq 5^\circ$	El, $ \text{Er}  \leq 1^\circ$ $ \text{Er}  \leq 5^\circ$
WF-1	85.76% 96.42%	85.84% 96.50%	99.81% 99.87%
WF-2	85.66% 96.47%	85.76% 96.55%	99.79% 99.85%
WF-3	85.64% 96.37%	85.71% 96.44%	99.83% 99.87%
WF-4	75.91% 91.19%	76.64% 91.32%	93.97% 96.69%

TABLE 7: Array-3 probability of AoA estimation using 1025 snapshots ( $0 \text{ dB} \leq \text{SNR} \leq 10 \text{ dB}$ ).

	Both Az and El, $ \text{Er}  \leq 1^\circ$ $ \text{Er}  \leq 5^\circ$	Az, $ \text{Er}  \leq 1^\circ$ $ \text{Er}  \leq 5^\circ$	El, $ \text{Er}  \leq 1^\circ$ $ \text{Er}  \leq 5^\circ$
WF-1	83.86% 96.19%	83.99% 96.27%	99.69% 99.78%
WF-2	83.11% 95.82%	83.22% 95.92%	99.71% 99.77%
WF-3	84.75% 96.14%	83.81% 96.20%	99.77% 99.85%
WF-4	59.92% 80.77%	61.85% 81.10%	82.06% 90.45%

TABLE 8: Array-3 probability of AoA estimation using 1025 snapshots ( $-10 \text{ dB} \leq \text{SNR} \leq 0 \text{ dB}$  and last line using 513 snapshots).

	Both Az and El, $ \text{Er}  \leq 1^\circ$ $ \text{Er}  \leq 5^\circ$	Az, $ \text{Er}  \leq 1^\circ$ $ \text{Er}  \leq 5^\circ$	El, $ \text{Er}  \leq 1^\circ$ $ \text{Er}  \leq 5^\circ$
WF-1	53.63% 81.48%	56.60% 81.54%	83.20% 91.35%
WF-2	52.32% 80.07%	55.31% 80.17%	82.03% 90.55%
WF-3	52.75% 80.66%	55.47% 80.72%	83.31% 90.11%
WF-4	26.30% 51.05%	30.01% 52.22%	49.32% 69.31%
WF-4	33.28% 67.64%	38.46% 67.93%	64.92% 83.51%

TABLE 9: Array-3 probability of AoA estimation using 1025 snapshots ( $-20 \text{ dB} \leq \text{SNR} \leq -10 \text{ dB}$  and last line using 513 snapshots).

	Both Az and El, $ \text{Er}  \leq 1^\circ$ $ \text{Er}  \leq 5^\circ$	Az, $ \text{Er}  \leq 1^\circ$ $ \text{Er}  \leq 5^\circ$	El, $ \text{Er}  \leq 1^\circ$ $ \text{Er}  \leq 5^\circ$
WF-1	3.33% 21.27%	7.14% 23.51%	17.46% 45.82%
WF-2	3.18% 20.74%	7.16% 23.14%	16.65% 45.60%
WF-3	3.18% 21.51%	7.21% 23.89%	17.68% 46.09%
WF-4	1.21% 9.10%	3.20% 11.76%	9.20% 31.07%
WF-4	1.05% 10.04%	3.32% 12.73%	9.36% 33.10%

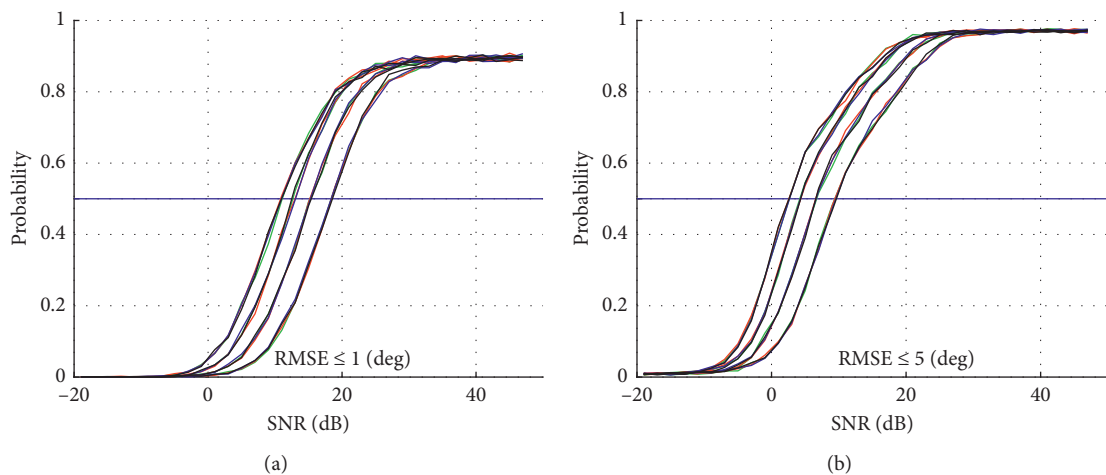
FIGURE 14: Probability of AoA estimation of Array-3 for 4 waveforms with  $M + 1 = 2, 3, 5,$  and  $9$ , from right to left in each subplot.



FIGURE 15: Six planar arrays; black dots are the 7-element NSA (see the text for more details).

15 dB SNR and 3 snapshots, the method can have 50% probability of AoA estimation with  $RMSE \leq 1^\circ$ .

6.5. Discussion. From all the subplots (a) in Figures 3–5 and Figure 14, one can find that, just by increasing SNR, it cannot make the method to yield close to 100% probability of AoA estimation with  $RMSE \leq 1^\circ$ . This is

determined by the density of the angles on the 2D-angle grid (for example,  $P_{total} = 29495$  in this study) in the 7-element NSA FOV and the number of frequency samples ( $F_{total} = 2401$ ) in [6, 18] GHz used to precalculate SV and  $\mathfrak{F}$  databases. Increasing these numbers will enhance the performance of the method. However, it will slow down the calculation on a regular desktop computer. By using other means of hardware such as dedicated FPGA with

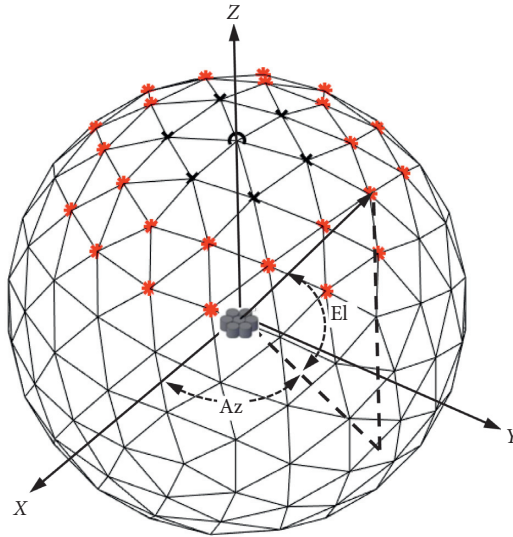


FIGURE 16: An example of a 2D-angle grid formed by an icosphere-based mesh; 7-element NSA phase-reference center and the icosphere center are collocated at the origin of the XYZ-coordinate system.

TABLE 10: Different 2D-angle grids.

$N_{\text{subdiv}}$	Number of angles within FOV ( $P_{\text{total}}$ )	Rough order of angle resolution (deg)
4	462	4.32
5	1841	2.16
6	7371	1.08
7	<b>29495</b>	<b>0.54</b>
8	117927	0.27

The bold text indicates that  $N_{\text{subdiv}} = 7$  is used in this study.

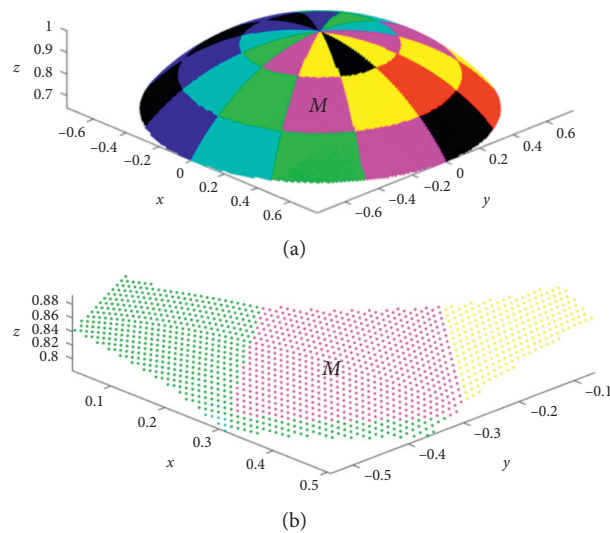


FIGURE 17: (a) The 2D-angle grid in the 7-element FOV ( $N_{\text{subdiv}} = 7$ ). The grid is subdivided into 36 angle zones that are defined by 12 equal divisions in Az-angle and 3 divisions in El-angle, i.e.,  $[40^\circ \text{ to } 53^\circ]$ ,  $[53^\circ \text{ to } 70^\circ]$ , and  $[70^\circ \text{ to } 90^\circ]$ . (b) A zoom-in plot of zone M in (a).



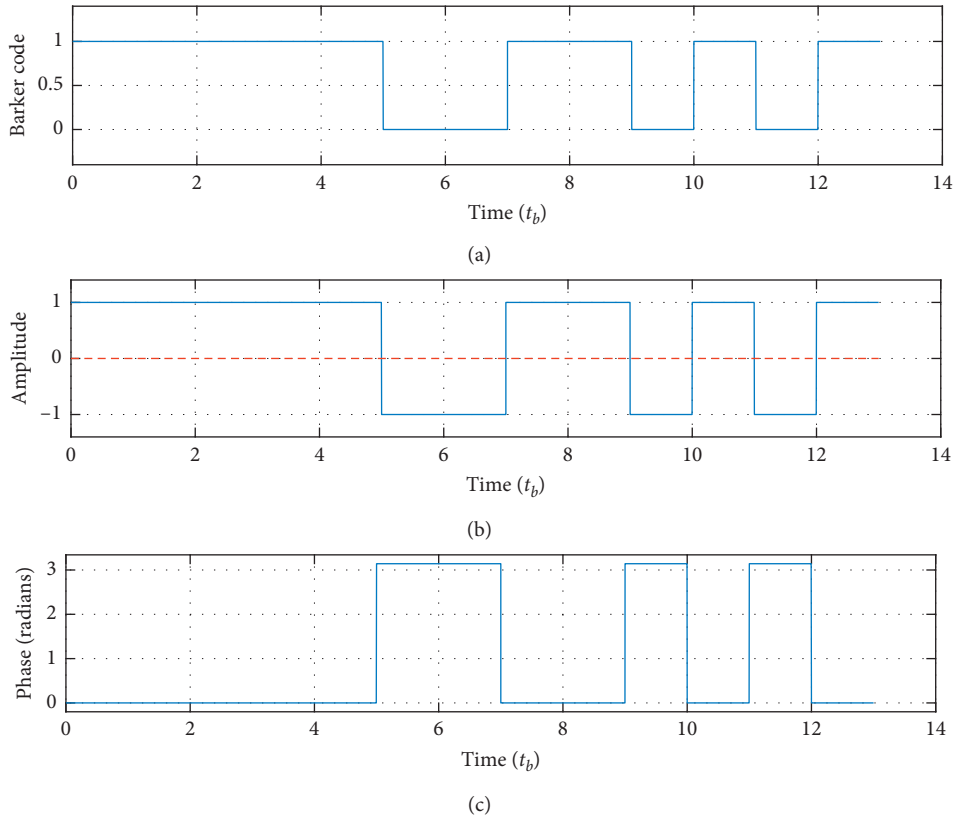


FIGURE 18: One pulse of Barker code: (a) 13-chip Barker code, (b) the Barker code  $I/Q$  waveform (solid and dashed lines are  $I$  and  $Q$ , respectively), and (c) phase in each chip of  $I/Q$  signal.

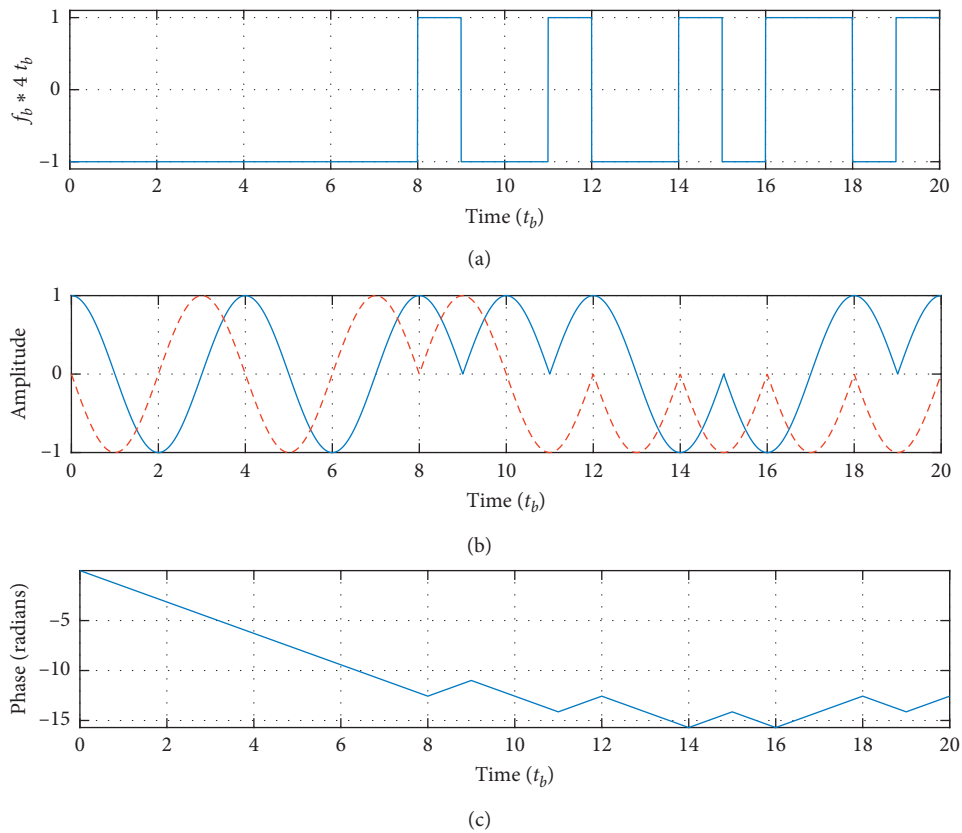


FIGURE 19: One pulse of a two-valued frequency-coded waveform: (a) a 20-chip two-valued frequency code, i.e., [00000000100100101 1 0 1], (b) the  $I/Q$  of the waveform (solid and dashed lines are  $I$  and  $Q$ , respectively), and (c) the phase in each chip of the signal.

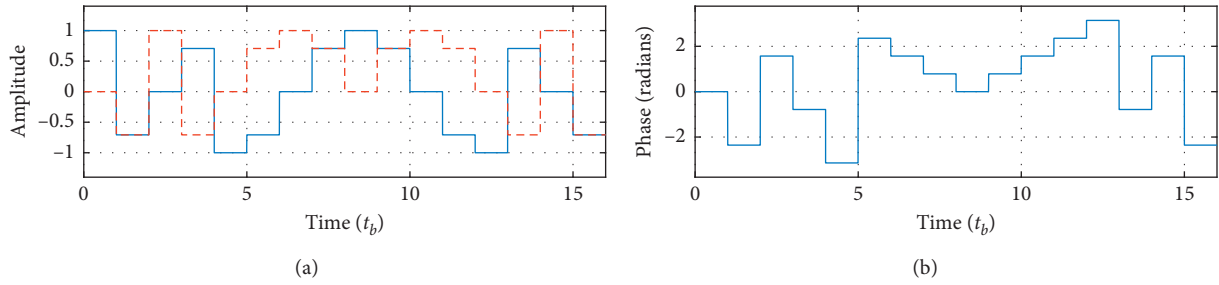


FIGURE 20: A pulse of a 16-chip P1 poly-phase waveform: (a)  $I/Q$  of the waveform (solid and dashed lines are  $I$  and  $Q$ , respectively) and (b) the phase in each chip of the signal.

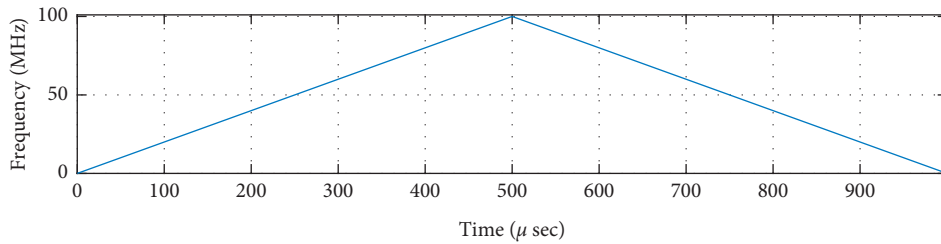


FIGURE 21: One period of a FMCW waveform.

TABLE 11: FMCW signal parameters.

Sweep bandwidth (MHz)	Sweep direction	Sweep time	Number of sweeps
100	Triangle	500 $\mu$ s	2

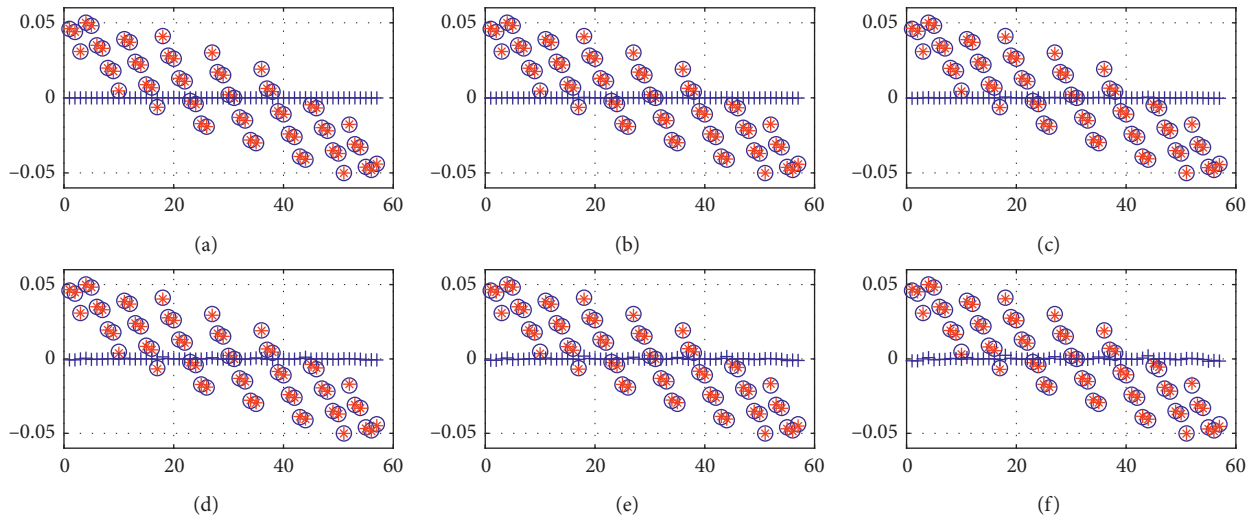


FIGURE 22: The comparison between the values of the first term (blue oooo) and the imaginary part of the second term (red \*\*\*) of (D.2) with  $SNR = \infty$ , when the frequency is at 10 GHz, the incident direction is from  $(143.75^\circ \ 84.66^\circ)$  to Array-3, the waveform is WF-1, and the number of snapshots is 512. Blue plus signs are the real part of the second term in (D.2). (a) Freq=6 GHz; (b) Freq=8 GHz; (c) Freq=10 GHz; (d) Freq=14 GHz; (e) Freq=16 GHz; (f) Freq=18 GHz.

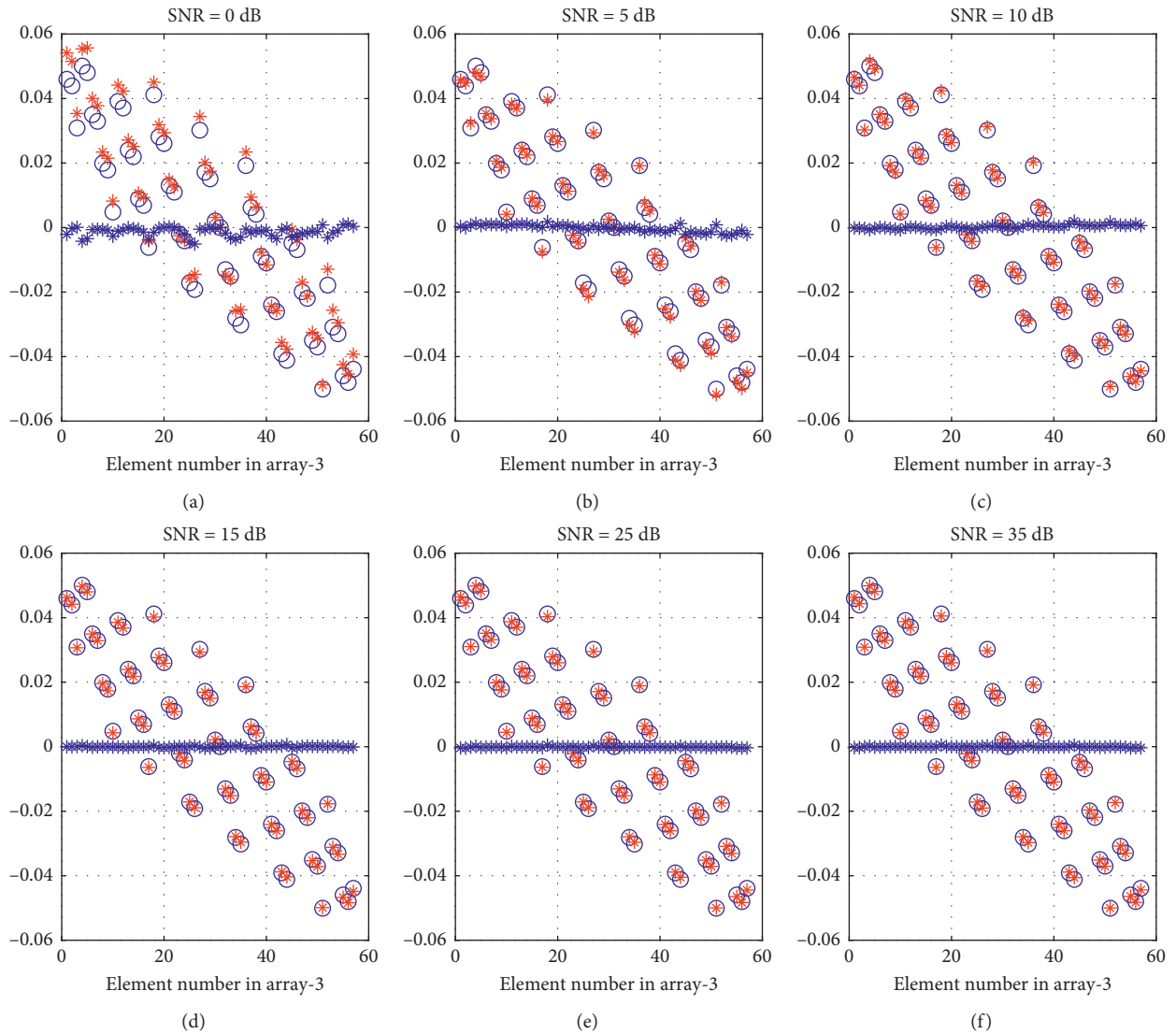


FIGURE 23: The comparison between the values of the first-term (blue oooo) and the imaginary part of the second-term (red \*\*\*\*) of (D.2) with different SNRs, when the frequency is at 10 GHz, the incident direction is from  $(143.75^\circ \ 84.66^\circ)$  to Array-3, the waveform is WF-1 and the number of snapshots is 512. Blue plus signs are the real part of the second term in (D.2). (a) SNR = 0 dB; (b) SNR = 5 dB; (c) SNR = 10 dB; (d) SNR = 15 dB; (e) SNR = 25 dB; (f) SNR = 35 dB.

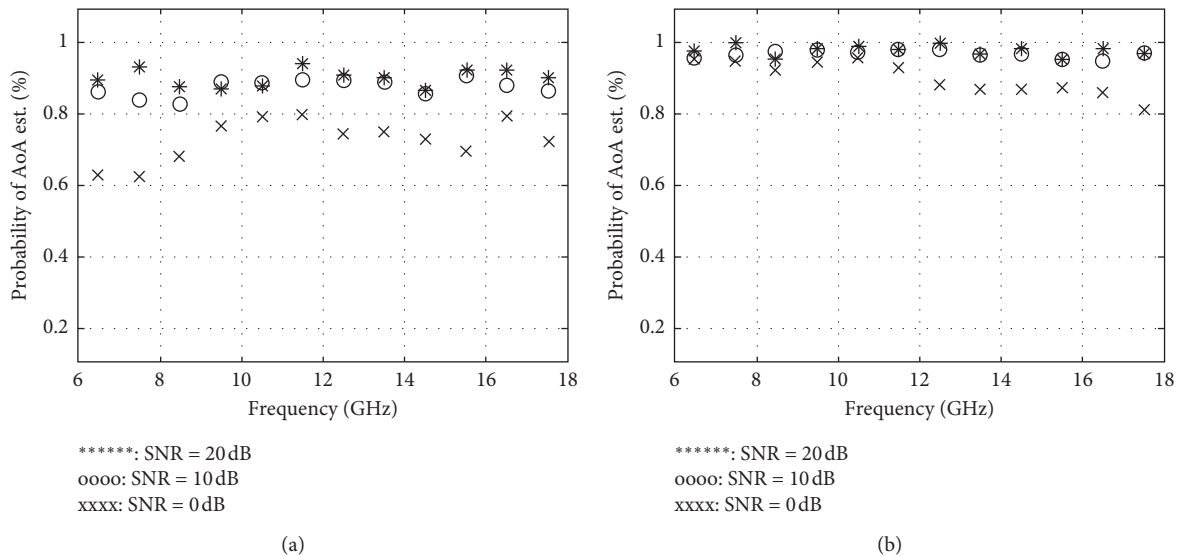


FIGURE 24: Frequency vs probability of AoA estimation for Array-3 and WF-1 with 512 snapshots: (a)  $RMSE \leq 1^\circ$  and (b)  $RMSE \leq 5^\circ$ .

fast access memory, the speed of the calculation can be accelerated.

## 7. Conclusions

This paper introduces a new radar signal AoA estimator using a 7-element 6–18 GHz CBSA NSA and a 2D D3 method suitable for ESM applications. Unlike the 3- and 5-element CBSA arrays that are commonly used by interferometry-based AoA methods, our array can be installed on small airborne platforms. The paper also introduces a 2D calibration and data-transformation method that allows an IEPA to use the 7-element NSA-measured data for AoA estimations and converts a full 3D antenna problem into a 3D free-space problem. To calculate the AoA, a new 2D AoA search method has been developed by taking the advantages of the SV of the IEPA and 2D D3 results, which avoids having to resolve the ambiguity encountered in interferometer arrays and also results in frequency-independent performance. The simulation results show that with high SNR ( $\geq 15$  dB), the estimator can have 50% probability of AoA estimation with  $\text{RMSE} \leq 1^\circ$  using just few temporal samples. More importantly, with more temporal snapshots, the estimator has 52% and 80% probabilities of AoA estimation with  $\text{RMSE} \leq 1^\circ$  and  $5^\circ$ , respectively, for phase- or frequency-modulated radar pulses, when the SNR is between  $-10$  and  $0$  dB. Although the performance can degrade for an ultra-wideband FMCW radar signal (for example, the 100 MHz chirp-signal used here), it can still achieve 33% and 67% probabilities of AoA estimation with  $\text{RMSE} \leq 1^\circ$  and  $5^\circ$ , respectively, when SNR is between  $-10$  dB and  $0$  dB. Future work is needed to improve the performance of the AoA estimation for ultra-wideband FMCW signals in low SNR conditions. The study also shows that the estimator prefers a circular-shaped planar array with a triangular interelement pattern, since this array presents more symmetrical characteristics when it is seen from different Az angles. In order to facilitate the practical use of this AoA estimator in ESM applications, i.e., as there is no a priori knowledge of the SOI, this paper also presents the use of precalculated SV and  $\mathfrak{S}$ -databases, which are built on a 2D-angle-grid with more uniformly distributed directions with a set of preselected frequency points. The AoA calculation can be further improved by using a denser 2D-angle-grid, more frequency points for database calculations, and dedicated hardware with fast access memory.

## Appendix

### A. 2D Planar Arrays with Isotropic Elements

Six different shapes of planar arrays were used in the study. These arrays are shown from Figure 15, and they are as follows:

- (i) Array-1 (a): uniform-spaced rectangular array with 81 elements (white circles); element spacing is 7 mm in both  $x$  and  $y$  directions. The array center is at the 41<sup>st</sup> element.
- (ii) Array-2 (b): uniform-spaced hexagonal array with 61 elements (white circles); the element spacing in

each triangular is 7 mm in both  $x$  and  $y$  directions. The array center is at the 31<sup>st</sup> element.

- (iii) Array-3 (c): circular planar array with triangular grid with 57 elements (white circles); the element spacing in each triangular grid is 7 mm. The array center is at the 31<sup>st</sup> element.
- (iv) Array-4 (d): hexagonal planar array with rectangular grid with 77 elements (white circles); the element spacing is 7 mm in both  $x$  and  $y$  directions. The array center is at the 39<sup>th</sup> element.
- (v) Array-5 (e): circular planar array with rectangular grid with 69 elements (white circles); the element spacing is 7 mm in both  $x$  and  $y$  directions. The array center is at the 35<sup>th</sup> element.
- (vi) Array-6 (f): rectangular planar array with triangular grid with 81 elements (white circles); the element spacing in each triangular grid is 7 mm. The array center is at the 41<sup>st</sup> element.

The following can be found:

- (i) Arrays have different isotropic-element distribution patterns;
- (ii) Since the patterns are different, the total number of isotropic elements ( $NN$ ) is also different;
- (iii) The aperture size of each plane array is about the same as that of the 7-element NSA;
- (iv) The center element in an array is collocated with the first element of the 7-element NSA.

### B. Definition of 2D-Angle Grid by Vertices of a Unit Icosphere

It is known that the incident angles defined on a UV-sphere [62], which are frequently used in antenna analysis, have much more dense directions near north and south poles than near the equator. In order to obtain more uniform angular distributions for AoA searching using (18), a 2D-angle grid defined by the unit icosphere [63] is used in this study. The 2D-angle grid is formed by subdividing the triangles of a regular icosahedron, and the number of subdivisions ( $N_{\text{subdiv}}$ ) determines the density of the vertices on the surface of an icosphere [64]. Figure 16 shows an example of the 2D-angle grid. Since the CBSA has about  $100^\circ$  3 dB antenna beamwidth, in this study, the FOV of the 7-element NSA is defined within  $[Az_1 Az_2] \times [El_1 El_2] = [-180^\circ 180^\circ] \times [40^\circ 90^\circ]$ , which are indicated by the asterisks in the example shown in Figure 16.

Table 10 gives the number of total directions (vertices) within the FOV and their corresponding angular resolutions with respect to the number of subdivisions of the triangles of a regular icosahedron. Averaged El-angle difference between the vertex on  $z$ -axis and surrounding 6 vertices (marked by “x” in Figure 16) gives a rough order of angle resolution. Considering the AoA estimation accuracy and calculation speed,  $N_{\text{subdiv}} = 7$  is used in this study. This 2D-angle grid with angle zones within the FOV is shown in Figure 17.

### C. Four Commonly Used Radar Signals

*C.1. Barker Code of Length Equal to 13.* The 13-chip Barker code is shown in Figure 18, which is a binary-phase shift-keying modulation. In our simulations, the duration of each chip ( $t_b$ ) is 200 ns, so the total pulse width (PW) is 2.6  $\mu$ s.

*C.2. Two-Valued Frequency-Coded Waveform.* Figure 19 shows the information of a 20-chip two-valued frequency-coded waveform, which is given in Table I of [58]. The two-valued frequency-coded waveforms presented in [58] can yield near-perfect periodic autocorrelation function for radar applications, when the number of chips is a multiple of 4 and the frequency values are  $\pm 1/4t_b$ , where  $t_b$  is the bit duration. The duration of each chip in Figure 19 is 200 ns, and the total PW is 4  $\mu$ s. The two frequency values are  $\pm 1.25$  MHz. This 20-chip two-valued frequency-coded waveform is a kind of binary-frequency shift-keying modulation.

*C.3. Poly-Phase Waveform.* A 16-chip P1 poly-phase waveform is shown in Figure 20. Each chip width is 1  $\mu$ s, and the total PW is 16  $\mu$ s.

*C.4. FMCW.* The frequency change of the FMCW waveform used in this study is shown in Figure 21. Its parameters are given in Table 11. Note that it has a very wide linear frequency change during chirping.

### D. Explanation of the Frequency-Independent Performance

From Figures 6–8, one can observe that, for a given AoA estimation accuracy requirement (e.g.,  $\text{RMSE} \leq 1^\circ$ ) and the probability of AoA estimation (e.g., 50%), the required SNR is close to a constant, when the frequency is from 6 to 18 GHz. The following gives the explanation.

Taking natural log of both (15) and squared of (17), (18) can be rewritten as

$$\min_{\substack{az=az_e \\ el=el_e}} \left\{ \left( \frac{1}{\lambda_{\text{est}}} \right) \sum_{n=1}^{NN} j4\pi [px_n \cos(el)\cos(az) + py_n \cos(el)\sin(az)] - \lambda_{\text{est}} \ln \left[ \frac{1}{C} \sum_{m=1}^M x_n^2(m)w_m \right] \right\}. \quad (\text{D.1})$$

In this equation, the  $\lambda_{\text{est}}^{-1}$  term can be removed, as it is a constant. Then, one has the following equation:

$$\min_{\substack{az=az_e \\ el=el_e}} \left\{ \sum_{n=1}^{NN} j4\pi [px_n \cos(el)\cos(az) + py_n \cos(el)\sin(az)] - \lambda_{\text{est}} \ln \left[ \frac{1}{C} \sum_{m=1}^M x_n^2(m)w_m \right] \right\}. \quad (\text{D.2})$$

It can be seen that during the solution search, the second term (after the minus sign in (D.2)) has to match or be very close to a variable (the first term before minus sign in (D.2)), which is only determined by the direction and locations of the elements in an IEPA. Since the first term is frequency independent, the second term must also be frequency independent. The following simulation results support this conclusion.

Figure 22 shows the comparison between the first term and the imaginary part of the second term in (D.2) at each element in Array-3, when SNR is equal to infinity. One can see that the imaginary part of the second term in (D.2) does not change when the frequency changes at a given incident direction.

Figure 23 shows that the values of the first term and the imaginary part of the second term in (D.2) at each element in Array-3 get closer to each other as SNR improves. The performances of the probability of AoA estimation at different frequencies are close to each other at different SNR levels as shown in Figure 24.

### Data Availability

The ways to generate the simulation data used to support the findings of this study are included within the article.

### Conflicts of Interest

The authors declare that there are no conflicts of interest regarding the publication of this paper.

### Acknowledgments

This research was supported by the Radar Electronic Warfare Capability Development in Radar Electronic Warfare Section at Defence Research and Development Canada-Ottawa Research Centre, Department of National Defence, Canada. Special thanks to Mr. Michael Low from Defence Research and Development Canada for many good discussion and comments to improve the quality of the paper.




## References

- [1] P. E. Pace, *Detecting and Classifying Low Probability of Intercept Radar*, Artech House, Norwood, MA, USA, 2nd edition, 2009.
- [2] E. Jacobs and E. Ralston, "Ambiguity resolution in interferometry," *IEEE Transactions on Aerospace and Electronic Systems*, vol. AES-17, no. 6, pp. 766–780, 1981.
- [3] W. B. Kendall, "Unambiguous accuracy of an interferometer angle-measuring system," *IEEE Transactions on Space Electronics and Telemetry*, vol. SET-11, no. 2, pp. 62–70, 1965.
- [4] R. C. Hansen, "Microwave scanning antennas," in *Array Systems*, vol. 3, Academic Press, Cambridge, MA, USA, 1966.
- [5] K. Pasala, R. Penno, and S. Schneider, "Novel wideband Multimode hybrid interferometer system," *IEEE Transactions on Aerospace and Electronic Systems*, vol. 39, no. 4, pp. 1396–1406, 2003.
- [6] E. Stephen Lipsky, *Microwave Passive Direction Finding*, Scitech Publishing, Inc., Raleigh, NC, USA, 2004.
- [7] J. B. Y. Tsui, *Microwave Receivers with Electronic Warfare Applications*, John Wiley & Sons, Hoboken, NJ, USA, 1986.
- [8] F. Neri, *Introduction to Electronic Defence Systems*, Artech House, Norwood, MA, USA, 2nd edition, 2006.
- [9] S. Chandran, *Advances in Direction-of-Arrival Estimation*, Artech House, Norwood, MA, USA, 2006.
- [10] A. De Martino, *Introduction to Modern EW Systems*, Artech House, Norwood, MA, USA, 2012.
- [11] T. E. Tuncer and B. Friedlander, *Classical and Modern Direction-of-Arrival Estimation*, Academic Press, Burlington, MA, USA, 2009.
- [12] R. Schmidt, "Multiple emitter location and signal parameter estimation," *IEEE Transactions on Antennas and Propagation*, vol. 34, no. 3, pp. 276–280, 1986.
- [13] R. Roy and T. Kailath, "ESPRIT-estimation of signal parameters via rotational invariance techniques," *IEEE Transactions on Acoustics, Speech, and Signal Processing*, vol. 37, no. 7, pp. 984–995, 1989.
- [14] X. Wang, L. Wan, M. Huang, C. Shen, and K. Zhang, "Polarization channel estimation for circular and non-circular signals in massive MIMO systems," *IEEE Journal of Selected Topics in Signal Processing*, vol. 13, no. 5, pp. 1001–1016, 2019.
- [15] H. Chen, C. Hou, W.-P. Zhu et al., "ESPRIT-like two-dimensional direction finding for mixed circular and strictly noncircular sources based on joint diagonalization," *Signal Processing*, vol. 141, pp. 48–56, 2017.
- [16] M. Coutino, R. Pribic, and G. Leus, "Direction of arrival estimation based on information geometry," in *Proceedings of the 2016 IEEE International Conference on Acoustics, Speech and Signal Processing (ICASSP)*, pp. 3066–3070, Shanghai, China, March 2016.
- [17] Y.-Y. Dong, C.-X. Dong, W. Liu, M.-M. Liu, and Z.-Z. Tang, "Scaling transform based information geometry method for DOA estimation," *IEEE Transactions on Aerospace and Electronic Systems*, vol. 55, no. 6, pp. 3640–3650, 2019.
- [18] A. D. Lonkeng and J. Zhuang, "Two-dimensional DOA estimation using arbitrary arrays for massive MIMO systems," *International Journal of Antennas and Propagation*, vol. 2017, Article ID 6794920, 9 pages, 2017.
- [19] V. Krishnaveni, T. Kesavamurthy, and B. Apama, "Beamforming for direction of arrival (DOA) estimation—a survey," *International Journal of Computer Applications*, vol. 61, no. 11, 2013.
- [20] M. Devendra and K. Manjunathachari, "Literature survey on high resolution direction of arrival (DOA) algorithms," *International Advanced Research Journal in Science, Engineering and Technology*, vol. 2, no. 2, pp. 23–31, 2015.
- [21] S. Barua, S. C. Lam, P. Ghosa, S. Xing, and K. Sandrasegaran, "A survey of direction of arrival estimation techniques and implementation of channel estimation based on SCME," in *Proceedings of the 2015 12th International Conference on Electrical Engineering/Electronics, Computer, Telecommunications and Information Technology (ECTI-CON)*, pp. 1426–1429, Hua Hin, Thailand, June 2015.
- [22] Z. Zheng and S. Mu, "Two-dimensional DOA estimation using two parallel nested arrays," *IEEE Communications Letters*, vol. 24, no. 3, pp. 568–571, 2020.
- [23] H. P. Shi, W. Leng, Z. W. Guan, and T. Z. Jin, "Two novel two-stage direction of arrival estimation algorithms for two-dimensional mixed noncircular and circular sources," *Sensors*, vol. 17, no. 6, p. 1433, 2017.
- [24] Y. Wu, G. S. Liao, and H. C. So, "A fast algorithm for 2-D directional-of-arrival estimation," *Signal Processing*, vol. 83, no. 8, pp. 1927–1831, 2003.
- [25] A.-J. van der Veen, "Asymptotic properties of the algebraic constant modulus algorithm," *IEEE Transactions on Signal Processing*, vol. 49, no. 8, pp. 1796–1807, 2001.
- [26] Q. Wang, H. Yang, H. Chen, Y. Y. Dong, and L. H. Wang, "A low complexity method for two-dimensional direction-of-arrival estimation using an L-shaped array," *Sensors (Basel, Switzerland)*, vol. 17, no. 12, p. 190, 2017.
- [27] A. B. Gershman, M. RübSamen, and M. Pesavento, "One- and two-dimensional direction-of-arrival estimation: an overview of search-free techniques," *Signal Processing*, vol. 90, no. 5, pp. 1338–1349, 2010.
- [28] S. O. Al-Jazzar, Z. Hamici, and S. Aldalahmeh, "Two-dimensional AoA estimation based on a constant modulus algorithm," *International Journal of Antennas and Propagation*, vol. 2017, Article ID 3214021, 6 pages, 2017.
- [29] E. J. Candes and T. Tao, "Decoding by linear programming," *IEEE Transactions on Information Theory*, vol. 51, no. 12, pp. 4203–4215, 2005.
- [30] D. L. Donoho, "Compressed sensing," *IEEE Transactions on Information Theory*, vol. 52, no. 4, pp. 1289–1306, 2006.
- [31] E. J. Candes, J. Romberg, and T. Tao, "Robust uncertainty principles: exact signal reconstruction from highly incomplete frequency information," *IEEE Transactions on Information Theory*, vol. 52, no. 2, pp. 489–509, 2006.
- [32] A. C. Gurbuz, J. H. McClellan, and V. Cevher, "A compressive beamforming method," in *Proceedings of the International Conference on Acoustics, Speech, and Signal Processing*, Las Vegas, NV, USA, March 2008.
- [33] A. C. Gurbuz, V. Cevher, and J. H. McClellan, "Bearing estimation via spatial sparsity using compressive sensing," *IEEE Transactions on Aerospace and Electronic Systems*, vol. 48, no. 2, pp. 1358–1369, 2012.
- [34] V. Cevher, A. C. Gurbuz, J. H. McClellan, and R. Chellappa, "Compressive wireless arrays for bearing estimation," in *Proceedings of the 2008 IEEE International Conference on Acoustics, Speech and Signal Processing*, pp. 2497–2500, Las Vegas, NV, USA, March 2008.
- [35] E. Candes and T. Tao, "The dantzig selector: statistical estimation when  $p$  is much larger than  $n$ ," *The Annals of Statistics*, vol. 35, no. 6, pp. 2313–2351, 2007.
- [36] C. Wu and J. Elangage, "Multi-emitter 2-dimensional angle-of-arrival estimator via compressive sensing," *IEEE Transactions on Aerospace and Electronic Systems*, vol. 56, no. 4, pp. 2884–2895, 2020.

- [37] Z.-M. Liu, Z.-T. Huang, Y.-Y. Zhou, and J. Liu, "Direction-of-arrival estimation of noncircular signals via sparse representation," *IEEE Transactions on Aerospace and Electronic Systems*, vol. 48, no. 3, pp. 2690–2698, 2012.
- [38] Z.-M. Liu, Z.-T. Huang, and Y.-Y. Zhou, "Array signal processing via sparsity-inducing representation of the array covariance matrix," *IEEE Transactions on Aerospace and Electronic Systems*, vol. 49, no. 3, pp. 1710–1724, 2013.
- [39] Z. Yang, J. Li, P. Stoica, and L. Xie, "Sparse methods for direction-of-arrival estimation," *Academic Press Library in Signal Processing*, Elsevier, vol. 7, pp. 509–581, Oxford, UK, 2018.
- [40] J. Cai, W. Liu, R. Zong, and B. Wu, "Sparse array extension for non-circular signals with subspace and compressive sensing based DOA estimation methods," *Signal Processing*, vol. 145, pp. 59–67, 2018.
- [41] Z. Zhang and B. D. Rao, "Sparse signal recovery with temporally correlated source vectors using sparse Bayesian learning," *IEEE Journal of Selected Topics in Signal Processing*, vol. 5, no. 5, pp. 912–926, 2011.
- [42] M. Carlin, P. Rocca, G. Oliveri, and A. Massa, "Bayesian compressive sensing as applied to directions-of-arrival estimation in planar arrays," *Journal of Electrical and Computer Engineering*, vol. 2013, Article ID 245867, 12 pages, 2013.
- [43] P. Rocca, M. A. Hannan, M. Salucci, and A. Massa, "Single-snapshot DoA estimation in array antennas with mutual coupling through a multiscaling BCS strategy," *IEEE Transactions on Antennas and Propagation*, vol. 65, no. 6, pp. 3203–3213, 2017.
- [44] T. K. Sarkar, S. Nagaraja, and M. C. Wicks, "A deterministic direct data domain approach to signal estimation utilizing nonuniform and uniform 2-D arrays," *Digital Signal Processing*, vol. 8, no. 2, pp. 114–125, 1998.
- [45] T. K. Sarkar, T. K. Sarkar, H. Wang et al., "A deterministic least-squares approach to space-time adaptive processing (STAP)," *IEEE Transactions on Antennas and Propagation*, vol. 49, no. 1, pp. 91–103, 2001.
- [46] K. Kim, T. K. Sarkar, and M. S. Palma, "Adaptive processing using a single snapshot for a non-uniformly spaced array in the presence of mutual coupling and near-field scatterers," *IEEE Transactions on Antennas and Propagation*, vol. 50, no. 5, pp. 582–590, 2002.
- [47] T. K. Sarkar, H. Schwarzlander, S. Seungwon Choi, M. S. Palma, and M. C. Wicks, "Stochastic versus deterministic models in the analysis of communication systems," *IEEE Antennas and Propagation Magazine*, vol. 44, no. 4, pp. 40–50, 2002.
- [48] T. K. Sarkar, M. C. Wicks, M. Salazar-Palma, and R. J. Bonneau, *Smart Antennas*, IEEE Press, A John Wiley & Son, Inc., Publication, Hoboken, NJ, USA, 2003.
- [49] K. J. Kim, T. K. Sarkar, H. Wang, and M. Salazar-Palma, "Direction of arrival estimation based on temporal and spatial processing using a direct data domain (D3) approach," *IEEE Transactions on Antennas and Propagation*, vol. 52, no. 2, pp. 533–541, 2004.
- [50] H. Chen, B. X. Huang, Y. L. Wang, and Y. Q. Hou, "Direction-of-arrival based on direct data domain (D3) method," *Journal of Systems Engineering and Electronics*, vol. 20, no. 3, pp. 512–518, 2009.
- [51] W. Mao, G. Li, X. Xie, and Q. Yu, "DOA estimation of coherent signals based on direct data domain under unknown mutual coupling," *IEEE Antennas and Wireless Propagation Letters*, vol. 13, pp. 1525–1528, 2014.
- [52] P. Zhang, J. Li, A. Z. Zhou, H. B. Xu, and J. Bi, "A robust direct data domain least squares beamforming with sparse constraint," *Progress In Electromagnetics Research C*, vol. 43, pp. 53–65, 2013.
- [53] N. Yilmazer and T. K. Sarkar, "2D unitary matrix pencil method for efficient direction of arrival estimation," *Digital Signal Processing*, vol. 16, pp. 767–781, 2006.
- [54] N. Yilmazer, R. Fernandez-Recio, and T. K. Sarkar, "Matrix pencil method for simultaneously estimating azimuth and elevation angles of arrival along with the frequency of the incoming signals," *Digital Signal Processing*, vol. 16, pp. 796–816, 2006.
- [55] C. Wu, "Wideband miniaturized digital receiver technology for micro/nanosat application," *Scientific Report*, 2015.
- [56] E. Poliakov and C. Wu, "Compact PCI computer control system and its control software update for UAV electronic support payload," *Technical Memorandum*, 2009.
- [57] C. Wu and A. Young, "Initial design considerations of small UAV EW payload," *Technical Memorandum*, 2012.
- [58] N. Levanon and U. Levanon, "Tow-valued frequency-coded waveform with favorable periodic autocorrelation," *IEEE Transactions on Aerospace and Electronic Systems*, vol. 42, no. 1, pp. 237–248, 2006.
- [59] X. Li and M. C. E. Yagoub, "Wideband cavity-backed spiral antenna design and mutual coupling study in a closely-spaced array," in *Proceedings of the 2018 18th International Symposium on Antenna Technology and Applied Electromagnetics (ANTEM)*, Waterloo, Canada, August 2018.
- [60] L3HARRISR Antenna System, Spiral Antenna, 2020, [https://www.l3t.com/randtron/antenna\\_products/elements\\_broadband\\_spirals.htm](https://www.l3t.com/randtron/antenna_products/elements_broadband_spirals.htm).
- [61] W. A. Gardner, *Cyclostationarity in Communications and Signal Processing*, IEEE Press, Piscataway, NJ, USA, 1994.
- [62] D. Lugg, "What is the difference between a UV sphere and an icosphere?" 2020, <https://blender.stackexchange.com/questions/72/what-is-the-difference-between-a-uv-sphere-and-an-icosphere#:~:text=A%20UV%20sphere%20has%20faces,compared%20to%20the%20UV%20sphere>.
- [63] Wikipedia the Free Encyclopedia, Icosphere, 2020, <https://en.wikipedia.org/wiki/Icosphere>.
- [64] W. O. C. Ward, "Icosphere, generate unit geodesic sphere created by subdividing a regular icosahedron," 2020, <https://www.mathworks.com/matlabcentral/fileexchange/50105-icosphere?focused=3865223&tab=function>.

## Research Article

# Spread Sea Clutter Suppression in HF Hybrid Sky-Surface Wave Radars Based on General Parameterized Time-Frequency Analysis

Zhuo-qun Wang <sup>1</sup>, Ya-jun Li <sup>1</sup>, Jun-nan Shi,<sup>1</sup> Peng-fei Wang,<sup>1</sup> Ai-hua Liu <sup>1</sup>,  
Xin-fan Xia,<sup>1</sup> and De-hong Chen<sup>2</sup>

<sup>1</sup>Shanghai Radio Equipment Research Institute, Shanghai 201109, China

<sup>2</sup>Shanghai Electro-Mechanical Engineering Institute, Shanghai 201109, China

Correspondence should be addressed to Ya-jun Li; liyajun1985happy@163.com

Received 18 March 2020; Revised 5 June 2020; Accepted 22 July 2020; Published 19 August 2020

Guest Editor: Qing Shen

Copyright © 2020 Zhuo-qun Wang et al. This is an open access article distributed under the Creative Commons Attribution License, which permits unrestricted use, distribution, and reproduction in any medium, provided the original work is properly cited.

In high-frequency (HF) hybrid sky-surface wave radar, the first-order sea clutter broadening is severe under the action of ionospheric phase disturbance and bistatic angles. In this paper, a cascaded method is described to suppress the spread sea clutter. Firstly, the radar configuration and sea clutter broadening model are introduced based on the newly developed integrated HF sky-surface wave experimental system. In the cascaded processing method, a new ionospheric decontamination method based on general parameterized time-frequency (GPTF) analysis is proposed to estimate or correct the ionospheric phase distortion with large amplitude. Then, the forward-backward linear prediction (FBLP) algorithm is used to suppress the spread sea clutter caused by bistatic angle. Simulation results show that such ionospheric decontamination method based on GPTF is helpful for the large-amplitude ionospheric contamination when the target masking effect happens even after ionospheric phase decontamination. Finally, the proposed method is examined by the measured data. Experimental results indicate that the proposed method can well suppress the broadening sea clutter for HF hybrid sky-surface wave radars.

## 1. Introduction

Ship detection is an important mission of the HF over-the-horizon radar. Based on the propagation mode associated with sky-wave transmitting and surface wave receiving, HF hybrid sky-surface wave radar not only maintains the superiority of HF sky-wave radar which has a long detection range and wide coverage, the advantage of HF surface wave radar which has a stable propagation channel but also keeps a good invisibility and anti-interference ability [1–4]. However, the sea clutter under this combined propagation mode with sky-wave transmitting and shore-based receiving is influenced by composite factors such as the bistatic angle and ionospheric phase disturbance. Among the influencing factors of the spectrum spread of sea clutter, it is unclear whether the ionospheric disturbance or the bistatic angle dominates. In addition, sea clutter is also affected by marine dynamics factors. Therefore, under this hybrid propagation

mode radar, the spectrum of first-order sea clutter is complicated [5, 6].

Based on the hybrid operating mode of sky-wave transmitting and ground-wave receiving, HF hybrid sky-surface wave radar is expected to improve detection probability for ships by overcoming defects of existing sky-wave and ground-wave OTH radar and making complementary advantages of both. Ionosphere is a dispersive, hierarchical, and nonstationary medium. Unfortunately, the ionospheric disturbance often causes the sea clutter spectrum and target to spread in the frequency domain, rendering extended coherent integration pointless. On the other hand, HF hybrid sky-surface wave radar is actually a bistatic radar system. The receiving beam width is wide for the array aperture of our radar experimental system. Thus, the sea clutter spectrum will show different broadening characteristics in the different resolution cells. What is worse, ionospheric phase disturbance further contributes to the sea



clutter spectrum broadening. Thus, the broadening of the first-order sea clutter spectrum is very severe under the influence of ionosphere and bistatic angles. In the process of cascade processing of broadened sea clutter in this paper, ionospheric phase decontamination was first processed. At this time, decontaminated broadening sea clutter is only caused by bistatic angles. Therefore, the broadening sea clutter suppression was processed after decontamination.

For the ionospheric phase path disturbance, the method of extracting the contamination function is often used for compensation. The current ionospheric phase disturbance suppression method extracts the frequency modulation function by estimating the instantaneous frequency variation of the broadened echo spectrum, thereby obtaining the ionospheric phase disturbance correction function, and then correcting the echo signal by using the obtained correction function. It can sharpen the broadened echo spectrum and improve the target detection performance of the radar. For ionospheric contamination with small amplitude, the maximum entropy spectrum estimation method, the phase gradient algorithm (PGA) method [7], the minimum entropy searching method, the eigendecomposition (ED) method, and the piecewise polynomial phase modeling (PPPM) method [8, 9] are typical methods. These methods require that the broadened Bragg peak is extracted to estimate the instantaneous frequency. Time-frequency analysis is a more effective method for ionospheric decontamination, especially large-amplitude ionospheric contamination. Currently, nonparametric time-frequency analysis methods are mainly used, such as short-time Fourier transform (STFT), Winger-Ville distribution (WVD), pseudo-WVD distribution (PWVD) method, and smooth pseudo-WVD distribution (SPWVD) method. However, those methods are sensitive to the signal-to-noise ratio and are affected by cross-term interference and resolution limitations. Especially for the ionospheric contamination with large amplitude, these methods often fail. Currently, the main technical approach to detect the ship target is the sea clutter suppression method. Representative algorithms include sea clutter cancellation method, subspace class method, and singular value decomposition (SVD) method, but these algorithms are difficult to effectively suppress nonstationary broadened sea clutter [8–10].

In 1997, Melyanovski [1] mentioned the HF hybrid sky-surface wave radar system and explored the feasibility. Riddolls [3, 4] discussed the ship target detection performance of this radar and analyzed the limits on the radar resolution capability in 2007 and 2008. Zhao et al. [5] presented an experimental study of HF passive bistatic radar via hybrid sky-surface wave mode based on Digital Radio Mondiale digital amplitude modulation broadcasting in 2013 and analyzed the target detection performance. In 2014, Li et al. [6] analyzed the characteristics of frequency shift and broadening sea clutter based on the newly developed integrated HF sky-surface wave experimental system. Experimental results show that some sea clutter broadening is serious and the ship target is difficult to effectively detect. In 2015, Li et al. [11] proposed a cascaded processing method for broadening sea clutter by  $S^2$ -method and FBLP. The  $S^2$  transform method is a nonparametric method, which can

suppress cross-term interference to a certain extent, but the resolution and the time-frequency characteristics of the signals cannot be accurately described. In this paper, a cascaded method for ionospheric decontamination and sea clutter suppression to enable detection of ship target is proposed. The method utilizes an important property of the GPTF and FBLP to suppress the broadening sea clutter. GPTF is a parameterized time-frequency analysis method. Compared with the  $S^2$ -method, it has better resolution and no cross-term interference. And a novel estimator for the instantaneous frequency of the Bragg lines based on GPTF is proposed.

The content of this paper is organized as follows. Firstly, the radar configuration and sea clutter broadening model are described based on the newly developed integrated HF sky-surface wave experimental system. Secondly, a cascaded processing method for ionospheric decontamination and sea clutter suppression is presented. In this method, the time-frequency analysis method based on GPTF is proposed to correct the ionospheric phase contamination with large amplitude. Then, the FBLP algorithm is used to suppress the broadening bistatic sea clutter caused by bistatic angle, which is based on the prior knowledge of distribution characteristics and the multidimensional feature of first-order sea clutter [12]. Finally, the proposed method is examined by the measured data. Compared with the traditional nonparametric time-frequency analysis method, the ionospheric pollution function extracted by the GPTF method is more accurate. Experimental results indicate that the proposed method can well suppress the broadening sea clutter for HF hybrid sky-surface wave radars. The research in this dissertation will provide the theory and technology foundation to detect the target over the horizon under the broadening sea clutter in HF hybrid sky-surface wave radar.

## 2. First-Order Sea Clutter Broadening Characteristics and Model

*2.1. System Layout.* Based on the propagation mode associated with sky and surface wave, the HF hybrid sky-surface wave radar not only maintains the superiority of HF sky-wave radar which has a long detection range and wide coverage, the advantage of HF surface radar which has a stable propagation channel but also keeps a good invisibility and anti-interference ability. The system layout of the HF hybrid sky-surface wave radar is shown in Figure 1 [6]. The beams generated by the sky-wave radar are reflected by ionosphere to monitored sea area (path  $P_1$  and  $P_2$ ). Then, the sea echo of the monitored sea area arrives at the surface wave radar station by ground-wave diffraction (path  $R_{r_1}$  and  $R_{r_2}$ ). In Figure 1,  $TR=L$  is the baseline length between the transmitting and receiving stations;  $R_{r_i}$  is the distance between the target and receiving station;  $\theta_{r_i}$  is the angle between the  $R_{r_i}$  and  $L$ ;  $h$  is the ionospheric height;  $D$  is the ground distance; and  $\beta_{H_i}$  is bistatic angle.

*2.2. First-Order Sea Clutter Bragg Frequency.* Thus, the total Bragg frequency expression for HF hybrid sky-surface wave radar can be written as follows [6, 13]:

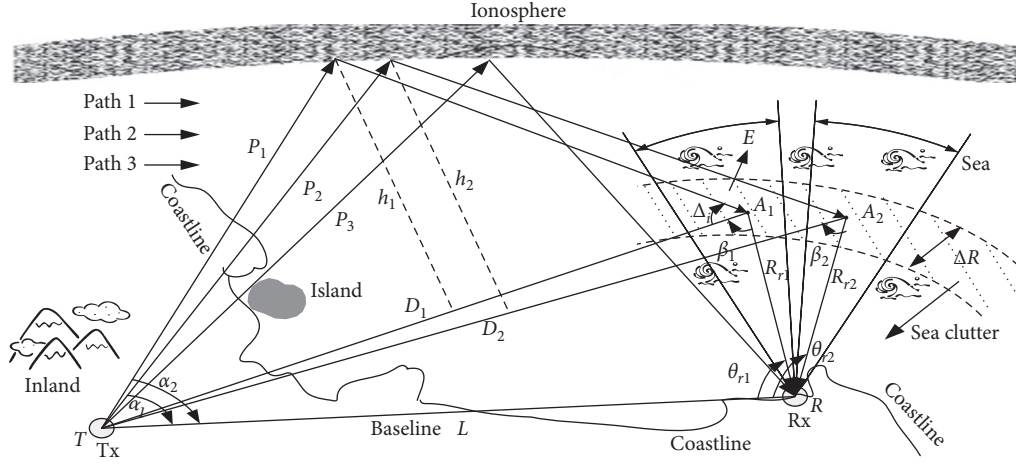


FIGURE 1: Geometry and layout diagram of HF sky-surface wave radar.

$$f_{\text{Bragg}} = \pm 0.102 \times 10^{-3} \sqrt{f_0 \cos\left(\frac{\beta_i}{2}\right) \frac{\cos \Delta_i + 1}{2}} + f_{\text{iono}}, \quad (1)$$

where  $f_{\text{iono}}$  is the Doppler shift caused by ionospheric disturbance,  $\beta_i$  is bistatic angle, and  $\Delta_i$  is the grazing angle.

Therefore, the maximum covering range of the first-order sea clutter Bragg frequency can be obtained by the following formula [6, 13]:

$$\left[ \begin{aligned} & -0.102 \times 10^{-3} \sqrt{f_0 \cdot \frac{\cos \Delta_{i \min} + 1}{2} \cdot \sqrt{\frac{1}{2} + \frac{R_{r_i} - L \cos \theta_{r_i \max}}{R_{r_i}^2 + L^2 - 2R_{r_i}L \cos \theta_{r_i \max}}} + f_{\text{iono}_{\min}}, \\ & -0.102 \times 10^{-3} \sqrt{f_0 \cdot \frac{\cos \Delta_{i \max} + 1}{2} \cdot \sqrt{\frac{1}{2} + \frac{R_{r_i} - L \cos \theta_{r_i \min}}{R_{r_i}^2 + L^2 - 2R_{r_i}L \cos \theta_{r_i \min}}} + f_{\text{iono}_{\max}} \end{aligned} \right] \quad (2)$$

$$\left[ \begin{aligned} & +0.102 \times 10^{-3} \sqrt{f_0 \cdot \frac{\cos \Delta_{i \max} + 1}{2} \cdot \sqrt{\frac{1}{2} + \frac{R_{r_i} - L \cos \theta_{r_i \min}}{R_{r_i}^2 + L^2 - 2R_{r_i}L \cos \theta_{r_i \min}}} + f_{\text{iono}_{\min}}, \\ & +0.102 \times 10^{-3} \sqrt{f_0 \cdot \frac{\cos \Delta_{i \min} + 1}{2} \cdot \sqrt{\frac{1}{2} + \frac{R_{r_i} - L \cos \theta_{r_i \max}}{R_{r_i}^2 + L^2 - 2R_{r_i}L \cos \theta_{r_i \max}}} + f_{\text{iono}_{\max}} \end{aligned} \right],$$

where  $f_{\text{iono}_{\max}}$  and  $f_{\text{iono}_{\min}}$  represent the maximum and minimum Doppler shift value caused by ionosphere. Thus, the Bragg frequency of first-order sea clutter is a function of frequency, azimuth, range, and ionospheric state.

**2.3. First-Order Sea Clutter Broadening Model.** For a sea clutter scattering cell at a certain range and beam direction in HF hybrid sky-surface wave radar, the broadening sea clutter model can be written as follows [6, 13], considering the combined actions of bistatic angle and ionosphere:

$$s(t) = \sum_{i=1}^K a_i(t) \cdot \left[ \exp(j2\pi f_{\text{Bragg}} t) + \exp(-j2\pi f_{\text{Bragg}} t) \right] \cdot \exp(j\phi_i(t)), \quad (3)$$

where  $a_i(t)$  is the amplitude of sea clutter signal, which meets Gaussian distribution;  $f_{\text{Bragg}}$  ( $i = 1, \dots, K$ ) is the  $K$  complex frequency component within the Bragg frequency band, and  $f_{\text{Bragg}_{\min}} \leq f_{\text{Bragg}} \leq f_{\text{Bragg}_{\max}}$ ; and  $\phi_i(t)$  is the ionospheric phase contamination function.

### 3. Ionosphere Decontamination Method Based on GPTF

**3.1. Basic Principle of GPTF.** Ionospheric disturbances have the characteristics of change rapidly over time. Compared with the nonparametric time-frequency analysis method, the parameterized time-frequency analysis method selects the appropriate kernel describing the nonstationary signal by introducing the model of the prior signal information. When the kernel form is consistent with the analyzed signal, the time-frequency resolution can be effectively improved. The typical methods have adaptive chirp wavelet decomposition, atomic decomposition, and polynomial Fourier transform, etc., but such methods mainly use polynomial kernels, which are not suitable for analyzing strong time-varying nonstationary signals that change faster with time.

The method of short-time Fourier transform (STFT) is to window the signal based on the Fourier transform. The default window signal is approximately stationary. It can simultaneously describe the signal in the time domain and the frequency domain, thus reflecting the variation of the signal spectrum over time. Since the fixed-length window function cannot capture the change of the signal frequency in time, the time-frequency representation of the STFT is poorly concentrated, and the time-frequency characteristics of the signals cannot be accurately described. The generalized parameterized time-frequency analysis method uses the frequency rotation operator to rotate the time-frequency characteristics of the nonstationary signal by introducing the frequency rotation and translation operator, so that the signal tends to be stable, and then, the STFT is used for the rotated signal, and finally, the frequency is utilized. The translation operator shifts the signal time-frequency characteristics to the true ridge position. Since the signal analyzed by STFT is an approximate stationary signal, the generalized parameterized time-frequency analysis can effectively improve the time-frequency resolution, and there is no cross-term interference.

Assuming that the instantaneous frequency of the signal is an arbitrary function  $f_m(t)$ , the complex signal form at this time is  $s_r(t) = e^{j2\pi \int f_m(t) dt}$ . The generalized parameterized time-frequency analysis of the signal can be expressed as follows [14]:

$$\left. \begin{aligned} \text{TF}(t_0, f; \mathbf{P}) &= \int_{-\infty}^{\infty} \bar{s}(\tau) g_{\sigma}^*(\tau - t_0) e^{-j2\pi f \tau} d\tau \\ \bar{s}(\tau) &= s_r(\tau) \cdot \Phi_{\mathbf{P}}^R(\tau) \cdot \Phi_{t_0, \mathbf{P}}^S(\tau) \\ \Phi_{\mathbf{P}}^R(\tau) &= e^{-j2\pi \int \kappa_{\mathbf{P}}(\tau) d\tau} \\ \Phi_{t_0, \mathbf{P}}^S(\tau) &= e^{j2\pi \tau \cdot \kappa_{\mathbf{P}}(t_0)} \end{aligned} \right\}, \quad (4)$$

wherein the instantaneous frequency of  $s_r(\tau)$  is an arbitrary function,  $\kappa_{\mathbf{P}}(\tau)$  is a transform kernel representing of the generalized parametric time-frequency analysis,  $\mathbf{P}$  is a transform kernel parameter,  $\Phi_{\mathbf{P}}^R(\tau)$  is a frequency rotation operator,  $\Phi_{t_0, \mathbf{P}}^S(\tau)$  is a frequency shift operator, and  $g_{\sigma}(\tau)$  is a window function of the time-frequency transform.

According to formula (4), the basic process of GPTF analysis can be described as follows. Firstly, the signal is rotated in the time-frequency plane, that is, the instantaneous frequency  $f_m(\tau)$  of the signal is subtracted from  $\kappa_{\mathbf{P}}(\tau)$ , and then, the signal is translated on the time-frequency plane by the frequency increment  $\kappa_{\mathbf{P}}(t_0)$ . Finally, the window function is used to make a STFT on the signal. When  $\kappa_{\mathbf{P}}(\tau) = f_m(\tau)$ , the signal forms after the signal  $s_r(\tau)$  is rotated and translated as shown in the following equation:

$$\begin{aligned} \bar{s}(\tau) &= s_r(\tau) \cdot \Phi_{\mathbf{P}}^R(\tau) \cdot \Phi_{t_0, \mathbf{P}}^S(\tau) \\ &= e^{j2\pi \int f_m(\tau) d\tau} \cdot e^{-j2\pi \int \kappa_{\mathbf{P}}(\tau) d\tau} \cdot e^{j2\pi \tau \cdot \kappa_{\mathbf{P}}(t_0)} \\ &= e^{j2\pi \tau \cdot \kappa_{\mathbf{P}}(t_0)}. \end{aligned} \quad (5)$$

At this time, the instantaneous frequency  $\kappa_{\mathbf{P}}(t_0)$  of the signal  $\bar{s}(\tau)$  does not change with time, and the signal  $\bar{s}(\tau)$  is a stationary signal. At this time, the STFT is performed on the signal  $\bar{s}(\tau)$ , and the time-frequency concentration is significantly improved compared to the nonstationary signal. It can be seen from (4) and (5) that the frequency rotation operator and the translation operator are determined by selecting appropriate transformation kernel parameters, and the nonstationary signal is rotated and translated to stabilize the signal for the purpose of improving the time-frequency resolution by the determined frequency rotation operator and the frequency translation operator. It can be seen that the time-frequency resolution of the GPTF analysis is closely related to the accuracy of the transform kernel parameters. From the above analysis, the key to GPTF analysis is to estimate the parameters of the transform kernel.

**3.2. Estimation Method for Transforming Kernel Parameters.** According to the introduction of the principle of GPTF in Section 3.1, the working mechanism is actually the STFT based on the frequency rotation operator and the translation operator. When the selected transform kernel matches the time-frequency characteristic of the analyzed signal, the rotated signal is close to the stationary signal, the time-frequency resolution is high after STFT. The description of the time-frequency characteristics of the stationary signal is accurate. It can be seen that the accuracy of the transform kernel parameter determines the performance of the GPTF method, which affects its performance in analyzing nonstationary signals. In [14], a method for estimating transform kernel parameters using the principle of time-frequency feature approximation is proposed. The time-frequency feature approximation principle indicates that the more accurate the transform kernel parameter estimation, the higher the time-frequency concentration. According to the time-frequency feature approximation principle, if the transform kernel parameter estimation is more accurate, the time-frequency concentration is higher. The principle of time-frequency approximation can be represented in Figure 2.

It can be seen from Figure 2 that the GPTF analysis method achieves the iterative optimization of the transform

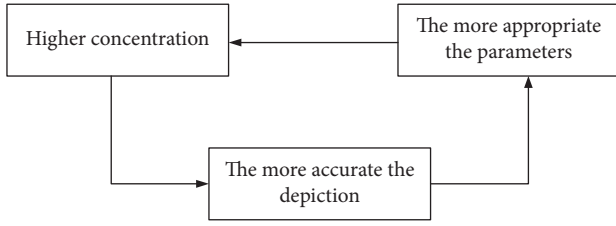


FIGURE 2: Time-frequency approximation principle.

kernel parameters by combining the precision of the transform kernel parameters with the time-frequency concentration. The above principle is based on the generalized parametric time-frequency analysis to cyclically approximate and solve the signal time-frequency characteristics, so as to obtain the most suitable transform kernel parameters. According to the principle of time-frequency approximation, the detailed steps of transforming the kernel parameter estimation are as follows:

Step 1: determining the transform kernel form according to the signal priori form.

Step 2: the number of iterations  $i = 0$ , initializing the transformation kernel parameters  $\mathbf{P}_0$ .

Step 4: performing parameterized time-frequency analysis  $\text{TF}(t_0, f; \mathbf{P}_i)$  on the signal according to equation (4).

Step 4: detecting the peak ridge line  $\tilde{f}_m^i(t)$  in the time-frequency diagram.

Step 5: according to the ridge line form, select a suitable fitting method, and fit the ridge line and estimate transformation kernel parameter  $\tilde{\mathbf{P}}_i$ .

Step 6: the number of iterations is increased by one, and the transformation kernel parameter is updated  $\mathbf{P}_i = \tilde{\mathbf{P}}_i$ .

Step 7: calculating a termination condition  $\Lambda = \int \tilde{f}_m^i(t) - \tilde{f}_m^{i-1}(t) dt / \int \tilde{f}_m^i(t) dt$ , where  $\tilde{f}_m^i(t)$  is the peak ridge of the  $i$ th iteration and  $\tilde{f}_m^{i-1}(t)$  is the peak ridge of the  $i-1$ th iteration, which needs to be noted that  $\tilde{f}_m^0(t) = 0$ .

Step 8: setting the termination condition parameter  $\zeta$ . The size of this value depends on the situation. If it is too large, the calculation amount is too large, and if it is too small, the accuracy of the extracted time-frequency line is not high.

Step 9: comparing the size of  $\Lambda$  and  $\zeta$ , when  $\zeta > \Lambda$ , return to step 3. When  $\zeta \leq \Lambda$ , perform step 10.

Step 10: outputting a transformation kernel parameter to obtain a time-frequency curve.

According to the above steps of transforming the kernel parameter estimation, the flowchart of the design is shown in Figure 3.

**3.3. Ionospheric Decontamination Based on GPTF.** Based on the above analysis process and steps, the derivation process of ionospheric decontamination based on GPTF is as follows:

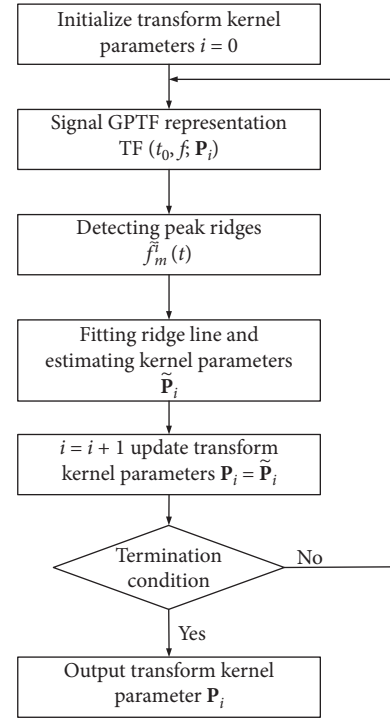


FIGURE 3: The flowchart of transform kernel parameter estimation.

Step 1: assume that the signal after the ionospheric contamination is expressed as follows [7–9]:

$$\text{sp} = \exp(jm2\pi \sin(2\pi f_0 t) \exp(j2\pi f_1 t)), \quad (6)$$

where  $m$  is the amplitude coefficient,  $f_0$  is the modulation frequency, and  $f_1$  is the fixed frequency.

Step 2: derive the signal and obtain the Doppler curve form, which can be expressed as follows:

$$f(t) = m2\pi f_0 \cos(2\pi f_0 t) + f_1. \quad (7)$$

Since the cosine Doppler curve of the signal has periodicity, the ridge line is fitted using the Fourier series for the curve. The Doppler instantaneous frequency form is known. Since the Doppler curve is known to be a cosine form by prior knowledge, the transform kernel of the applied harmonics is as follows:

$$f(t) = \sum_{m=1}^{\infty} b_m \cos(m2\pi f_c t) + b_0. \quad (8)$$

There is a certain relationship between the cosine series coefficient of the curve and its Fourier transform coefficient. Consider the Fourier transform to find the coefficients of the cosine series of each order. The discrete form of the Doppler curve parameter estimation method is derived as follows.

Radar sampling interval  $\Delta t = 1/\text{PRF}$ ; equation (8) discretization is expressed as follows:

$$f(n \cdot \Delta t) = f_d(n \cdot \Delta t) + b_0, \quad (9)$$

where  $f_d(n \cdot \Delta t) = \sum_{m=1}^{\infty} b_m \cos(m \cdot 2\pi f_c n \Delta t)$ .

After equation (9) is truncated by adding a rectangular window, the spectrum of each order cosine series becomes a sinc function form. In this case, in order to eliminate the influence of the sinc side lobes of the cosine series spectrum of each order on the spectrum of other order cosine series, the rectangular window length is set to  $TT = (1/f_c), (2/f_c), (3/f_c)$ . In this way, the peak of the cosine series spectrum of other orders will be located at the zero point of the side lobe of the spectrum of each order cosine series, so as to eliminate the interference between the spectra. Therefore, in the latter experiment, the accumulation time is required to be an integer multiple of the period. When the accumulation time is not an integer multiple, the signal can be truncated, so this method requires at least one periodic signal. Without loss of generality, set  $TT = i/f_c$ , at this time  $N = i/f_c \Delta t$ . Similarly, the Fourier transform of the  $N$  point in the harmonic form  $f_d(n \cdot \Delta t)$  in (9) is obtained as follows:

$$\begin{aligned} F_d(k) &= \sum_{n=0}^{N-1} f_d(n\Delta t) e^{-j(2\pi/N)kn} \\ &= \sum_{n=0}^{N-1} \left[ \sum_{m=1}^{\infty} b_m \cos\left(m \frac{2\pi i}{N} n\right) \right] e^{-j(2\pi/N)kn} \\ &= \sum_{m=1}^{\infty} b_m \left[ \sum_{n=0}^{N-1} \cos\left(\frac{2\pi i}{N} n \cdot mi\right) \cos\left(\frac{2\pi}{N} n \cdot k\right) \right] \\ &\quad - j \sum_{m=1}^{\infty} b_m \left[ \sum_{n=0}^{N-1} \cos\left(\frac{2\pi}{N} n \cdot mi\right) \sin\left(\frac{2\pi}{N} n \cdot k\right) \right]. \end{aligned} \quad (10)$$

According to the characteristics of the orthogonal trigonometric function set, formula (10) can be reduced to

$$F_d(k) = \begin{cases} b_m \frac{N}{2}, & k = mi, \\ 0, & \text{else.} \end{cases} \quad (11)$$

The transformation kernel parameter can be obtained as follows:

$$\begin{aligned} b_m &= \frac{2}{N} (\text{real}(F_d(k)))_{k=mi}, \\ b_0 &= \frac{\lambda}{2} \frac{2\text{real}(F_d(1))}{N\Delta t}. \end{aligned} \quad (12)$$

#### 4. Bistatic Sea Clutter Suppression Method Based on FBLP Algorithm

If the dominant factor of sea clutter broadening is the bistatic angle, or the sea clutter disturbed by the ionospheric phase path has been dedisturbed, then the suppression of bistatic

sea clutter is required. At present, there are few studies on the problem of HF radar bistatic sea clutter suppression. The bistatic sea clutter shows different characteristics from monostatic sea clutter, and it makes the traditional Bragg line theoretical prediction or monostatic sea clutter characteristic suppression methods fail. At present, there are two main ideas for the bistatic sea clutter suppression method [15–17]: one is the sea clutter method based on singular value decomposition (SVD) [15], and the other is based on the sinusoidal signal parameter estimation method, such as the root cancellation method and the CLEAN method. The root cancellation method and the CLEAN algorithm are simple to implement, but the number of iterations is difficult to determine accurately. The SVD algorithm can suppress sea clutter better, but the amount of computation is large. When the target is located near the first-order Bragg peak, the three algorithms may lose part of the target information.

Based on this, this paper uses the FBLP algorithm to suppress the sea clutter. The FBLP algorithm of this paper was previously a conference paper by authors, which was published in [12]. This algorithm uses the first-order sea clutter Bragg band distribution feature as a priori knowledge and combines the multidimensional characteristics of the measured sea clutter data. The method can effectively and accurately identify the first-order sea clutter and can better suppress the sea clutter while retaining the target. And the calculation amount is small. Firstly, the bistatic first-order sea clutter signal model is introduced. Secondly, the theoretical Bragg band range is determined in advance on the first-order sea clutter distance-Doppler spectrum. Then the FBLP algorithm is used to establish the forward and backward prediction matrix to estimate the sea clutter signal parameters. Then, based on the multidimensional characteristics of the measured sea clutter, the first-order sea clutter signal is better identified and extracted by the signal-to-noise ratio threshold method and the symmetry detection matrix. Finally, the amplitude of each sea clutter frequency component is zeroed to achieve the purpose of suppressing sea clutter.

*4.1. Multidimensional Feature Analysis of Sea Clutter Spectrum.* When the CLEAN or root cancellation algorithms are used to suppress sea clutter for traditional SVD, it is necessary to detect sea clutter firstly in order to suppress sea clutter. However, due to the influence of wind direction or ocean current in the actual marine environment, the characteristics of the sea clutter spectrum are complex, which makes the identification and extraction of the first-order sea clutter difficult, resulting in insufficient sea clutter suppression and the formation of false targets and tracks.

Figure 4(a) shows the range-Doppler spectrum of the first-order sea clutter measured by high-frequency hybrid sky-surface wave radar. From the measured graphs, we can also see that the first-order sea clutter exhibits multidimensional characteristics. It can be seen from Figure 4(a) that the first-order sea clutter spectrum of the close-range gate shows good continuity and symmetry in both the range and the Doppler dimension. Figure 4(a) shows the sea clutter spectrum

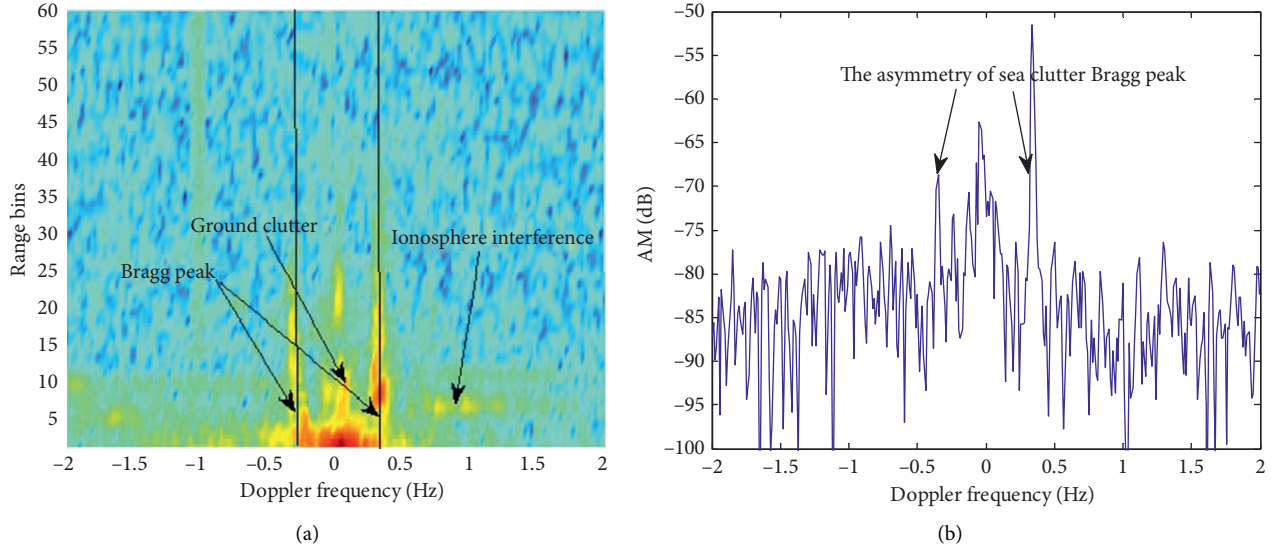


FIGURE 4: The range-Doppler spectrum and asymmetry of the measured sea clutter in HF sky-surface wave radar. (a) Range-Doppler spectrum of actual sea clutter. (b) The asymmetry of actual sea clutter spectrum.

of continuous distance gates. Due to the influence of wind direction, the amplitude of the first-order sea clutter positive and negative Bragg peaks shows asymmetry in Figure 4(b).

**4.2. Parameter Estimation of Sea Clutter Signal Based on Linear Prediction Model.** For a bistatic HF radar with the hybrid operating mode of sky-wave transmitting and ground-wave receiving, it is assumed that there are  $K$  complex sinusoidal components in the Bragg band in the scattering unit. Therefore, the bistatic first-order sea clutter model after ionospheric phase path disturbance suppression can also be written as follows [6, 12]:

$$y(n) = \sum_{i=1}^K a_i e^{j2\pi f_{B_i}(n-1)T_s + j\varphi_i}, \quad n = 1, 2, \dots, N, \quad (13)$$

where  $a_i$ ,  $f_{B_i}$ , and  $\varphi_i$  are, respectively, the amplitude of each signal component, first-order sea clutter Bragg frequency, and phase.  $T_s$  is the signal sampling period, and  $N$  is the signal sequence length. Here,  $f_{B_{\min}} \leq f_{B_i} \leq f_{B_{\max}}$ ,  $[f_{B_{\min}}, f_{B_{\max}}]$  is the boundary of the frequency band caused by the bistatic angle in the scattering unit.

The parameters of each sea clutter signal are estimated below based on a linear prediction method. When the signal-to-noise ratio (SNR) is sufficiently high, the sea clutter signal can be written as the sum of the first  $L$  weights:

$$y(n) = - \sum_{i=1}^L y(n-i) \cdot \alpha_i, \quad (14)$$

where  $\alpha_i$  stands for the weight coefficients.

Besides, so as to track the time-varying behavior of the sea clutter, the coefficients of the prediction error filter must be estimated over short data segments so that the filter coefficients could be updated adaptively. And the prediction equation matrix, which is defined in [18], could be expressed as follows:

$$\begin{bmatrix} y(L) & y(L-1) & \dots & y(1) \\ y(L+1) & y(L) & \dots & y(2) \\ \vdots & \vdots & \ddots & \vdots \\ y(N-1) & y(N-2) & \dots & y(N-1) \\ y^*(2) & y^*(3) & \dots & y^*(L+1) \\ y^*(3) & y^*(4) & \dots & y^*(L+2) \\ \vdots & \vdots & \ddots & \vdots \\ y^*(N-L) & y^*(N-L+1) & \dots & y^*(N) \end{bmatrix} \begin{bmatrix} \alpha_1 \\ \alpha_2 \\ \vdots \\ \alpha_L \end{bmatrix} = - \begin{bmatrix} y(L+1) \\ y(L+2) \\ \vdots \\ y(N) \\ y^*(1) \\ y^*(2) \\ \vdots \\ y^*(N-1) \end{bmatrix}. \quad (15)$$

Simply, we denote as

$$\mathbf{A} \cdot \boldsymbol{\alpha} = -\mathbf{y}. \quad (16)$$

And the weight coefficient matrix  $\boldsymbol{\alpha}$  could be estimated by the following equation:

$$\boldsymbol{\alpha} = -\mathbf{A}^{-1}\mathbf{y}. \quad (17)$$

As the linear equations above are overdetermined, the total least square method is used to solve this problem [18], namely:

$$\boldsymbol{\alpha} = -\mathbf{A}^{-1}\mathbf{y} = -(\mathbf{A}^H \mathbf{A})^{-1} \mathbf{A}^H \mathbf{y}, \quad (18)$$

where  $H$  indicates the conjugate transpose. Simultaneously, the order of prediction error filter polynomial  $L$  could be determined in [18], which satisfies the inequality as follows:

$$M \leq L \leq \left(N - \frac{M}{2}\right). \quad (19)$$

That is to say, the order of prediction error filter should exceed the estimated signal number. Afterwards, we define frequency estimation matrix as follows:

$$\mathbf{f} = [f_1, f_2, \dots, f_M], \quad (20)$$

where

$$f_k = (1, e^{-s_k}, e^{-2s_k}, \dots, e^{-Ls_k}), \quad k = 1, 2, \dots, M. \quad (21)$$

It is easy to observe that each row in  $\mathbf{A}$  is a linear combination of  $L$  linearly independent vectors in  $f_k$ . That is to say, the rank of  $\mathbf{A}$  is  $M$  as long as  $\mathbf{A}$  has at least  $M$  rows. Thus, the dimension of null space in  $\mathbf{A}$  is  $L + 1 - M$  dimension. In addition, as  $\alpha_k$  lies in the null space of  $\mathbf{A}$ , we have

$$\alpha_0 + \alpha_1 e^{-s_k} + \alpha_2 e^{-2s_k} + \dots + \alpha_L e^{-Ls_k} = 0. \quad (22)$$

The signal frequency could be estimated from the roots of (22). Besides, in order to obtain the amplitude and initial phase of each signal, we define the following matrix equation as follows:

$$\begin{bmatrix} \beta_1^0 & \beta_2^0 & \dots & \beta_M^0 \\ \beta_1^1 & \beta_2^1 & \dots & \beta_M^1 \\ \vdots & \vdots & \vdots & \vdots \\ \beta_1^{N-1} & \beta_2^{N-1} & \dots & \beta_M^{N-1} \end{bmatrix} \begin{bmatrix} h_1 \\ h_2 \\ h_3 \\ h_4 \end{bmatrix} = \begin{bmatrix} y(1) \\ y(2) \\ \vdots \\ y(N) \end{bmatrix}. \quad (23)$$

Simply, we denote as

$$\mathbf{R} \cdot \mathbf{h} = \mathbf{Y}, \quad (24)$$

where  $\beta_i^k = e^{j2\pi f_i k / f_s}$ ,  $\mathbf{h} = (\mathbf{R}^H \mathbf{R})^{-1} \mathbf{R}^H \mathbf{Y}$ , in which  $f_s$  represents the sampling frequency and  $N$  is the sampling number. In addition, the amplitude and initial phase could be obtained after taking the manipulation of the absolute and angular value of  $h$ , respectively:

$$\begin{aligned} a_k &= |h_k|, \quad k = 1, \dots, M, \\ \varphi_k &= \arctan\left(\frac{\text{Im}(h_k)}{\text{Re}(h_k)}\right) \quad k = 1, \dots, M, \end{aligned} \quad (25)$$

where  $\text{Im}(\cdot)$  and  $\text{Re}(\cdot)$  represent taking the imaginary and real parts of the signal, respectively.

**4.3. First-Order Sea Clutter Suppression.** Through the previous analysis, in order to better achieve the purpose of suppressing sea clutter based on the FBLP algorithm, we use the first-order sea clutter obtained in the theoretical Bragg band of the range-Doppler spectrum, combined with the multidimensional features of the measured first-order sea clutter to better identify and suppress sea clutter. First, the range of the sea clutter Bragg band is determined in advance

on the range-Doppler spectrum, and then, the FBLP algorithm is used to extract and estimate the parameters of the sea clutter signal. Based on the previous processing, we use the SNR threshold method defined below to determine the number of first-order sea clutter signals of interest. Specially, we suppose  $S$  as the number of signals, and the total power of sea clutter echo could be obtained by the following equation:

$$P = \sum_{n=1}^N |y_n|^2, \quad (26)$$

where  $N$  is the number of signal sampling points. Then the power of each signal and noise is given by

$$\begin{aligned} P_k &= \frac{1}{N} \sum_{n=1}^N |a_k \beta_k^{n-1}|^2 = |a_k|^2 \frac{1 - |\beta_k|^{2N}}{N(1 - |\beta_k|^2)} \quad k = 1, 2, \dots, S, \\ P_{\text{noise}} &= \frac{1}{N} \sum_{n=1}^N \left| y_n - \sum_{k=1}^S a_k \beta_k^{n-1} \right|^2. \end{aligned} \quad (27)$$

The SNR of each signal is given by

$$\text{SNR}_k = \frac{P_k}{P_{\text{noise}}}, \quad k = 1, 2, \dots, S. \quad (28)$$

According to the local dominant characteristics of sea clutter, the SNR of each signal component can be compared with the threshold to screen out the suspected sea clutter signal. Then, according to the frequency domain symmetry property of the sea clutter, combined with the frequency estimation matrix  $f$ , each estimated frequency is pre-processed as follows:

$$f'_i = \begin{cases} f_i + f_B, & f_i < 0, \\ f_i - f_B, & f_i > 0, \end{cases} \quad (29)$$

where  $f_B$  is the theoretical Bragg scattering frequency,  $\lambda$  indicates the wave length, and  $g$  is the acceleration of gravity. Afterwards, we define the feature detection matrix (FDM) as follows [12]:

$$\mathbf{F} = \begin{bmatrix} f(1,2) & f(1,3) & f(1,4) & \dots & f(1,M) \\ 0 & f(2,3) & f(2,4) & \dots & f(2,M) \\ 0 & 0 & f(3,4) & \dots & f(3,M) \\ 0 & 0 & 0 & \dots & f(M-1,M) \end{bmatrix}, \quad (30)$$

where  $f(i, j) = |f'_i - f'_j|$ ,  $i = 1, \dots, S-1$ ;  $j = i+1, \dots, S$ .

The processing diagram of bistatic sea clutter suppression based on FBLP algorithm is shown in Figure 5. By performing a two-dimensional search on the triangular matrix  $\mathbf{F}$  and finding the minimum value, the frequency component  $(f_x, f_y)$  satisfying the symmetry is obtained, that is, the component is the Bragg frequency corresponding to the first-order sea clutter. Finally, the corresponding amplitude in the amplitude matrix  $\mathbf{A}$  corresponding to the component is zeroed  $A_x = 0$  and  $A_y = 0$ . This completes the cancellation of the first-order sea clutter. In addition, considering the asymmetry of the first-order sea clutter

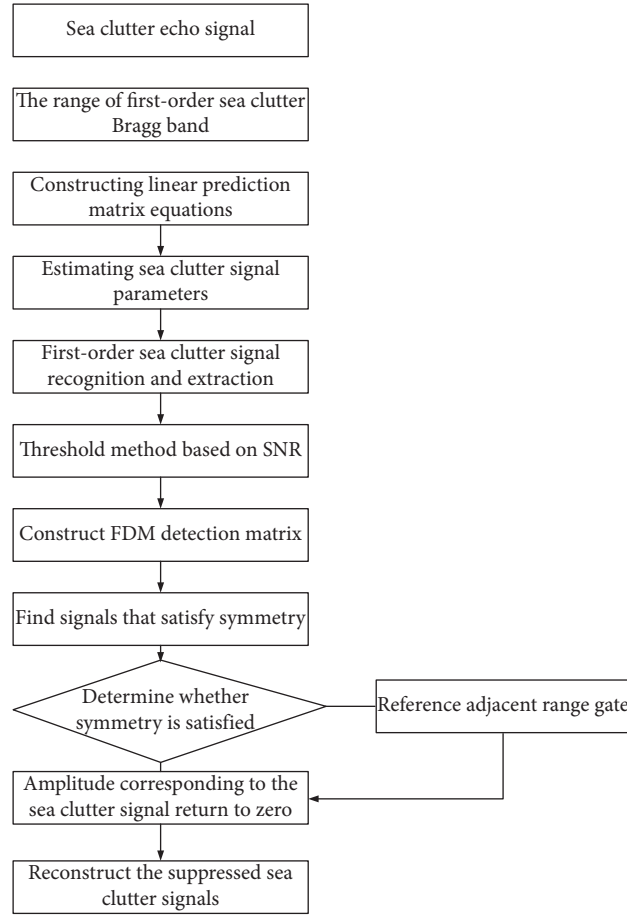


FIGURE 5: The processing diagram of bistatic sea clutter suppression based on the FBLP algorithm.

positive and negative peaks caused by the wind direction, since the sea clutter maintains good continuity in the range dimension, it can be adopted as a reference by using adjacent distance gates. The above FDM detection step is then corrected.

## 5. Cascaded Decontamination and Suppression Algorithm Performance Analysis

**5.1. Simulation Data Analysis.** Simulation parameter setting is as follows: the signal type is a linear frequency modulated (LFM) signal, pulse repetition period is  $PRT = 40$  ms, pulse accumulation time is  $T = 40$  s, operating frequency is  $f_0 = 13$  MHz, sea clutter Bragg frequency is  $f_B = 0.3750$  Hz, signal-to-noise ratio (SNR) is  $SNR = 10$  dB, and ionosphere contamination function is  $sp(t) = 0.5 * 2 * \pi * \sin(2 * \pi * 0.1 * t)$ . Figure 6(a) shows the contaminated sea clutter and decontaminated sea clutter spectrum by  $S^2$ -method, STFT, and GPTF, Figure 6(b) shows the estimated phase contamination by  $S^2$ -method, STFT, and GPTF, Figure 6(c) shows decontaminated sea clutter spectrum by GPTF, Figure 6(d) shows the broadening sea clutter suppression based on the FBLP algorithm.

Figure 6 shows the simulation results of sea clutter suppression with ionospheric phase disturbance based on GPTF and FBLP and the target Doppler frequency

$f_{\text{target}} = 0.75$  Hz. It can be seen from Figure 6 that the sea clutter can still be effectively suppressed by GPTF and FBLP and the target can be clearly seen. As can be seen from the above results, the approach based on GPTF can be used for correcting ionospheric contamination with large amplitude. And compared to the traditional time-frequency analysis methods, this method has high time-frequency resolution and no cross-term interference.

**5.2. Experimental Data Analysis.** The performance of ionosphere decontamination based on GPTF is verified by the measured data of HF sky-wave radar. The measured data have been processed by the traditional range-Doppler-azimuth processing. The echo accumulation time is 40 ms. The results of ionospheric decontamination based on GPTF at range gate = 60 and azimuth angle  $DBF = 3^\circ$  and at range gate = 100 and azimuth angle  $DBF = 5^\circ$  are shown in Figures 7(a)-7(b). The green curve in the figure represents the contaminated echo spectrum. The red curve in the figure represents the decontaminated echo spectrum after the GPTF. The black curve in the figure represents the decontaminated echo spectrum after the  $S^2$ -method. It can be seen from the above processing results that the GPTF method has better ionospheric decontamination performance than the  $S^2$ -method.



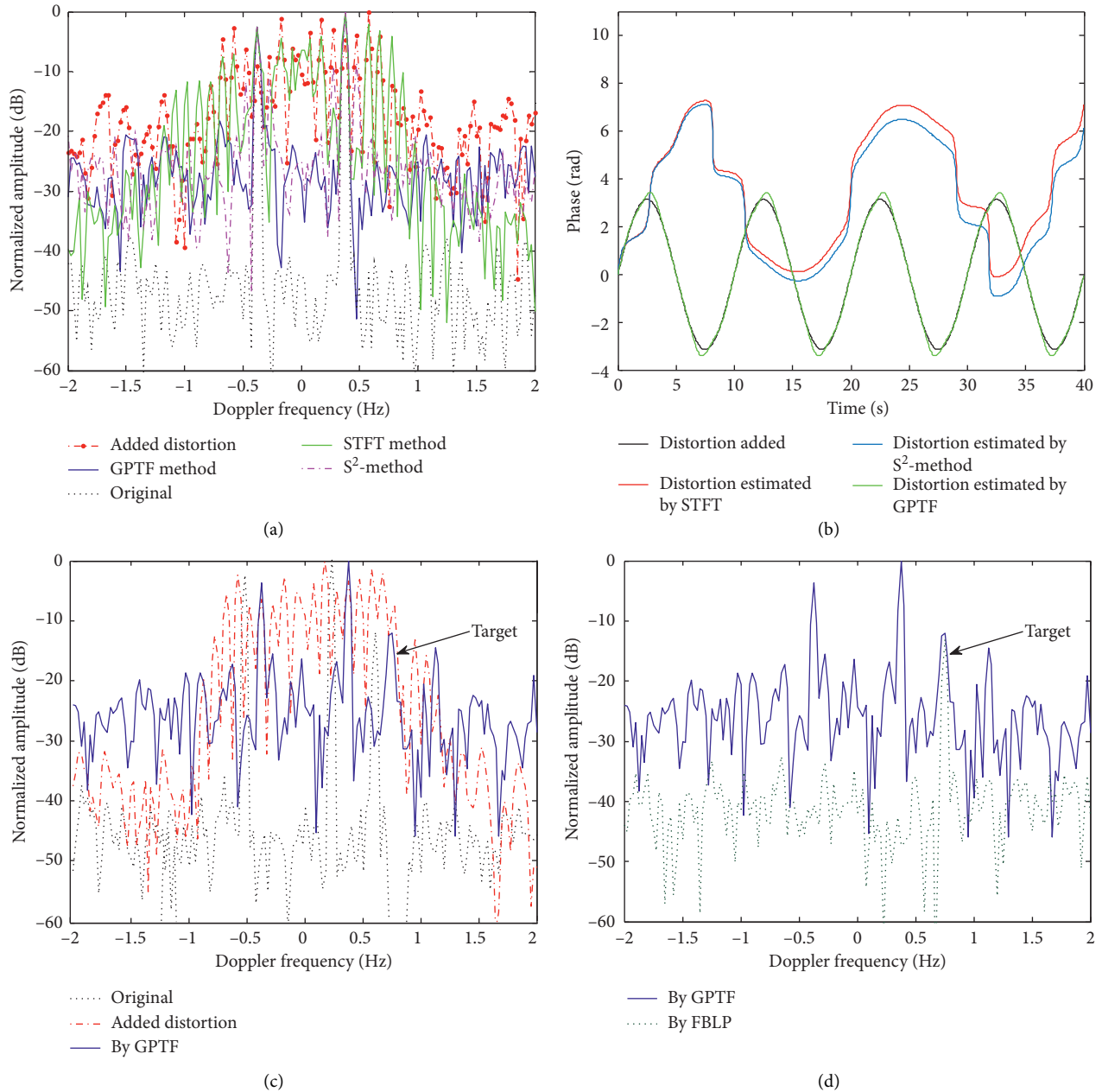


FIGURE 6: Sea clutter suppression with ionospheric phase disturbance based on GPTF and FBLP. (a) Contaminated sea clutter and decontaminated sea clutter spectrum by  $S^2$ -method, STFT, and GPTF. (b) Estimated phase contamination by PGA, STFT, and GPTF. (c) Decontaminated sea clutter spectrum by GPTF. (d) The broadening sea clutter suppression based on the FBLP algorithm.

In order to justify the effectiveness of the cascade suppression processing method based on GPTF and FBLP proposed in this paper, the following uses the measured data of HF sky-surface wave radar to verify. The measured data were acquired using the newly developed “high-frequency sky-surface wave radar experimental platform.” The measured data have been processed by the traditional range-Doppler-azimuth processing. The echo accumulation time is 50 s. The suppressed sea clutter spectrum by GPTF and FBLP algorithm at range gate = 35 and azimuth angle  $DBF = 10^\circ$  is shown in Figures 8(a)-8(b) among them, the added target Doppler velocity  $f_{\text{target}} = -0.6$  Hz.

As shown in Figures 8(a)-8(b), the contaminated sea clutter can be effectively suppressed by GPTF and the broadening sea clutter is obviously sharpened, as indicated by the red line. On this basis, the FBLP algorithm can effectively suppress the sea clutter, as indicated by the green line. From Figures 8(a)-8(b), we can see that the target can be effectively detected and SCR increased. This method can steadily and effectively sharpen severe sea clutter spectrum contaminated by ionospheric phase perturbation with large amplitude. Finally, it should be pointed out that we use different measured data to make many tests for the cascaded suppression method. And we found that, in most cases, this

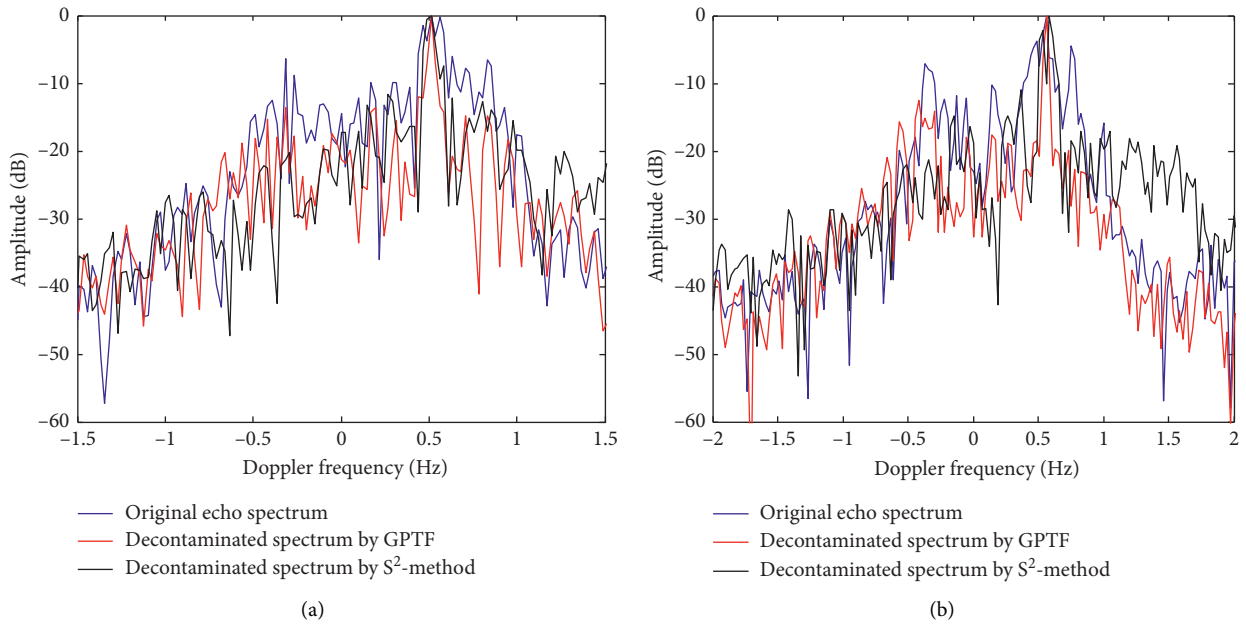


FIGURE 7: Decontamination results based on the GPTF method using the HF sky-wave radar. Decontamination result by the GPTF method (a) at range gate = 60 and azimuth angle DBF = 3° and (b) at range gate = 100 and azimuth angle DBF = 5°.

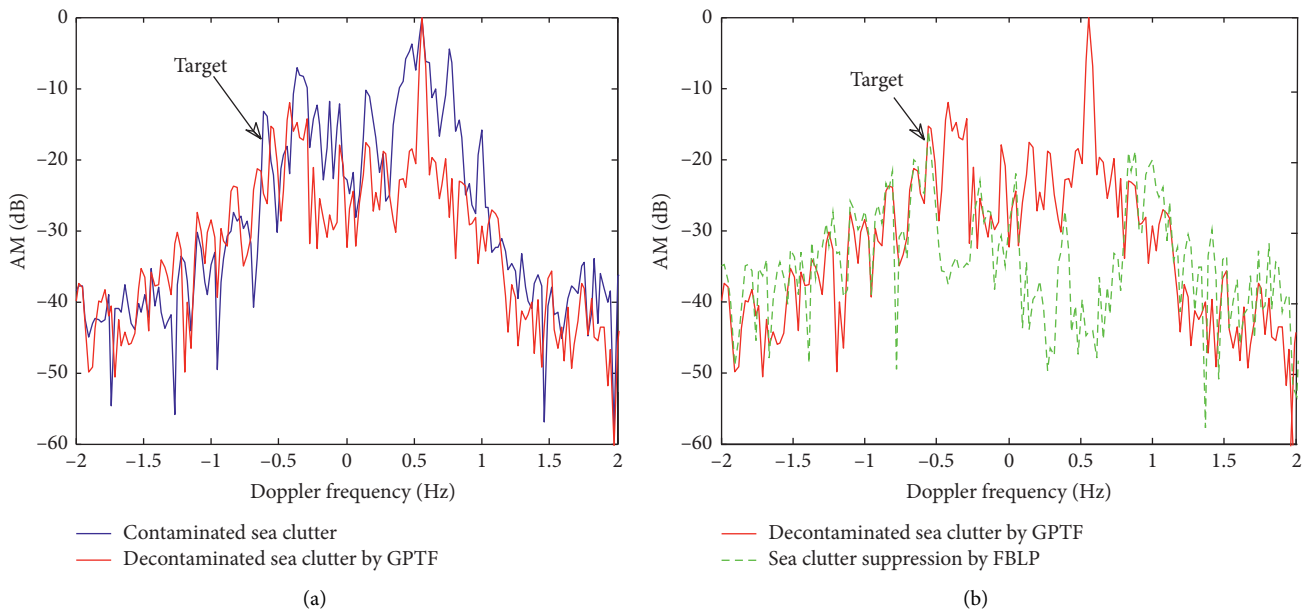


FIGURE 8: The broadening sea clutter suppression based on GPTF and FBLP algorithm. (a) Decontamination result by GPTF method. (b) Sea clutter suppression by FBLP.

method can lead to good decontamination and suppression effect, which sufficiently shows its robustness.

## 6. Conclusions

Ship detection is an important mission of the HF hybrid sky-surface wave radar. The sea clutter spectrum is influenced by composite factors such as the bistatic angle and ionospheric phase disturbance. Thus, an ionospheric decontamination and sea clutter suppression method for HF hybrid sky-

surface wave radars based on GPTF analysis is proposed. In this method, the time-frequency analysis method based on GPTF is proposed to correct the ionospheric phase contamination with large amplitude. Compared with the traditional nonparametric time-frequency analysis method, the phase contamination function extracted by this GPTF method has higher accuracy. At this time, the FBLP algorithm is used to suppress the sharpened sea clutter spectrum. Finally, the proposed method is examined by measured data. Experimental results indicate that the proposed method can

well suppress the broadening sea clutter for HF hybrid sky-surface wave radar. Although some positive results have been obtained, it must be pointed that there is still a need for more studies and improvements.

### Data Availability

The data used to support the findings of this study are available from the corresponding author upon request.

### Conflicts of Interest

The authors declare that they have no conflicts of interest.

### Acknowledgments

The authors would like to express their sincere thanks to the National Natural Science Foundation Project (grant no. 61701309), the Shanghai Natural Science Fund (grant nos. 17ZR1428800 and 20ZR1455000), the Shanghai Sailing Program (grant no. 17YF1418500) and members of the Shanghai Radio Equipment Research Institute for technical support.

### References

- [1] P. A. Melyanovski and I. S. Tourgenev, "Bistatic HF radar for oceanography applications with the use of both ground and space waves," *Telecommunications and Radio Engineering*, vol. 51, no. 2-3, pp. 73-79, 1997.
- [2] R. L. Galeazzi, L. B. Sheiner, T. Lockwood, and L. Z. Benet, "The renal elimination of procainamide," *Clinical Pharmacology and Therapeutics*, vol. 19, no. 1, pp. 55-62, 1976.
- [3] R. J. Riddolls, *Ship Detection Performance of a High Frequency Hybrid Sky-Surface Wave Radar*, Defense R&D, Ottawa, Canada, 2007.
- [4] R. J. Riddolls, "Limits on the detection of low-Doppler targets by a high frequency hybrid sky-surface wave radar system," in *Proceedings of the IEEE Radar Conference*, pp. 1-4, Rome, Italy, May 2008.
- [5] Z. Zhao, X. Wan, D. Zhang, and F. Cheng, "An experimental study of HF passive bistatic radar via hybrid sky-surface wave mode," *IEEE Transactions on Antennas and Propagation*, vol. 61, no. 1, pp. 415-424, 2013.
- [6] Y. J. Li, Y. S. Wei, and R. Q. Xu, "Simulation analysis and experimentation study on sea clutter spectrum for high-frequency hybrid sky-surface wave propagation mode," *IET Radar, Sonar and Navigation*, vol. 8, no. 8, pp. 917-930, 2014.
- [7] X. Li, W. B. Deng, and P. N. Jiao, "An improved PGA algorithm for ionosphere phase perturbation correction," in *Proceedings of the 9th International Symposium on Antennas, Propagation and EM Theory*, pp. 1-6, Guangzhou, China, November 2010.
- [8] A. Bourdillon, F. Gauthier, and J. Parent, "Use of maximum entropy spectral analysis to improve ship detection by over-the-horizon radar," *Radio Science*, vol. 22, no. 2, pp. 313-320, 1987.
- [9] J. Parent and A. Bourdillon, "A method to correct HF skywave backscattered signals for ionospheric frequency modulation," *IEEE Transactions on Antennas and Propagation*, vol. 36, no. 1, pp. 127-135, 1988.
- [10] P. E. Howland and D. C. Cooper, "Use of the Wigner-Ville distribution to compensate for ionospheric layer movement in high-frequency sky-wave radar systems," *IEEE Proceedings F Radar and Signal Processing*, vol. 140, no. 1, pp. 29-36, 1993.
- [11] Y. J. Li, Y. S. Wei, and Y. P. Zhu, "Cascaded method for ionospheric decontamination and sea clutter suppression for high-frequency hybrid sky-surface wave radar," *IET Signal Processing*, vol. 9, no. 7, pp. 562-571, 2015.
- [12] Y. P. Zhu, C. Shang, and Y. J. Li, "A FBLP based method for suppressing sea clutter in HF/SWR," in *Proceedings of the International Symposium on antennas & propagation (ISAP)*, vol. 2, pp. 1090-1093, Osaka, Japan, January 2013.
- [13] Y. J. Li, Y. S. Wei, Y. P. Zhu, and R. Q. Xu, "Analysis and simulation for broadening first-order sea clutter spectrum in high frequency hybrid sky-surface wave propagation mode," *IET Radar Sonar and Navigation*, vol. 9, no. 6, pp. 609-621, 2014.
- [14] Y. Yang, Z. K. Peng, X. J. Dong, W. M. Zhang, and G. Meng, "General parameterized time-frequency transform," *IEEE Transactions on Signal Processing*, vol. 62, no. 11, pp. 2751-2764, 2014.
- [15] M. W. Y. Poon, R. H. Khan, and S. Le-Ngoc, "A singular value decomposition (SVD) based method for suppressing ocean clutter in high frequency radar," *IEEE Transactions on Signal Processing*, vol. 41, no. 3, pp. 1421-1425, 1993.
- [16] B. T. Root, "HF radar ship detection through clutter cancellation," in *Proceedings of the IEEE Radar Conference*, pp. 281-286, Dallas, TX, USA, May 1998.
- [17] Z. Bao, G. Wang, and L. Luo, "Inverse synthetic aperture radar imaging of maneuvering targets," *Optical Engineering*, vol. 37, no. 5, pp. 1582-1588, 1998.
- [18] R. Kumaresan, "On the zeros of the linear prediction-error filter for deterministic signals," *IEEE Transactions on Acoustics, Speech, and Signal Processing*, vol. 31, no. 1, pp. 217-220, 1983.

## Research Article

# Two-Dimensional Beampattern Synthesis for Polarized Smart Antenna Array and Its Sparse Array Optimization

Zhikun Chen , Tao Li, Dongliang Peng, and Kang Du

*School of Automation, Hangzhou Dianzi University, Xiasha Higher Education Zone, 2nd Street, Hangzhou 310018, China*

Correspondence should be addressed to Zhikun Chen; [czk@hdu.edu.cn](mailto:czk@hdu.edu.cn)

Received 21 March 2020; Accepted 25 May 2020; Published 13 June 2020

Guest Editor: Lei Yu

Copyright © 2020 Zhikun Chen et al. This is an open access article distributed under the Creative Commons Attribution License, which permits unrestricted use, distribution, and reproduction in any medium, provided the original work is properly cited.

Polarized smart antenna array has attracted considerable interest due to its capacity of matched reception or interference suppression for active sensing systems. Existing literature does not take full advantage of the combination of polarization isolation and smart antennas and only focuses on uniform linear array (ULA). In this paper, an innovative synthesis two-dimensional beampattern method with a null that has cross-polarization for polarized planar arrays is proposed in the first stage. This method aims to further enhance the capability of interference suppression whose optimization problem can be solved by second-order conic programming. In the second stage, a new sparse array-optimized method for the polarized antenna array is proposed to reduce the high cost caused by the planar array that is composed of polarized dipole antennas. Numerical examples are provided to demonstrate the advantages of the proposed approach over state-of-the-art methods.

## 1. Introduction

Smart antennas increase the capacity of communication systems by improving signal-to-noise ratio (SNR) in mobile communications [1, 2]. Adaptive array coherently combines multipath components of the desired signal and null interfering signals from different directions of arrival from the desired signal. In terms of the capability to match reception and suppress interference, the adaptive array is also applied in modern radar systems [3, 4]. However, this kind of conventional space-time adaptive technology has its own limitations, especially in intentional interference. Thus, polarization diversity is a potential solution [5–8]. Polarization diversity not only reflects complete information on electromagnetic waves of targets but also is an additional degree of freedom that can be exploited in response to dynamic environments. Polarization diversity can maximize the received SNR when matching the target polarization and can isolate the interfering signal from the desired signal when cross-polarizing the interfering signal. Considering this advantage, two synthesizing methods are introduced to design an electromagnetic beam with desired power and polarization [5, 9]. According to the literature [5, 9], dipole

antennas are suitable for generating arbitrary polarization with a pair of orthogonal far-field electric vectors. Polarized arrays can transmit a beampattern that can be selected freely to design a desired null and polarization around areas of interest. An effective approach to suppress strong interference is based on the principle of polarization mismatch factor; that is, the polarization in the specific region that corresponds to the direction of strong interference is crossed to that of strong interference to isolate the interference signal energy at the receiver as much as possible. Thus, the beamforming for polarized antenna array has become a popular research topic in recent years [10, 11]. However, most existing literature studies on polarized beamforming are only based on a simple uniform linear array (ULA) due to the high-dimensional weight matrix. A Fábry-Perot cavity antenna with a reconfigurable partially reflecting surface is proposed to produce dual-polarized 2D beams [12]. Realizing the compatibility of this kind of antenna with space-time adaptive processing technology based on ULA is difficult, additionally, for the planar array composed of polarized dipole antennas. A planar array generally comprises dozens or even hundreds of dipole antenna elements at the cost of high-precision hardware for its

implementation [13]. Thus, sparse array design is essential for satisfying the function of using a finite number of elements to realize the polarization vector beam.

Unlike the conventional phase arrays, the sparse array design for polarized smart array must be a constrained optimization problem [14–18]. One particular constraint is polarization matching, which is an inequality constraint. This constraint means that the optimization problem cannot be solved by the single-objective optimization algorithm. Transforming constraint optimization into multiobjective optimization or adding a penalty function in the fitness function is necessary to solve such a constrained optimization problem [19]. Scholars proposed multiobjective algorithms based on a new evolutionary pattern in recent decades. According to [20], the optimization problem with inequality constraint can be transformed into a multi-objective optimization problem. This problem can be solved using the multiobjective differential evolution (MODE) algorithm. In this work, the multiobjective design of a sparse antenna array for polarized smart antennas is addressed following the MODE algorithm.

The rest of this paper is organized as follows. The signal model for the polarized antenna is introduced in Section 2. Second-order cone programming (SOCP) is presented in Section 3 to solve the optimization problem of the 2D polarized beampattern design. Multiobjective differential evolution is applied to solve the multiobjective optimization problem in Section 4. Numerical simulations are presented in Section 5, and the conclusions are presented in Section 6.

## 2. Signal Model

**2.1. Representation of Polarization State.** The polarization state of the far-field electric field can be characterized by its polarization ellipse. The polarization ellipse is the most frequently used representation of polarization states. The polarization angle can be defined as the angle between the major axis of the ellipse and a reference vector to orient the ellipse in space. In the ellipse, the polarization state can be defined by its polarization axial ratio and angle. The electric field produces an ellipse over one period when plotted on a 2D plane normal to the propagation direction. The polarization axial ratio is the ratio of the major to minor axes of the ellipse. This ratio also determines the circularity (low axial ratio) and linearity (high axial ratio) of the polarization.

In Figure 1,  $\alpha$  is called the orientation angle (the angle between the major semiaxis of the ellipse and the  $H$ -axis) and  $\beta$  is the ellipse angle (the angle measuring the ratio of the two semiaxes). If the amplitude of the electromagnetic wave is ignored, then the polarization state of electromagnetic waves can be characterized by parameter pair  $(\alpha, \beta)$ . This state is called the geometric descriptor of polarization state. When  $\beta = 0$ , the resultant polarization is linear; moreover,  $\alpha = 0$  provides a horizontal polarization and  $\beta = (\pi/2)$  leads to a vertical polarization. However, for  $\beta = \pm (\pi/4)$ , the resultant polarization is circular for any orientation angle  $\alpha$ .

The mathematical relationship between electric field and polarization ellipse parameters can be expressed as follows:

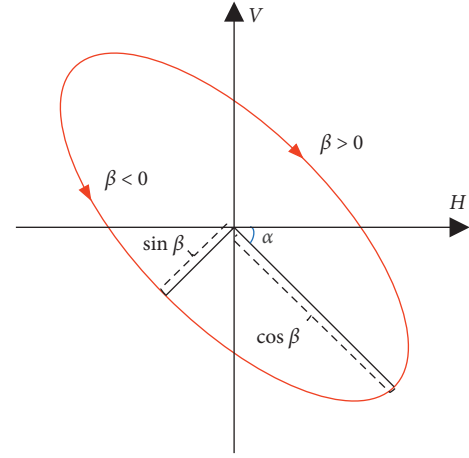


FIGURE 1: Polarization ellipse.

$$\begin{aligned} E &= A \cdot \begin{bmatrix} \cos \alpha & -\sin \alpha \\ \sin \alpha & \cos \alpha \end{bmatrix} \cdot [\cos \beta \quad j \sin \beta]^T \\ &= A \cdot \begin{bmatrix} \cos \alpha \cos \beta - j \sin \alpha \sin \beta \\ \sin \alpha \cos \beta + j \cos \alpha \sin \beta \end{bmatrix} \\ &= \begin{bmatrix} E^H \\ E^V \end{bmatrix}. \end{aligned} \quad (1)$$

In (1), the first item on the right is the rotation matrix, and second one is the ellipticity vector;  $A = \sqrt{|E^H|^2 + |E^V|^2}$  represents the energy of an electromagnetic wave.

The complex electric field vector can also be defined as follows:

$$\mathbf{E} = A \begin{bmatrix} \cos \gamma \\ \sin \gamma e^{j\delta} \end{bmatrix}. \quad (2)$$

In (2),  $\tan \gamma = (A_H/A_V)$  represents the ratio between the amplitude of vertical and horizontal channel electric fields,  $\delta = \phi_V - \phi_H$  is the phase difference between the vertical and the horizontal channel components,  $\gamma \in [0, (\pi/2)]$ , and  $\delta \in [0, 2\pi]$ . Given that the energy information of electromagnetic wave is not considered in this study, the parameter pair is reversible to the polarization state of electromagnetic wave. Thus, the parameter pair can be called the phase descriptor of polarization state of electromagnetic wave. If  $(E^H/E^V) = \gamma e^{j\delta}$  and  $(E^H)^2 + (E^V)^2 \neq 0$ , then the relationship between geometric and phase descriptors can be expressed as follows:

$$\begin{aligned} \alpha &= \tan^{-1} \left( \frac{-2\gamma \cos \delta}{1 - \gamma^2} \right), \\ \beta &= \arcsin \frac{\sqrt{1 - (2\gamma/(1 + \gamma^2)) \sin \delta} - \sqrt{1 + (2\gamma/(1 + \gamma^2)) \sin \delta}}{2}. \end{aligned} \quad (3)$$

**2.2. Polarized Vector Array Response.** Suppose  $\mathbf{r}$  is a unit vector representing a spatial direction in  $\mathbb{R}^3$ , which can be expressed as follows:

$$\mathbf{r} = [\sin \theta \cos \varphi \quad \sin \theta \sin \varphi \quad \cos \theta]^T. \quad (4)$$

In (4),  $\theta \in [-\pi/2, \pi/2]$  is pitch, and  $\varphi \in [0, 2\pi]$  is azimuth:

$$\hat{\boldsymbol{\theta}} \triangleq \frac{\partial \mathbf{r}}{\partial \theta} = [\cos \theta \cos \varphi \quad \cos \theta \sin \varphi \quad -\sin \theta]^T, \quad (5)$$

$$\hat{\boldsymbol{\varphi}} \triangleq \frac{1}{\sin \theta} \frac{\partial \mathbf{r}}{\partial \varphi} = [-\sin \varphi \quad \cos \varphi \quad 0]^T,$$

where  $(\mathbf{r}, \hat{\boldsymbol{\theta}}, \hat{\boldsymbol{\varphi}})$  can be described as a right-hand coordinate system, as shown in Figure 2.

If the plane wave is traveling along the  $\vec{\mathbf{r}}$ -direction, the electric field is orthogonal to  $\tau$  and lies in the plane spanned by  $(\mathbf{r}_H, \mathbf{r}_V)$ . Polarized vector antennas comprising orthogonal electric and magnetic dipoles are considered. In this spatial coordinate system  $(\mathbf{r}_H, \mathbf{r}_V)$ , each of the six dipoles has the following responses (ignoring a common constant that is determined by the antenna parameters and the distance to the antenna).

In this paper, we simplified the representation of polarization state in the coordinate system and only considered the electric field and magnetic field along the  $x$  direction. Thus, the polarized antennas have the responses as follows (regardless of the antenna parameters and the distance to the antenna):

$$\begin{aligned} \mathbf{v}_x^E(\mathbf{r}) &= [-\sin \varphi \quad \cos \theta \cos \varphi], \\ \mathbf{v}_x^M(\mathbf{r}) &= [\cos \theta \cos \varphi \quad \sin \varphi]. \end{aligned} \quad (6)$$

If the antenna only comprises electric and magnetic dipole elements along  $\mathbf{r}$ , then the response is as follows:

$$\mathbf{V}(\mathbf{r}) = [\mathbf{v}_x^E \quad \mathbf{v}_x^M]^T. \quad (7)$$

Moreover, for a given antenna response  $\mathbf{V}(\mathbf{r}) \in \mathbb{C}^{p \times 2}$ ,  $\mathbf{v}(\mathbf{r}; H)$  and  $\mathbf{v}(\mathbf{r}; V)$  are used to denote the response to the  $H$  and  $V$  channels, respectively, or as a formula.

$$\mathbf{V}(\mathbf{r}) = [\mathbf{v}(\mathbf{r}; H), \mathbf{v}(\mathbf{r}; V)]. \quad (8)$$

### 3. Two-Dimensional Beampattern Synthesis for Polarized Smart Antenna Array

A two-dimensional beamforming method for polarized smart antenna array is proposed in this section. Xiao and Nehorai designed a null and sidelobe polarization for the polarized beampattern [6]. However, the null and polarization controls of the sidelobe are independent, which did not maximize the advantages of polarization isolation and null. SOCP is still adopted to deal with the two-dimensional beamforming for polarized antenna arrays. Different from the previous literature, this section extends it to two-dimensional polarization beamforming. Here, the weight matrix  $\boldsymbol{\omega}$  is synthesized to generate a beampattern. Suppose a uniform planar array comprises  $N \times N$  antennas with an element spacing  $d$  (half wavelength), as shown in.

According to the array model shown in Figure 3, the weighting matrix  $\boldsymbol{\omega}$  is introduced in this section to be the concatenation of all  $\boldsymbol{\omega}_{n \times n}$ :

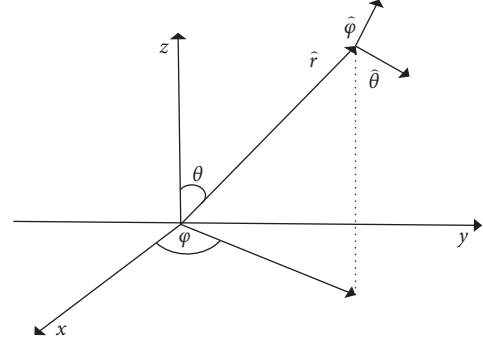


FIGURE 2: Spatial coordinate system.

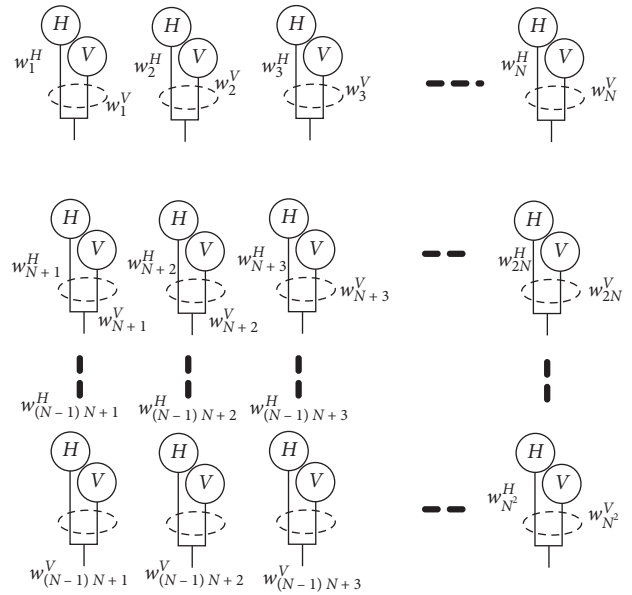


FIGURE 3: Dual-polarized smart antenna array.

$$\boldsymbol{\omega} = \begin{bmatrix} \boldsymbol{\omega}_{11}^T & \boldsymbol{\omega}_{12}^T & \cdots & \boldsymbol{\omega}_{1N}^T \\ \boldsymbol{\omega}_{21}^T & \boldsymbol{\omega}_{22}^T & \cdots & \boldsymbol{\omega}_{2N}^T \\ \vdots & \vdots & \ddots & \vdots \\ \boldsymbol{\omega}_{N1}^T & \boldsymbol{\omega}_{N2}^T & \cdots & \boldsymbol{\omega}_{NN}^T \end{bmatrix}, \quad (9)$$

where

$$\boldsymbol{\omega} = [\boldsymbol{\omega}^H, \boldsymbol{\omega}^V]^T. \quad (10)$$

For convenience of calculation, the  $N \times N$  matrix  $\boldsymbol{\omega}_{NN}^T$  is transformed into  $1 \times N^2$  column vectors as follows:

$$\begin{aligned} \boldsymbol{\omega}^H &= [\omega_1^H, \omega_2^H, \dots, \omega_{N^2}^H], \\ \boldsymbol{\omega}^V &= [\omega_1^V, \omega_2^V, \dots, \omega_{N^2}^V]. \end{aligned} \quad (11)$$

Given the location of actual element  $\mathbf{x}_n$ ;  $1 \leq n \leq N^2$ , which has the  $N^2$  candidate positions, the array response, as a function of spatial direction  $\mathbf{r}$ , can be expressed as follows:

$$\mathbf{A}\mathbf{F}(\mathbf{r}) = \left[ e^{-j\psi_1(\mathbf{r})}, e^{-j\psi_2(\mathbf{r})}, \dots, e^{-j\psi_{N^2}(\mathbf{r})} \right]^T, \quad (12)$$

where  $\psi_n(\mathbf{r}) = k\mathbf{r} \cdot \mathbf{x}_n$  and  $k = (2\pi/\lambda)$  is the wave number.

Thus, in terms of the vector antenna response  $\mathbf{V}(\mathbf{r})$ , the  $N^2 \times 2$  vector antenna array response is further obtained as follows:

$$\mathbf{A}(\mathbf{r}) = \mathbf{A}\mathbf{F}(\mathbf{r}) \otimes \mathbf{V}(\mathbf{r}) = \left[ e^{-j\psi_1(\mathbf{r})}\mathbf{V}(\mathbf{r}) \dots e^{-j\psi_{N^2}(\mathbf{r})}\mathbf{V}(\mathbf{r}) \right]^T. \quad (13)$$

The antenna array response of  $H$  and  $V$  channels is defined as follows:

$$\begin{aligned} \mathbf{A}(\mathbf{r}; H) &= \mathbf{A}\mathbf{F}(\mathbf{r}) \otimes \mathbf{v}(\mathbf{r}; H), \\ \mathbf{A}(\mathbf{r}; V) &= \mathbf{A}\mathbf{F}(\mathbf{r}) \otimes \mathbf{v}(\mathbf{r}; V). \end{aligned} \quad (14)$$

The normalized electrical field emitted from the antenna array (ignoring the common carrier and the baseband signal  $s(t)$ ) can be expressed as follows:

$$\mathbf{E}(\mathbf{r}) = \mathbf{A}(\mathbf{r})^T \boldsymbol{\omega}, \quad (15)$$

where  $\mathbf{E}(\mathbf{r}; H)$  and  $\mathbf{E}(\mathbf{r}; V)$  are used to denote the decomposition of  $\mathbf{E}(\mathbf{r})$ :

$$\mathbf{E}(\mathbf{r}; H) = \mathbf{A}(\mathbf{r}; H)^T \boldsymbol{\omega}, \quad (16)$$

$$\mathbf{E}(\mathbf{r}; V) = \mathbf{A}(\mathbf{r}; V)^T \boldsymbol{\omega}. \quad (17)$$

Along  $\mathbf{r}$ , the polarization state can be determined by the ratio between  $\mathbf{E}(\mathbf{r}; H)$  and  $\mathbf{E}(\mathbf{r}; V)$ , and the transmitting power can be expressed as  $\|\mathbf{E}(\mathbf{r})\|^2 = |\mathbf{E}(\mathbf{r}; H)|^2 + |\mathbf{E}(\mathbf{r}; V)|^2$ :

$$\begin{aligned} \mathbf{E}(\mathbf{r}) &= (\mathbf{A}\mathbf{F}(\mathbf{r}) \otimes \mathbf{V}(\mathbf{r}))^T \boldsymbol{\omega} \\ &= \mathbf{V}(\mathbf{r})^T [s^H \ s^V]^T, \end{aligned} \quad (18)$$

where  $\omega_n^H$  and  $\omega_n^V$  are the complex weights of the horizontal and vertical channels, respectively.  $s^H(\mathbf{r})$  and  $s^V(\mathbf{r})$  are, respectively, defined as follows:

$$\begin{aligned} s^H(\mathbf{r}) &\triangleq \mathbf{A}\mathbf{F}(\mathbf{r})^T \boldsymbol{\omega}^H, \\ s^V(\mathbf{r}) &\triangleq \mathbf{A}\mathbf{F}(\mathbf{r})^T \boldsymbol{\omega}^V. \end{aligned} \quad (19)$$

The selection of  $\omega$  under maximal sidelobe minimization is one of the problems in achieving the following goals.

- (1) Maximize the power of the main beam (at direction  $\mathbf{r}_0$ ) and match polarization parameter pair  $(\mu, \nu)$ ; the region of main beam is denoted by  $S_m$ )
- (2) Minimize power of sidelobe (this region is denoted by  $S_r$  at direction  $\mathbf{r}_s$ )
- (3) A desired null in the directions of interferers (generally located in the sidelobe region and denoted by  $S_n$ ), which has cross-polarization constraint  $(\alpha_p, \beta_p)$

Based on above, the polarized beampattern synthesis problem can be formulated as follows:

$$\begin{aligned} \min_{\mathbf{r}_s \in S_r} \quad & \tau \\ \text{subject to} \quad & \begin{cases} \mathbf{E}(\mathbf{r}_0) = \sqrt{E_0} e^{j\phi} \begin{bmatrix} \cos \mu & -\cos \mu \\ \sin \mu & \cos \mu \end{bmatrix} \begin{bmatrix} \cos \nu \\ j \sin \nu \end{bmatrix} \\ \max_{\mathbf{r}_s \in S_r} \left\{ \|\mathbf{E}(\mathbf{r}_s; H)\|^2 + \|\mathbf{E}(\mathbf{r}_s; V)\|^2 \right\} \leq \tau^2, \quad \mathbf{r}_s \in S_r \\ \begin{bmatrix} E^H(\mathbf{r}_n) \\ E^V(\mathbf{r}_n) \end{bmatrix} = \sqrt{P} e^{j\phi} \begin{bmatrix} \cos \alpha_p & \sin \alpha_p \\ -\sin \alpha_p & \cos \alpha_p \end{bmatrix} \begin{bmatrix} \cos \beta_p \\ j \sin \beta_p \end{bmatrix} \\ \|\mathbf{E}(\mathbf{r}_n; H)\|^2 + \|\mathbf{E}(\mathbf{r}_n; V)\|^2 \leq \varepsilon^2, \quad \mathbf{r}_n \in S_n. \end{cases} \end{cases} \quad (20)$$

where  $\tau$  is the optimal solution, which measures the beampattern power gain over the sidelobes and does not depend on the main beam polarization. The third constraint directly determines the polarization of notch and its depth ( $\varepsilon = \sqrt{P}$ ). When  $\omega$  is a column vector of  $1 \times N^2$ , the above optimization mode is also applicable to the synthesis of the polarized beampattern for ULA. This condition is a vector optimization problem that is difficult to solve using an optimization algorithm. Thus, this optimization problem is split into two equivalent scalar optimization problems as follows:

Horizontal channel is

$$\begin{aligned} \min_{\omega^{(H)}} \quad & \max_{\mathbf{r}_s \in S_r} |E^H(\mathbf{r}_s)|^2 \\ \text{subject to} \quad & E(\mathbf{r}_m) = (\cos \mu \cos \nu + j \sin \mu \sin \nu) \\ & E(\mathbf{r}_n) = \varepsilon(p - c, q - c) \cdot (\cos \alpha_p \cos \beta_p + j \sin \alpha_p \sin \beta_p), \quad \mathbf{r}_n \in S_n. \end{aligned} \quad (21)$$

Vertical channel is

$$\begin{aligned} \min_{\omega^{(V)}} \quad & \max_{\mathbf{r}_s \in S_r} |E^V(\mathbf{r}_s)|^2 \\ \text{subject to} \quad & E(\mathbf{r}_0) = (-\sin \mu \cos \nu + j \cos \mu \sin \nu) \\ & E(\mathbf{r}_n) = \varepsilon(p - c, q - c) \cdot (-\sin \alpha_p \cos \beta_p + j \cos \alpha_p \sin \beta_p), \quad \mathbf{r}_n \in S_n. \end{aligned} \quad (22)$$

In (21) and (22),  $\varepsilon$  is called the null concave matrix for polarized smart antenna array and is introduced as follows:

$$\varepsilon = \begin{bmatrix} 20\lg \varepsilon_{(p-c,q-c)} & 20\lg \varepsilon_{(p-c+1,q-c)} & \cdots & 20\lg \varepsilon_{(p+c,q-c)} \\ 20\lg \varepsilon_{(p-c,q-c+1)} & 20\lg \varepsilon_{(p-c+1,q-c+1)} & \cdots & 20\lg \varepsilon_{(p+c,q-c+1)} \\ \vdots & \vdots & \ddots & \vdots \\ 20\lg \varepsilon_{(p-c,q+c)} & 20\lg \varepsilon_{(p-c+1,q+c)} & \cdots & 20\lg \varepsilon_{(p+c,q+c)} \end{bmatrix}, \quad (23)$$

where  $\mathbf{p} = (p-c, \dots, p-1, p, p+1, \dots, p+c)$ ,  $\mathbf{q} = (q-c, \dots, q-1, q, q+1, \dots, q+c)$ , and  $c$  is a constant. The above optimized problem is convex and is also an SOCP problem.

#### 4. Sparse Array Design for Polarized Smart Antenna

Pattern performance and polarization constraint for the polarized smart antenna must be considered in the sparse

process of antenna array [21]. The optimization model must be a multiconstraint problem, including the unequal constraints, to accomplish both purposes. Following [22, 23], a two-stage design approach is adopted to deal with the sparse array design for polarized smart antenna. In the first stage, the weight matrix  $\omega$  is synthesized to generate a pattern for  $N \times N$  polarized antenna array with an  $N^2$  antenna element, as mentioned in Section 3. In the second stage, the element positions of the full array are treated as candidate positions that are selected by a sparse array with  $M$  antenna elements.

Mean square error of polarization matching in interest area (PMSE) is defined as an objective function, whereas the peak sidelobe levels (PSLLs) minimization of sparse array design is another objective function [24]. This optimization problem of PMSE can be constructed as follows:

$$f(x) = \frac{1}{K} \sum_{k=1}^K \{ [\mathbf{a}(\theta_k, \varphi_k) - \mathbf{a}_{\text{best}}(\theta_k, \varphi_k)]^2 + [\mathbf{\beta}(\theta_k, \varphi_k) - \mathbf{\beta}_{\text{best}}(\theta_k, \varphi_k)]^2 \}, \quad (24)$$

where  $K$  is the number of sampling points in the far-field area for the optimal polarized beampattern.

The optimization problem for a sparse antenna array design aimed at polarization matching to control the designed polarization as desired in the interesting region can be written as follows:

$$\min f(\mathbf{x})$$

$$\text{subject to} \left\{ \begin{array}{l} -N_x \leq m \leq N_x, \quad -N_y \leq n \leq N_y \\ a(N_x, 0) = 1, a(-N_x, 0) = 1 \\ a(0, -N_y) = 1, a(0, N_y) = 1 \\ \text{PSLLs} - \delta < 0 \\ \sum_{m=-N_x}^{N_x} \sum_{n=-N_y}^{N_y} a_{mn} = T \\ \left| \frac{E(\theta_{i-c}, \varphi_{j-c})}{\text{FF}_{\text{max}}} \right| \leq \varepsilon(i-c, j-c), \quad i, j = 1, 2, \dots \end{array} \right. \quad (25)$$

where the first three constraints fix the four sides of the antenna aperture,  $\delta$  is the tolerance value for PSLLs in the fourth constraint (which is an inequality constraint), the fifth constraint sets the actual number of elements ( $T$ ), and

the last constraint realizes the depth and polarization of null ( $\text{FF}_{\text{max}}$  is the peak of the main lobe). Following the idea of multiobjective optimization, the inequality constraint can be regarded as another objective function in the evolution process [24]. This constraint can be optimized in parallel implementation as follows:

$$\min (f_1(\mathbf{x}), f_2(\mathbf{x}))$$

$$\text{subject to} \left\{ \begin{array}{l} -N_x \leq m \leq N_x, \quad -N_y \leq n \leq N_y \\ a(N_x, 0) = 1, a(-N_x, 0) = 1 \\ a(0, -N_y) = 1, a(0, N_y) = 1 \\ \sum_{m=-N_x}^{N_x} \sum_{n=-N_y}^{N_y} a_{mn} = T \\ \left| \frac{E(\theta_{i-c}, \varphi_{j-c})}{\text{FF}_{\text{max}}} \right| \leq \varepsilon(i-c, j-c), \quad i, j = 1, 2, \dots \end{array} \right. \quad (26)$$

where  $f_1(\mathbf{x})$  is defined in (23) and  $f_2(\mathbf{x}) = \text{PSLLs}$ . Inspired by [23], the MODE algorithm is suitable for this kind of multiobjective optimization problem and is designed to handle a multiset of solutions in a single iteration. In the multiobjective domain, the MODE aims to identify a set of Pareto optimal solutions to operate the selection of the best individual for the mutation (Appendix A). At the end of the



evolutionary search, the nondominated solution archive is passed through a dominance filter to yield the global near-Pareto-optimal frontier (Appendixes B and C) [23, 25]. The individual representation (Initial and Coding) needs to be explained as follows.

**4.1. Initial.** Let  $x_{i,G}^j$  denote the initial value of the  $j$  parameter in the  $i^{\text{th}}$  population at generation  $G$ , which is shown as follows:

$$x_{i,G}^j = \text{rand}(0,1) \cdot (x_{\max}^j - x_{\min}^j) + x_{\min}^j, \quad i = 1, \dots, \text{NP}, j = 1, \dots, D, \quad (27)$$

where  $D = N^2 - 4$ , and  $\text{rand}(0,1)$  is a uniformly distributed random variable within the range  $[0, 1]$ , and  $x_{\max}^j$  and  $x_{\min}^j$  are the lower and upper bounds of the  $j^{\text{th}}$  variable parameter, respectively. The individual in the  $i^{\text{th}}$  population at generation  $G$  can be obtained in its vector form as follows:

$$\mathbf{x}_{i,G} = [x^1, x^2, \dots, x^D]. \quad (28)$$

**4.2. Coding.** The initial value of the antenna position is set as the partition points of a planar array aperture. The random perturbation is controlled by  $x_{i,G}$ , and binary coded  $\mathbf{p}_s$  denotes the location of actual elements, which is shown as follows:

$$\mathbf{p}_s(n, n) = \text{sort}(\mathbf{x})^T, \quad n = 1, \dots, N^2 - 4, \quad (29)$$

where  $\text{sort}(\cdot)$  denotes the real variables that are sorted by size as integer variables converted into binary codes.

The whole process of sparse array design using MODE algorithm can be summarized as follows (Algorithm 1).

Steps 3–5 evaluate the fitness function at these 2NP solutions at each generation  $G$ , select the NP fittest solutions via fast nondominated sorting, and store them in the current population  $\text{pop}_c$ . In our approach, fast nondominated sorting is applied to guarantee that the population maintains its original size, and the nondominated solutions in the population are identified at each generation of the evolution process. The nondominated solutions are saved in the advanced population that corresponds to the feasible solution [26]. Otherwise, the infeasible solution is reserved in the current population.

## 5. Numerical Example

The simulation results are presented in this section to illustrate the effectiveness of the proposed method. Considering the preliminary results reported in [6, 9], the application of the SOCP to polarized beam pattern synthesis must be investigated. Thus, the polarized beam pattern synthesis is introduced for polarized smart antenna based on ULA in Example 1. This example highlights the continuity and innovation of the proposed method. The cross-polarization is added on the null of the beam pattern to improve the capability of interference suppression in the sidelobe region, which is different from [6]. Example 2 synthesizes the 2D polarization beam pattern and obtains the corresponding

polarization state for the polarized smart antenna array. Example 3 realizes the sparse array design of the 2D polarized smart antenna array.

**5.1. Polarized Beampattern with a Null that Has Cross-Polarization Based on ULA.** Assume that a strong interference is located at an azimuth angle of  $\theta = 23^\circ$ , and its polarization state can be depicted with polarization ellipse parameters of  $\alpha = 80^\circ$  and  $\beta = 25^\circ$ . Thus, a desired null ( $\text{SLL} \leq -50$  dB) with ( $\alpha = -10^\circ$  and  $\beta = 25^\circ$ ) that is located at  $\theta \in (20^\circ, 25^\circ)$  must be designed. The entire angle area is  $\theta \in (-90^\circ, 90^\circ)$  with  $1^\circ$  angular spacing (such that  $K = 181$ ). Assume a strong interference is at the azimuth angle of  $\theta = 23^\circ$ . The polarization state of this strong interference can be depicted with polarization ellipse parameters of  $\alpha = 80^\circ$  and  $\beta = 25^\circ$ . The desired null ( $\text{SLL} = -50$  dB) with  $\alpha = -10^\circ$  and  $\beta = 25^\circ$ , which is located at  $\theta = [20^\circ, 25^\circ]$ , must be designed.

Figure 4(a) depicts a polarized beampattern with one desired polarization. The result shows that the polarization can be controlled such that the interference of the known source is isolated, and the gain of the main lobe is 16 dB. Figure 4(b) presents that the desired polarization ellipse parameter is a constant in the entire angle region. Figure 5(a) depicts a polarized beampattern with the desired null. The result also shows that the depth of the obtained null can reach  $-24$  dB compared with the maximum peak sidelobe level. However, Figure 5(b) displays that the curve of the polarization ellipse parameter in the entire angle area is not constant, except for the main lobe region; that is, no law exists.

Figure 6(a) shows the beampattern of the proposed method. Figure 6(b) displays that the curve of the polarization ellipse parameter in the entire angle area is not constant; that is, no law exists. However, this curve meets the interests in that region, such as the main lobe and jamming direction. Thus, all these findings justify the efforts to prevent jamming due to polarization mismatch.

**5.2. Two-Dimensional Beampattern Synthesis for Polarized Smart Antenna Array.** Similar to Example 1, SOCP is applied to optimize the 2D polarized beamform as mentioned in Section 3. The only difference from the previous example is that the variable is no longer a column vector but a matrix. Thus, the weight matrix must be transformed into column vectors again. Assume that a planar array of  $10 \times 10$  ( $N = 10$ ) is synthesized and satisfies the following constraints: (1) The distance between any pair of elements is equal to  $d_c = 0.5\lambda$ . (2) All elements are allocated on a fixed aperture of  $4.5\lambda \times 4.5\lambda$ . (3) The main beam is targeted at  $\varphi = 20^\circ$  and  $\theta = 20^\circ$  with beam width of  $7.5^\circ$  and polarization constraint  $(\mu, \nu) = (10^\circ, 20^\circ)$ . (4) The null is located at  $\varphi \in (60^\circ, 63^\circ)$  and  $\theta \in (60^\circ, 62^\circ)$  with the polarization constraint  $(\alpha_i, \beta_i) = (25^\circ, 35^\circ)$ . Therefore, the coordinate vector of the null concave in the sidelobe region is equal to  $\mathbf{p} = (60^\circ, 61^\circ, 62^\circ)$ ,  $\mathbf{q} = (60^\circ, 61^\circ, 62^\circ)$ , and the depth is  $20 \cdot \lg \varepsilon = 60$  dB ( $\varepsilon = 0.001$ ). According to the optimization model defined by equations (16) and (17), CVX MOSEKY

**Input:**  $\omega$ , NP,  $M$ ,  $N$ ,  $G_{\max}$

Step 1: **initial.**  $a(N_x, 0) = 1, a(-N_x, 0) = 1, a(0, -N_y) = 1, a(0, N_y) = 1$ ;  $G = 1, \dots, G_{\max}$   $x_{i,G}^j = \text{rand}(0, 1), i = 1, \dots, \text{NP}, j = 1, \dots, N^2$

Step 2: **coding.**  $\mathbf{x}_{i,G} \rightarrow \mathbf{p}_s, f_1(x)$  is defined in (24),  $f_2(x) = \text{PSLLs}(\mathbf{x})$

For  $p \leftarrow 1$  to NP do

Step 3: **mutation.** Randomly select three distinct individuals,  $\mathbf{x}_{r1}, \mathbf{x}_{r2},$  and  $\mathbf{x}_{r3}$ , who are all different from the target individual. Generate a perturbed individual  $\mathbf{U}_i$  by  $\mathbf{U}_{i,G+1} = \mathbf{x}_{\text{tb},G} + F(\mathbf{x}_{r2,G} + \mathbf{x}_{r3,G})$

The scaling factor  $F \in [0, 2]$  is constant.  $\mathbf{x}_{\text{tb},G}$  denotes the best individuals among the three individuals, which is mean that the one has best fitness function value

Step 4: **crossover.** The objective function value of each trial vector  $f(\mathbf{v}_{i,G})$  is compared with that of its corresponding target vector  $f(\mathbf{x}_{i,G})$ . The vector with the smaller fitness value will be retained in the next generation. Generate a trial individual as follows:

$$\mathbf{v}_{i,G+1} = \begin{cases} \mathbf{v}_{i,G}, & \text{if } f(\mathbf{v}_{i,G}) < f(\mathbf{x}_{i,G}), \\ \mathbf{x}_{i,G}, & \text{otherwise.} \end{cases}$$

calculate the fitness value of  $\mathbf{V}_{i,G+1}, p = p + \text{NP}$

Step 5: **Pareto dominance**

If ( $\mathbf{V}_i$  dominates  $\mathbf{x}_i$ )

replace  $\mathbf{x}_i$  by  $\mathbf{V}_i$  in the current population pop\_c, and then add  $\mathbf{x}_i$  to the advanced population pop\_a

Else

add  $\mathbf{V}_i$  to the advanced population pop\_a

End

end

NP fittest solutions is select in every fast nondominated sorting and save them in pop\_c;  $\mathbf{p}_{s,\text{best}}$  is the  $\mathbf{p}_s$  with the lowest fitness value of  $f_1(x)$

**Output:**  $\mathbf{p}_{s,\text{best}} \rightarrow \mathbf{A}_s \rightarrow \mathbf{p} = \mathbf{A}_s^H \omega$

ALGORITHM 1: MODE algorithm.

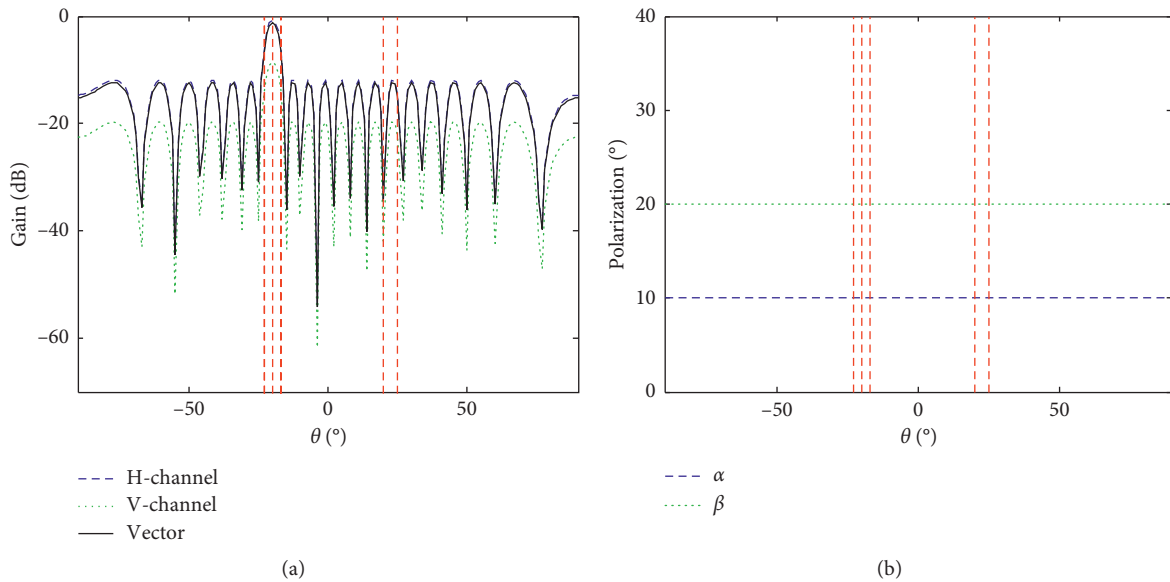


FIGURE 4: First method of polarized beampattern in [6]. (a) Beampattern. (b) Polarization.

solver is used to solve the two equivalent scalar problems [27]. The following results are obtained.

For clarity, 3D and contour figures represent the optimized beampattern. A null concave with the average depth of  $-91.5$  dB is located at  $\theta \in (60^\circ, 62^\circ)$  and  $\phi \in (60^\circ, 62^\circ)$  in Figure 7. Compared to the maximum peak sidelobe ( $-16.5$  dB), the polarized beampattern obtained a suppression gain with  $-75$  dB.  $\alpha$  and  $\beta$  are also represented by a surface to verify the polarization state of 2D polarized beampattern, as shown in Figure 8. Different from the

previous example, the polarization state of interesting area cannot be directly observed from the curved surface. However, if the tangent of the surface is used for representation, then the polarization state values of null concave cannot be fully expressed. Thus, a table is used to express the corresponding polarization state values at several sampling points of interesting areas, as shown in Tables 1 and 2.

Tables 1 and 2 suggest that the polarization parameter pair  $(\alpha, \beta)$  is consistent with the experimental setting, where

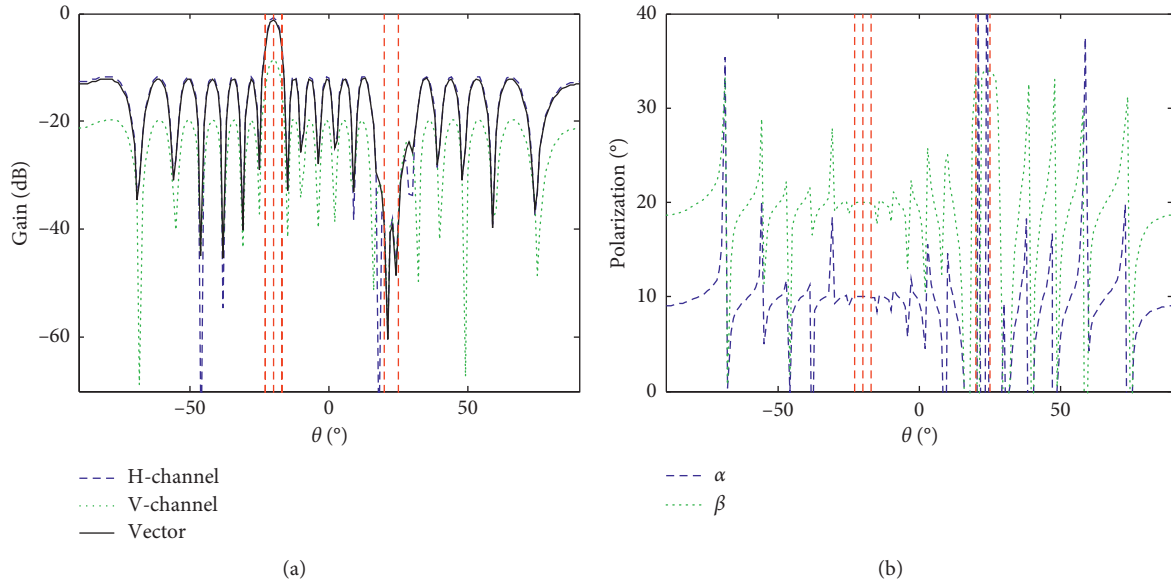


FIGURE 5: Second method of polarized beampattern in [6]. (a) Beampattern. (b) Polarization.

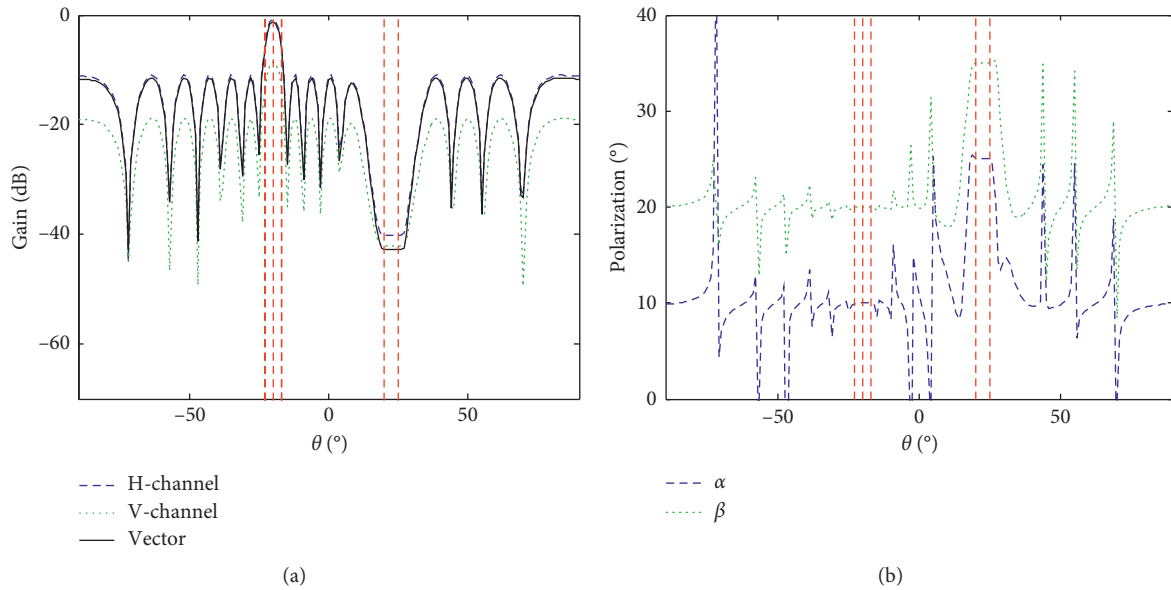


FIGURE 6: Proposed method of polarized beampattern. (a) Beampattern. (b) Polarization.

$p$  and  $q$ , respectively, refer to the sampling points of the main lobe and null concave, as defined in (18). Similar to Example 1, the constraint of polarization matching cannot guarantee the polarization state outside the region of interest.

**5.3. Sparse Array Optimization of Polarized Smart Antenna Using MODE.** The MODE algorithm is applied for sparse antenna array design to verify the effectiveness of the method mentioned in Section 4. Given its particularity, this optimization problem is suitable for the multiobjective differential evolution algorithm. Thus, we only apply the multiobjective differential evolution algorithm to its sparse

array optimization. Herein, the sparse rate is set as 75%. Thus,  $M = 75$  antenna elements selected from 100 candidate positions ( $N = 10 \times 10$  planar array) are used. Other simulation conditions remain the same as those in Example 2. The parameters of MODE are defined and applied as follows:

- (1) Population size:  $NP = 100$
- (2) Initial range:  $x_{\max} = 1, x_{\min} = 0$
- (3) Mutation probability:  $F = 0.8$
- (4) Crossover probability:  $CR = 0.3$
- (5) Maximum number of iterations:  $G_{\max} = 200$

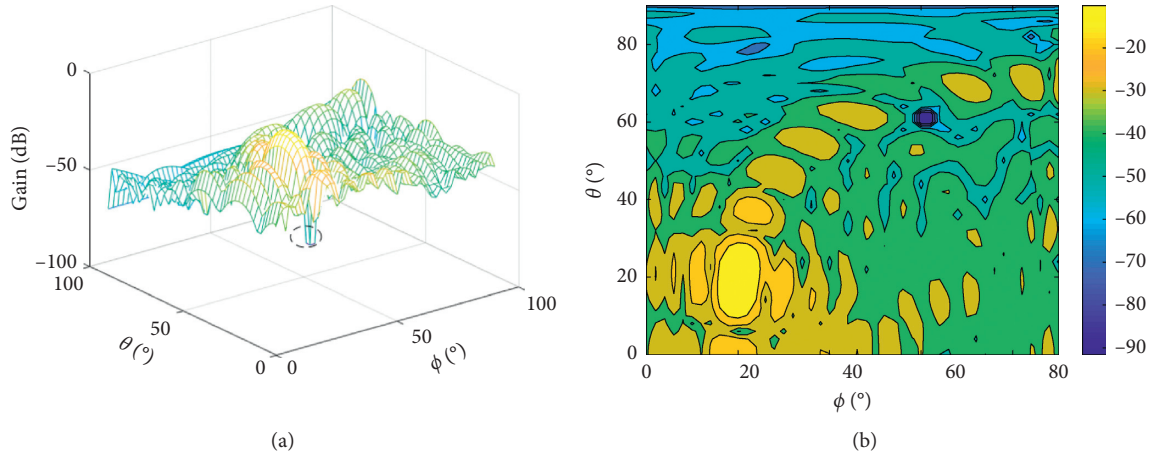


FIGURE 7: Polarized beampattern using the proposed method. (a) The 3D polarized beampattern. (b) The contour of polarized beampattern.

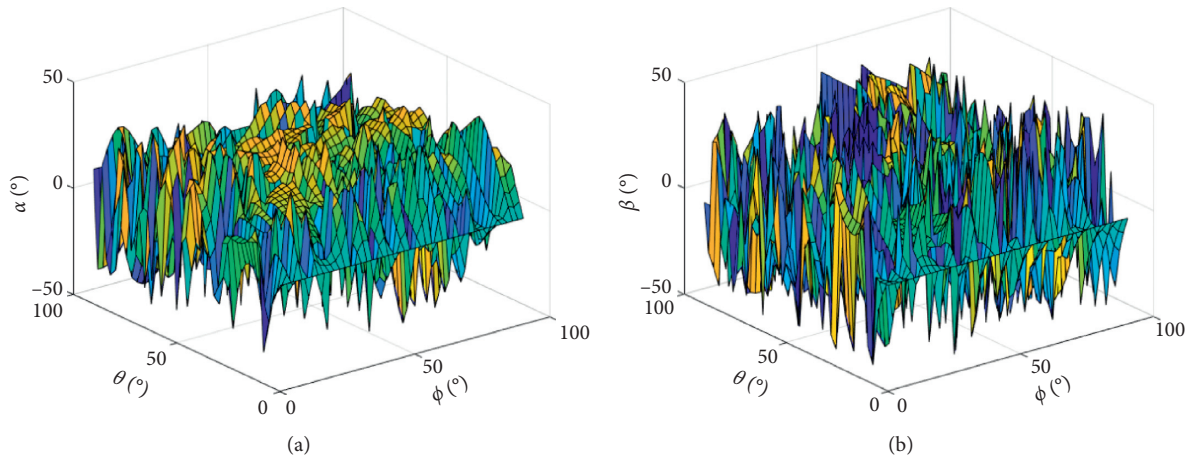


FIGURE 8: The surface of polarization parameter pair using the proposed method. (a) Orientation angle. (b) Ellipse angle.

TABLE 1: Polarization state in the main lobe.

Sampling points	1	2	3	4	5	6	7	8	9
$p$	19	19	19	20	20	20	21	21	21
$q$	19	20	21	19	20	21	19	20	21
$\mu$	9.80	9.90	8.05	10.00	10.00	9.01	8.05	9.20	9.80
$\nu$	19.79	19.90	19.99	20.97	20.97	20.00	20.05	21.95	21.70

TABLE 2: Polarization state in the null.

Sampling points	1	2	3	4	5	6	7	8	9
$p$	60	60	60	61	61	61	62	62	62
$q$	60	61	62	60	61	62	60	61	62
$\alpha_i$	24.79	24.90	24.99	25.00	25.00	25.00	25.05	24.95	24.70
$\beta_i$	34.89	33.34	36.89	35.00	35.00	37.90	34.56	36.90	39.00

SOCp is repeated to establish the optimum covariance matrix  $\omega$ , and the evolution process continues until the maximum number of iterations for testing convergence is reached. The results are shown as follows.

The red asterisks in Figure 9(a) record all the infeasible solution sets, and the black diamonds represent the feasible solution sets in one run. To balance the performance of both PMSE and PSL, the solution (PMSE = 0.0086 and

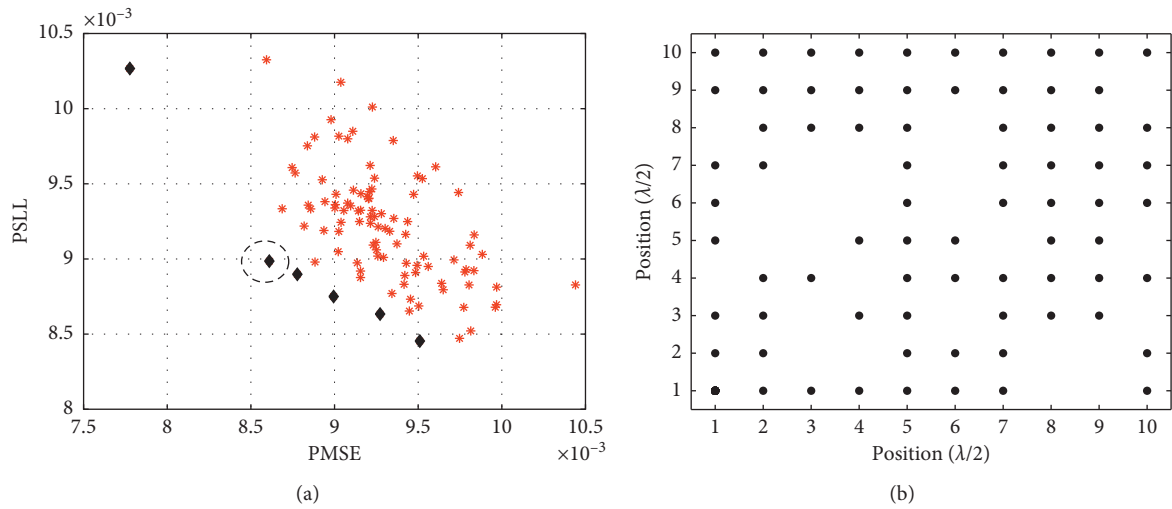


FIGURE 9: Pareto fronts produced by MODE. (a) Pareto fronts. (b) Position of antenna.

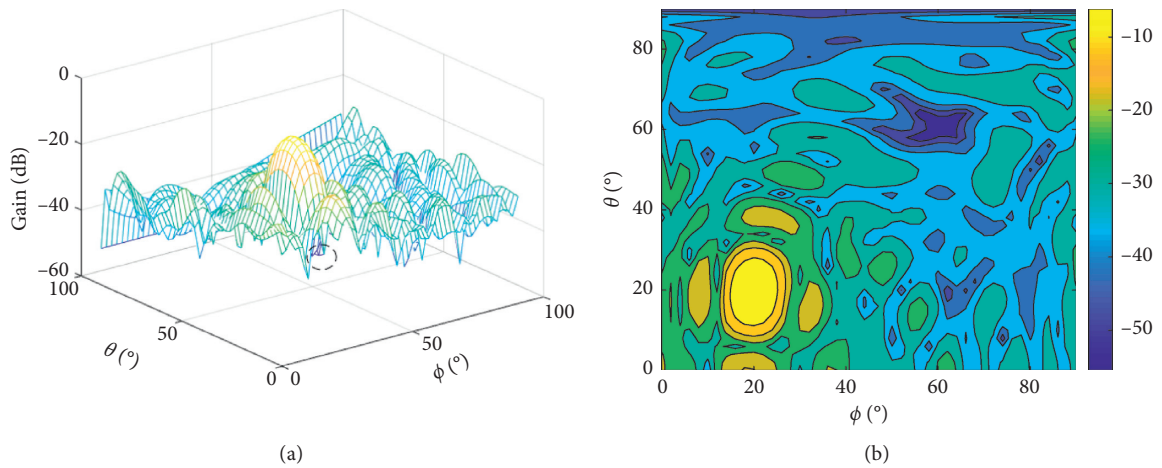


FIGURE 10: Beampattern produced by MODE. (a) The 3D polarized beampattern. (b) The contour of polarized beampattern.

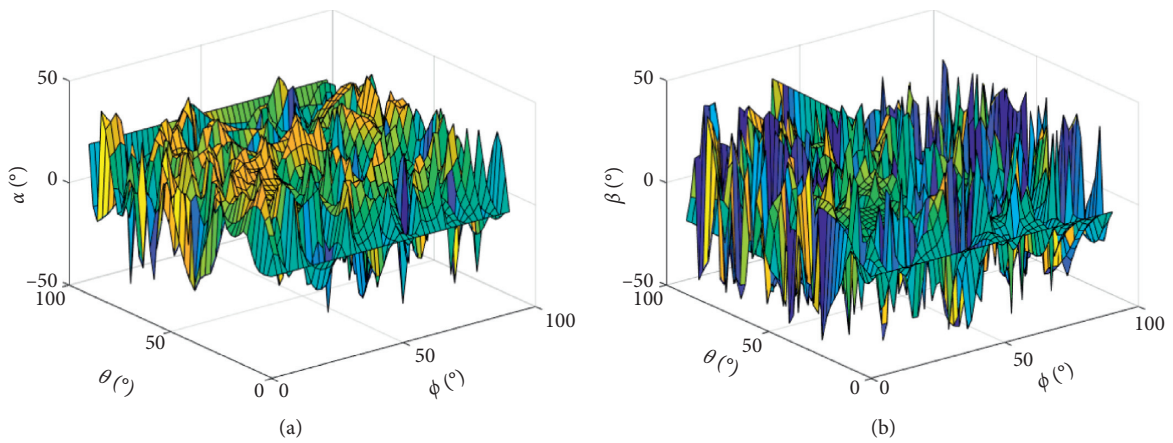


FIGURE 11: The surface of polarization parameter pair using the MODE. (a) Orientation angle. (b) Ellipse angle.

TABLE 3: Polarization state in the region of the main lobe.

Sampling points	1	2	3	4	5	6	7	8	9
$p$	19	19	19	20	20	20	21	21	21
$q$	19	20	21	19	20	21	19	20	21
$\mu$	9.32	8.85	9.2621	10.91	10.00	10.07	10.00	10.01	10.80
$\nu$	19.85	20.00	20.05	19.86	20.00	20.00	21.11	20.00	21.30

TABLE 4: Polarization state in the region of null concave.

Sampling points	1	2	3	4	5	6	7	8	9
$p$	60	60	60	61	61	61	62	62	62
$q$	60	61	62	60	61	62	60	61	62
$\alpha_i$	23.79	25.49	24.50	23.30	24.20	26.11	25.52	28.7782	25.2064
$\beta_i$	32.15	31.89	32.25	35.04	35.46	34.24	34.20	35.00	36.56

TABLE 5: Performance of MODE in 10 runs.

Algorithm: MODE	Index of runs									
	1 <sup>st</sup>	2 <sup>nd</sup>	3 <sup>rd</sup>	4 <sup>th</sup>	5 <sup>th</sup>	6 <sup>th</sup>	7 <sup>th</sup>	8 <sup>th</sup>	9 <sup>th</sup>	10 <sup>th</sup>
PMSE	0.0086	0.0086	0.0087	0.0086	0.0086	0.0086	0.0086	0.0086	0.0086	0.0086
PSLLs	0.0090	0.0090	0.0091	0.0090	0.0090	0.0091	0.0091	0.0090	0.0090	0.0089
Iterations	27	27	27	27	27	27	28	25	28	26
Runtime	15/00	15/04	15/66	15/20	15/25	15/23	15/12	15/00	15/27	15/25

PSLL = 0.009) marked by the dotted circle should be the best choice in experience. Figure 9(b) shows the selected antenna positions corresponding to the best solution, and the sparse rate is set to 75%. In Figure 10, it is easy to see that the average PSLL is about  $-10$  dB, and the depth of null obtained is  $-50$  dB. Those performances are worse than those in Figure 7. This finding is due to the decrease in the number of array elements, which leads to increased sidelobe levels. However, the performance of polarization matching in the interesting area and the PSLLs outside the beampattern is balanced. The restriction for the polarization matching in this study is to maintain the best approximation of polarization matching while keeping the sidelobe level as flat as possible, as shown in Figures 9 and 10. Figure 11 shows the surface value of the polarization ellipse parameter that uses the MODE. As previously described, we still cannot see the polarization state of interest region in Figure 11. Thus, the corresponding polarization states are shown in Tables 3 and 4, respectively.

Table 5 shows the chosen PMSE and PSLLs in ten independent runs.

Table 5 summarizes the results of MODE in 10 runs. The highest PMSE is below 0.0091, whereas all PSLLs slightly fluctuate around 0.009. This finding suggests the stability of PSLLs obtained using MODE. MODE has almost the same running time as DE despite the constraint added by the former to the optimization problem. Moreover, MODE has a simpler algorithm structure than that of DE. These arguments justify efforts to prevent PMSE.

## 6. Conclusions

A novel two-stage design approach for the sparse antenna array design of 2D polarized smart antenna arrays is

proposed in this work. A new model of optimal polarized beampattern optimization problem based on SOCP is formulated in the first stage. A multiobjective optimization problem for sparse arrays, which can be solved by MODE, is then proposed in the second stage. Compared with the existing method in [6], the cross-polarization on the null is constrained to maximize the capability of interferer suppression while retaining the polarization matched reception in the main lobe. This method is extended to the two-dimensional polarized antenna array. Given the substantial hardware cost, the MODE algorithm based on Pareto technique is proposed to obtain the sparse array. In this algorithm, the PMSE in the interest area is presented as another objective function to be optimized. The simulation results reveal that MODE outperforms other algorithms in terms of sparse arrays while maintaining polarization matching performance.

Although only beampattern synthesis and sparse array for polarized smart antenna array are considered, the effect of the matching reception and interference suppression is not evaluated in practical application. The extension of this method to the detection and interference suppression of systems is part of future studies.

## Appendix

### A. Opposition-Based Learning

*Proof.* The opposition-based learning is introduced to generate opposite solutions in the initialization to increase the chances of starting with the fittest solution [20], which can be expressed as follows:

$$y_i^j = (x_{\max}^j + x_{\min}^j) - x_i^j, \quad i = 1, \dots, NP, j = 1, \dots, D. \quad (\text{A.1})$$

□

## B. Pareto Dominance

*Proof.* A solution  $x_1$  is said to dominate another solution  $x_2$  under the following conditions:

- (1)  $\forall m \in (1, \dots, M_{\text{obj}}): f_m(x_1) \leq f_m(x_2)$
- (2)  $\exists m \in (1, \dots, M_{\text{obj}}): f_m(x_1) < f_m(x_2)$

where  $M_{\text{obj}}$  is the number of objective functions and  $f_m(\cdot)$  is the corresponding fitness function. Any individual that is not dominated by any other member is considered nondominated. □

## C. Fast Nondominated Sorting

*Proof.* Assume a Pareto optimal set denoted by  $S$ .  $n_p$  denotes the number of dominated solutions, while  $S_p$  is a set of solutions dominated by the solution  $p$  [20].

For every solution  $p$  in  $S$ , both  $n_p$  and  $S_p$  are calculated. All solutions in the first nondominated front  $F_1$  clear their domination count to zero. Afterwards, when  $n_p = 0$ , each solution  $p$  visits each member  $q$  of its set  $S_p$ , and  $n_p = n_p - 1$ . Any member  $q$  is saved in a separate list  $\tilde{P}$ . These members belong to the second nondominated front  $F_2$ . Each member of  $\tilde{P}$  and the third front  $F_3$  are identified. This process continues until all fronts have been identified. □

## Data Availability

The data used to support the findings of this study are available from the corresponding author upon request.

## Conflicts of Interest

The authors declare no conflicts of interest regarding the publication of this article.

## Acknowledgments

This work was supported by the National Natural Science Foundation of China (Grant nos. 61701148, 61703128, 61703131, and 61703129).

## References

- [1] C. B. Dietrich, W. L. Stutzman, B.-Ki Kim et al., "Smart antennas in wireless communications: base-station diversity and handset beamforming," *Antennas and Propagation Magazine IEEE*, vol. 42, no. 5, pp. 42–151, 2000.
- [2] A. Alexiou and M. Haardt, "Smart antenna technologies for future wireless systems: trends and challenges," *IEEE Communications Magazine*, vol. 42, no. 9, pp. 90–97, 2004.
- [3] F. R. . Castella, "Adaptive antenna nulling for a phased array monopulse radar," in *Proceedings of the International Conference of the 1992 IET Radar*, Cambridge, UK, October 1992.
- [4] V. Tocca, D. Vigilante, L. Timmoneri et al., "Adaptive beamforming algorithms performance evaluation for active array radars," in *Proceedings of the IEEE Radar Conference (RadarConf18)*, Oklahoma City, OK, USA, April 2018.
- [5] N. H. Noordin, W. Zhou, A. O. El-Rayis et al., "Single-feed polarization reconfigurable patch antenna," *Progress in Electromagnetics Research B*, vol. 54, no. 54, pp. 1-2, 2012.
- [6] J. J. Xiao and A. Nehorai, "Optimal beampattern synthesis of a polarized array. statistical signal processing, SSP '07," in *Proceedings of the IEEE/SP 14th Workshop on IEEE*, St. Louis, MO, USA, May 2007.
- [7] P. Jacob, A. S. Madhukumar, and A. Alphones, "Interference mitigation through cross polarized transmission in femto-macro network," *IEEE Communications Letters*, vol. 17, no. 10, pp. 1940–1943, 2013.
- [8] A. Ali, H. Liang, and S. Shetty, "Polarized beamforming for enhanced countermeasure of wireless jamming attacks," in *Proceedings of the IEEE 35th International Performance Computing and Communications Conference (IPCCC)*, IEEE, Las Vegas, NV, USA, December 2016.
- [9] J.-J. Jin-Jun Xiao and A. Nehorai, "Optimal polarized beampattern synthesis using a vector antenna array," *IEEE Transactions on Signal Processing*, vol. 57, no. 2, pp. 576–587, 2009.
- [10] S. M. Bowers, A. Safaripour, and A. Hajimiri, "Dynamic polarization control," *IEEE Journal of Solid-State Circuits*, vol. 50, no. 5, pp. 1224–1236, 2015.
- [11] Y. Lu, Y. Xu, Y. Huang, and Z. Liu, "Diversely polarised antenna-array-based narrowband/wideband beamforming via polarisational reconstruction matrix inversion," *IET Signal Processing*, vol. 12, no. 3, pp. 358–367, 2018.
- [12] P. Xie, g.-m. Wang, H. Li et al., "A dual-polarized two-dimensional beam steering fabry-pérot cavity antenna with a reconfigurable partially reflecting surface," *IEEE Antennas & Wireless Propagation Letters*, vol. 16, no. 1, p. 1, 2017.
- [13] M. V. Komandla, "Investigations on dual slant polarized cavity-backed massive MIMO antenna panel with beamforming," *IEEE Transactions on Antennas and Propagation*, vol. 65, no. 12, pp. 6794–6799, 2017.
- [14] K. Chen, X. Yun, Z. He, and C. Han, "Synthesis of sparse planar arrays using modified real genetic algorithm," *IEEE Transactions on Antennas and Propagation*, vol. 55, no. 4, pp. 1067–1073, 2007.
- [15] C. Chuan Lin, A. Anyong Qing, and Q. Quanyuan Feng, "Synthesis of unequally spaced antenna arrays by using differential evolution," *IEEE Transactions on Antennas and Propagation*, vol. 58, no. 8, pp. 2553–2561, 2010.
- [16] D. G. Kurup, M. Himdi, A. Rydberg et al., "Synthesis of uniform amplitude unequally spaced antenna arrays using the differential evolution algorithm," *IEEE Transactions on Antennas and Propagation*, vol. 51, no. 9, pp. 2210–2217, 2003.
- [17] R. Bhattacharya, T. K. Bhattacharyya, and R. Garg, "Position mutated hierarchical particle swarm optimization and its application in synthesis of unequally spaced antenna arrays," *IEEE Transactions on Antennas and Propagation*, vol. 60, no. 7, pp. 3174–3181, 2012.
- [18] D. Caratelli and M. C. Vigano, "A novel deterministic synthesis technique for constrained sparse array design problems," *IEEE Transactions on Antennas and Propagation*, vol. 59, no. 11, pp. 4085–4093, 2011.
- [19] R. Farmani and J. A. Wright, "Self-adaptive fitness formulation for constrained optimization," *IEEE Transactions on Evolutionary Computation*, vol. 7, no. 5, pp. 445–455, 2003.

- [20] A. Anders, J. Andersson, and J.-O. Aidanpaa, "Constrained optimization based on a multiobjective evolutionary," in *Proceedings of the 2003 Congress on Evolutionary Computation*, Canberra, ACT, Australia, December 2003.
- [21] A. B. Smolders, S. J. Geluk, and A. C. F. Reniers, "Circularly polarized sparse arrays realized by randomly rotated linearly polarized antennas," *IEEE Antennas & Wireless Propagation Letters*, vol. 99, p. 1, 2017.
- [22] Z. Cai and Y. Wang, "A multiobjective optimization-based evolutionary algorithm for constrained optimization," *IEEE Transactions on Evolutionary Computation*, vol. 10, no. 6, pp. 398–417, 2006.
- [23] Z.-k. Chen, Y. Feng-Gang, Q. Xiao-Lin, and Z. Yi-Nan, "Sparse antenna array design for MIMO radar using multi-objective differential evolution," *International Journal of Antennas and Propagation*, vol. 2016, Article ID 1747843, 12 pages, 2016.
- [24] F. Xue, A. C. Sanderson, and R. J. Graves, "Pareto-based Multi-objective differential evolution," in *Proceedings Of The 2003 Congress On Evolutionary Computation*, Canberra, Australia, December 2003.
- [25] M. Ali, P. Siarry, and M. Pant, "An efficient differential evolution based algorithm for solving multi-objective optimization problems," *European Journal of Operational Research*, vol. 217, pp. 404–416, 2012.
- [26] S. K. Goudos and J. N. Sahalos, "Pareto optimal microwave filter design using multiobjective differential evolution," *IEEE Transactions on Antennas and Propagation*, vol. 58, no. 1, pp. 132–144, 2010.
- [27] CVX Research Inc: sedumi\_1.3 toolbox, 2014, <http://cvxr.com>.